RHEOLOGY AND DESIGN OF YIELD-STRESS FLUIDS

BY

ARIF Z. NELSON

DISSERTATION

Submitted in partial fulfillment of the requirements
for the degree of Doctor of Philosophy in Mechanical Engineering
in the Graduate College of the
University of Illinois at Urbana-Champaign, 2018

Urbana, Illinois

Doctoral Committee:

Associate Professor Randy H. Ewoldt, Chair & Director of Research
Professor Charles M. Schroeder
Professor Ralph G. Nuzzo
Professor Nancy R. Sottos

Abstract

Yield-stress fluids are materials that transition from solid-like to fluid-like at a critical applied stress and are currently the most utilized rheological phenomenon. Yield-stress fluids have found use in drug delivery, food products, batteries, surface coatings, 3D printing materials, and many other applications. This rheological phenomenon can be achieved by a diverse range of microstructures including polymeric gels, colloidal glasses, and more. Rationally designing such rheologically complex materials requires the determination of the relationships between processing, structure, properties (rheology), and ultimately performance. This research is composed of distinct but interconnected experimental studies of these design relationships for yield-stress fluids. This work presents a paradigm for the design of rheologically-complex materials focused on the rheology-to-structure inverse problem for model yield-stress fluids which forms the basis for the subsequent studies that focus on a particular secondary property (extensibility), particular applications (direct-write 3D printing and performance magic), and appropriate processing to obtain a yield-stress fluid material. I generate a design space for material selection and design of extensible yield-stress fluids and introduce model materials with this important behavior. One model material is the subject of a case study on direct-write 3D printing; an emulsion with high extensibility is used to establish key property targets for direct-writable materials. Another study discusses the role of a yield stress and high extensibility in a resin used in performance magic, “Mystic Smoke”. The final study focuses on the connection between processing and rheology for a particular material, aqueous methylcellulose, and investigates the effects of dynamic conditions on the linear and nonlinear mechanical properties of gelling materials or yield-stress fluids.

Acknowledgements

The work presented in this thesis would not be possible without the support of many incredible people that I have had the pleasure and good fortune to meet.

I thank my research advisor Randy H. Ewoldt who has been an inexhaustible source of enthusiasm, creativity, and expert support. It is due to Randy's mentorship and the freedom he provided me to invest in numerous pursuits—from developing lectures on design and creativity, to research on performance magic, to video-editing of science experiments done by visiting speakers—that has kept me intellectually energized and excited throughout my graduate career. He has been a marvelous advisor; I am fortunate to have been in the first class he taught at the University of Illinois and that he recognized some potential in me that led us to this point.

I thank my doctoral committee, Drs. Charles Schroeder, Ralph Nuzzo, and Nancy Sottos, for insightful questions, suggestions, and encouragement. I thank all my collaborators, but especially Dr. Brittany Rauzan and Jia En Aw for teaching me about direct-write 3D printing techniques and materials; Drs. Rafael Bras and Jingping Liu at Wm. Wrigley Jr. Company which sponsored my initial work on the design of extensible yield-stress fluids; and Drs. Bob Sammler, Aslin Izmitli, and Josh Katz at Dow Chemical Company which sponsored my work on dynamic gelation. I acknowledge the support of U.S. Department of Energy, Office of Science, Basic Energy Science (DE-FG02-07ER46741). I thank Dr. Simon Rogers for his insightful questions and encouraging me to begin my research on the rheology of performance magic materials.

I thank all my fellow graduate students in the Ewoldt Research Group, but especially Rebecca Corman, Piyush Singh, and Gaurav Chaudhary; former members Drs. Ashwin Bharadwaj, Brendan Blackwell, and Jeremy Koch; and honorary members Kate Dahlke, and Dr. Ritu Raman.

They have been excellent colleagues, mentors, and friends. I thank all of my past undergraduate assistants for all of their hard work and for contributing to my growth as a mentor. In particular, I thank Jennifer Lin, Yushi Wang, and Anthony Margotta, who I am proud of for their own personal and professional achievements. For all of their entertaining antics that have kept me sane through long work sessions, I thank all of the past and present members of the website, Giant Bomb, but especially Jeff Gerstmann, Vinny Caravella, and Austin Walker. I thank all my friends from the Chemical Engineering Department. I thank my parents, Faruq Nelson and Norsidah Saabin, as well as my sister, Amirah, for their support and encouragement throughout my life.

Finally, I thank my amazing wife, Jiaxun Xie, whose love, care, and hard work motivates me to be the best and the most amazing that I can be.

Table of Contents

Chapter 1: Introduction 1

Chapter 2: Design of yield-stress fluids 5

2.1 Introduction 5

2.2 Background 7

2.2.1 Design Process Theory 7

2.2.2 Materials Design Approaches 8

2.3 Materials and Methods 11

2.4 Design Methods for Yield-Stress Fluids 13

2.4.1 Rheology-to-Structure Inverse Problem & Organization 13

2.4.2 Yield Stress Scaling Behavior 19

2.4.3 Low-Dimensional Descriptions for Selection of Yield-Stress Fluids 24

2.4.4 Visualizing Secondary Properties 28

2.4.5 Synthesis Approaches for Yield-Stress Fluids 34

2.5 Case Studies 36

2.5.1 Case Study 1: Yield-stress fluid adhesive design (material selection) 36

2.5.2 Case study 2: Extensible yield-stress fluid design (material concept synthesis) 40

2.5 Conclusions and Outlook 42

Chapter 3: Characterization and design of highly-extensible yield-stress fluids 44

3.1 Introduction 44
3.2 Background 46
3.3 Materials and Methods 48
3.4 Results 51
3.4.1 Archetypal Yield-stress Fluids and Consumer Products 51
3.4.2 Design and Analysis of a Model Material 56
3.5 Conclusions and Outlook 62
Chapter 4: The rheology of magic – Mystic Smoke 65
4.1 Introduction 65
4.2 Methods 67
4.3 Results 68
4.3.1 Apparent Yield Stress Behavior 68
4.3.2 Extensional Behavior 69
4.4 Discussion 70
4.4.1 Filament Formation 70
4.4.2 Filament Shape Retention 72
4.5 Conclusions and Outlook 73
Chapter 5: Direct-write 3D printing model-material design 75
5.1 Introduction 75
5.2 Results and Discussion 79

5.2.1 Fabrication of Particle-Free Emulsions and 3D Printed Filament Resolution 79
5.2.2 Rheological Properties Enable 3D Printed Structures 82
5.2.3 Synthesis of 3D Printed Mechanically Robust Elastomers 92
5.3 Conclusions and Outlook 97
5.4 Materials and Methods 98
Chapter 6: Gelation under stress of hydrogels 105
6.1 Introduction 105
6.2 Materials and Methods 108
6.3 Results 112
6.3.1 Gel Point and Liquid Properties 112
6.3.2 Hot Gel Properties 117
6.4 Conclusions and Outlook 123
Chapter 7: Conclusions and outlook 125
References 130
Appendix A: Supplementary Information for Chapter 2 158
A.1 Detailed Rheological Data 158
A.2 Comparison of High-dimensional Data 165
Appendix B: Supplementary Information for Chapter 3 166
B.1 Considère Criteria for a Generalized Newtonian Fluid 166
B.2 Detailed Extensional Rheology Data 167

B.3 Characterization of 50 wt% oil model formulation 174

Appendix C: Supplementary Information for Chapter 5 175

Appendix D: Supplementary Information for Chapter 6 182

D.1 Application Stress Magnitudes 182

D.1.1 Gravitational stress on a vertical surface. 182

D.1.2 Characteristic stress of droplet impact. 183

D.1.3 Characteristic stress of particle settling. 184

D.2 Full Rheological Data 185

D.2.1 Quiescent Gel Point 185

D.2.2 Dynamic Gel Point 188

D.2.3 Hot Gel Properties 190

Chapter 1: Introduction*

Rheologically-complex fluids have the potential to meet numerous and diverse design objectives[1]. Inspiration can be found in biological systems with complex fluids [2] and soft solids [3,4], and many engineered systems use rheologically-complex behavior as a design strategy [5,6]. Currently the most utilized rheological phenomenon is the dramatically shear-thinning "yield-stress fluid," the reversible transition from solid-like to liquid-like behavior at a critical applied stress. Above the yield stress, these materials flow readily, facilitating deposition or distribution; below the yield stress, shapes or suspended components are held in place. An example of this type of fluid is shown in Figure 1.1; a green acrylic paint with a yield stress of approximately 10 Pa was squeezed between two plates that were then separated, producing a viscous fingering instability [7,8] that holds its final shape.

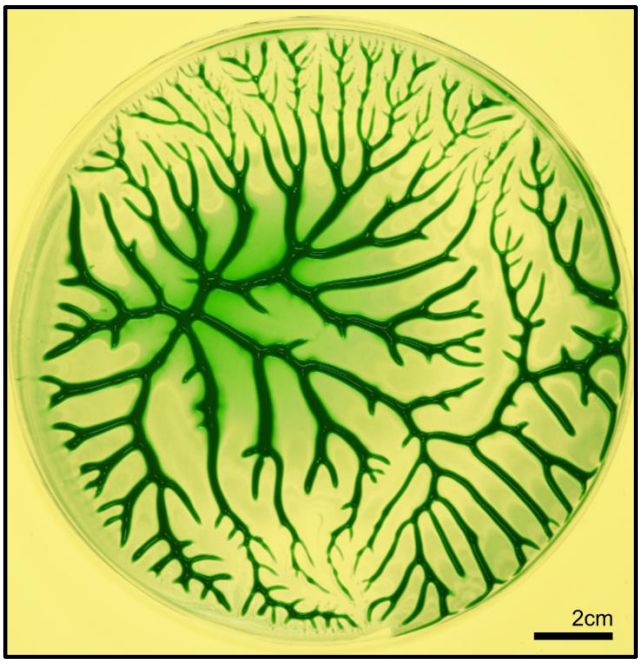

Figure 1.1 A yield-stress fluid (acrylic paint) holding the fractal-like shape of a viscous-fingering instability.

* Portions of this chapter appeared in the following peer-reviewed publications (re-used with permission):
A.Z. Nelson, R.H. Ewoldt, Design of yield-stress fluids: a rheology-to-structure inverse problem, Soft Matter. 13 (2017) 7578–7594. doi:10.1039/C7SM00758B.

The importance of yield-stress fluids in daily life and industry cannot be overstated as the concept applies to products as pedestrian as paint and toothpaste but also to applications as esoteric as crude oil gelation and rocket fuel [9–11]. Consider a few other examples. A yield stress was a sufficient property to enable a new production technique for tailorable ceramic beads [12]. In the food industry, the yield stress is of great importance for processing, manufacturing, and functional properties, as well as for correlation with sensory indices [13]. In 3D printing applications, yield-stress materials have been taken advantage of for inks that hold their extruded shape, for cellular composites [14]; and for a medium in which to print large complicated structures with microscopic precision [15]. Electrically or magnetically responsive yield-stress fluids can be used as active mechanical elements that respond to their environment [16,17]. An optimal yield stress value in flow batteries balances an increased electrical conductivity through plug flow with the cost of increased mechanical pumping [18]. For biomedical applications, an emerging paradigm of moldable hydrogels is based on yield-stress fluids capable of drug delivery [19].

Though it has been debated whether a "true" yield stress exists [10,20], yield-stress fluids are accepted as a practical reality, with definitions hinging on the critical value of stress that results in flow. Example definitions include: "[a yield-stress fluid] does not flow if the imposed stress is below a threshold value, but it can flow rather easily after this value is exceeded [9]", and, "[a yield-stress fluid combines] solid-like behavior at low stresses with a fluid-like response at high stress [21]." The controversy over a "true" yield stress comes from observations of extremely slow flow below any critical stress value [10], however on the timescales of many applications this deformation is not significant. Additionally, several reviews focus on the numerous ways a yield stress may be determined including steady flow tests, oscillatory shear tests, and compressional

tests to name a few examples [11,13,22]. Any yield stress value obtained is representative of a (typically narrow) range of stresses to induce a particular type of flow or irreversible deformation.

The objective of this work is to establish the design relationships between performance, rheological properties, material structure/formulation, and processing for key yield-stress fluids, and to provide methodologies that can be applied to a wide variety of other rheologically-complex materials; these design relationships are shown schematically in Figure 1.2.

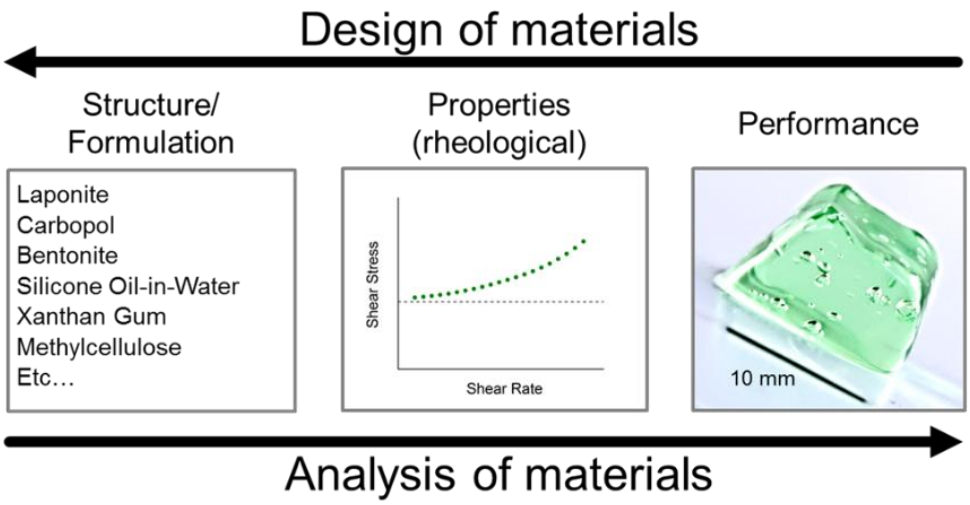

Figure 1.2. Design is the inverse of analysis and starts with a desired performance and results in what material best achieves that performance. Determining the relationships between performance, properties, and structure is key for effective design. Not depicted is the material processing, which often strongly impacts the resulting structure.

This work begins by adapting engineering design theories to yield-stress fluids, organizing and guiding subsequent research across material classes of soft matter based on desired rheological properties. This thesis develops a design framework by first by considering well-studied *archetypal* yield-stress fluids, i.e. materials one may regard as "classic" yield-stress fluids within rheological literature (Chapter 2). With this framework in place, and in collaboration with Wm. Wrigley Jr. Company, this work moves on to considering the available design space for a particular

secondary property of yield-stress fluids, extensibility (i.e. strain to rupture in extension). The results illustrate a huge gulf in the extensional properties of the model archetypal materials and some yield-stress fluids used in application, motivating the development of a model highly-extensible yield-stress fluid (Chapter 3). Motivated in-part by a personal hobby, I perform an in-depth study of a material used in performance magic, Mystic Smoke (Chapter 4). I show how the performance of this material seems to rely on its rheological properties of being both a yield-stress fluid and highly extensible. A second model highly-extensible yield-stress fluid was developed to investigate the role of extensibility in direct-write 3D printing performance in collaboration with Dr. Brittany Rauzan, Dr. Sean Lehman, and Professor Ralph Nuzzo in the Department of Chemistry. With this model fluid, particle-free emulsions are introduced as a novel class of materials for direct-write 3D printing, and by varying the composition of the emulsion system, the relationships between microstructure, critical rheological properties, and printing performance are developed (Chapter 5). This thesis concludes by investigating the effect of shear flow on the gelation and properties of aqueous methylcellulose (MC), a thermally gelling material that conventionally would not be classified as a yield-stress fluid since it fractures rather than flows. However, under appropriate processing conditions (e.g. strong shear while heating), completely different properties result, and a soft granular yield-stress fluid is obtainable. In collaboration with The Dow Chemical Company, a protocol for gelation under constant unidirectional shear stress is developed and significant softening and weakening of a low molecular weight MC aqueous dispersion is observed (Chapter 6).

Chapter 2: Design of yield-stress fluids*

2.1 Introduction

In the field of rheology, most works in the public domain focus on the *analysis* of materials rather than researching and developing more useful *design* practices and methodologies; these complementary approaches are depicted in Figure 1.2. By *analysis*, this work means that, starting with known ingredients or a known microstructure, a material is characterized, and these properties are related to the macroscopic performance. Of course, carrying out the analysis perspective is non-trivial for rheologically-complex materials; the characterization of properties can be especially arduous due to their function-valued nature, and so several complicated structural and observational dependencies are used to describe a single material. To *design* a material is the inverse of this analysis process and fundamentally is about making decisions [23]; starting with the desired macroscopic performance, decisions must be made on what properties might achieve that objective, and in turn what ingredients or microstructure might result in those properties.

We emphasize that designing does not *only* mean formulating or building entirely new materials. It also includes determining a set of target specifications (qualitative or quantitative), as well as generating a set of concepts that *may* satisfy these specifications by surveying and organizing *existing* materials as well as ideating new material concepts. After generation of concepts, selection of existing materials and of candidate new material concepts to prototype and formulate is carried out. Additional downstream processes then take place. This work contributes to the necessary upstream steps of the design process, providing methodologies for establishing

* Preliminary work on this topic appeared in the author's master's thesis and this chapter appeared in the following peer-reviewed publications (re-used with permission):
A.Z. Nelson, R.H. Ewoldt, Design of yield-stress fluids: a rheology-to-structure inverse problem, Soft Matter. 13 (2017) 7578–7594. doi:10.1039/C7SM00758B.

target specifications, generating concepts of yield-stress fluids, and comparing and selecting based on rheological properties. This work does not provide tools for the equally important—but often over-prioritized—downstream steps of the design process such as material formulation, material optimization, and production ramp-up. Predictive tools and models for these downstream steps are, of course, immensely difficult to develop for real materials and likely need to be developed on an individual basis. Specific aspects outside the scope of this work are down-selection based on non-rheological criteria, formulation guidelines or optimization of a specific material microstructure, and application-specific performance objectives; our focus is broader and contributes to earlier stages of the design process [24].

Our goal here is to adapt engineering design theories to rheologically-complex materials, specifically yield stress fluids, thus organizing research efforts across material classes of soft matter by using *functional requirements* based on desired rheological properties. As specific contributions, this work examines: (i) organization of structure-to-property design strategies based on jammed versus networked microstructures, (ii) collected scaling laws for predictive property design, (iii) low-dimensional descriptions of function-valued flow properties, (iv) property visualization (Ashby-style charts) that consider secondary properties including viscous behavior, and (v) a strategy for material concept synthesis (ideation) based on the juxtaposition of microstructure design strategies to generate new ideas. By successfully applying design techniques to yield-stress fluids, this work will demonstrate design paradigms that can more generically be used with other rheologically-complex properties.

To study and develop design methodologies for rheologically-complex materials, this work characterizes well-studied *archetypal* yield-stress fluids, i.e. materials one may regard as “classic” yield-stress fluids within rheological literature. These yield-stress fluids were chosen to survey a

wide variety of chemistries, as well as different microstructures which can be categorized by the mechanism by which the yield stress comes about (discussed in detail in Section 2.4.1.). Characterized materials are Carbopol 940 (jammed microgel), silicone oil-water and mineral oil-in-water emulsions, Bentonite and Laponite RD (colloidal clays), and xanthan gum (polymer gel). Sample formulation, preparation steps, and characterization details are given in Section 2.3. Experimental results at multiple gaps are given in Appendix A. For this chapter, parallel disk steady flow is used for characterization, with corrected shear-stress values as a function of shear rate. By this method, I obtain the dynamic yield stress and the shear rate dependent flow behavior which is likely to be one of the most important secondary properties of interest. Equally important properties outside the scope of this work include critical yield strain and pre-yield modulus (oscillatory measurement), and static yield stress (creep, increasing shear rate flow tests) [20]. Although the chemistry and microstructure vary, these archetypal materials have overlapping ranges of dynamic yield stress as weight percentage of additive is varied. Clearly there are numerous ways to achieve the same yield stress with these materials, and therefore designing such materials is an inverse problem.

2.2 Background

2.2.1 Design Process Theory

In this section, I will briefly describe how I will map concepts from engineering design onto yield-stress fluids. This work makes contributions to the concept development phase of design. While the downstream optimization and detail design phases are necessary, they are premature without first considering multiple concepts.

To set the stage for concept development, the functional requirements and target specifications of a material must first be described. Since functional requirements cannot specify a particular solution without imposing creativity-stifling restrictions [24–26], for the design of a yield-stress fluid, a poor functional requirement might be, "a polymeric network that flows under stress and reversibly solidifies at low stress" (particular material structure specified).

Using a suitable functional requirement, a set of numerous possible concepts are obtained through surveying existing materials and through various brainstorming and ideation strategies. Methodologies for these processes build on approaches from lateral thinking [27] including generating potentially unfeasible concepts, and delaying concept evaluation to a later stage of the design. In this work, multiple material structure concepts are considered as ways to achieve a particular rheological behavior, that of a yield-stress fluid. Numerous techniques exist for systematic concept generation; in this work I use "categorization of concepts" (Section 2.3.1) and "juxtaposition" (Section 2.3.5), the latter involves combining two concepts to produce something new [27]. Following their generation, concepts would be evaluated for further development. For the design of complex fluids, concept evaluation often involves material formulation and rheological analysis.

2.2.2 Materials Design Approaches

The design process of concept generation (surveying and ideation) maps to *material selection* and *material synthesis*. For a new product or application, a material can either be selected from existing concepts or newly synthesized.

For materials that are not rheologically-complex, theories and methodologies of material selection have been well developed; the most influential methods are described by Ashby [28]. A

flowchart depicting Ashby's selection process is shown in Figure 2.1 with an example material-property co-plot. For this process, a far-reaching and robustly organized database of material properties is the required starting point; relevant constraints and rankings of suitability are then applied. This process has found great success for simple materials whose properties are scalar parameters (e.g. density, modulus), in contrast to the function-valued properties (material functions) that describe rheological behavior.

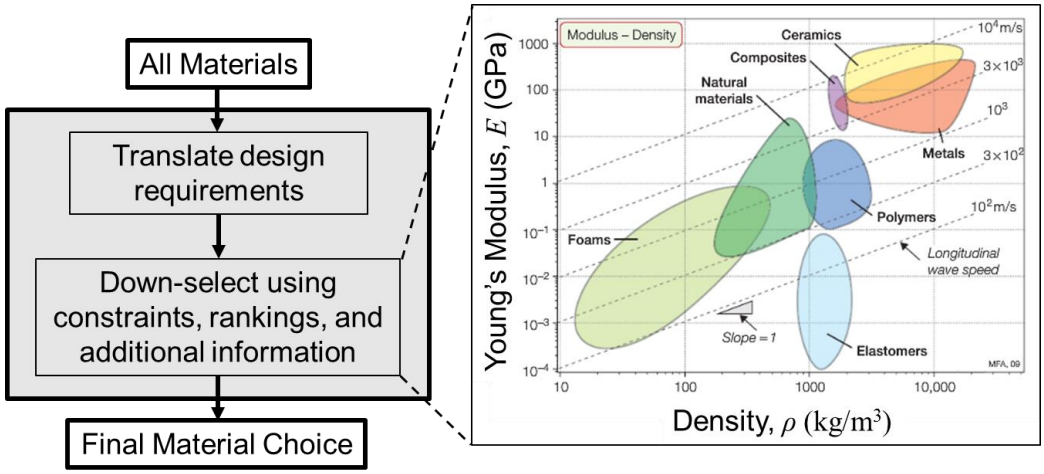

Figure 2.1. Flowchart representation of material selection method (adapted from [28]). Starting from a database of all surveyed materials, design constraints and further research enable one to down-select to a final material choice. A common tool used in the down-selection process is the "Ashby diagram" (pictured from [28]), which is a material-property co-plot used to compare and show trends of multiple material properties across different material types. Rheological properties are challenging to visualize in this way when they are functions, rather than constants.

For rheologically-complex materials, material selection databases and design textbooks are completely absent (in the public domain), with the next best things being rheological modifier handbooks [29,30] and material class specific texts [31]. While useful, the available handbooks lack much of the needed information for effective, creative, rational design. The greatest inadequacy of such handbooks is the general failure to express or acknowledge the function-valued nature of properties. As an example, though the ubiquity of yield-stress fluids has already been stated, available handbooks, Braun [29] and Ash [30], only mention the phenomenon *once* out of

all the numerous rheological modifiers they list, with Braun [29] providing only viscosity values at a single reference shear rate for particular weight percentages of additive (for a nonlinear viscoelastic material).

The lack of a database of rheological data sets in the public domain has been identified previously, along with the necessity for a standard that these data sets conform to for facilitating comparison [32]. There are several unique difficulties that must be addressed in establishing a more effective organization and design database for yield-stress fluids: i) function-valued properties (e.g. no single value of viscosity exists), ii) some rheological phenomena are not achieved by all materials, iii) the conceptual model of a yield-stress fluid still being somewhat controversial. These issues are generally not present in solid materials which all have a basic set of simply-defined material properties such as density and Young's modulus.

There is an increasing interest in using inverse design methods to create materials that achieve functional requirements [33–39] including a focus on properties which may be achieved by numerous formulations [40]. Principles of material selection were applied by Ewoldt [1,41] in designing a material for use in robotic adhesive locomotion; a minimum yield-stress was the primary design objective and a low post-yield viscosity at a reference shear rate was the secondary objective. This previous work is built upon with the specific contributions mentioned in Section I. By applying inverse design methods to rheologically-complex material properties this work hopes to enable more creativity for these materials, broadening the concept generation space before fixating on any particular structure. In this work, the fundamental strategies and methodologies known to exist for designing a yield-stress fluid are explicitly stated, thereby forming an ontology and the basis for a database for the engineering of rheologically-complex materials [42]. This work then demonstrates the usefulness of this ontology and database through several case studies.

2.3 Materials and Methods

Table 2.1 describes the specific material compositions presented in this paper; sample preparation steps are as follows. This section also details the experimental setup and model fitting protocol.

Aqueous suspensions of polymer microgel particles were prepared from Carbopol 940 obtained from Acros Organics. Powdered material was mixed with steam distilled water for thirty minutes before being neutralized to a pH of 7 using a sodium hydroxide solution, resulting in the swollen microgel particles that are jammed at sufficiently high concentrations [43].

Silicone oil-in-water emulsions were formulated with 1000 cSt (at 25 °C) silicone oil obtained from Sigma-Aldrich and deionized water; sodium dodecyl sulfate (SDS) from Fisher Scientific was used as the emulsifier. The mixture was homogenized at 5000 rpm for 10 minutes using an IKA T-18 homogenizer with an S18N-19G dispersing element attachment. Mineral oil-in-water emulsions were synthesized by the same procedure using light mineral oil from Sigma Aldrich which has a viscosity between 14.2 and 17.0 cSt at 40 °C.

Bentonite from Sigma Aldrich was dispersed in steam distilled water using an overhead stirrer at approximately 300 rpm until mixed, at which point the clay particles form a percolated gel network [20]. The Laponite RD suspension, which also has particles that can attractively interact, was synthesized by the same procedure as the Bentonite suspensions with powder obtained from Conservation Support Systems. Bentonite and Laponite suspensions were allowed to stand quiescently for one week before testing to hydrate [44].

Xanthan gum from *Xanthomonas Campestris*, a polymer which is known to form structure in solution through self-associative intermolecular attractions [45], was obtained from Sigma-

Aldrich. Solutions were formulated by slowly adding xanthan gum powder to deionized water being mixed with an overhead stirrer at between 300 and 600 rpm. Solutions were mixed for 5 minutes before being covered with tin foil and placed on a hotplate at 80 °C to mix at 400 rpm for an additional 30 minutes.

Table 2.1. Material formulations organized by material and weight-percentage of additive. In all cases, remaining wt% is of water

Material	wt% Solid Content	
Carbopol	0.1, 0.15, 0.2, 0.25, 0.5	
Bentonite	7, 8, 9, 10, 11, 12	
Laponite	3, 4, 5	
Xanthan Gum	2, 4, 5	
	wt% Oil	wt% SDS
Silicone Oil-in-Water Emulsion	65	11.7
	70	10
	75	8.3
	80	6.7
Mineral Oil-in-Water Emulsion	65	11.7
	75	8.3

Rheological characterization of steady flow properties was performed on rotational rheometers (combined motor/transducer instruments, TA Instruments DHR-3 or AR-G2) using a parallel-plate geometry with a diameter of 40 millimeters. Depending on the sample, either a sandblasted plate or adhesive-backed silicon carbide sandpaper (600 grit or 60 grit) was used to prevent slip. Materials were tested at multiple gaps to verify the absence of slip [46]. Parallel-plate corrections

were used to identify the true shear stress. Apparent stress, σ_A, was fit to a polynomial curve and corrected to the stress at the rim using,

$$\sigma_{True} = \frac{\sigma_A}{4}\left[3 + \frac{d\ln\sigma_A}{d\ln\dot{\gamma}_{True}}\right], \tag{2.1}$$

where $\dot{\gamma}_{True}$ is the apparent applied shear rate at the rim [47]. Unless otherwise specified, all steady flow tests are performed from high-to-low shear rates, thus the yield stress is a dynamic yield stress rather than a static yield stress [20]. All materials except Bentonite and Laponite (see above), were tested within one week of formulation. Full steady shear flow curves are shown in Appendix A.

Shear flow measurements were fit to parameterized equations (Bingham and Herschel-Bulkley, details in Section 2.4.3). For some materials, especially at smaller gaps, an increasing stress was observed as the shear rate was lowered, creating a non-monotonic flow curve [48]. In the case of these materials, the fitting was only done with the higher shear rate data lying between the highest and lowest values of corrected stress. When fitting the Bingham model, the yield-stress parameter was constrained to the lowest corrected stress value. All fitting was performed using OriginPro 9.0 software with variance weighting where the residual sum of squares, RSS, is calculated by,

$$\sum_{i=1}^{n}\left(\frac{\sigma_{Data,i} - \sigma_{Model}}{\sigma_{Data,i}}\right)^2. \tag{2.2}$$

2.4 Design Methods for Yield-Stress Fluids

2.4.1 Rheology-to-Structure Inverse Problem & Organization

There have been past attempts at categorizing yield-stress fluids based on the presence of a material restructuring time [20], the microscopic mechanism by which the yield stress emerges for

certain particulate systems [9], and the concepts of glasses and gels [49], however none are from the perspective of design. To facilitate design, the typical perspective of structure-to-rheology must be flipped to a property-based rather than microstructure-based organization. This represents an ontology, or taxonomy, to organize design solutions for yield-stress fluids.

The first step to ideate the many possible ways to achieve a yield-stress fluid is to describe the desired functionality, or *functional requirements* [25,50,51]. As described in Section 2.2.1, it is non-trivial to balance overly-narrow and overly-broad functional requirement descriptions to avoid unnecessarily limiting the possible design options. A good functional requirement contains only what is general and essential [50]

Existing functional requirement descriptions are available as *definitions* of a yield-stress fluid (quoted earlier in Chapter 1). These definitions are well-crafted in that they are completely formulation- and structure-agnostic, not presupposing anything about the material and only describing behavior. However, I feel they can be too broad for design ideation, since there is no concept of *reversibility* or *mechanical connectivity*, concepts which may help focus creative ideation of new microstructure designs and avoid implausible solutions. For example, the phenomenological definition "[a material] that shows little or no deformation up to a certain level of stress [and] above this yield stress the material flows readily [47]" lacks concepts of mechanical connectivity and reversibility. A formulation chemist might think to use entangled polymer solutions, but topological entanglements in solution do not bear static loads for long times, thus polymer solutions generally will not produce a yield stress fluid. Given a too-broad definition, one may also be limited to relying on only pre-existing lists of materials which, as discussed in Section 2.2.2, are themselves sorely lacking.

We propose the following more precise functional requirement that includes the structural concept of mechanical connectivity, which is fundamental to yield-stress fluids:

> *A yield-stress fluid is able to bear a static load for long timescales (suitably high viscosity at low stress) with mechanical connectivity that yields, flows (measured by a dramatic drop in viscosity above a characteristic yield stress), and is recoverable.*

While somewhat long-winded to address the debated low-stress behavior, this newly proposed functional requirement provides physical insight into how one might achieve a yield-stress fluid in a precise way that is both formulation- and structure-agnostic, so as to not overly constrain the concept generation process. Rather than attempting to invent a way for viscosity to transition across multiple orders of magnitude, a designer can instead use intuition and experience about methods of bearing static loads that are able to reform after mechanical disruption. Additionally, after significant disruption by shear flow, some materials may show an increasing viscosity over time at low stresses [48,52], leading eventually to a stoppage of flow. To an observer it would be unclear if these materials are yield-stress fluids before the flow stoppage event. However, it is this signature of flow stopping for some finite applied stress (i.e. bearing a static load) that indicates that though the behavior of these materials is not that of an ideal yield-stress fluid, they are still yield-stress fluids. The buildup or recovery of this capacity to bear a static load is necessary for a material to be considered a yield-stress fluid. To be clear, by "recovery", I am not referring to elastic strain recovery, but instead the ability to yield, flow, and recover a yield stress again, even if not the same yield stress as before.

For existing yield-stress fluids, there are two known mechanical interactions by which our proposed functional requirement is satisfied: (i) jammed, repulsive interactions; and (ii)

networked, attractive interactions. Of course, these may co-exist in complex systems. These concepts of arrested structures have been well developed as “glasses” and “gels” respectively [53,54], and have been used to organize certain yield-stress fluids in the context of particle sedimentation [49]. Here this work uses this organization to provide insight into designing yield-stress fluids and to compare properties and behavioral trends across different microstructures.

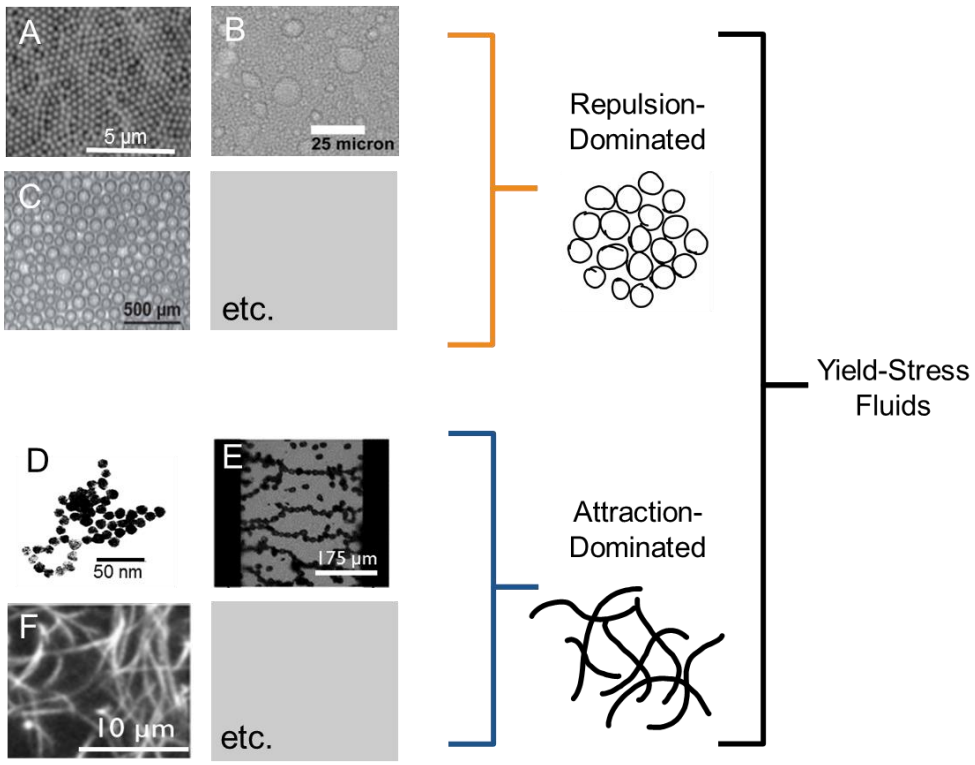

Figure 2.2. Organization of design strategies aids in concept generation, for both existing and new materials. For yield-stress fluid design, two generic strategies can be grouped as ‘repulsion-dominated’ and ‘attraction-dominated’ (although combinations also exist, e.g. attractive glasses). Examples shown are (A) particulate suspensions [55], (B) emulsions [56], (C) foams [57], (D) particulate gels [58], (E) electro/magneto-rheological fluids [59], and (F) fiber gels [60].

Figure 2.2 organizes yield-stress fluids based on the two mechanisms (or *design strategies*) of jammed versus networked microstructures. This work uses the term “repulsion-dominated” for materials where a static load is borne primarily by the microstructural elements jamming, pushing against nearest neighbors, with macroscopic yielding once the internal structure is able to rearrange

and slide past itself to flow. Examples within this repulsion-dominated design strategy include suspensions of polymer microgel particles (e.g. suspensions of crosslinked polyacrylic acid (Carbomer) [43] or Poly(N-isopropylacrylamide) (PNIPAm) [61]), oil-in-water emulsions [62–67], and foams [57,62,67,68], which are each pictured in Figure 2.2. Additional examples include spherical and star-like micelle solutions [69,70], suspensions of hard particles (colloidal [71–73] or non-Brownian, athermal, granular matter [74,75]), and suspensions of charged-particles, which are effectively jammed through electrostatic rather than steric repulsion [76]. Though the chemistry varies widely within and across these material classes, yield-stress fluid behavior is caused by the same fundamental mechanism of effectively crowded microstructural elements interacting repulsively. As seen in the images in Figure 2.2, morphologically these material classes are very similar. From these examples, one may ideate other possible materials that use this same mechanism. The characterized materials in this work that will be considered as "repulsion-dominated" are Carbopol 940 suspensions of swollen microgel particles that are jammed at sufficiently high concentrations [43], and silicone oil-in-water and mineral oil-in-water emulsions.

This work calls the second design strategy in our taxonomy "attraction-dominated", meaning materials where a static load is borne primarily by attractive mechanical connectivity (i.e. pulling on nearest neighbors). Attraction-dominated microstructures resist being pulled apart, eventually yielding once these re-formable attractions have been broken. Examples within this group include particulate gels (e.g. colloidal clays Bentonite [20,77–79] and Laponite [80–82]), magneto- and electro-rheological fluids [16,17,59,83–85], and fibrillar or polymer solutions that have physical crosslinks that can re-form after rupture (in contrast to covalent or non-recoverable crosslinks) [45,49,60,86–89]. Morphologically, material microstructures within this group typically are a sparse percolated network spanning the sample that must be destroyed for yielded flow to occur.

The characterized materials in this work that will be considered as “attraction-dominated” are suspensions of Bentonite and Laponite colloidal clay particles that can attractively interact [20], and xanthan gum which forms structure through self-associative intermolecular attractions [45].

For both of these design strategies, the “-dominated” qualifier has been used to acknowledge that combinations of both mechanisms are possible, such as attractive glasses [53]. Note that both the repulsion-dominated and attraction-dominated categories are capable of including materials that may have very similar ingredients. For instance, colloidal suspensions can exist as either glasses or gels [81,90] and thus this structural organization transcends the traditional academic organization by ingredient such as by “particle” versus “polymer”.

For material selection, the creation of any material property database is hindered by the fact that not all materials will have all properties. Rather than needing to laboriously characterize the hundreds of entries in a rheological modifiers handbook, one can instead consider if the modifier might possibly satisfy the functional requirement and only characterize those expected to have a yield stress. While mistakes will most certainly be made in this process, e.g. materials anticipated to have a yield stress will show no such signature or materials that do have a yield stress may be overlooked, it will be far less onerous and implausible than characterizing every possible formulation of every ingredient hoping to see a particular signature.

With our proposed functional requirement and the resulting classification tree, the material design methodologies of both selection and synthesis are greatly facilitated. Selection strategies benefit by being able to effectively generate lists of existing (but perhaps not relevantly analyzed) candidate materials to choose from, as well as insights into the comparative relations between material classes. With an adequate functional requirement, creative synthesis based on physical

insight can occur, with the classification tree allowing for ideation through structured concept generation.

2.4.2 Yield Stress Scaling Behavior

When evaluating and comparing concepts, an important aspect to consider is the degree of available predictive analysis. For example, deterministic models greatly facilitate phases of the design process involving prototyping and testing [51]. Models allowing for predictive analysis for yield-stress fluids are reviewed in this section, but the further downstream phases of the design process are not. The full scientific understanding of all material structures currently known to produce a yield-stress is underdeveloped due to the complexity of calculating macroscopic properties from the underlying microstructure and molecular features. In contrast to complex fluids, developed areas of mechanical design have very clear mathematical models to represent system behavior (e.g. stress fields in solid bodies, linkage dynamics, etc.).

A unique aspect of material synthesis for rheological properties is that governing equations are not always known. In the specific case of yield-stress fluids, if any predictive equations are available, they are often scaling laws that relate the yield stress to underlying structure. Available scaling laws for yield-stress fluids are collected in Table 2.2. While the large variety of model structures of the collected scaling relationships makes it clear that any sort of universal scaling law for a wide range of materials is still a monumental undertaking, general guidelines are still available by using these relationships. Between two otherwise comparable concepts, one would prefer a concept with a readily available predictive scaling law. Thus, this table is useful for the evaluation of concepts and can demonstrate the feasibility of a concept to achieve a particular performance.

Table 2.2. Structure-rheology scaling relationships and equations for yield-stress fluid material classes. These relationships are useful for concept evaluation and synthesis as they allow one to predict the resulting yield-stress to varying degrees. See Table 2 for the definitions of all variables.

Material Class	Scaling Relationship (Eqn. #)		Notes
Hard Spheres [91]	$\sigma_Y = \sigma_{Crit} + 112\sqrt{\phi - \phi_{Crit}}$	(2.3)	$\phi > \phi_{Crit}$
Charged Particles [92]	$\sigma_Y \approx K\left(\frac{W(r_m) - k_B T}{(r_m/2)^3}\right)$	(2.4)	$r_m < d_{eff}$ $K = constant$
Soft Particles [66]	See Reference		
Emulsions and Foams [62]	$\sigma_Y = \frac{\Gamma}{R_{mean}}\phi^{\frac{1}{3}}Y(\phi)$	(2.5)	$\phi > 0.9069$
Particulate Gels [93]	$\sigma_Y \sim \frac{\phi^2}{a^2}W'_{\max}$	(2.6)	$\phi < 0.64$
Electrorheological Fluids [83]	$\sigma_Y \sim \phi\varepsilon_0\varepsilon_S\beta^2E^2f_m$	(2.7)	
Magnetorheological Fluids [85]	$\sigma_Y \sim H^2$	(2.8)	Low field strength
	$\sigma_Y = \sqrt{6}\phi\mu_0 M_S^{\frac{1}{2}}H^{\frac{3}{2}}$	(2.9)	Intermediate field strength
	$\sigma_Y^{Sat} = 0.086\phi\mu_0 M_S^2$	(2.10)	Fully-saturated yield strength

Table 2.3. Variable definitions for yield stress scaling relationships. Note: *F* indicates units of force, *L* units of length, *A* units of electrical current, *t* units of time.

Variable	Definition
$\phi_{Crit} \doteq [-]$	Critical volume fraction for yield stress scaling to apply
$\sigma_{Crit} \doteq \left[\frac{F}{L^2}\right]$	Yield stress at critical volume fraction
$W(r_m) \doteq [FL]$	Interaction potential at average interparticle separation
$d_{eff} \doteq [L]$	Effective diameter of particle, where $W(r = d_{eff}) \approx k_B T$
$\Gamma \doteq [F / L]$	Surface tension
$R_{mean} \doteq [L]$	Sauter mean radius, $R_{mean} = 3\frac{Volume}{Surface\ Area}$
$Y(\phi) \doteq [-]$	Scaled contribution per drop to yield stress, $Y(\phi) = -0.08 - 0.114\log(1-\phi)$
$a \doteq [L]$	Particle radius
$W'_{\max} \doteq [F]$	Maximum spatial gradient of interaction potential
$\varepsilon_0 \doteq \left[\frac{(At)^2}{FL}\right]$	Permittivity of space
$\varepsilon_S \doteq [-]$	Relative permittivity of solvent
$\beta \doteq [-]$	Effective polarizability of particle
$E \doteq \left[\frac{F}{At}\right]$	Electric field strength
$f_{\max} \doteq [-]$	Maximum dimensionless restoring force between particles
$H \doteq \left[\frac{A}{L}\right]$	Magnetic field strength
$M_S \doteq \left[\frac{A}{L}\right]$	Saturated magnetic field strength
$\mu_0 \doteq \left[\frac{F}{A^2}\right]$	Permeability of space

While not the focus of this work, these scaling laws are eminently useful further downstream in the design process when attempting to determine final formulations in the system-level and detail design phases. Additionally, all of the listed scaling laws are for the single parameter of the yield stress; predictive structure-rheology equations for entire flow curves are even more difficult to formulate, though in a few cases they do exist [66].

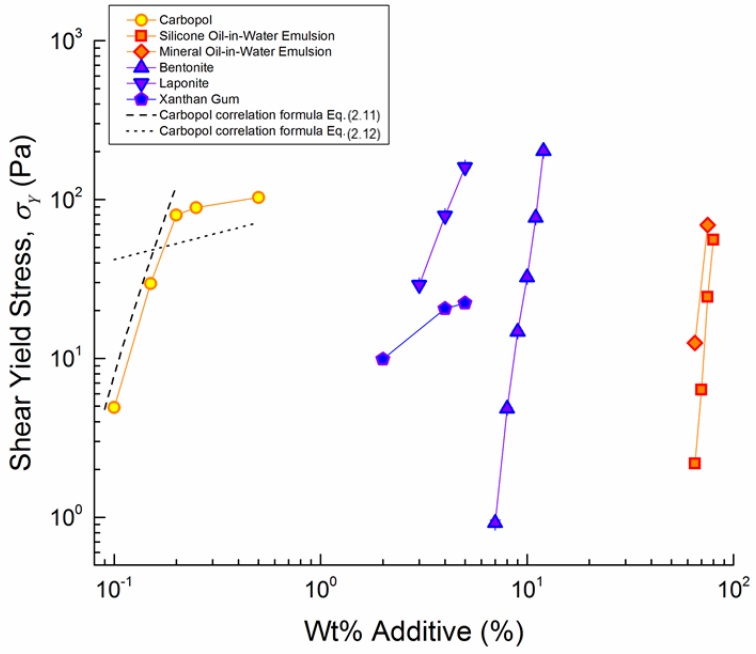

Figure 2.3. Shear Yield Stress versus wt% additive. Percentage of additive, and constraints thereof, is often crucial for achieving design targets. Each data point represents a steady shear flow curve. See Appendix A for full steady shear flow data at multiple gaps used for this plot.

Most of the presented structure-rheology scaling relationships involve the volume fraction of some dispersed phase of the material, however oftentimes in formulation it is much easier to control the weight-percentage of an additive rather than its volume. Carbopol 940 has specific scaling equations obtained by correlation with many different experimental studies to relate the

weight-percentage additive, C, directly to the yield stress for two different concentration regimes [43],

$$\sigma_Y = \left(\frac{C}{0.0335} - 1 \right)^3 \tag{2.11}$$

$$\sigma_Y = 45 \left(\frac{C}{0.124} \right)^{1/3}. \tag{2.12}$$

These correlation formulae agree reasonably well with our experimental results for Carbopol, seen in Figure 2.3 alongside the other tested material systems. The weight-percentage of additive is often of great importance when designing a completely new material or modifying an existing material to give it a yield stress.

To the authors' knowledge, the considered material systems besides Carbopol do not have yield stress data organized in the open literature in such a way as to form concentration scaling relationships, except that some type of power law dependence occurs close to a jamming transition. The yield stress of Xanthan gum solutions scales approximately linearly with concentration, while the yield stresses of the two-other attraction-dominated systems, Bentonite and Laponite, have power law slopes of approximately three and nine respectively. The yield stresses of jammed emulsions have the strongest dependence on weight-percentage, with power law slopes of between twelve and fifteen.

Typically, a low percentage of additive is desirable, since it will be less costly and less likely to modify other properties, such as the flavor and texture of food products. Based on the classification tree of yield-stress fluids one can see that the networked, attractive systems achieve yield stresses at moderate values of weight-percentage, while both jammed, repulsive emulsions require a significant percentage of added-oil for comparable yield stress values. The swollen nature of the Carbopol microgels are what result in such a low weight-percentage of additive giving rise

to a jammed yield-stress fluid; this is the reason that Carbopol is considered a “high-efficiency” rheological modifier [29]. Obviously, there are endless parameters and material properties that might be crucial for one’s application such as transparency and other optical properties, conductivity, biocompatibility, and biodegradability. In the next section, this work will consider rheological properties beyond the yield stress by introducing representations of the steady flow behavior to enable the application of material selection principles to function-valued properties.

2.4.3 Low-Dimensional Descriptions for Selection of Yield-Stress Fluids

Since a particular value of yield stress can be achieved by multiple materials, applying additional design constraints on secondary parameters or properties is a critical step in converging on a final design choice in a rational, non-arbitrary way. However, due to the function-valued nature of rheologically-complex material properties, low-dimensional representations are necessary for their easy comparison. Appendix A shows the full flow curves of all materials measured here and demonstrates how infeasible the rational selection of one particular material would be without using a low-dimensional representation. Of course, information is always lost when representing complicated data in a low-dimensional way. Here this work will consider different models which communicate information to varying degrees of completeness and discuss the situations in which the loss of information can be acceptable.

The most common models for yield-stress fluids are the three-parameter Herschel-Bulkley model and two-parameter Bingham model. The Herschel-Bulkley model is typically written as,

$$\sigma = \sigma_Y + K\dot{\gamma}^n \tag{2.13}$$

which I prefer to re-write as,

$$\sigma = \sigma_Y \left[1 + \left(\frac{\dot{\gamma}}{\dot{\gamma}_{critical}} \right)^n \right]. \tag{2.14}$$

This updated representation of the Herschel-Bulkley model is better for design comparisons because the dimensions are fixed for all parameters, independent of other parameter values. It results in the parameter $\dot{\gamma}_{critical}$ that is physically meaningful as a critical shear rate at which the flow stress is twice the value of the yield stress, σ_Y. This physical intuition is desirable compared to the parameter *K*, which has units that depend on the parameter *n*. Unless otherwise specified, our reported values of a material's yield-stress were taken from the Herschel-Bulkley model fit, but the widely-used Bingham model was also fit for comparison. The two-parameter Bingham model which fits the yield stress and infinite shear viscosity, η_∞, is

$$\sigma = \sigma_Y + \eta_\infty \dot{\gamma}. \tag{2.15}$$

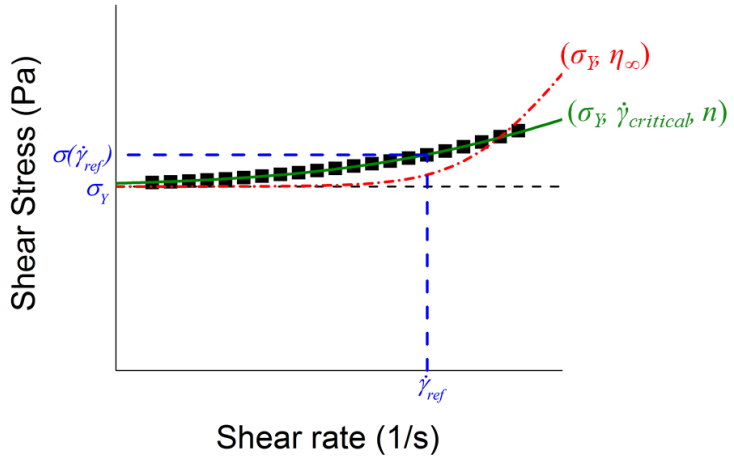

Figure 2.4. Low-dimensional representations of function-valued rheological data; here, a steady flow curve. Low-dimensional descriptions are required for easy comparison of materials when selecting or evaluating with Ashby-style diagrams. More accurate representations can come at the cost of decreased physical meaning and added complexity. Here, three possible representations of a yield-stress fluid are shown: (blue dashed) two stress values, the yield stress and the stress at some reference shear-rate; (red dash-dot) the two-parameter Bingham model; and (green solid) the three-parameter Herschel-Bulkley model.

Shown in Figure 2.4 are three possible low-dimensional descriptions of the steady flow behavior of a yield-stress fluid: two values of shear stress (the yield-stress parameter from the Herschel-Bulkley model and the stress at a reference shear rate); the Bingham model, Equation (2.15); and the Herschel-Bulkley model, Equation (2.14). Clearly the reference-shear-rate representation loses a significant amount of information about the flow curve, though it has been used when selecting for minimum rheological criteria [41]. Our work focuses on the Bingham and Herschel-Bulkley model representations since they preserve substantially more information. In most cases, the two-parameter Bingham representation can do a reasonable job of capturing the yield stress and the high shear-rate viscosity and has been useful as the simplest model interpretation and for obtaining a successful dimensionless group to characterize droplet impact of yield-stress fluids [94]. However, the Bingham model can completely miss information regarding intermediate shear rates for materials shown here, and so in most cases for an accurate representation of the entire flow-curve a model with more parameters, such as Herschel-Bulkley, is necessary; this of course comes at the cost of added complexity (higher-dimensional co-plots) and may result in decreased physical meaning. In the case of the model reformat shown in Equation (2.14), this latter issue is limited to the interpretation of parameter *n*, which this work interprets as the degree to which a material shear-thickens for $n > 1$ or shear-thins for $n < 1$.

Of course, the Bingham and Herschel-Bulkley models are not without limitations. These models are the most common yield-stress fluid models not because they *explain* the greatest number of complex phenomena, but because they can accurately *describe* the representative steady shear flow behavior of a large number of yield-stress fluids across a wide range of experimental conditions. Phenomena that the structure of these models obviously cannot describe include pre-yield flow behavior [10], sample aging and time-dependent properties [95], and the effect of flow

history including non-monotonic flow curves [11,48]. Models that describe these phenomena are far outside the scope of this work.

As the starting point for a design database, one require a model that gives a reasonable representation of a wide variety of materials at the time of characterization with physically meaningful parameters. As will be discussed in Section III.D, the characterized flow curves are well represented by the Herschel-Bulkley model. Regarding the effects of aging and flow history, in the worst case scenario, a material could completely lose a yield stress that is recoverable [96]. In the best case, the yield stress could change over some definable range greater than zero. Similarly, some yield stress fluids are thermodynamically unstable and at long times can lose their yield stress [62,68]. This does not mean that simple yield-stress fluid models are irrelevant to the description of these materials, it means that when using these models, one must be rigorous in reporting the characterization methodology and time of characterization relative to formulation. In an ideal scenario, the relative time of characterization and application will match. However, if this is not the case, a designer must take into account the time-dependent nature of the materials. Perhaps someday there will be a universal constitutive model that describes all the possible phenomena of all materials capable of apparent yield-stress behavior for any flow history and at any time after formulation only using physically meaningful parameters. However, in order to facilitate the development of a useful design database *today*, one is required to use simpler models. As previously stated, these simple models of yield-stress fluid behavior have already been demonstrated sufficient in modeling or helping solve real design problems such as enabling adhesive locomotion [41], tuning droplet impact behavior [94,97], controlling droplet shape for some yield-stress fluids [98,99], and creating field-responsive dampers [100]. For these and many

other situations, the considered models are representative of the behavior in application of many materials, and more complex models are not always necessary.

Low-dimensional descriptions will be relevant for other function-valued rheological properties, beyond just yield-stress fluids, including linear viscoelastic functions such as the relaxation modulus [101]. Whatever the degree of the low-dimensionality, visualization of the property values will be a relevant question, which will be considered in the following section.

2.4.4 Visualizing Secondary Properties

As stated previously, for applications involving yield-stress fluids, the yield stress will most likely be the primary design objective and there is no end to the number of secondary design objectives one might consider. For example, secondary objectives might be material properties such as viscosity, or linear storage modulus, G'; they might be features such as necessary weight-percentage of additive, or cost of material; or even the presence (or absence) of non-ideal behavior such as fatigue, non-homogeneous yielding, or ductile versus brittle yielding [9,102,103]. The characterization and representation of these properties and effects will be key to the development of a useful design database, however those properties and many others are outside the scope of this work. Rather, this work focuses on the challenges in representing the steady flow behavior, which is likely to be—but not necessarily—one's most important secondary objective.

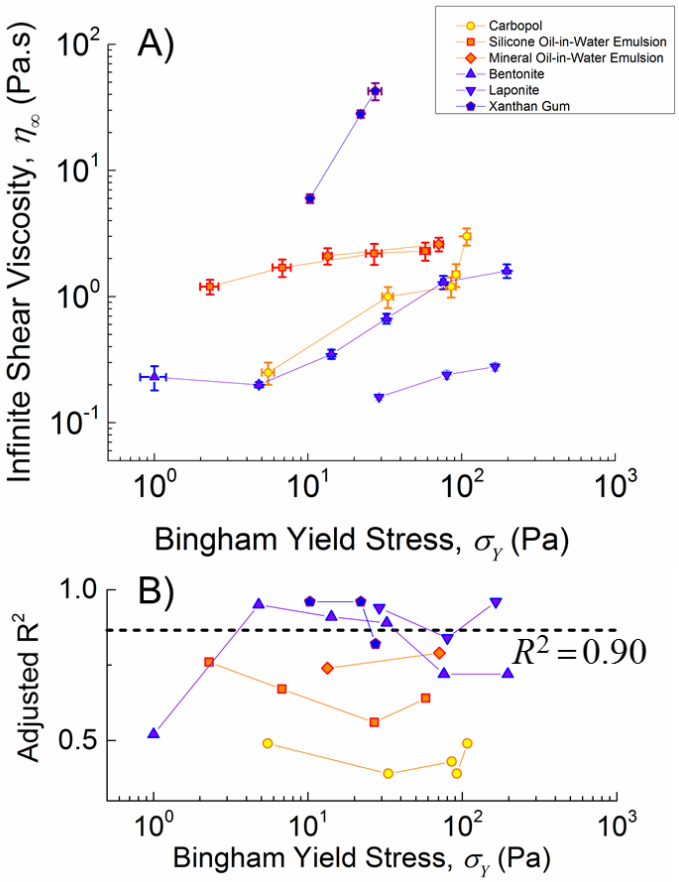

Figure 2.5. A) Ashby-style co-plot of the two-parameter Bingham model description of archetypal yield-stress fluids, $\sigma = \sigma_Y + \eta_\infty \dot{\gamma}$ (c.f. Figure 2.4, red dash-dot line). B) Adjusted Coefficient of Determination from model fitting with variance weighting. See Appendix A for the full steady shear flow data which these Bingham parameters describe, verified by testing at multiple gaps. Uncertainty bars indicate the standard error of the parameters from fitting.

Shown in Figure 2.5A is the comparative plot of the parameters from the Bingham model fit (Equation 2.15), the simplest whole-curve representation of a yield-stress fluid (full flow curves shown in Appendix A). Important insights into designing new materials can be obtained from the comparison of the trends and regions of the Bingham model parameters of different materials. Until such time as every yield-stress fluid one could possibly want has already been made and characterized, people will always need to try to expand the performance limits of materials; the scaling behaviors and inhabited regions give an idea of what material concepts are likely to be

successful strategies when expanding the parameter space. For example, in Figure 2.5A both oil-in-water emulsions show the interesting scaling behavior of the infinite shear viscosity, η_∞, being nearly flat, varying by less than half an order of magnitude, across one-and-a-half orders of magnitude in yield stress, σ_Y. Therefore, one can expect that if one wanted to design a material with an increased yield stress without substantially increasing the high-shear-rate viscosity, an oil-in-water emulsion would be one possible candidate for doing so. Studying the reason for this (Analysis of materials, Figure 1.2) could lead to other design concepts for achieving this. Similarly, due to the region they inhabit, one can infer that particulate gel systems will have the lowest viscosities at high shear rates.

The simplicity of interpreting the Bingham model comes at the cost of accuracy; the adjusted R^2 values of the model fits are shown in Figure 2.5B and indicate that for many materials the Bingham model can be unacceptably inaccurate and thus the three-parameter Herschel-Bulkley model (Equation 2.14) is next considered.

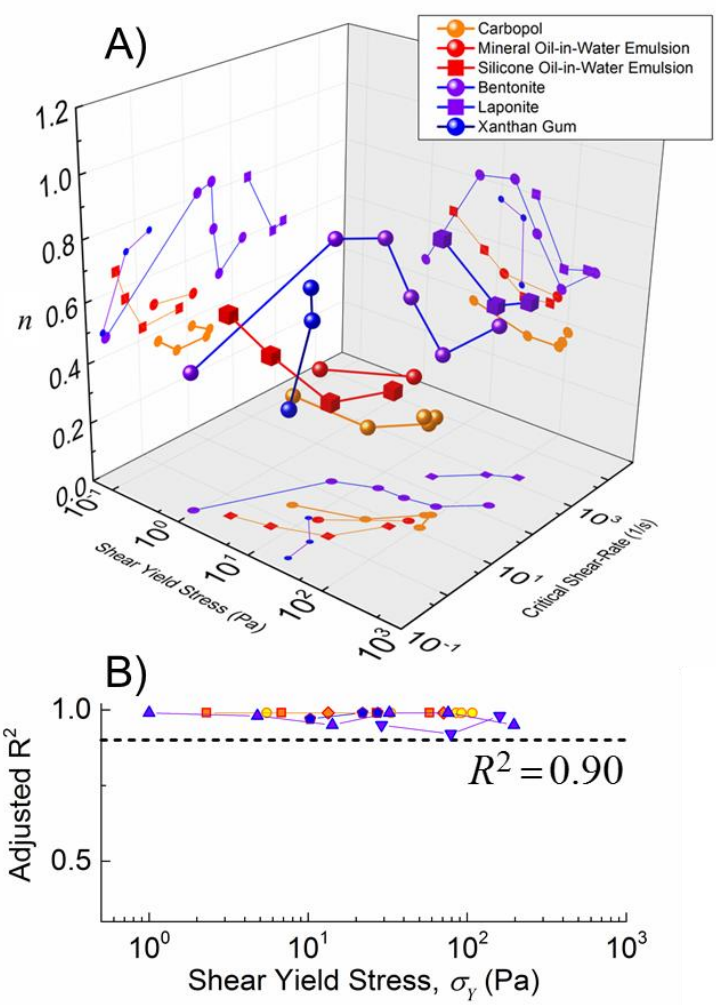

Figure 2.6) (A) Ashby-style co-plots of design-appropriate three-parameter Herschel-Bulkley model descriptions of archetypal yield-stress fluids, Eq. (12). (c.f. Figure 5, green solid line). Shaded 2-D projections shown in detail in Figure 2.7. (B) Adjusted Coefficient of Determination from model fitting with variance weighting (same symbol labeling as Figure 6). See Appendix A for the full steady shear flow data which these Herschel-Bulkley parameters describe, verified by testing at multiple gaps.

The Herschel-Bulkley model fit results in the parameters shown in Figure 2.6A with the adjusted R^2 values shown in Figure 2.6B indicating a minimum adjusted R^2 value of 0.90. The added complexity of this representation is immediately apparent in that three separate comparative plot projections are necessary to see the full relationships between fit parameters. In some cases, it is unclear if any meaningful relation can be determined such as in the plot of *n* versus critical

shear rate, where the parameter curves of some materials are non-monotonic, bending back around on themselves with varying concentration. In such a case, this behavior may be more indicative of a region of the property space that a material tends to inhabit, rather than any sort of scaling relationship. Here I will only comment on the behaviors of $\dot{\gamma}_{critical}$ and n versus σ_Y shown in Figures 2.7A and 2.7B respectively. Even considering only these two projections, one is still afforded great insight into how the materials will behave across a wide range of shear rates without needing to see the material flow curves at all, and this with just a three-parameter fit.

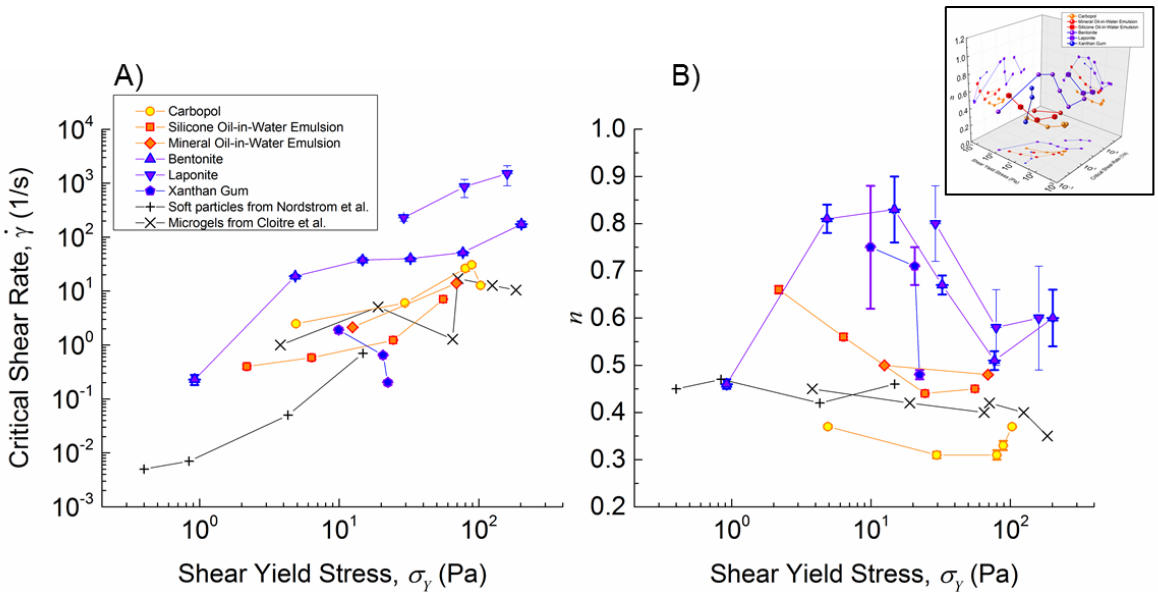

Figure 2.7. Detailed projections of Ashby-style co-plot from Figure 2.6. See Appendix A for the full steady shear flow data which these Herschel-Bulkley parameters describe. Uncertainty bars indicate the standard error of the parameters from fitting (error bars for data from [104,105] are smaller than symbol size and are omitted for clarity).

Starting with Figure 2.7A, the critical shear rate, $\dot{\gamma}_{critical}$, allows us to determine when the flow stress will deviate from the yield stress by a factor of one-hundred percent. The approximate range of critical shear rates for measured systems is $0.2 \leq \dot{\gamma}_{critical} \leq 3000\ s^{-1}$ with oil-in-water emulsions having very low values of critical shear rate, followed by Carbopol, then by the particulate gel systems. These trends in critical shear rate can be confirmed by directly examining the full data in

Appendix A, that shows Bentonite and Laponite have comparatively flat flow curves. Using Figure 2.7B, one can also anticipate even more features of the sensitivity of the flow stresses to applied shear rate. As seen in Figure 2.7B, all the Bentonite samples have values of *n* that are significantly higher than the Carbopol samples. Per Equation (2.14), what this means is that while the Bentonite flow curves are flatter than the Carbopol flow curves for $\dot{\gamma} < \dot{\gamma}_{critical}$, above $\dot{\gamma}_{critical}$ the Bentonite flow stresses will increase significantly faster than Carbopol.

Figure 2.7B showcases differentiation of the materials correlating with the classification tree (Figure 2.2); systems with networked attractions have higher values of *n* that vary significantly with the yield stress, while the repulsive jammed systems have lower values of *n* that are much flatter as the yield stress is varied. Taken together, Figures 2.7A and 2.7B allow one to make qualitative comparative statements on the behavior of the material classes. For example, the resultant stress on the networked systems will increase as a function of shear-rate much more strongly than for the jammed systems, but the stress to flow the jammed systems will typically deviate from the yield stress earlier (excepting xanthan gum). A simple case study of how these property spaces might be used is presented in Section 2.5.1.

This initial database can be continually grown by fitting the proposed Herschel-Bulkley model in Equation (2.14) to new and existing published data, as was done in Figures 2.7A and 2.7B with data from [104,105]. As the database grows, the broader possibilities of material behavior are immediately apparent. For example, though many studies consider only $n = 0.5$ [62,66,67,104], this assumption is shown to only apply to a limited subset of the yield-stress fluids shown here.

It is important to note that these comparative co-plots with the Herschel-Bulkley model are only possible due to the re-write of the model seen in Equation (2.14); the parameter *K* in the traditional Herschel-Bulkley model (Equation (2.13)) cannot be used in co-plots as *K* changes units

as a function of the *n* parameter. These qualitative comparisons come in addition to being able to accurately reproduce the complete flow curve for a wide range of shear rates if one's application dictates it since all the necessary parameters are specified.

2.4.5 Synthesis Approaches for Yield-Stress Fluids

In addition to the physical insight afforded by our functional requirement (Section 2.4.1), which is crucial to successfully ideate new material concepts, the classification tree (Figure 2.2) allows for a systematic framework for concept generation and further organization and understanding of existing materials.

Here I present one possible strategy for ideating new design concepts, a vision for the future design of yield-stress fluids. Shown in Figure 2.12 is a visualization of a juxtaposition/combination concept generation process (a known design methodology [27,106]) applied to material microstructures that can achieve a yield stress. This framework organizes ideated combinations of two individual material classes with representative classes pictured. In Figure 2.8, the general state of knowledge for each entry is indicated in the matrix. Each entry will be referred to using "(row, column)" notation with each grey square representing an individual material class using the same A-F notation as in Figure 2.2. Combinations of microstructures exist off-diagonal and include studied materials, as in the case of a mixture of a magnetorheological fluid and fibrillar gel (grease) [84], and material structures that have never been described in the open literature to the authors' knowledge. Of course, any particular combination is subject to the constraints of chemical compatibility or the ability to actually synthesize the material. Additionally, just as in mechanical design, a conceptual combination in no way assures that the functional specifications will be met, but it does broaden the available possibilities.

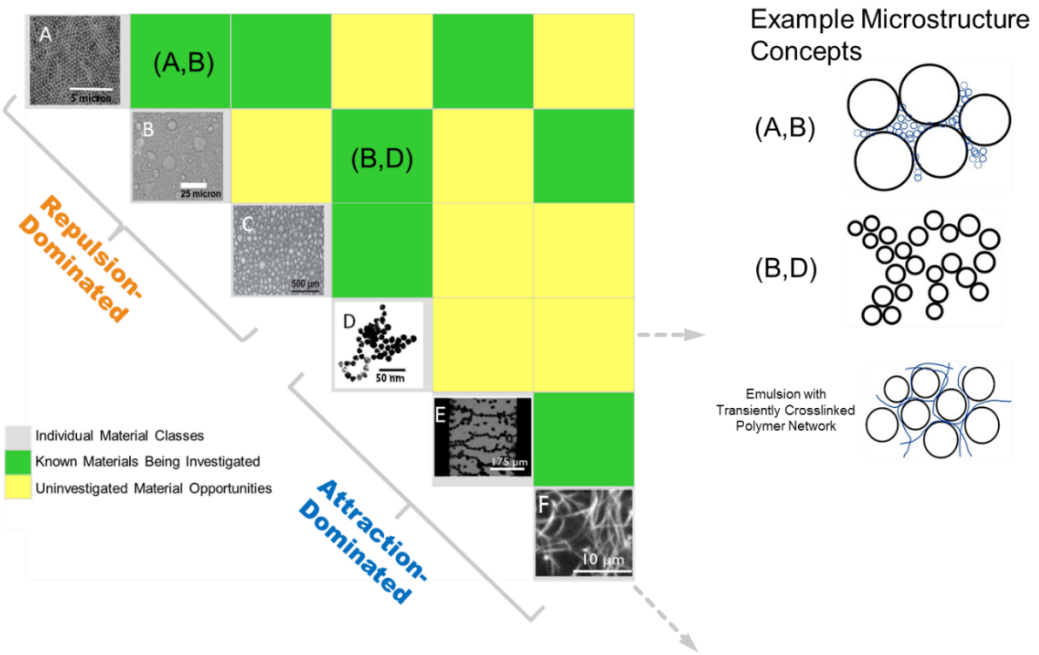

Figure 2.8. One possible concept generation strategy for material microstructures and combinations thereof. Each entry on the diagonal (same labeling as Figure 2.2, (A) particulate suspensions [55], (B) emulsions [56], (C) foams [57], (D) particulate gels [58], (E) electro/magneto-rheological fluids [59], and (F) fiber gels [60]) represents an individual material class and serves as a label for off-diagonal combinations. Off-diagonal entries represent combinations of microstructures. Two example combinations are shown schematically: (A,B), a particulate suspension as the interstitial fluid in an emulsion; and (B,D), emulsified droplets networked in a structure similar to a particulate gel. A combination of an emulsion with a microstructure with no yield-stress, a transiently crosslinked polymer network, is shown on the right.

Though many of the presented juxtapositions in Figure 2.8 at first glance may not necessarily suggest any additional benefit over others, this method is a quick and simple way of generating a very large number of possible ideas. In fact, many of the combinations in Figure 2.8 are being studied because they are either scientifically interesting, have novel properties, or both. For example, a combination of particulates and emulsion droplets, as pictures in (A,B) is being investigated in the form of bimodal dispersions of starch and fat droplets [107]. Microgels made field-responsive would correspond to (A,E) [108]. Entry (C,D) applies to whipped cream which can be conceptualized as a foam stabilized by a particulate gel network [109]. Entries on this juxtaposition table are not limited to a single incarnation. For example, entry (A,C) could describe

a foam stabilized by a crowded colloidal suspension [110], or a particulate suspension that has been foamed as in the case of foamed concrete [111].

Composite microstructures appearing very recently in scientific literature include photocrosslinkable nanoemulsions which fall into the category of emulsion gels (B,D) [112,113], and nanoparticle solutions used as an adhesive between polymer gels [114]. The latter concept is not pictured but can be conceptualized as a composite of particulate and polymer gels. Other composite materials not pictured include field-responsive polymer gels [108] and yogurt, which is a combination of a polymer gel and an emulsion [109]. Of course, in juxtaposition, one is not limited only to combining two yield-stress fluid concepts. For example, ice cream might be conceptualized not as a combination of two concepts, but three: a foam, an emulsion, and a jammed particulate suspension [109]. Using the technique of juxtaposition, one could combine any number of concepts, or perhaps combine a yield-stress fluid concept with a structure that would have no yield stress, but attains a different rheological function. An example of the usefulness of this juxtaposition process is provided in the next section on case studies.

2.5 Case Studies

Here this work demonstrates the usefulness of our proposed paradigm through two simple design problems that make use of the different methods presented in Section 2.4.

2.5.1 Case Study 1: Yield-stress fluid adhesive design (material selection)

This design problem is *to constrain one surface to another*. Here I will assume the following requirements as our "customer needs": the surfaces must resist a peak separating force of at least 8 Newtons (for context, approximately the weight of a piñata filled with candy), one of the surfaces is a semi-infinite flat plate that cannot be modified (no permanent deformation), the

surfaces must be separable without destroying either surface. Typical solutions to this problem such as mechanically separable fasteners and welding are unable to satisfy all design constraints, leaving us with the strategy of using an adhesive. The use of yield-stress fluids as adhesives has been investigated [7,115,116], and for obvious reasons I will limit our consideration of this problem to yield-stress fluids.

Derks et. al [115] derived the following equation for the peak adhesive force for an incompressible yield-stress fluid between circular flat surfaces for small gaps (shear-dominated deformation) at very low shear rates,

$$F_{Peak} = \frac{2}{3}\sigma_Y \left(\pi R_0^2\right)\left(\frac{R_0}{D_0}\right) \tag{2.16}$$

for surface radius, R_0, and initial gap height, D_0. This equation was validated using a material with behavior well described by Herschel-Bulkley model parameters. Thus, this simple model (that neglects thixotropy and many other phenomena) is entirely sufficient for this design problem provided the properties at the time of characterization are representative of the properties at the time of use.

Whether a static or a dynamic yield-stress is more relevant for this particular design problem is entirely dependent on unspecified details of the application. However, it is nearly always the case that a static yield stress will be greater than or equal to the dynamic yield stress. Given the vague nature of this (and many) design problems, since our primary design objective translates only to a *minimum* yield-stress, it is prudent to use the dynamic yield stress regardless of which yield stress is closer to application conditions.

Choosing for now that the radius of the circular surface and initial gap height are to be 27 and 0.5 millimeters, respectively, solving for σ_Y gives us approximately 100 Pa as our minimum

yield stress target specification. Consulting Figure 2.3 to generate product concepts from the limited number of formulations presented here, there are 3 materials for us to choose from: 0.5wt% Carbopol, 12wt% Bentonite, and 5wt% Laponite. With multiple materials satisfying our primary design objective, one could stop their design process here and select all 3 formulations as candidates to formulate and validate in application, however this would be premature since this case study has yet to consider any secondary properties. Additionally, the geometry here was chosen simply for demonstrative purposes. For a situation where the surface radius is 40 millimeters, the minimum yield stress would be approximately 30 Pa, and the number of candidate materials increases four-fold to 12. Thus, it is easy to see how a more open-ended design, as well as a larger database, quickly lead to situations where it is impractical to compare, formulate, and test all material concepts, and therefore secondary properties are necessary to down-select to materials more likely to be best.

Equation (2.16) was derived assuming low shear rates, and therefore the peak force only depends on the yield stress value and not the flow behavior. However, if yielding and larger shear rates were to occur in application, a material with a strongly increasing stress response would lower the risk of catastrophic debonding. Thus, one can use sensitivity of the flow curve as a measure of the robustness of the material, and rank the suitability of the 3 candidate materials. In terms of the parameters this work has characterized, a material with a lower $\dot{\gamma}_{critical}$ has a more sensitive flow curve. Of less importance here, a higher value of *n* contributes to a more sharply increasing flow curve after $\dot{\gamma}_{critical}$ and could be used as an additional ranking index were two materials to have the same critical shear rate. In general, the decision of which parameter is more important depends on the details of the functional requirements and application conditions.

Consulting Figure 2.7A to select our product concepts, I am seeking a material in the lower-right portion of this plot. Ranking the three formulations that meet the minimum yield stress requirement, Carbopol has the lowest critical shear rate, followed by Bentonite, with Laponite in last. While the number of materials a designer selects to move on to downstream design processes can be subjective, this ranking of suitability based on secondary criteria is not dependent on designer input. Should these materials fail in the concept testing phase (e.g. due to non-ideal conditions), a designer could use the scaling behavior seen in Figures 2.3 and 2.7 to predict how more concentrated formulations might behave in further tests. Additionally, if there is need to look beyond the current set of known materials, surveying using only a rheological modifiers hand-book or similar tool would be an overwhelming process given the issues discussed in Section 2.2.2. If this is the case, the functional requirement and organization presented in Section 2.4.1 can be used to select candidate materials based on anticipated microstructure rather than ingredient.

Of course, this simplified down-selection process was performed only with the available parameter space. Secondary properties of interest that may affect performance for this particular design that are outside the scope of this work include pre-yield (ultra-low shear rate) viscosity and aging behavior if the adhesive is to be used for long times, thixotropic restructuring times that will affect the initial adhesion process, and pre-yield modulus that will dictate how well the material adheres to a rough surface similar to the Dahlquist criterion [117]. This is not to say that one should be paralyzed and rendered impotent in our design process due to our lack of description of all possible properties and phenomena. Relevant and meaningful decisions can still be made using the simplified—but still representative—descriptions that are present in this initial work.

2.5.2 Case study 2: Extensible yield-stress fluid design (material concept synthesis)

Obtaining a highly-extensible yield-stress fluid is the second design problem case study. This work is detailed in Chapter 3, but I briefly describe a portion of the work here as an example of the presented design paradigm, specifically the juxtaposition process (Section 2.4.5). For the materials formulated here, the characterized shear data does not necessarily allow one to draw any conclusions about "stretchability". However, extending these materials between one's thumb and index finger suggests they are generally incapable of stretching to a length comparable to materials such as bubble gum. High extensibility of materials is known to be important for sensory characteristics for foods including bubble gum [118]. It has also been conjectured that high extensibility stabilizes a filament extrusion process such as in direct-write 3D printing [119].

We have no options from our surveyed concepts capable of satisfying our qualitative target specifications, and chose to generate a set of new concepts using the process detailed in Section 2.4.5. To be explicit, I carried out this process to ideate numerous concepts that I could choose to develop based on qualitative arguments of suitability. At this very early phase of the design process, I was not seeking to evaluate the feasibility of formulation, I was not seeking a list of chemicals that could be used to make such a material, and I certainly was not seeking to generate constitutive models to predict the properties of completely new concepts for materials. This last task in particular is not feasible during a typical design process given that a model for a radically new material cannot be validated until after the design has already been decided upon and formulated [23]. Certainly, after the concept generation process, the process of selecting a product concept requires consideration of how a given concept might be formulated, but prescribed methodologies for this are outside the scope of this work. Though many concepts were generated,

I will focus on the qualitative reasoning for the final concept I selected for downstream design process development.

Shown in Figure 2.8 is a schematic for a concept for a material is characterized in detail in Chapter 3, a juxtaposition of an emulsion that is a yield-stress fluid with an interstitial transiently crosslinked polymer network of moderate molecular weight. A major reason this concept was selected was to attempt to minimize interactions between the juxtaposed microstructures, since interactions have the potential to be enormously complex. The emulsion microstructure provides a yield stress and little-to-no extensibility, whereas the polymer network microstructure provides high extensibility but no yield stress. In this way, the material has conceptually decoupled design parameters [120]. Interactions will always be present with multi-component systems, e.g. the emulsion stability may be affected by the polymer component. However, some structures are, of course, more sensitive than others. For example, the Bentonite, Laponite, Carbopol, and xanthan gum are sensitive to salt concentration and pH to different degrees. The emulsion structure, while still having multi-component interactions, is, in principle, robust in the compartmentalization of additives (water- and oil-soluble additives separated). This aspect of emulsions allowed for more freedom when choosing the high-extensibility microstructure and formulation. The rationale for the extensibility-providing microstructure is provided in Chapter 3 along with characterization in both shear and extension.

Even without detailing the real material microstructure to confirm consistency with the generated concept, the juxtaposed idea is what enabled the formulation to occur at all. Additionally, only through generating a large number of material concepts—many of which were not feasible to formulate or did not satisfy the functional requirement—was it possible to carry out the downstream design processes and obtain a completely new material. To create completely new

material systems, one cannot be limited to incrementally modifying existing systems or only considering material structures with properties that are predictable in a straightforward way. If these approaches are all that one considers, this is tantamount to design fixation [121], and radically new solution spaces of materials will never be achieved without the provocation of approaches such as juxtaposition [27]

2.5 Conclusions and Outlook

Here this work has presented an ontology for the design of yield-stress fluids. I have provided methodologies and insights for broadening the available design space, and for the evaluation of design concepts based on available predictive analysis and the comparison of simply represented flow data. Moving forward, this work recommends usage of our revised representation of the Herschel-Bulkley model since it preserves the flow data while having physically meaningful parameters. Anyone wishing to utilize yield-stress fluids in some product or application would benefit from the methods presented here, by making use of our early-stage database framework and more importantly considering all possible concepts rather than blindly accepting the most immediately obvious approach.

The design-space presented here is obviously incomplete. Not all materials and microstructure types that produce a yield-stress fluid are known by the authors or by anyone else. However, by following the functional requirement proposed here, significant progress can be made on effectively deciding what materials are capable of producing a yield-stress fluid to then be evaluated and characterized appropriately. These same methods of design can and should also be applied to other rheological phenomena (e.g. linear viscoelasticity) that are currently under-utilized.

Everything presented here has only been to relate a particular rheological parameter, the yield-stress, to numerous structures, the lower level stage of the "Design of Materials" schematic outlined in Figure 1.2 (left portion). To effectively design complex materials in the future will mean completely integrating the higher-level stage of performance-to-rheology target setting (e.g. [1,41,101]) with the lower level stage of rheology-to-structure ideation (the focus of our work), followed by formulation and the optimization of specific material formulations, e.g. with computational material science or otherwise [122–124]. To further develop the full design toolbox for yield-stress fluids and other materials, the fields of engineering design [50,125], product design [24,31,40,126], and design science [25,33,35,51,127,128] can be embraced for other methodologies and insight. This will enable the rheology and soft matter communities to better design materials to achieve novel functionality due to the unique aspects of rheologically-complex soft materials.

This work has been published and forms the foundational paradigm for subsequent work that focuses on a particular secondary property (extensibility), a particular application (direct-write 3D printing), and appropriate processing to obtain a yield-stress fluid material. The initial work presented in my master's thesis was expanded on for publication to include additional experimental data, a more precise functional requirement that acknowledges subtleties of non-ideal yield-stress fluid materials, and the detailed case studies that demonstrate the usefulness of the proposed paradigm.

Chapter 3: Characterization and design of highly-extensible yield-stress fluids*

3.1 Introduction

In this chapter, I expand on the design paradigm and database presented in Chapter 2. I expand the focus by looking now at secondary property beyond the steady shear flow behavior, extensibility. Shown in Figure 3.1, there is an obvious discrepancy in the extensional behavior between well-studied laboratory yield-stress fluids such as those investigated in Chapter 1 (Figure 3.1A) [20] and common industrial and consumer yield-stress fluid materials (Figure 3.1B,C). Figures 3.1A and 3.1B depict the materials immediately after rupture occurs. When compared to model materials, the application-relevant yield-stress fluids are often able to survive enormous extensional strains. Due to this discrepancy, this work suggests a silicone oil-in-water emulsion with a transiently crosslinked network of poly(vinyl alcohol) as a model for studying the behavior of highly extensible yield-stress fluids (Figure 3.1D).

In bubble gum (Figure 3.1C), it is important that the material be able to reach large extensional strains because this contributes to consumer perception as well as the ability to blow bubbles [118]. Prior to the work presented in Chapter 5, the importance of high-extensibility had not been directly established for applications involving printing of yield-stress fluids such as the resin shown in Figure 3.1B. Though not the focus of this work, it has been conjectured that a printed filament of highly-extensible material will not rupture as easily during extrusion, contributing to a smoother and more desirable surface finish [119]

* Preliminary work on this topic appeared in the author's master's thesis and this chapter appeared in the following peer-reviewed publications (re-used with permission):
A.Z. Nelson, R.E. Bras, J. Liu, R.H. Ewoldt, Extending yield-stress fluid paradigms, J. Rheol. (N. Y. N. Y). 62 (2018) 357–369. doi:10.1122/1.5003841.

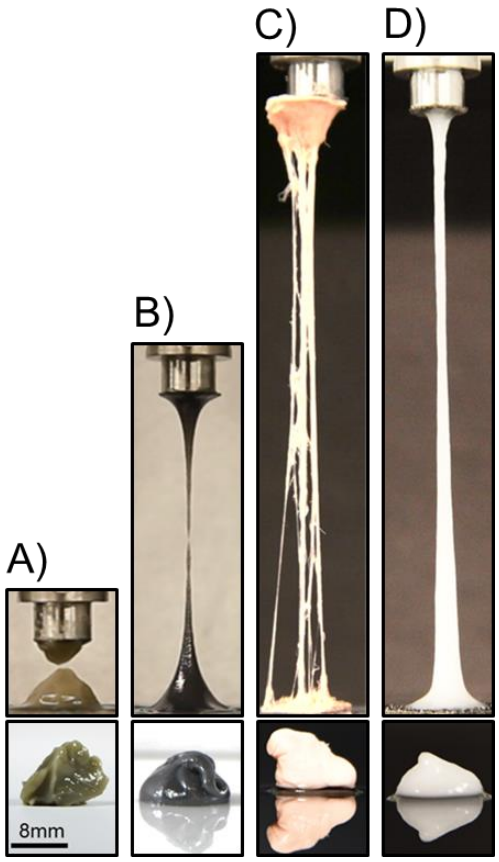

Figure 3.1. The extensional behavior of yield-stress fluids. A) Bentonite clay suspension, a commonly studied material that fails to match the extensibility of other yield-stress fluids; B) a resin used in printing by the company HexArmor; C) the bubble gum, Hubba Bubba Bubble Tape; and D) a model material introduced here. The scale bar shown applies to all images.

While previous studies of yield-stress fluids have been extensive, none have conceived of the materials as being highly extensible. There are certainly many yield-stress fluids that cannot survive large extensional strains. However, the works investigating yield-stress fluids in extension do not recognize materials that *are* able to reach large strains, instead typically focusing on more paste-like yield-stress fluids [7]. Yield-stress fluids in extension have been of interest for understanding the pinch off dynamics in a separating plate [98,129,130] and drop formation configuration [131], and to measure critical flow and separation stresses in extension [99,132,133]. The lack of studies on highly-extensible yield-stress fluids is an imbalance in the current paradigm which this work hopes to rectify here by (i) demonstrating the extent to which common model

materials differ from application-relevant materials in terms of extensibility, and (ii) introducing a simply-formulated material that is both highly extensible and has a yield stress (Figure 3.1D).

For the common model materials, the same formulations as Chapter 2 were used (shear flow data given in Appendix A). As discussed in Chapter 2, there are two primary structural mechanisms by which the yield stress comes about, jamming or attractive interactions (Figure 2.2). However, combinations of both mechanisms are of course possible, and it is there that most application-relevant materials with complex formulations are likely to exist, although frequently the precise microstructure is simply unknown.

3.2 Background

The importance of characterizing the extensional properties of various materials has been widely recognized for polymer processing with polymer solutions and melts [134–138], biological fluids such as saliva [139], magnetic industrial fluids used in vibration dampers [140], surface coatings [130], food materials [98], and consumer confectionary products such as chewing gum [118,141]. For the characterization of the uniaxial extensional properties of these materials, the most common methods are the imposition of either a constant extensional strain rate or a step extensional displacement (filament stretching or capillary breakup) [134,142]. This work characterizes materials by imposing a constant extensional strain-rate to measure the strain at which rupture occurs (strain-to-break). The two methods by which this work imposes extensional strain rates are by (i) exponentially increasing the separation velocity of two parallel plates (referred to here as “filament-stretching”) and (ii) using a counter-rotating-drum fixture at a fixed velocity. For the filament-stretching experiments for initial radius, R_0, and initial plate separation, R_0, the aspect ratio,

$$\Lambda_0 = H_0 / R_0 , \tag{2.1}$$

should be approximately unity for homogeneous uniaxial extensional flow [137]. The counter-rotating-drum method was used when the filament-stretching experimental setup could not access the strain-to-break of a material (due to finite travel length). The true strain (also known as Hencky strain),

$$d\varepsilon_{true} = \frac{dL}{L} \tag{2.2}$$

and engineering strain,

$$\varepsilon_{eng} = \frac{L_{final} - L_{initial}}{L_{initial}} \tag{2.3}$$

are related by [143],

$$\varepsilon_{true} = \ln(\varepsilon_{eng} + 1) . \tag{2.4}$$

For the stability of a material in extension, the Considère criterion has been used in both solid mechanics [144] and for polymeric materials [138,145] to quantitatively predict the critical strain beyond which homogeneous extension no longer occurs. The necking behavior of some materials has been found to be strain-rate dependent [136,146], but in the limit of "fast" extension (i.e., where no molecular relaxation occurs), the critical strain of the Considère criterion has been used to predict the failure strain (strain-to-break) for constitutive equations that describe the behavior of polymer melts [147]. By this same method, it can be shown (see Appendix B) that the tensorial Herschel-Bulkley model (see Section 2.4.3) predicts that yield-stress fluids never undergo stable uniaxial extension (i.e., have a critical strain value of zero). Thus, this simple model fails to capture the failure strains shown in Figures 3.1B and 3.1C.

Of course, it must be noted that the strain-to-break is an *extrinsic* material property that may vary for different initial geometries. This is not to diminish the importance of this parameter, as it

is extremely useful in solid mechanics for informing material selection choices by comparing the ductility of materials through their "percent elongation" [148]. However, just as in the characterization of solid materials, care must be taken when comparing materials to standardize the initial sample geometry and extension rate, which I do here as much as possible.

3.3 Materials and Methods

Materials include the well-studied archetypal yield-stress fluids presented in Chapter 2, commercial products, and a proposed new model material for yield-stress fluids with extensibility (Refer to Tables 2.1 and 3.1 for the specific material formulations presented in this paper). The preparation of the archetypal yield-stress fluids is the same as detailed in Chapter 2.

For our proposed model material, hereafter referred to as a PVA-borax emulsion, 1000 cSt silicone oil with a density of 0.97 g/ml obtained from Sigma Aldrich was blended using an overhead stirrer at 600 rpm for 5 minutes with a 4wt% solution of poly(vinyl alcohol) (molecular weight 85,000 – 124,000, 99+% hydrolyzed) in deionized water and then added to a test tube containing a 4wt% solution of sodium tetraborate in deionized water and shaken vigorously and occasionally stirred for 5 minutes. The overall weight-percentages of the oil, PVA, and sodium tetraborate were varied as detailed in Table 3.1. The poly(vinyl alcohol) and sodium tetraborate were both purchased from Sigma-Aldrich. Using this method of formulating the model system, at wt% oil of 50 and below, no apparent yield-stress behavior was observed; above a wt% oil of 60, there was insufficient PVA (emulsifier) to form a stable emulsion.

Using the density of the oil and assuming the continuous phase has approximately the same density as water, lower bound estimates of the volume fraction are obtained and are given in Table 3.1. It is possible that the adsorption of PVA at the oil-water interface results in a larger effective

volume fraction [149], but this is unconfirmed and outside the scope of this work. Additionally, the chosen mixing method likely entrains air bubbles that contribute to the jammed volume fraction.

The industry-relevant products tested were Nutella Hazelnut Spread (Ferrero), Whipped Frosting (Duncan Hines), Laffy Taffy (Nestlé), Hubba Bubba Bubble Tape (Wm. Wrigley Jr. Company), resin used in the production of HexArmor personal protective equipment, and Mystic Smoke (a material used in performance magic, Loftus International). Before testing, the Hubba Bubba Bubble Tape was chewed for 20 minutes, at which point the weight of the material ceased to depend on chewing time. All other consumer products were tested as received. Unless noted otherwise, all rheological experiments were repeated 3 times.

Table 3.1. Proposed model material formulations. In all cases, poly(vinyl alcohol) and borax content was supplied from 4wt% stock solutions in water. For specific synthesis procedure refer to Section III. Materials and Methods.

	wt% Oil	wt% PVA	wt% Borax	vol% Oil
PVA-Borax	50	1	1	51
Emulsion	55	0.9	0.9	56
	60	0.8	0.8	61

For this chapter, yield-stress characterization was performed in one of two ways depending on the sample: either velocity-controlled steady flow tests, or step-stress creep compliance tests. The procedure of the steady flow tests was the same as given in Section 2.3. Velocity-controlled tests were problematic for materials prone to edge failure at high shear-rates, including the Laffy Taffy, Hubba Bubba Bubble Tape, and the proposed model material. For these cases, a series of step-stress creep tests were imposed (Figure 3.2). Materials were allowed to reach a steady shear-rate, allowing for the determination of steady shear viscosity as a function of the applied stress. The yield-stress in this case was taken from within the stress range over which the viscosity declines by over a half-order of magnitude. Note that because no simple correction is available for step-

stress tests with parallel disks, the yield stresses of the materials tested in creep are apparent stresses rather than true stresses.

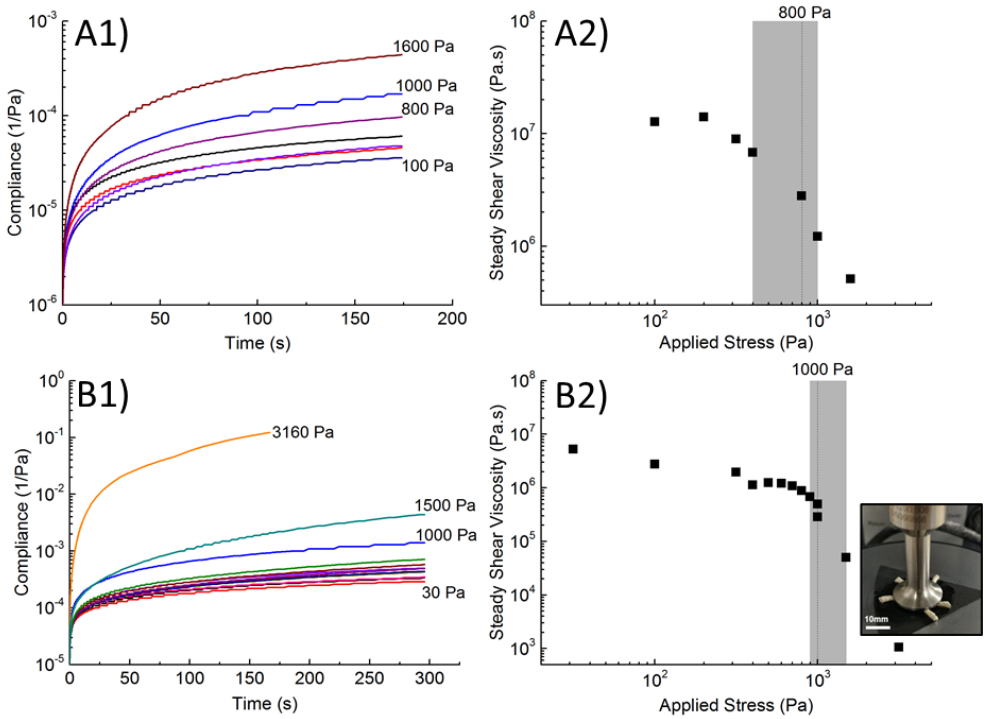

Figure 3.2. Shear creep compliance curves for difficult-to-test materials, A) Laffy Taffy, and B) Hubba Bubba Bubble Tape. Velocity-controlled flow tests were not feasible for these materials due to edge failure behavior (inset image in B2). Constant applied stress tests were used to obtain the compliance over time, with the applied stresses increasing monotonically between the labeled compliance curves (A1 and B1). From the compliance, the resulting steady shear viscosity curves (A2 and B2) show gradual yielding. The grey shaded regions identify the stresses over which viscosity has begun to decrease substantially, the yield stress for each material is taken as the stress for the data point within the shaded regions. Error bars are smaller than data points.

Characterization with filament stretching for the extensional strain-to-break was performed on a TA Instruments ARES-G2 rheometer (separated rotational motor/transducer, combined axial motor/transducer). For the filament-stretching experiments a parallel-plate geometry with a diameter of 8 millimeters and advanced Peltier system bottom plate were used. The samples were loaded at a gap of 4 millimeters, resulting in an aspect ratio of $\Lambda_0 = H_0 / R_0 = 1$. Samples were loaded as near to the initial height as possible to minimize compression. Samples were not pre-sheared for extensional tests. The maximum gap on the ARES-G2 allowed for a maximum

engineering strain of $\varepsilon_{eng} = 2000\%$ ($\varepsilon_{true} \approx 3.04$). A constant true strain rate, $\dot{\varepsilon} = 0.2s^{-1}$, was used for all tests.

The counter-rotating-drum experiments were performed on the previously mentioned DHR-3 rotational rheometer using an SER2 or SER3 Universal Testing Platform fixture from Xpansion Instruments. For the counter-rotating-drum experiments, samples were loaded as per the recommended dimensions and procedure [135]. A constant true strain rate, $\dot{\varepsilon} = 0.2s^{-1}$, was used for all tests. Videos were taken during all extensional tests, and images were correlated with the measured load and displacement to determine the extensional strain-to-break. See Appendix B for all extensional stress-strain curves from both filament-stretching and counter-rotating-drum experiments.

For microstructural characterization of the PVA-Borax emulsion, optical microscopy with transmitted bright-field illumination was performed using a Nikon Eclipse Ti-U inverted microscope with an EM-CCD camera. Micrographs were recorded with a 20x objective lens at various locations across multiple samples.

3.4 Results

3.4.1 Archetypal Yield-stress Fluids and Consumer Products

The shear and extensional behavior of the studied archetypal yield-stress fluids are shown in Figure 3.3 with images of representative systems just before rupture occurs. All data points in Figure 3.3 are simplified descriptions of the full data from shear flow and extensional flow (See Appendix A for shear data and Appendix B for extensional data). The steady simple-shear flow characterization for the three representative systems in Figure 3.3 is shown in Figure 3.4, and the extensibility characterization is shown in Figure 3.5. While these materials span a range in yield

stresses of over two decades, the engineering strain-to-break only varies by approximately a factor of two.

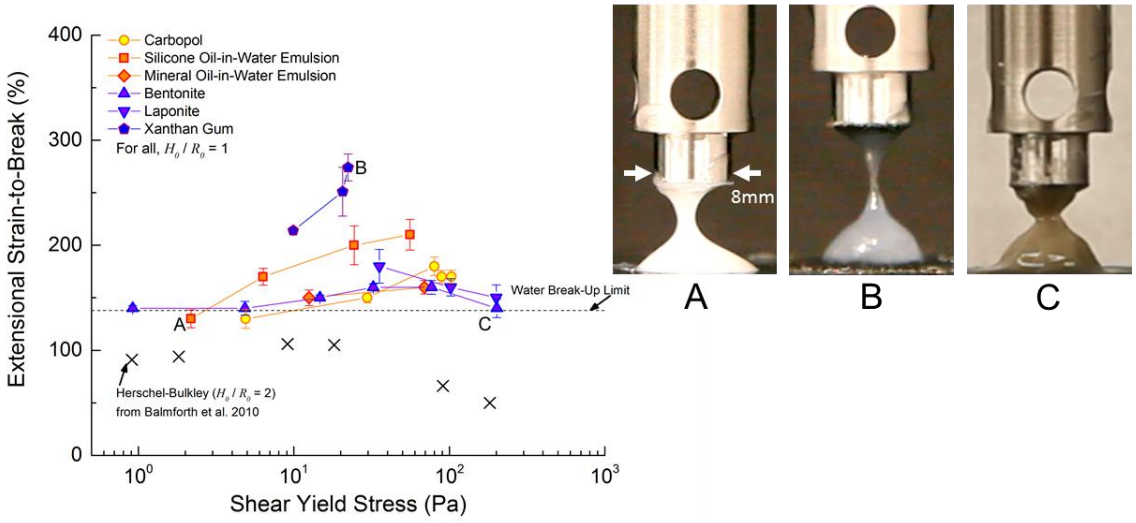

Figure 3.3. Ashby-style co-plot of the shear and extensional behavior of archetypal yield-stress fluids. All filament stretching tests were performed with an initial aspect ratio, $\Lambda_0 = H_0 / R_0 = 1$. Shown are three representative materials: A) a silicone oil-in-water emulsion that is 65wt% oil, B) 5wt% xanthan gum in water, and C)12wt% bentonite in water. Error bars are the standard deviation from repeated experiments. The water break-up limit for a volume equivalent to those in our experiments is 135% and was determined for zero-gravity conditions [150]. The values from [129] were found using a Herschel-Bulkley model for an initial aspect ratio double that of our experiments. See Appendices A and B for the full steady shear flow and extensional engineering stress curves that these points represent, respectively.

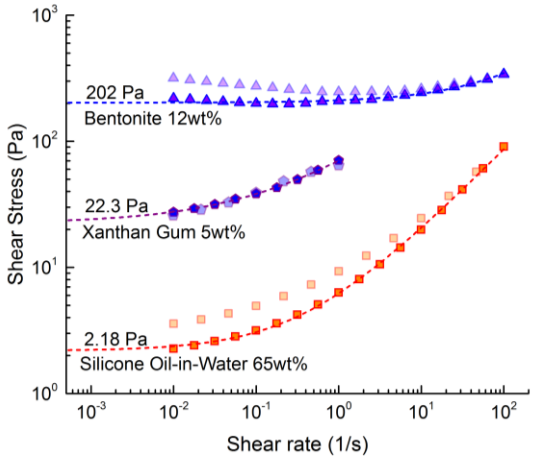

Figure 3.4. Steady simple shear flow for the three representative materials shown in Figure 3.3. The lightened data points are tests performed at a smaller gap, and from these tests no evidence of slip is seen. Rather, a confinement effect (higher flow stress at lower gap) is observed. All yield-stress parameters are fit to the flow data at the highest tested gap. The dashed lines show the fit Herschel-Bulkley model for each material.

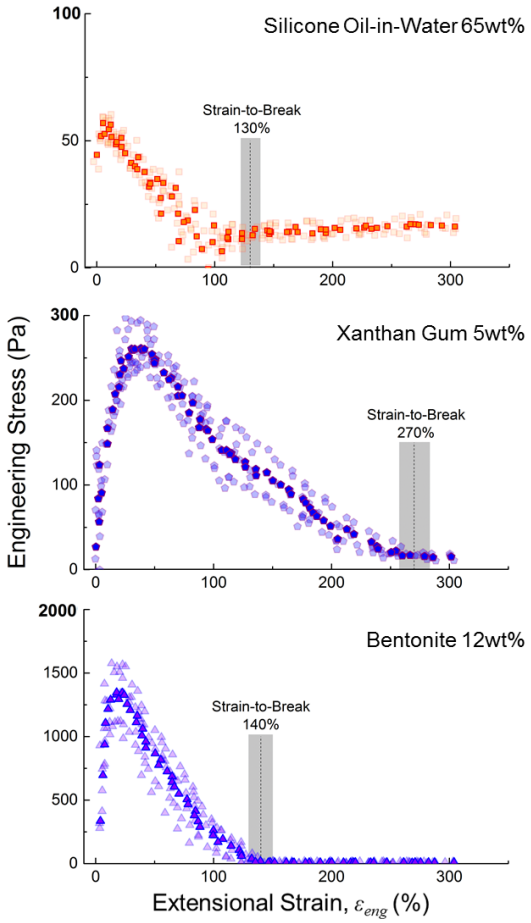

Figure 3.5. Extensional engineering stress curves for the three representative materials shown in Figure 3.3 tested using the ARES-G2 filament stretching experimental setup. The bold data points are the average of repeated experiments (lightened data points) The vertical dashed lines depict the average strain-to-break which was found by correlating the extensional stress curves with video images. The width of the shaded region depicts the standard deviation in the strain-to-break from repeated experiments. A constant true strain-rate of $\dot{\varepsilon} = 0.2\ \mathrm{s}^{-1}$ was used for all extensional tests.

As shown in Figure 3.3, there is no clear correlation between the extensibility and yield-stress for the data set taken as a whole. However, correlations can be seen within distinct material systems. Carbopol and the silicone oil-in-water emulsions, both repulsion-dominated systems, show a slight increase in extensibility as their yield stresses increase, with the extensibility of Carbopol saturating at the same concentration as the measured yield stress value. The extensibility of Bentonite and of the mineral oil-in-water emulsion are essentially constant as their yield stresses

are increased. Laponite is the one tested system that shows a decrease in extensibility as the yield stress is increased. Xanthan gum, a long-chain polymer system, shows the largest extensibility, as may be expected from a stretchy attractive network. However, comparing Figures 3.1 and 3.3, the extensibility of Xanthan gum shown in Figure 3.3B is far less than the extensibility behavior seen for the application-relevant materials in Figures 3.1B and 3.1C (though Xanthan does show necking behavior somewhat similar to the printing resin in Figure 3.1B).

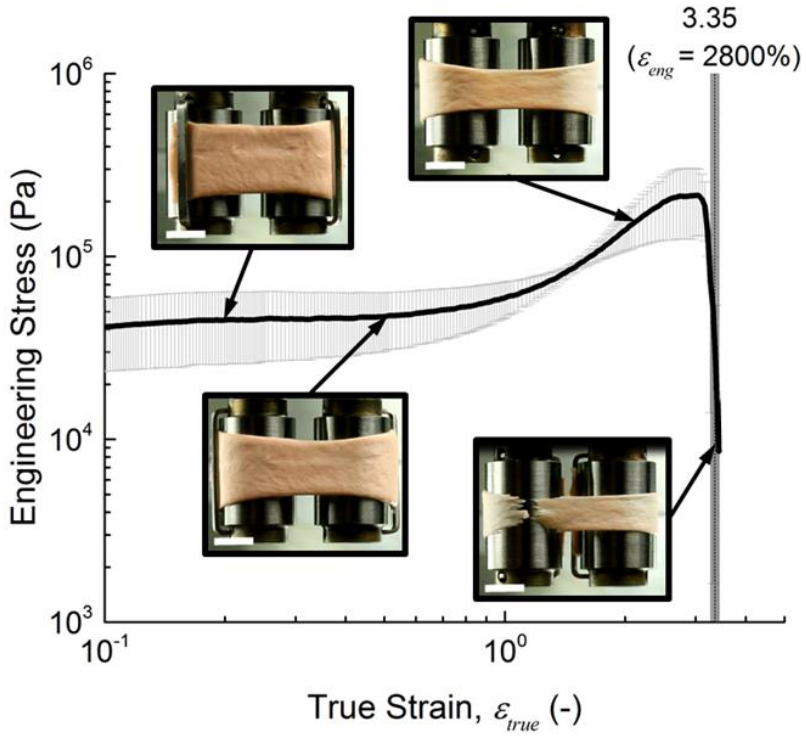

Figure 3.6. Extensional engineering stress versus true strain for a commercial product, Hubba Bubba Bubble Tape. Extensional data for materials which reach the limit of extensibility for the ARES-G2 filament stretching experimental setup (shown in Figure 3.1) were obtained using an SER3 counter-rotating-drum stretching experiment as shown. The white scale bar in each image is 5mm. The dashed line indicates the strain-to-break. For comparison with other materials, the true strain was related to engineering strain with Equation 2. The error bars are the standard deviation from repeat experiments.

The tested materials with the lowest yield-stresses rupture in a qualitatively similar way to water (e.g., Figure 3.3A), and in this regard the lowest concentrations of Carbopol and the silicone oil-in-water emulsion (repulsion-dominated systems) have strain-to-break values slightly below

the indicated water break-up limit under zero gravity of 135% determined for our initial volume from Sanz and Martinez [150]. The surface tension of water was used to calculate the values taken from simulations for the 3D tensorial Herschel-Bulkley model [129], as all of our material systems have a continuous water-phase. For those simulations, an aspect ratio of $\Lambda_0 = 2$ was used and thus a smaller strain-to-break is expected. The simulations show non-monotonic behavior of ε_{break} versus σ_Y , with ε_{break} varying by at most a factor of two for the shown range of yield stresses, similar to the variation in the archetypal materials. For these archetypal materials, I find that the least extensible materials belong to the repulsion-dominated category, while the highest extensibility is achieved by an attraction-dominated material composed of long-chain polymers.

As shown in Figure 3.1, when considering application-relevant materials, the strain limit for the filament-stretching experimental method was reached for some materials and thus it was necessary to make use of the counter-rotating-drum experimental setup shown in Figure 3.6. As pointed out in Section 3.2, ε_{break} is an *extrinsic* material property that may depend on the initial geometry. Thus, one should not necessarily expect consistency when comparing between the filament-stretching and counter-rotating-drum setups. In the particular cases of the consumer products tested here (Laffy Taffy and Hubba Bubba Tape) there is some consistency in the fact that ε_{break} on the counter-rotating-drum setup is larger than the maximum strain of the filament stretching setup.

Comparing the consumer products to the archetypal fluids in Figure 3.7, while the laboratory systems approach the behaviors of Nutella and whipped frosting, they come nowhere near the HexArmor resin, Mystic Smoke, or confectionary products. Thus, archetypal model materials and mathematical constitutive models may be irrelevant for understanding of some materials in applications in which physics associated with both yield stress and high extensibility is required.

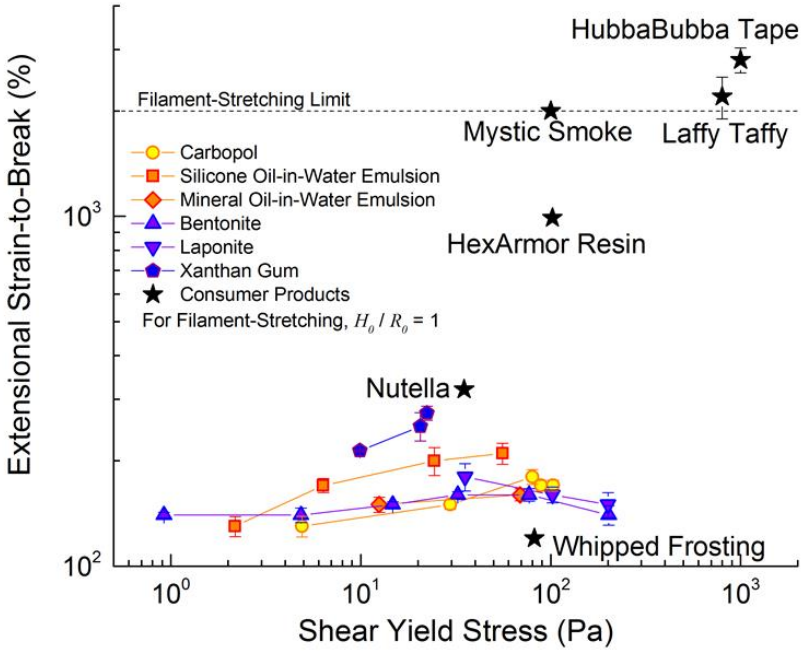

Figure 3.7. Ashby-style co-plot of archetypal yield-stress fluids and consumer products. For Mystic Smoke which could not be loaded in the counter-rotating-drum setup, the filament-stretching limit is taken as the lower bound of the strain-to-break. Error bars shown are the standard deviation from repeat experiments. Note that, compared to Figure 3.3, both axes are logarithmic scales. See Appendices A and B for the full steady shear flow and extensional engineering stress curves that these points represent.

3.4.2 Design and Analysis of a Model Material

In attempting to match the performance of materials shown in Figure 3.1B and 3.1C with that of a model material, I followed a methodology for the design of a yield-stress fluid described in Chapter 2. The design methodology contrasts with analysis strategies in that it is built upon generic principles of inverse problem solving: the performance objective (material behavior) is specified in a chemistry- and structure-agnostic way, allowing for creative concept generation. Ideally, one would be able to select materials matching the necessary properties from a material database. However, since the paradigm of highly extensible yield-stress fluids is under-developed, this work carried out the analysis/characterization (described in previous section). Because as I have shown,

none of the surveyed archetypal yield-stress fluids could achieve the properties or performance displayed by the application-relevant materials, the only choice was to formulate a new material. For this new material, I sought to make it a model highly extensible yield-stress fluid. This work defines a model material as i) having a simple, controllable formulation; and ii) having an interrogatable microstructure.

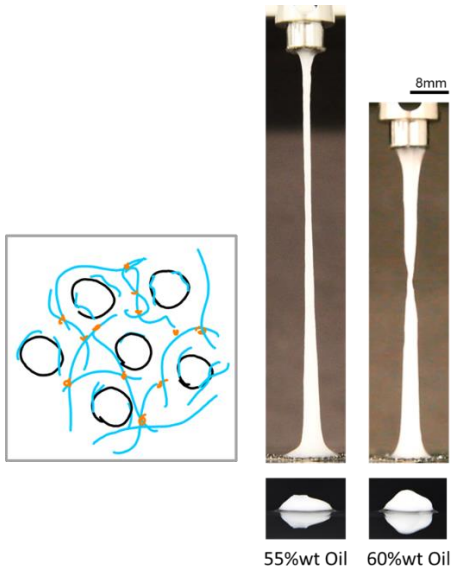

Figure 3.8. Proposed highly extensible model yield-stress fluid, a silicone oil-in-water emulsion combined with a transiently-crosslinked network of polyvinyl alcohol (MW 85,000 – 124,000). Shown on the left is a sketch of the microstructural concept used to conceive of this material: the emulsified droplets (shown in black) provide the material with a structure with which to bear static loads (a yield stress), while the transiently-crosslinked polymer network (blue lines with orange crosslinks) prevents the droplets from coalescing and allows the structure to survive large extensional strains. Shown on the right are the two synthesized formulations which manifested the desired qualitative performance objectives. The 8mm scale bar shown applies to all four images on the right.

For this process, numerous microstructure concepts were envisioned using a technique of juxtaposing two different existing microstructures as detailed in Section 2.4.5. As briefly introduced in Section 2.5.2, the material concept chosen to develop is shown in Figure 3.8 and was conceived of as the combination of a yield-stress-providing microstructure (a packed emulsion) and an extensibility-providing microstructure (a transiently-crosslinked network).

An emulsion was chosen as the yield-stress-providing microstructure since it conceptually allows for the compartmentalization of different additives into the water (continuous) and oil (dispersed) phases, thus allowing for more freedom when choosing the method of providing high extensibility. As stated, one of the preferred goals was for the model system to have a simple formulation. For this reason, poly(vinyl-alcohol) with a moderately high molecular weight was chosen to provide the extensibility since it has dual functionality as an emulsifier, removing the need for an additional emulsifying ingredient. To further increase the extensibility, I chose to add borax as a transient crosslinker; an alternative strategy for increasing extensibility might be to use a very high molecular weight poly(vinyl-alcohol), but in practice this made emulsification more difficult and this strategy was not pursued.

As desired of our model system, the microstructure is directly observable. Images of the microstructure obtained by microscopy and measurements of the radii of the resolvable droplets in the respective images are shown in Figure 3.9 for a range of oil content. As envisioned, there exists a dispersed oil droplet microstructure which packs together, providing a mechanism for yield-stress behavior to occur. Figure 3.9 shows that some areas of the 50wt% formulation (which did not show yield-stress behavior) are relatively open with few oil droplets. This was not the case for the 55 and 60wt% formulations which always have significant oil-droplet packing. From the measurements of droplet radii of the 50, 55, and 60wt% images, the mean droplet sizes were 16.3, 11.5, and 10.1 μm respectively. For the same measurements fit to a lognormal distribution, the lognormal means were 2.5, 2.2, and 2.1 μm respectively. For either distribution, the mean droplet radius does not decrease significantly with increasing oil content. The maximum droplet radii with increasing oil content were 105, 64, and 75 μm respectively, and again no clear trend was seen.

The smallest measured droplet radius across all samples was 2.4 μm, but it is likely that smaller but unresolvable droplets exist within all samples.

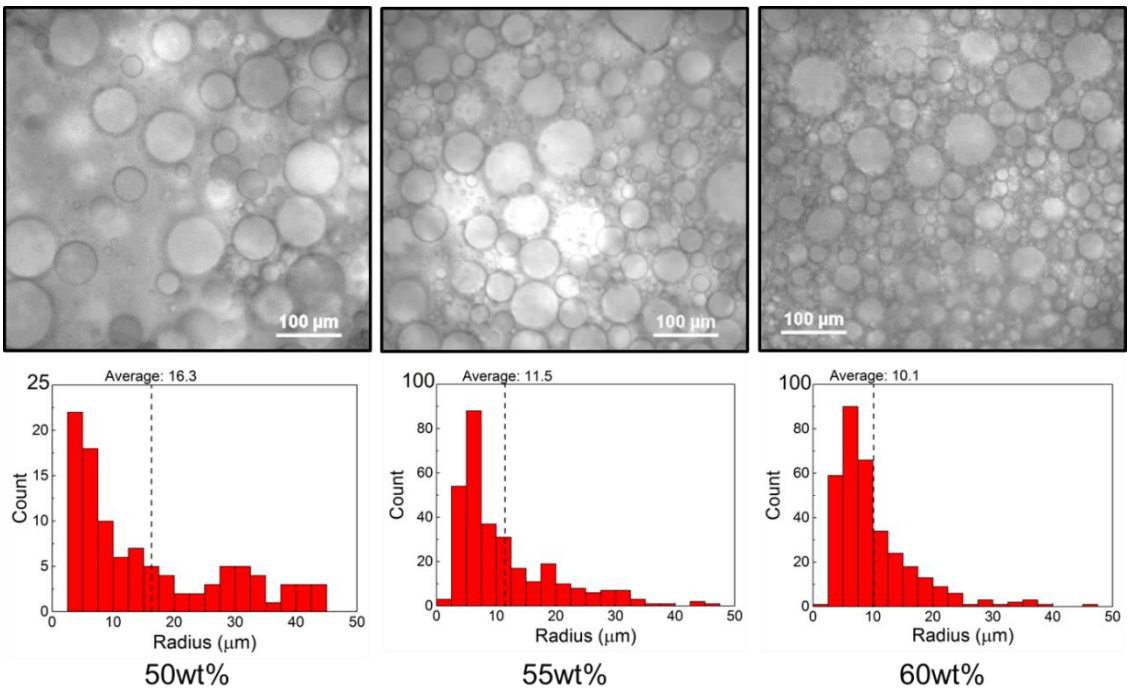

Figure 3.9. Micrographs and droplet size distributions of the designed PVA-borax emulsion at different oil content formulations. The 50wt% formulation has areas of the microstructure with relatively loose packing of oil droplets, whereas the 55wt% and 60wt% formulations always have a high oil-droplet packing. The droplet size distributions were quantified using the resolvable droplets in the images shown.

With this microscopy technique one is unable to view the structure of the PVA; however, PVA is known to move to the interface of oil and water [149]. Since I am unable to determine any microstructure composed of PVA and Borax, it is unknown how accurately the formulated material matches my synthesized design concept. However, based on this concept, this work was able to achieve the performance shown in Figure 3.8, which can match the extensibility of existing consumer products.

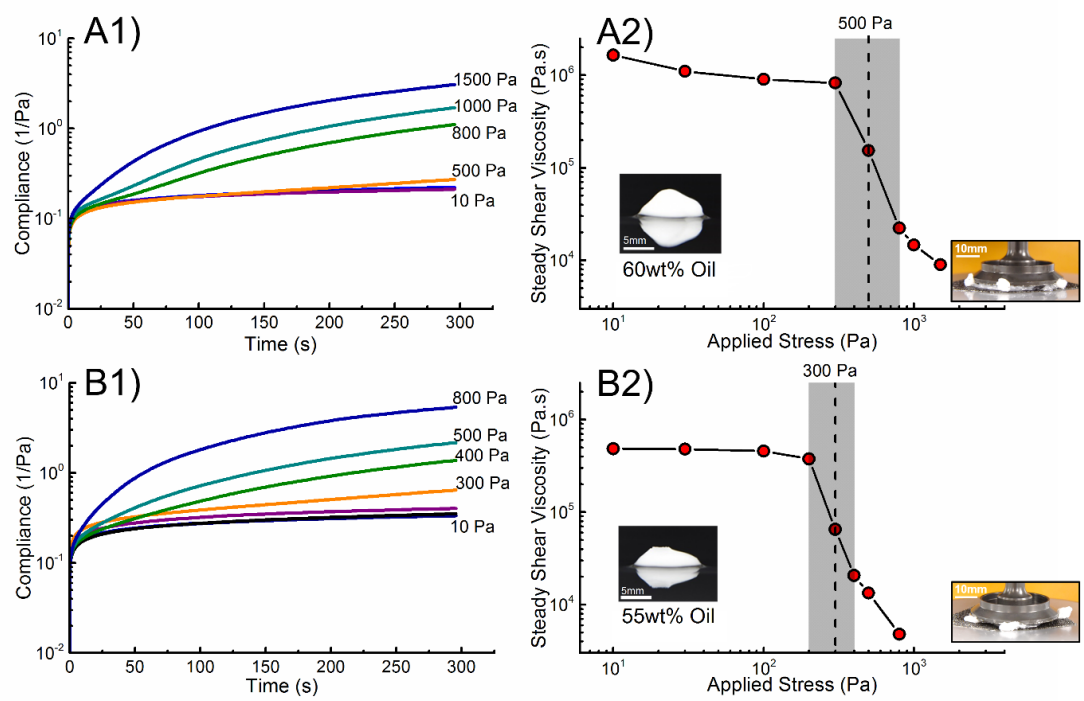

Figure 3.10. Shear creep compliance curves for two formulations of the proposed model material with A) 60 and B) 55 wt% silicone oil. Compliance over time at various levels of applied stress (A1 and B1), resulted in steady shear viscosity curves (A2 and B2) which show yielding. The grey shaded regions are bounded by the stresses over which viscosity decreases by over half an order of magnitude, the yield stress for each material is taken as the stress for the data point within the shaded regions. Inset images depict sample fracture which occurs at stresses higher than the reported data points.

Figure 3.10 shows the shear creep compliance characterization for the PVA-borax emulsions with two different oil loadings. Above 50wt% oil (see Appendix B), the material transitions from a shear-thinning material with no yield stress to a yield-stress fluid with yield stresses of 300 Pa and 500 Pa for the 55 and 60wt% oil formulations, respectively.

Though these materials can achieve the yield stress performance objectives that were sought, there are numerous experimental challenges with the system including edge fracture at high stresses or shear rates (Figure 3.10 inset), and a propensity towards slip and confinement artifacts.

Figure 3.11 shows the characterization of the PVA-borax emulsions in extension in both the filament-stretching and counter-rotating-drum experimental setups. As was desired for matching the behavior of the application-relevant products, the 55wt% oil reached the strain-limit of the

filament-stretching setup (Figure 3.11 A2), and thus necessitated testing on the counter-rotating-drums. Due to the softness of the material, reproducible loading for this setup was extremely challenging for both formulations, resulting in the standard deviation error bars shown. The 60wt% formulation was the only observed material that was capable of being tested on both experimental setups. For comparison between the two formulations, the strain-to-break values were both taken from the counter-rotating-drum setup (A1 and B1).

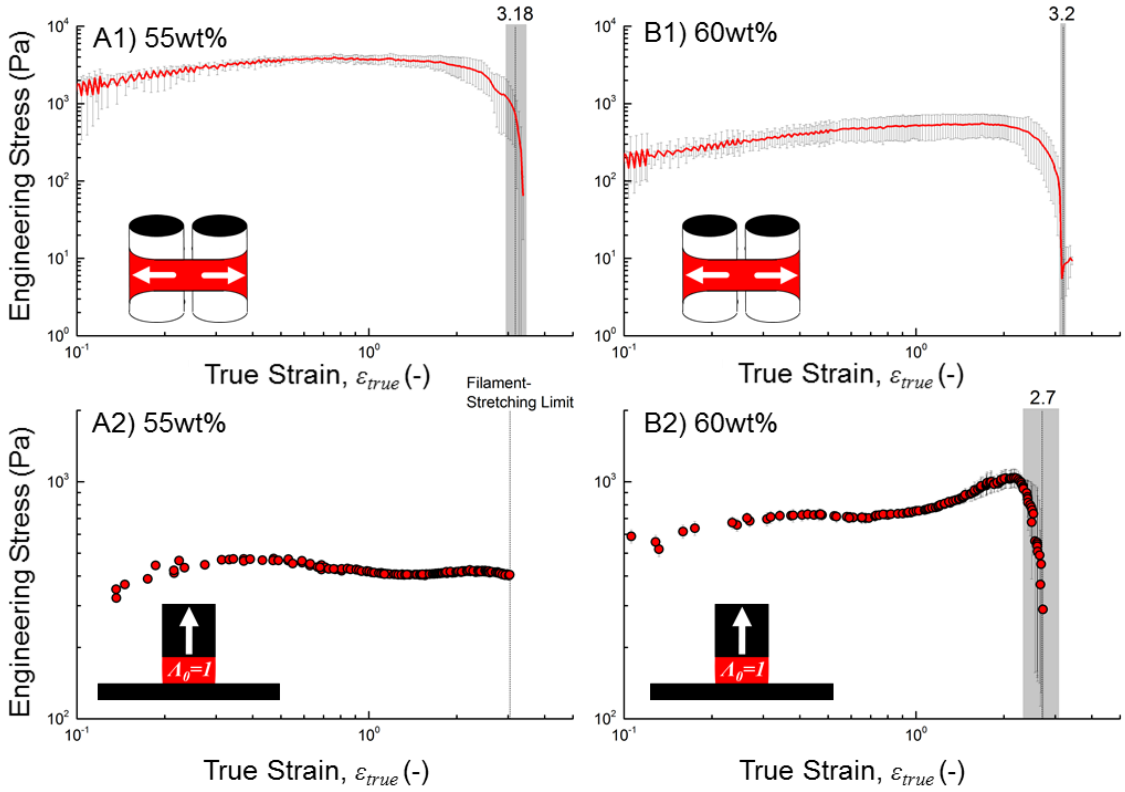

Figure 3.11. Extensional engineering stress curves for proposed model highly-extensible yield-stress fluid. A) 55wt% and B) 60wt% formulation. A1) and B1) depict experiments performed using the SER3 experimental setup with the average of repeated experiments in red and error bars in gray. A2) and B2) depict experiments performed using the ARES-G2 experimental setup. Curves were correlated with video to determine the engineering strain-to-break. For subsequent figures, values of strain-to-break are taken from A1) and B1). Error bars shown are the standard deviation from repeated experiments.

In Figure 3.12, characterization results for the designed yield-stress fluid system are shown compared to archetypal and consumer/industrial yield-stress fluids. With our synthesized material,

I am able to match the extensibility performance of the most extensible consumer products shown here.

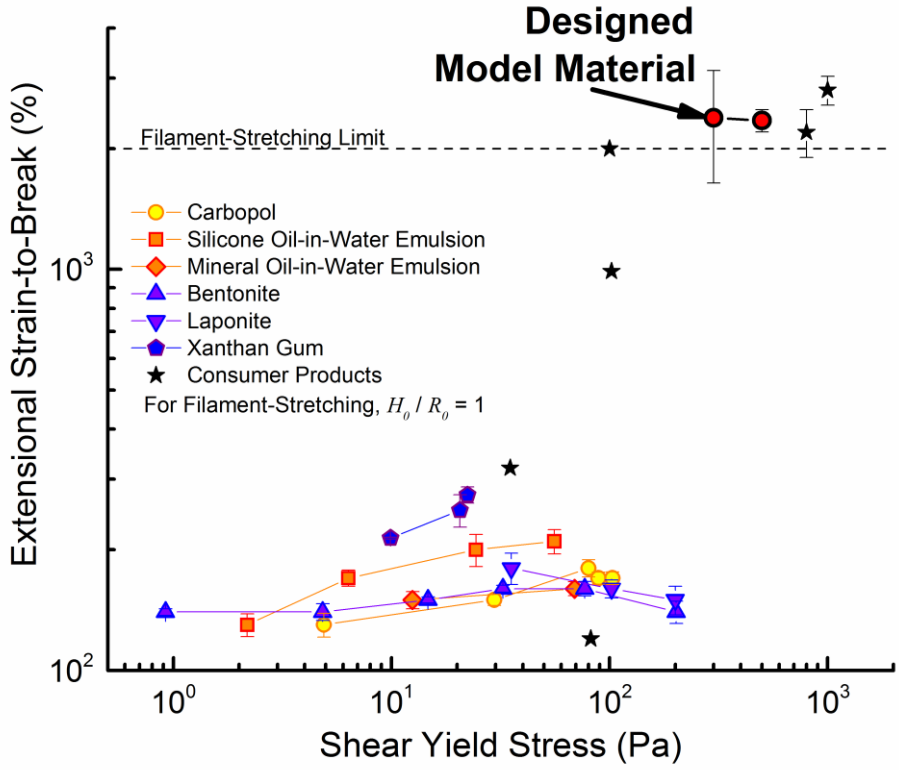

Figure 3.12. Ashby-style co-plot of all materials studied here. For data points above the filament-stretching limit, values from the counter-rotating-drum setup were used. See Appendices A and B for the full steady shear flow and extensional engineering stress curves that these points represent. Error bars shown are the standard deviation from repeated experiments.

3.5 Conclusions and Outlook

Here this work has presented a new paradigm of yield-stress fluids as capable of being highly-extensible materials. I introduced a methodology for characterizing yield-stress fluids capable of capturing a wide range of yield stress and extensibility behavior. Lacking a suitable model highly-extensible yield-stress fluid, I generated a concept for a new material based on a combination of microstructures, synthesized our candidate material, and then carried out rheological characterization. Though there are numerous experimental challenges associated with the newly

synthesized material, I have shown that it is capable of quantitatively matching the behavior of highly extensible yield-stress fluid consumer products. Schematic relations of the design and analysis processes I carried out are shown in Figure 3.13.

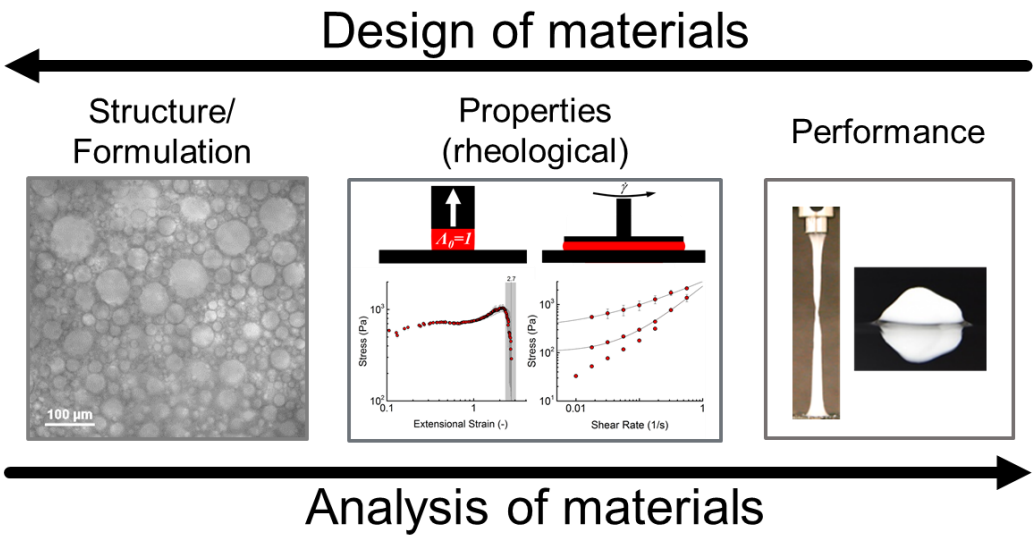

Figure 3.13. Schematic relations of design and analysis of materials (adapted from [33] and applied to rheological properties). The process presented in this work demonstrates the complementary nature of analysis and design. Starting with the observable performance goal (on the right) of yield-stress fluids that are highly extensible (Figure 3.1B,C), attempts were made to match this by analyzing and evaluating simple model systems; when this failed a new microstructure concept was conceived and formulated (on left, also Figure 3.8), and analyzed for validation that the performance goal had been met. Following these principles I have demonstrated the design process of a new material that is built upon a strong foundation of analysis.

This work has shown here that the archetypal yield-stress fluids are not acceptable models when studying materials where high extensibility is important, and has provided a candidate model material for study. However, this work has also shown that the inverse is true: when studying applications where a low extensibility is preferred or expected, one may choose from many well-characterized model materials and need not worry about the physics associated with high extensibility. For the high-extensibility materials, new constitutive models are required that capture the appropriate physics. In order to satisfy the Considère criterion, a candidate constitutive model would have to capture yield-stress fluid behavior as well as viscoelasticity and extension-

rate dependence [151,152]. As stated when introducing our characterization method, the results are dependent on initial geometry and extension rate. Though our initial geometry was chosen to have a near-optimal initial aspect ratio, our choice of extension rate was somewhat arbitrary. It has yet to be investigated what effect extension rate would have on the materials tested here.

Shown here are only a few material formulations, and thus the full performance space available for our designed system is unknown and is certainly un-optimized — not to mention the plethora of un-synthesized or even un-considered materials that may also match the target performance. Extremely high extensibility will also not be the intended target performance for different applications. For instance, the HexArmor resin (Figure 3.1B) used in printing only reaches a moderate extensibility. This work conjectures that the extensibility of this material contributes to a smoother extrusion or spraying process, but it is unknown where in the design space would be "ideal" for printing. The characterization methodology provides a framework for determining areas of the design space that are consistent with ideal performance for applications where it is suspected that extensibility plays a role. In Chapter 5 this framework is used to investigate the impact of extensibility on direct-write 3D printing performance.

Chapter 4: The rheology of magic – Mystic Smoke

4.1 Introduction

In this chapter, I discuss one of the application-relevant materials presented in Chapter 2 in more detail. As briefly introduced, "Mystic Smoke" is a product distributed by Loftus International and is available at toy and magic stores (Figure 4.1a). Shown in Figure 4.1d is the fabulous functional behavior of Mystic Smoke. Though the material is a viscous liquid that can be spread between one's fingers, rapid separation results in many long thin fibers that are light enough to float away if "thrown" with a vigorous hand motion but are stable and do not collapse. This behavior of the material lends itself to magical performances, giving a performer/magician the capability of producing smoke from one's hands in conjunction with other effects such as disappearing items.

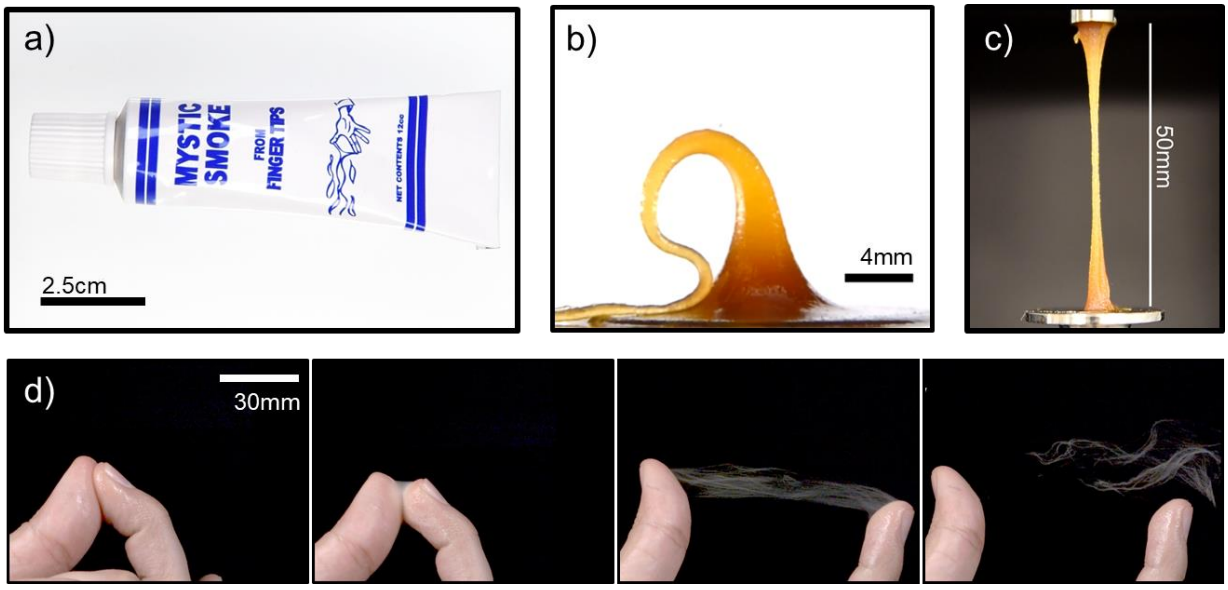

Figure 4.1 a) Retail packaging of Mystic Smoke. b) Extruded Mystic Smoke holding a shape for long times (image taken 5 minutes after deposition). c) Mystic Smoke in extension. d) Image sequence of Mystic Smoke showing filament formation, extension, and breakage, the 30mm scale bar applies to all images in this sequence.

The measurements performed here show that Mystic Smoke is an apparent yield-stress fluid with marvelous if-not-exactly magical behavior. On viewing the behavior of this material, I hypothesized that the success of the magical effect relies on the interesting and uncommonly studied rheological combination of yield stress behavior (Figure 4.1b) and high extensibility (Figure 4.1c). Table 4.1 lists the functional requirements of the material, and how the hypothesized properties would contribute to each of these requirements.

Table 4.1 Functional requirements for performance of Mystic Smoke, and the hypothesized properties that would satisfy them.

Performance / **Property**	Spreadable (on fingers)	Adhere to surface	Form several thin filaments	Large extension (high aspect ratio filaments)	Filament shape retention
Yield Stress		✓	✓		✓
shear viscosity (post-yield)	✓		✓		
Large strain-to-break				✓	

Motivated by a personal interest in performance magic, I performed the characterization protocols detailed in Chapter 3 to test whether these properties were in fact present. The measurements reported here serve as a useful pedagogical tool. As has been discussed, there are myriad uses of yield-stress fluids that are incredibly important and useful. However, in my experience of demonstrating rheologically complex materials to non-technical audiences (elementary school through undergraduate college students and older), the most easily available yield-stress fluids are often perceived as mundane (e.g. hand sanitizer, toothpaste, etc.) compared to the other key phenomena of rheology [47]. Demonstrations of the complex rheology of Mystic Smoke are consistently surprising and intriguing to my audiences.

4.2 Methods

Yield-stress characterization was performed by step-stress creep compliance tests. Velocity-controlled tests were problematic for this material, which would often exhibit edge fracture and evacuate the gap. Shear tests were performed on a TA Instruments DHR-3 rheometer (combined motor/transducer) with a 20mm diameter flat plate geometry and temperature-controlled bottom Peltier plate. For the creep tests, materials were allowed to reach a steady shear-rate, allowing for the determination of steady shear viscosity as a function of the applied stress. The yield-stress in this case was taken from within the stress range over which the viscosity declines by over a half-order of magnitude.

Extensional rheology was characterized by the filament-stretching protocol introduced in Section 3.3. Characterization with filament stretching for the extensional strain-to-break was performed on a TA Instruments ARES-G2 rheometer (separated rotational motor/transducer, combined axial motor/transducer). For the filament-stretching experiments a parallel-plate geometry with a diameter of 8 millimeters and advanced Peltier system bottom plate were used. The samples were loaded at a gap of 4 millimeters, resulting in an aspect ratio of $\Lambda_0 = H_0 / R_0 = 1$. Samples were loaded as near to the initial height as possible to minimize compression. Samples were not pre-sheared for extensional tests. The maximum gap on the ARES-G2 allowed for a maximum engineering strain of $\varepsilon_{eng} = 2000\%$ ($\varepsilon_{true} \approx 3.04$). A constant true strain rate, $\dot{\varepsilon} = 0.2 s^{-1}$, was used for all tests.

The Mystic Smoke was tested as received. I note that the composition of Mystic Smoke is largely unknown but labeled non-toxic; the available ingredients list is only given as “waxes, rosin, oil & latex”. Because of this, one does not know the specific microstructure or chemistry that

results in the performance or rheological properties but can still connect the properties to the performance.

4.3 Results

4.3.1 Apparent Yield Stress Behavior

Shown in Figure 4.2 are the creep compliances of Mystic Smoke at 23 °C (room temperature) and 37 °C (body temperature), and the resulting steady shear viscosity as a function of the applied stress. At room temperature, at low stresses, the steady shear viscosity is approximately 300,000 Pa.s (~30,000 times more viscous than honey [153]), and after the yielding region (30 – 300 Pa), the material has shear thinned by a factor of approximately 1000, but still has a relatively high viscosity of several hundred Pa.s. Though there is a measurable viscosity at stresses below 30 Pa, this material can be considered an apparent yield-stress fluid because the pre-yield viscosity is so high for practical usage [10] and a relatively large change in viscosity occurs with increasing stress. On the other hand, at 37 °C, though I do observe shear-thinning, the low-stress viscosity is only ~10^3 Pa.s, not high enough to be considered effectively a solid.

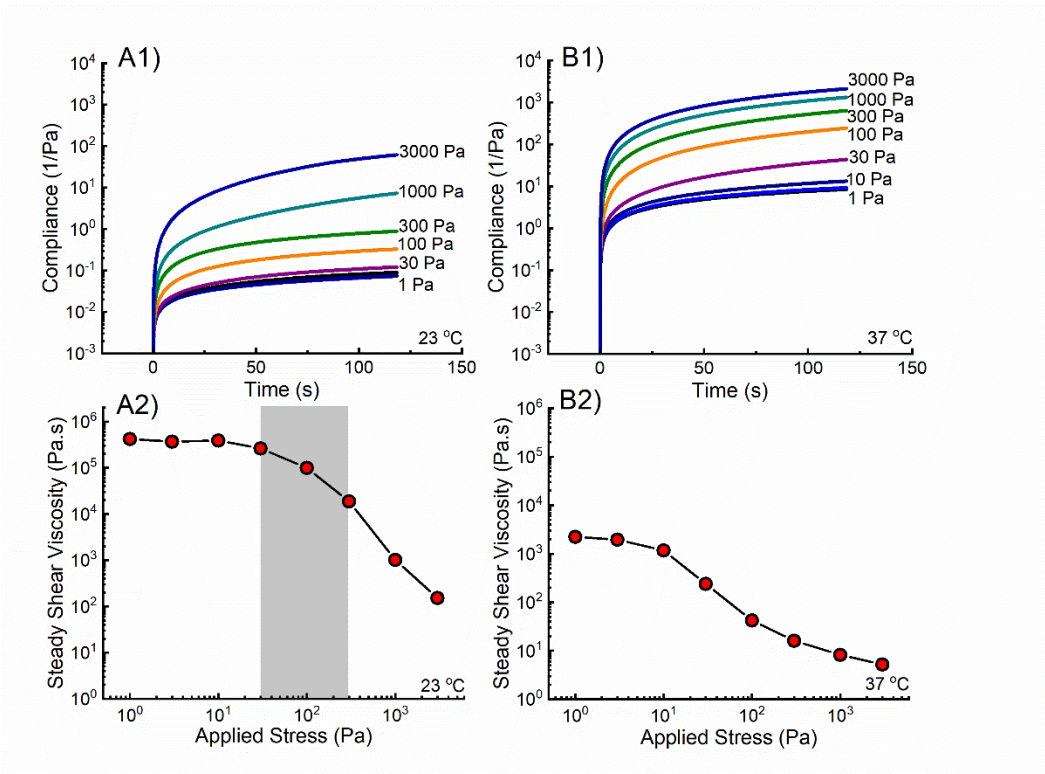

Figure 4.2. Shear creep compliance curves of Mystic Smoke at A) 23 °C (room temperature) and B) 37 °C (body temperature). Compliance over time at various levels of applied stress (A1 and B1), resulted in steady shear viscosity curves (A2 and B2) which show yielding. Mystic Smoke shows apparent yield-stress behavior at 23 °C and not at 37 °C. The grey shaded region is bounded by the stresses over which viscosity decreases by over half an order of magnitude. Error bars for steady shear viscosity from 3 repeat measurements are smaller than the data points.

4.3.2 Extensional Behavior

Shown in Figure 4.3 is the engineering stress-strain curves from the filament stretching characterization where the initial aspect ratio, $\Lambda_0 = H_0 / R_0 = 1$ for initial gap, $H_0 = 4\text{mm}$, and the true extensional strain-rate was $\dot{\varepsilon} = 0.2\ \text{s}^{-1}$. From this characterization method I find that Mystic Smoke at room temperature can survive extensional engineering strains up to 2000% (true strain of ~3), far greater than what is seen in model yield-stress fluids (see Chapter 3). Though this shows that Mystic Smoke is an impressively extensible yield-stress fluid—essentially reaching the strain

limit for our filament stretching experimental setup—this strain is far below what is seen in application as in Figure 4.1d.

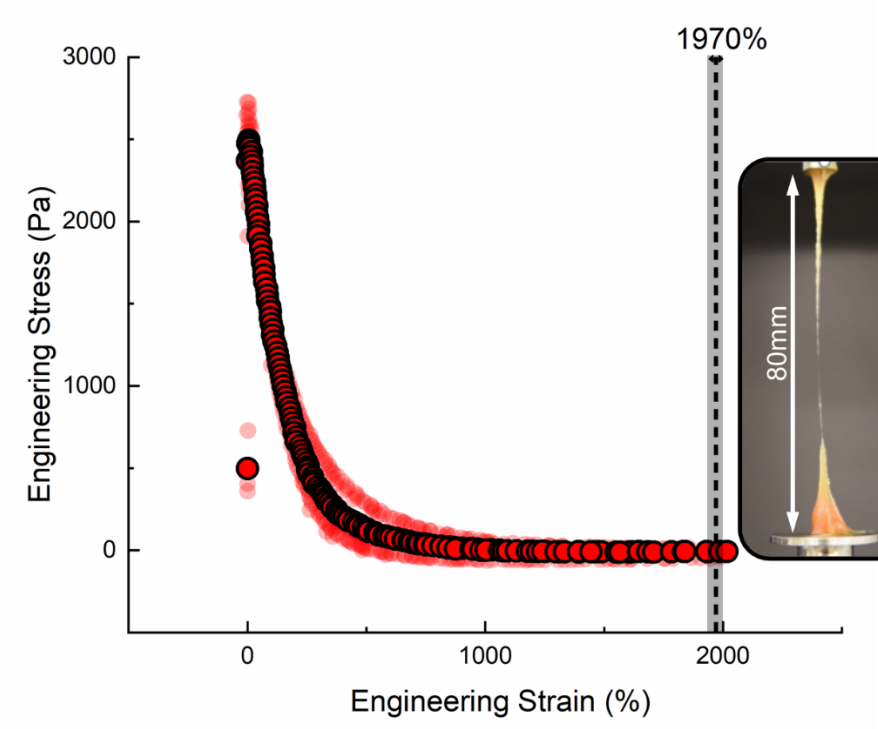

Figure 4.3. Extensional engineering stress curves for Mystic Smoke at 23 °C tested using the ARES-G2 filament stretching experimental setup where the initial aspect ratio, $\Lambda_0 = H_0 / R_0 = 1$. The bold data points are the average of three repeated experiments (lightened data points) The vertical dashed line depicts the average strain-to-break which was found by correlating the extensional stress curves with video images. The width of the shaded region depicts the standard deviation in the strain-to-break from repeated experiments A constant true strain-rate of $\dot{\varepsilon} = 0.2\ s^{-1}$ was used for all extensional tests. The image on the right depicts the material immediately after rupture occurred.

4.4 Discussion

4.4.1 Filament Formation

The formation of many small filaments, which is key for the smoke effect, has been observed in peeling geometries for adhesives [154,155], and can be attributed to the Saffman-Taylor (viscous fingering) instability which has been investigated for yield-stress fluids [7,8,115]. Another possible contributor to filament formation could be cavitation within the thin film [155].

Giving a material a yield stress has been found to induce the viscous fingering instability due to the additional resistance to inward shear flow. Barral et al. [7] developed a parameter space involving shear yield stress and initial geometry that can be used to predict when the flow of a yield-stress fluid between two separating plates would be unstable, producing viscous fingering. For Figure 4.1d, a volume of 0.2 ml was spread across an area between my thumb and index finger of approximately 600 mm^2. Assuming a uniform layer thickness, this gives an initial gap of 333 microns, and a very small initial aspect ratio. This initial geometry and the characterized yield stress value for Mystic Smoke falls within the unstable flow regime determined by Barral et al. [7], suggesting that the Saffman-Taylor instability is a significant factor in the formation of filaments. For cavitation to take place (as with gum in Figure 3.1c) a high stress is required during flow (i.e. high post-yield viscosity). Regardless of which of these processes is responsible for the filament formation, the presence of a yield stress contributes to their formation in either case. Assuming that the small filaments form immediately (i.e. deformation is dominated by extension rather than inward shear flow), the final gap shown in Figure 4.1 is approximately 15 cm, which equates to a final engineering strain of nearly 45,000% (true strain of ~6). This engineering strain during performance is over twenty times what is observed in the filament stretching setup. Although the true strain is only larger by a factor of two, this difference still deserves discussion. This value of rupture strain in application serves as an upper bound estimate since some initial shear flow must occur, and thus the local aspect ratio at the filament location will be closer to 1.

Despite the large difference, one can rationalize the much larger strain-to-break in performance compared to the rheological characterization as being due to the vastly different extensional strain-rates. In our experimental setup I am limited to an extension rate of 0.2 s^{-1}, whereas in application the extension is a is limited only by the stresses and velocities that a human hand can produce. The

extension process depicted in 4.1d took place over approximately 100 ms. Assuming a constant speed of separation and the previously assumed final and initial gaps of 15 cm and 333 microns, respectively, this gives an initial extensional strain rate of 4500 s^{-1}. Though experimentally we are unable to access rates faster than 0.2 s^{-1}, we have no issues going slower. Shown in Figure 4.4 is a comparison of the extensional rupture behavior of Mystic Smoke at extensional strain rates of $0.02\ s^{-1}$ and $0.2\ s^{-1}$ ($\Lambda_0 = 1$ for both). At 0.02 s^{-1} the rupture strain is much lower at 480%. Thus, one can expect for this material that as the rate of extension increases, the value of strain-to-break will increase. This rationalizes the much larger rupture strain seen in application since the estimated maximum application strain rate is over 20,000 times higher.

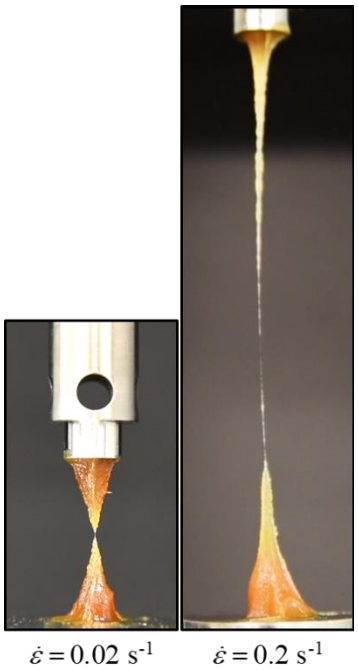

Figure 4.4 Extensional behavior of Mystic Smoke at different extensional strain rates. Images taken just after rupture. The extensional failure strain increases with strain rate.

4.4.2 Filament Shape Retention

For a yield-stress fluid in a cylindrical shape with radius *R*, one expects that it will be stable against surface-tension-driven pinch-off for,

$$\sigma_Y > \frac{\gamma}{R} \tag{4.1}$$

where I will approximate the surface tension, γ, as 20 mN/m—the surface tension of silicone oil in air [156]. We can treat this as a rheological criterion to sustain a filament of radius *R*. If one takes the yield stress, σ_Y, as 300 Pa—the high end of the yielding region—then the critical radius is approximately 65 microns. This compares well with the filaments shown in Figure 4.1d, which are approximately 150 microns in diameter and do not break-up into droplets. Thus, the shear rheological characterization is consistent with the hypothesis of yield stress behavior stabilizing the filaments.

4.5 Conclusions and Outlook

We have demonstrated that Mystic Smoke is a highly extensible yield-stress fluid. The rheological properties characterized are consistent with what is seen in application and contribute towards producing the "magical" effect. As a non-toxic, readily available material, it is a highly entertaining and novel demonstration of apparent yield-stress fluid behavior coupled with high extensibility. Possible future studies of this material include characterization of the extensional viscosity at more relevant extension rates. It is possible that capillary breakup extensional rheometery (CaBER) technologies may approach the extension rates seen in application [157,158]. To test whether the properties characterized here are sufficient, and what other property targets might be necessary for the full performance, model highly extensible yield-stress fluids with comparable yield stresses and extensional failure strains but with other differing properties (e.g. extensional viscosity, viscoelastic moduli, etc.) could be formulated.

In the next chapter, I will discuss how the combination of apparent yield-stress behavior and high extensibility is also relevant for direct-write 3D printing. Furthermore, the behavior of Mystic Smoke inspires a novel method for the production of extremely thin structures via the rapid extension of yield-stress materials that are highly-extensible. I conjecture that a precisely engineered surface similar to that presented by Islam & Gandhi for controlling the shape of a Saffman-Taylor instability [159] would provide locations where filaments would preferentially form, allowing for control of the filament size and spacing. Techniques similar to the rapid extension of Mystic Smoke have been shown to have applications in 3D printing [160]. This technique could potentially be applied to some frontally polymerizable materials [161]. Preliminary work with frontally polymerizable materials, in collaboration with the Autonomic Materials Systems group at the University of Illinois at Urbana-Champaign, has shown that their materials can indeed be highly-extensible yield-stress fluids.

Chapter 5: Direct-write 3D printing model-material design*

5.1 Introduction

In this chapter, we make use of the design methods presented in Chapter 2, as well as the characterization protocols for extensible yield-stress fluids presented in Chapter 3, and apply them to a particular application, 3D printing. This work was done in collaboration with Dr. Brittany Rauzan, Dr. Sean Lehman, and Professor Ralph Nuzzo in the Department of Chemistry at the University of Illinois. My general responsibilities on this work were the design and formulation of a model 3D printing ink, rheological characterization, and microstructure imaging. My collaborators were responsible for 3D printing, post-3D printing transformation processes and the characterization associated with those stages including thermogravimetric analysis, Fourier transform infrared spectroscopy, and gel permeation chromatography measurements.

3D printing is a rapidly expanding field due to the ability to fabricate customizable structures with applications for actuators [162], soft robotics [163], tissue engineering [164], and electronics[165]. The majority of commercial 3D printing systems currently available to fabricate items for these industries are limited to using either metal, ceramics, or thermoplastics. This restricted material set limits widespread adoption and use of 3D printing to generate customizable and tunable structures for desired applications. Yield-stress fluids that are direct writable using

* Portions of this chapter appeared in the following Ph.D. thesis:
B.M. Rauzan, 2017 "Characterize the molecular dynamics of materials for 4D printing," Ph.D. thesis, University of Illinois, Champaign, IL.
and as the following peer-reviewed publication (re-used with permission):
Rauzan, B. M.[≠], Nelson, A. Z.[≠], Lehman, S. E., Ewoldt, R. H. & Nuzzo, R. G. Particle-Free Emulsions for 3D Printing Elastomers. Adv. Funct. Mater. 1707032 (2018). doi:10.1002/adfm.201707032
[≠]These authors contributed equally to this work

pneumatic extrusion are a nascent material class that is being explored to address the growing need for new inks for 3D printing.

The reported challenges in developing yield-stress fluid inks are to allow for the ability to both build structures and print small diameter filaments (l00 μm or smaller) with high shape-retention. A large variety of yield-stress fluids have been studied for use as inks for 3D and 4D printing (Figure 5.1a)[166–177]. As introduced in Section 2.4.1, these materials may be organized according to the employed design strategy and microstructural mechanism by which the yield-stress occurs (e.g. particulate gels, polymer gel, jammed suspensions, emulsions, foam, etc.) While the range of reported yield stresses is very large (1 to over 1000 Pa), the resolution for the smallest reported nozzle diameter is approximately 10 to 30 μm. It has been noted that for applications that are limited by diffusion kinetics (e.g. biological [178,179], actuation [162], etc.), smaller filament diameters are required for the necessary mass-transport properties.

In most inks systems, reducing the filament diameter is only possible through decreasing the diameter of the nozzle used for printing. A major challenge in reducing the nozzle diameter is microstructural jamming through the tip. It has been shown that even with particles on the order of nanometers in diameter, large aggregates can form and result in clogging of the tip, with the additional complication of material drying at the tip [174]. A possible approach to overcome this might be to reduce the loading/density of the material microstructure, however this comes at the cost of a reduced yield stress [177]. A previous attempt at this approach has resulted in materials that have too low of a yield stress or modulus to build large, open, self-supporting (i.e. gap-spanning) structures [180]. This trade-off creates a limitation on the types of 3D structures that may be built with available inks.

Extensible particle free-emulsions, which have not been previously studied as direct-write 3D printing materials, are here explored as an alternative yield-stress fluid to particle-stabilized or polymer-based gels. The dispersed phase of these emulsions act as pseudo-particles that jam against each other in order to support a static load (Figure 5.1b). However, unlike hard colloidal nanoparticles, the emulsified droplets are able to deform to the shape of the tip and, if necessary, split to continue printing [181]. The importance of extensional rheology has been established for extrusion processes such as injection molding and film formation [134], but has not been investigated for direct-write 3D printing. It has been conjectured that a higher extensibility would stabilize a filament during extrusion, improving printing performance [119]. The ability to both deform/conform to the restrictions of the tip geometry and diameter and exhibit high extensibility (500% or greater) introduces a novel class of inks for 3D printing.

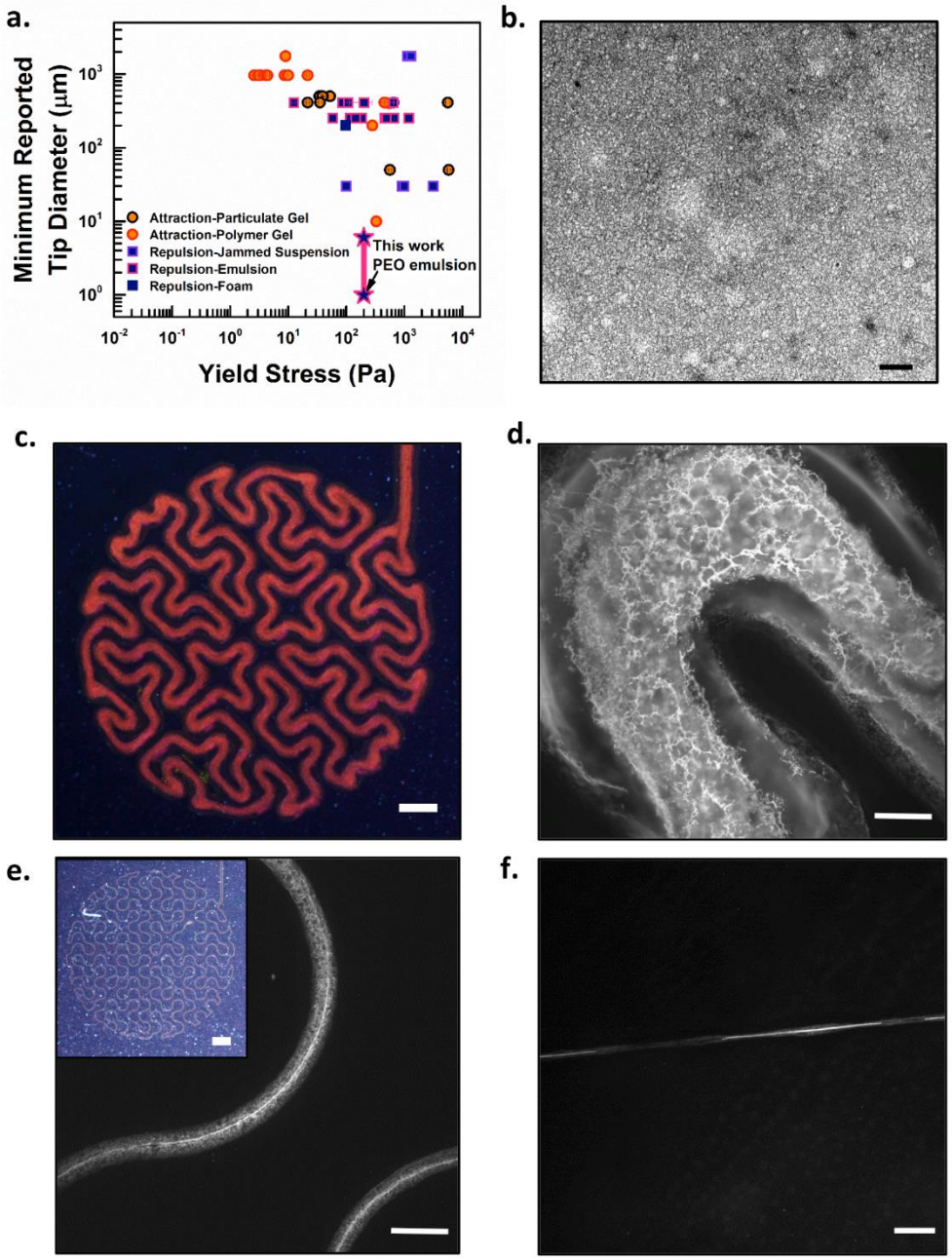

Figure 5.1. a. Minimum reported tip diameter as a function of yield stress for 3D printing yield stress fluids organized by microstructure and yield-stress mechanism (attraction-particulate gel, attraction-polymer gel, repulsion-jammed suspension, repulsion-emulsion, repulsion-foam, [6] and PEO emulsion [reported in this work] b. transmitted brightfield microscopy of 8M PEO emulsion with Congo Red, scale bar 50 μm, c. macro fluorescence image of serpentine pattern of 8M PEO emulsion with Rhodamine 6G printed with 100 μm diameter tip at 1 mm/s, scale bar 1 mm, d. fluorescence microscopy of serpentine pattern of 8M PEO emulsion with Congo Red printed with 100 μm diameter tip at 1 mm/s, scale bar 50 μm, e. fluorescence microscopy of serpentine pattern of 8M PEO with Congo Red emulsion printed with 1 μm diameter tip at 1 mm/s, scale bar 100 μm, inset macro fluorescence image of serpentine pattern of 8M PEO emulsion with Rhodamine 6G printed with 1 μm diameter tip at 1 mm/s, scale bar 1 mm, f. fluorescence microscopy of line pattern of 8M PEO emulsion with Congo Red printed with 1 μm diameter tip at 20 mm/s scale bar 50 μm.

In this work, we examined the fabrication of particle-free silicone oil-in-water emulsions with a polymer additive, poly (ethylene oxide) (PEO), to form elastomeric structures. We used a printing-centric approach addressing three key areas of 3D printing performance (filament diameter, nozzle movement rate, and gap spanning). The molecular weight of PEO was varied to understand the relationship between microstructure, critical rheological properties (shear flow properties and extensibility, which as discussed in Section 3.2 has previously been limited to low-extensibility yield-stress fluids), and printing performance. Post-printing chemical and thermal annealing was performed on the particle-free emulsions to prepare elastomers, which have new properties including mechanical buckling, and recovery from extreme compressive strain, which is not innate to the initial particle-free emulsions.

5.2 Results and Discussion

Particle-free emulsions are examined as an alternative microstructure for 3D printing inks to fabricate 3D structures and intricate small diameter filament patterns. In contrast to many of the reported inks in the literature, this novel material does not require incorporation of particles to achieve a sufficient yield stress for building (Figure 5.1a). The yield stress (approximately 200 Pa in shear) is achieved with a microstructure that allows for extrusion of the material through a 1 μm diameter tip.

5.2.1 Fabrication of Particle-Free Emulsions and 3D Printed Filament Resolution

The emulsion was prepared as a stock particle-free silicone oil-in-water emulsion using sodium dodecyl sulfate (SDS) as a surfactant. The advantage of using a stock particle-free emulsion was that it provided a simple method for using a printing-centric approach to understand the impact on polymer additive on rheological properties and 3D printing performance of the

material. PEO of different average molecular weights ranging from 400 K – 8 M g/mol (0.4 – 8 M) was incorporated into the stock-emulsions such that the final overall weight percent for all molecular weights is 0.1 wt% PEO. Transmitted brightfield microscopy of the 8M PEO emulsion with the aqueous phase dyed with Congo Red (Figure 5.1b) showed a homogeneous emulsion with the dispersed phase of silicone oil droplets on the order of 10 μm in diameter.

PEO has been shown to form a complex with SDS micelles in surfactant solutions[182]. Dynamic light scattering and zeta potential measurements of aqueous solutions of SDS and 8M PEO at the concentrations used in the emulsions were examined to determine interactions between the surfactant and polymer additive in the emulsion materials and are given in Appendix C. The hydrodynamic diameter for both SDS and SDS with 8M PEO are polydisperse with the majority of micelles for SDS approximately 1 nm and SDS with 8M PEO ranging between 10-100 nm. The increase in hydrodynamic diameter was expected due to the interaction between SDS and PEO and formation of micelles, which is further confirmed by a decrease in the zeta potential for the SDS with 8M PEO solution. The addition of PEO is proposed to interact with the electrical double layer present at the surface of the oil droplets in a way that does not disrupt the native microstructure of the emulsion.

The emulsion enables 3D printing to fabricate intricate patterns using multiple tip diameters. A fluorescence image of a serpentine pattern printed with an 8M PEO emulsion dyed with Rhodamine 6G is shown in Figure 5.1c using a 100 μm diameter tip. The material displays excellent filament shape retention and was stable under normal conditions without filament distortion (dehydration or cracking). There was no apparent disruption to the microstructure of the emulsion evident when the serpentine pattern dyed with Congo Red was examined using fluorescence microscopy (Figure 5.1d). Due to an ability to easily deform the dispersed phase, the

emulsion was able to be extruded through a 1 μm diameter tip [181], which is not possible with commonly used inks due to the microstructure jamming. Using the same serpentine pattern (Figure 5.1e inset), the emulsion was printed using a 1μm diameter tip; both macroscopic (dyed with Rhodamine 6G) and microscopic (dyed with Congo Red) fluorescence images are shown in Figure 5.1e. In comparison to the sample printed with a 100 μm diameter tip, the reduction in the tip diameter and corresponding filament diameter allowed for improved resolution of the features of the pattern as seen in the ability to resolve precise curvature of the pattern (Figure 5.1e), whereas the resolution of the curvature is compromised when the pattern is printed with a larger (100 μm) tip (Figure 5.1c). The ability to access smaller tip diameters as seen in the contrast between images is highly significant in expanding the capabilities to pattern intricate, complex patterns using 3D printing. It is also noted that reduction in filament diameter is not solely limited to reduction in nozzle size, but also can be accomplished through modification of nozzle movement rate. By increasing the nozzle movement rate to 20 mm/s and using the same conditions with a 1 μm tip used in Figure 5.1e, the filament diameter was reduced to approximately 6 μm. The ability to use nozzle movement rate as an alternative method to regulate filament diameter will be discussed later.

At low nozzle movement rates (around 1 mm/s), die swell was observed, where the size of the extruded filament is greater than the diameter of the nozzle. The filaments printed through the 100 μm tip can swell to as large as 200 μm in diameter, while the filaments printed through the 1 μm diameter tip can swell to as large as 40 μm in diameter. The impacts of die swell can be mitigated by increasing the nozzle movement rate. Increasing the linear motion nozzle movement rate (20 mm/s) while maintaining the same tip and pressure conditions used in Figure 5.1e, the extruded filament of 8M PEO achieved a filament diameter of 6.4 μm. Despite the continued

presence of die swell in the filament, the smallest tip diameter this material may be extruded through and the final filament diameter are well below the limits seen with other yield-stress inks reported in the literature (Figure 5.1a) [166–177]. We emphasize that Figure 5.1a summarizes the reported minimum *tip diameter* of the cited works, and thus effects such as die swell in the filament are not accounted for. The 3D printing performance of these novel emulsions warranted careful examination of the relationship between microstructure, rheological properties, and printing performance.

5.2.2 Rheological Properties Enable 3D Printed Structures

The rheological properties of the emulsion and the impact of the PEO and its molecular weight were examined to explore the relationships that exist between rheology and printing performance. The specific performance criteria examined in this work were filament resolution, maximum nozzle movement rate with continuous extrusion, and filament gap-spanning distance.

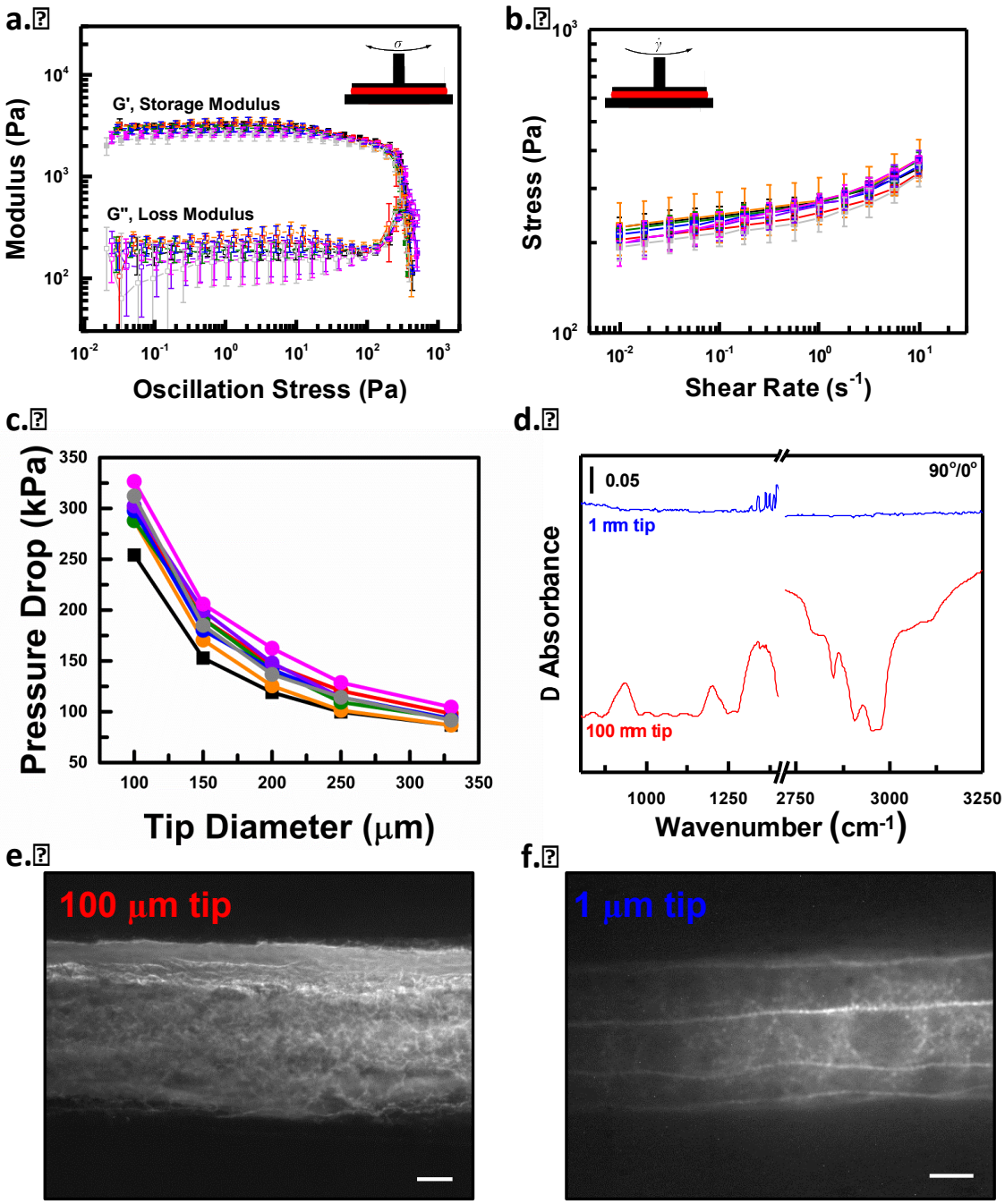

Figure 5.2. a. Storage modulus (*G'*) and loss modulus (*G"*) as a function of oscillation stress, error bars are from repeat measurements, No PEO (black), 400 K PEO (red), 600 K PEO (orange), 900 K PEO (green), 1 M PEO (blue), 4 M PEO (purple), 5 M PEO (pink), 8 M PEO (gray), (a)-(c) are same, b. shear stress as a function of shear rate, c. average pressure drop at the piston of syringe for extrusion at 1 mm/s as a function of tip diameter, d. polarized FTIR of filament extruded at 1 mm/s from tip diameter of 100 μm (red) and 1 μm (blue), fluorescence microscopy of line pattern of 8M PEO emulsion with Congo Red extruded at 1 mm/s from tip diameter of e, 100 μm, scale bar 50 μm, f. 1 μm, scale bar 10 μm.

Shear flow properties of the emulsions were studied using bulk rheology. For the emulsion without PEO, the stock emulsion was diluted such that the fraction of oil to water was held constant for all samples. To within the reproducibility of characterization, there was no effect on the storage modulus (G') or loss modulus (G'') of the material due to changing the molecular weight of the PEO (Figure 5.2a). Trends in the average linear viscoelastic moduli were non-monotonic with the molecular weight of PEO, indicating that no clear functional dependency exists between these parameters. Steady shear flow behavior also was not significantly affected by the molecular weight of the PEO (Figure 5.2b), to within the range of the statistical significance of the measurements. At low applied shear-rates, the measured stresses approach a plateau, characteristic of the extreme shear-thinning of apparent yield-stress fluids (Appendix C). The addition of polymer additives to particle-stabilized emulsions has been shown to result in changes to the shear flow properties, requiring optimization of the material for each polymer additive to restore the initial rheological properties [173]. Such impacts were notably absent in the current ink system, where (as we will show) the addition of the polymer additive provides a method to systematically vary only the extensional rheological properties and their consequent impact on 3D printing performance.

Tip flow properties were studied to determine how the polymer additive impacts the printing performance of the emulsion. To do so, the pressure drop at the piston of the syringe (P_{flow}) was determined during the pneumatic extrusion of a filament at a velocity of 1 mm/s at the given diameter of the nozzle (Figure 5.2c). Given that the pressure drop was independent of the amount of material in the syringe, we assume that the pressure drop at the piston of the syringe (P_{flow}) is approximately the same as that at the tip of the nozzle (P_{tip}). The incorporation of PEO and increasing molecular weight of polymer (i.e. more extensible emulsion) did not hinder flow through the tip, which shows that shear rheology dominates the flow resistance in the nozzle. The

printing of material through two different tip diameters was examined using polarization-dependent FTIR spectroscopy measurements to determine differences in birefringence that might be present in the extruded filaments. The filament extruded from a 100 μm diameter tip was birefringent (Figure 5.2d), whereas the filament from a 1 μm diameter tip was not. The noted differences in optical properties are believed to be due to alignment of PEO domains due to tip confinement, and were further examined by fluorescence microscopy using filaments dyed with Congo Red. The material from the 100 μm diameter tip resembles the bulk 8M PEO material (Figure 5.2e) and no difference was observed in microstructure for filaments extruded at this tip diameter without PEO (Appendix C). In contrast, the 8M PEO material from the 1 μm diameter tip contains stripes, which are believed to be aqueous channels that extend continuously throughout the sample (Figure 5.2f). These channels are not present in the emulsion formed without PEO (Appendix C). As the molecular weight of PEO increased, the longer chains result in a higher extensibility of the material, an effect made visible as the drawing of thin filaments.

Following the protocol for measuring extensibility presented in Section 3.3, results from Filament Stretching Extensional Rheology measurements, (FiSER), at constant deformation rate ($\dot{\varepsilon} = 0.2\ s^{-1}$) are shown in Figure 5.3a. The presence and variations in the molecular weight of PEO did not cause any measurable differences in the extensional stress in the emulsion. Due to visual observations of thin filaments of material forming for high molecular weights of PEO, a very minute difference in the force response would be present at high strains. This was, however, below the force measurement resolution of our experimental setup. Although there was no measurable difference in extensional stress, changes made in the molecular weight of the PEO and tip diameter do affect the ability of the emulsion to span a gap when printed (Figure 5.3b). Maximum gap spanning distances were determined by measuring the largest distance a printed filament was able

to span without visual distortion (thinning) or sagging of the filament (Appendix C). High nozzle movement rate are desirable in general, and are more convenient for the assessment of gap-spanning properties. Thus, the linear motion nozzle movement rate was adjusted to 10 mm/s.

Gap-spanning properties were evaluated at a range of nozzle diameters (100 μm – 330 μm). For tip diameters less than or equal to 200 μm, all of the emulsions were able to span a gap of 10 mm and there was minimal difference between all of the emulsions to gap span 10 mm with a 250 μm diameter tip (Figure 5.3b). Since the viscoelastic moduli and shear yield stress of the emulsions are comparable, it is not surprising that there was minimal difference in performance at these tip diameters. The gap-spanning filaments were stable for greater than one month without any observed sagging or distortion. The ability to form intricate tubes interconnected with suspended filaments is highlighted in Figure 5.3c. Two noticeable features of the gap-spanning properties are: 1) the ability to fabricate a flying buttress-like structure with a filament that spans from a high point (structure) to a low point (substrate); and 2) an ability for gap-spanning filaments to support a second filament printed across to form a cross in the center of each tube. As noted with the spanning filaments, the tubes are also stable for greater than one month without observed distortion to the structure. A more apparent difference in the ability to span gaps occurs when using a 330 μm diameter tip. With this tip diameter, only 4M, 5M, and 8M molecular weight PEO are able to span gap distances greater than 6 mm. Since these materials are not distinguishable from the lower molecular weight materials in terms of shear rheological properties, there must be a component of the extensional behavior that allows for molecular chain elongation and reinforcement of the emulsion to span large gaps using this large tip diameter.

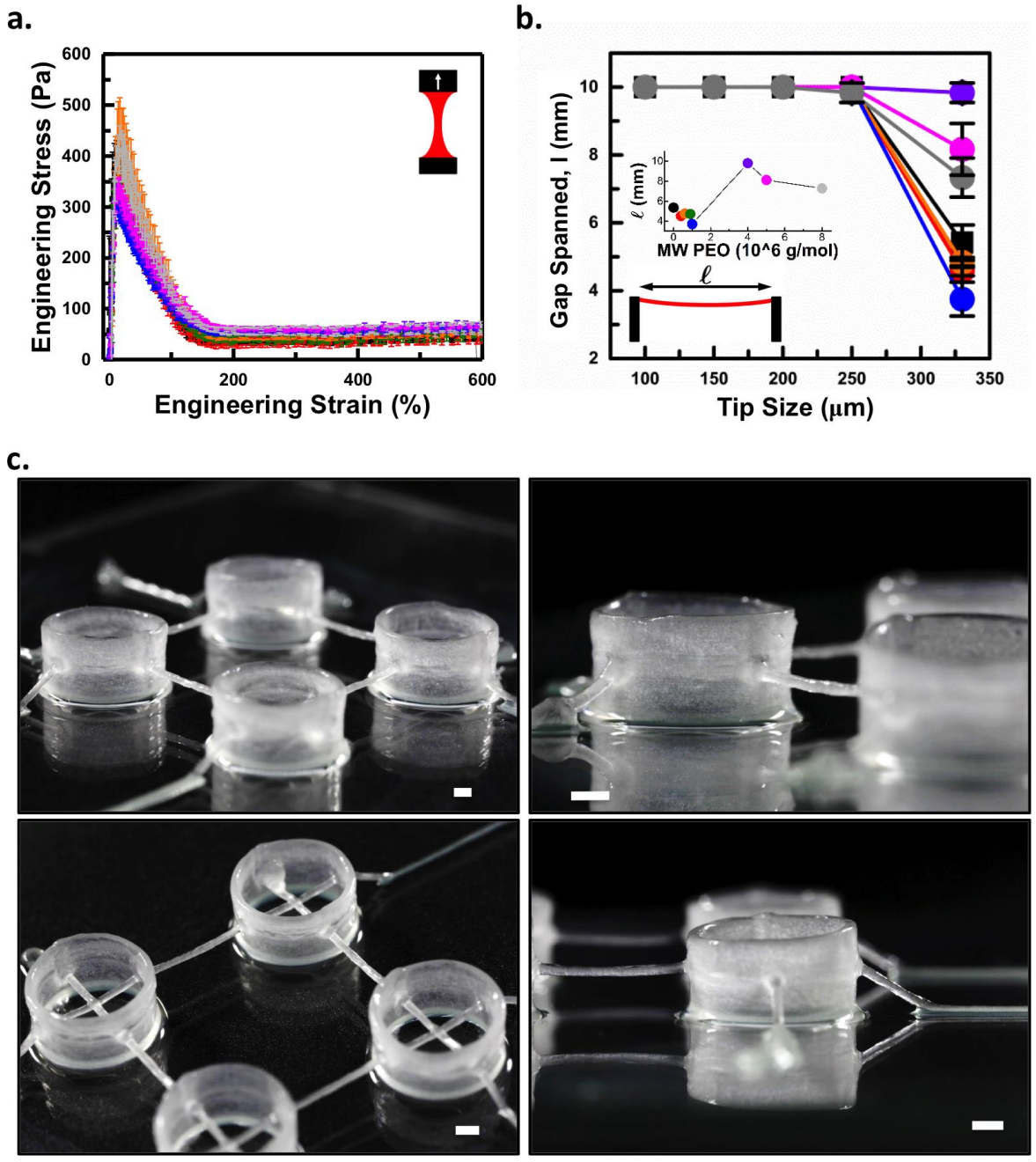

Figure 5.3. a. Extensional filament stretching, error bars are from repeat measurements, No PEO (black), 400 K PEO (red), 600 K PEO (orange), 900 K PEO (green), 1 M PEO (blue), 4 M PEO (purple), 5 M PEO (pink), 8 M PEO (gray), same for (a)-(b), b. gap spanned as a function of tip size, inset shows gap spanned as a function of molecular weight of PEO for the largest diameter tip with error bars omitted in inset for clarity, c. macro image of tubes interconnected with suspended filaments of 8M PEO emulsion printed with 100 μm diameter tip and exposed to silicon tetrachloride vapor chemical anneal, scale bar 1 mm.

Extensional failure strain was the final rheological property examined to understand the role of extensional rheology in printing performance. The percent strain-to-break for the emulsions was measured as a function of the molecular weight of the PEO (Figure 5.3c). Emulsions with extensional failure strain greater than or equal to 500% correlate directly with gap-spanning capabilities seen at large tip diameters.

Increased extensibility creates an interplay between pneumatic and drag extrusion of the inks. For most inks, increasing the nozzle movement rate for a structure requires an increase in the pressure applied to maintain a constant flow of material through the tip. Highly-extensible materials maintain a tensile stress that increases with nozzle movement rate to supplement the pressure-driven flow. This allows nozzle movement rate to be used to regulate filament diameter and produce filaments with a diameter smaller than the extrusion tip diameter.

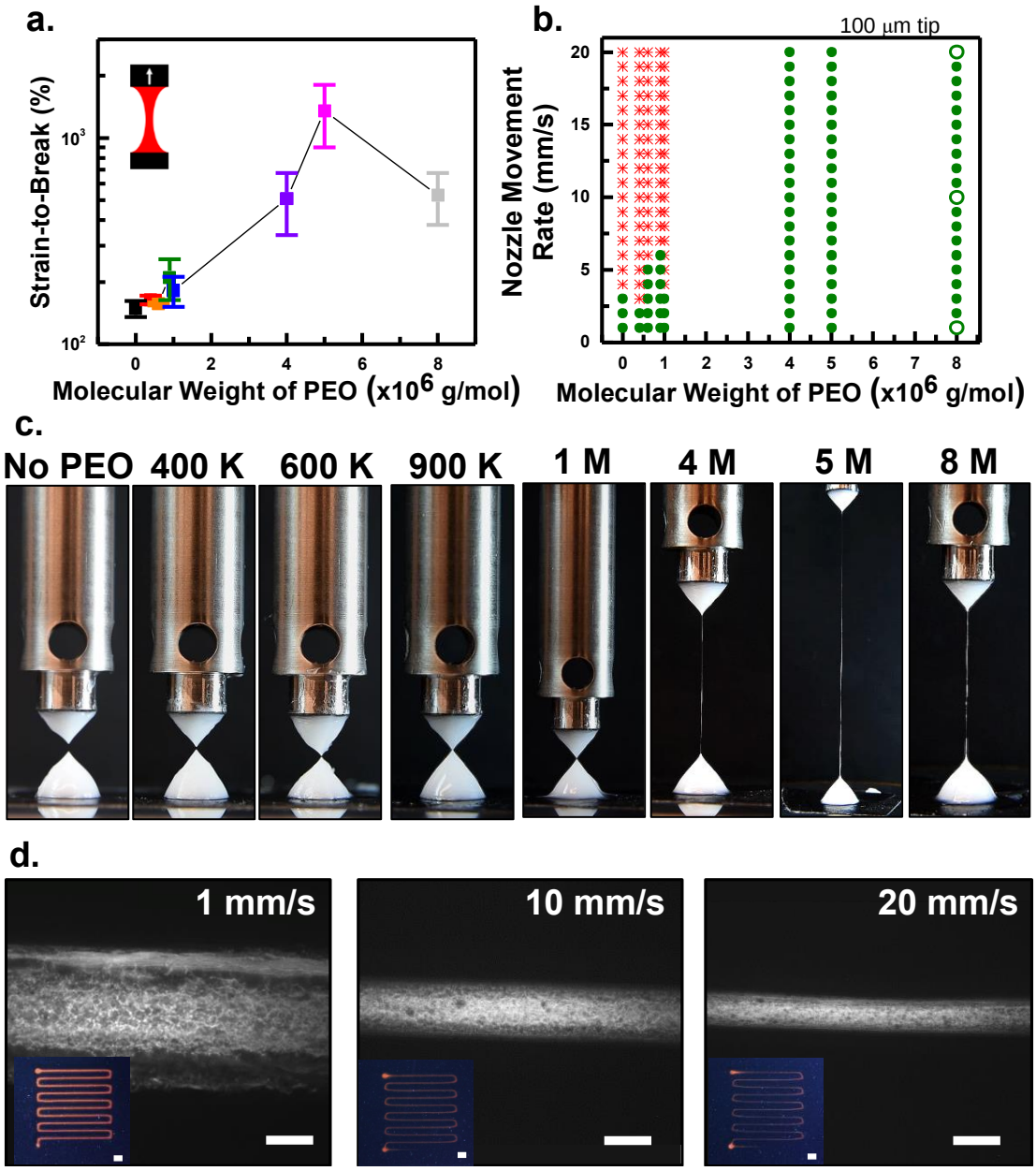

Figure 5.4. a. Extensional strain-to-break (%) as a function of molecular weight of PEO, b. maximum nozzle movement rate for continuous extrusion (green symbol) of filament as a function of molecular weight of PEO, see Supplemental Information for images of discontinuous extrusion (red symbol), c. macro images at maximum filament extension with increasing molecular weight of PEO, the diameter of the upper geometry is 8 mm in all images, d. fluorescence microscopy of line pattern of 8M PEO emulsion with Congo Red printed with 100 μm diameter tip at 1 mm/s, 10 mm/s, and 20 mm/s (open data points in b.), scale bar 100 μm, inset macro fluorescence image of line patterns, scale bar 1 mm.

The maximum nozzle movement rate of each emulsion was determined at the pressure that produces a linear rate of 1 mm/s through a 100 μm diameter tip. For each sample, maximum nozzle

movement rate was determined by the rate at which the material can be extruded continuously to complete a defined line pattern. The emulsions with extensional failure strains of 500% or greater are able to print continuous filaments at 20 mm/s (Figure 5.4c and SI Video 3). In contrast, samples with low extensional failure strain, such as the emulsion without PEO, are not able to print at these high nozzle movement rates. When low extensibility materials are printed, instead of continuous filaments, elongated discrete dots of material are formed, with the spacing between the dots dependent on the nozzle movement rate (Appendix C). Printing materials with high extensional failure strain, such as the 8M PEO emulsion shown in Figure 5.4d, results in the ability to decrease filament diameter by counteracting die swell. The high extensibility of the material allows for fast novel movement rates to be used to draw filaments of the material when printing. The ability to use extensional failure strain to moderate die swell behavior is a novel approach, which can easily be applied in general to the 3D printing other inks by incorporating additives, such as high molecular weight PEO. When the PEO emulsion was printed at a rate of 1 mm/s using a 100 μm diameter tip, the diameter of the filament is approximately 180 μm. Increasing the nozzle movement rate to 20 mm/s produces a filament that is 100 μm in width, the same diameter as the tip. While the maximum nozzle movement rate for our printer setup was limited to 20 mm/s, we expect the high extensibility of these materials would enable printing of filaments that are smaller than the tip diameter if higher nozzle movement rates are accessible. This provides an opportunity for greater control over filament diameter by using nozzle diameter coupled with nozzle movement rate to fine tune filament diameter and access small diameter filaments without the limitation of using small diameter nozzles as are required with most materials for 3D printing.

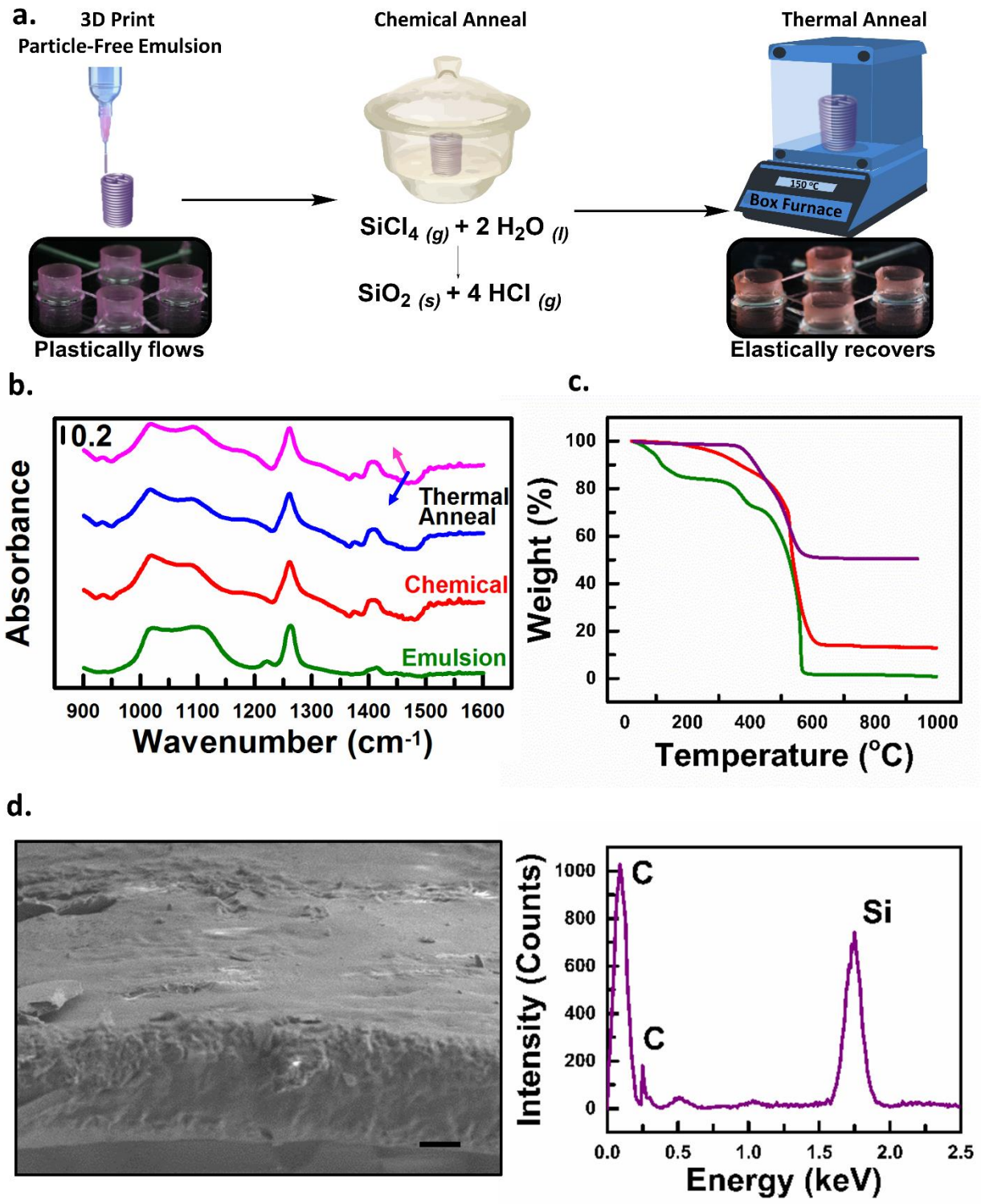

Figure 5.5. a. Two-step preparation process, chemical and thermal anneal, of elastomer from printed particle-free emulsion, b. FTIR of printed particle-free emulsion as printed (green), after chemical anneal (red), after annealing at 80ºC for 30 min (blue), after annealing at 80ºC for 30 min and 150ºC for 1 h (pink), c. TGA of particle-free emulsion (green), after chemical anneal (red), after chemical and thermal anneal (purple), d. SEM and EDX of thermally annealed tube coated with a 2.5 nm layer of a 60:40 Au/Pd alloy, scale bar 20 μm.

5.2.3 Synthesis of 3D Printed Mechanically Robust Elastomers

3D printing emulsions open the possibility for post-transformation chemistry to introduce new properties and/or structures into the printed structures that are not innate to the native material. Due to the high stability of the structures, no observed distortion of the 3D structure after one month, the structures do not have to undergo post-transformation chemistry immediately to ensure retention of the intricate 3D printed geometries.

We present a two-step approach, chemical annealing followed by thermal annealing (Figure 5.5a), to convert the emulsion into an elastomer that is stable in solvent (organic and aqueous) and mechanically tough and resilient, two properties not native to the emulsions directly after printing.

For this conversion of emulsion to an elastomer, we took advantage of the water in the continuous phase of the printed structure to react with gaseous silicon tetrachloride, which generates a thin silica shell on the exterior of the structure. This silica shell provides only a minimal enhancement of mechanical stability, and the structure was able to be easily compressed. Doing so between ZnSe plates for FTIR studies, we found that there is only a slight peak shape change seen in the Si-O-Si (1000 cm^{-1} to 1100 cm^{-1}) region after chemical annealing (Figure 5.5b), which is attributed to the formation of silica. The peak shape for the Si-O-Si region remains broad, which resembles what would be expected for stretching vibrations for a predominantly silicone composition and not silica [183]. This further confirms that the silica formed during chemical annealing is only a thin shell. As an additional control, after chemical annealing but before thermal annealing, the sample is irreversibly compressed when 50g weight is applied to the glass coverslip on top of the structure (Appendix C).

Thermogravimetric analysis of the emulsion and chemical annealed emulsion also confirms formation of silica as evidenced by the residual mass for the sample that had been chemically treated. This is compared to the initial emulsion in which total mass loss is observed only once the temperature exceeds approximately 600 °C. The mass loss from 0 ^{o}C to 200 ^{o}C is attributed to water and out-gassing of the material (as has been reported previously in the literature [184]).

The chemically annealed emulsion structures can be subsequently transformed via thermal processing. To do so, the structures bearing a thin silica shell were thermally annealed through a multi-step temperature ramp from room temperature to 292 °C. This treatment leads to the thermal polymerization of the silicone oil used to formulate the ink emulsion. This silicone oil, used unmodified from Sigma Aldrich source, is polydisperse (GPC analysis (THF) M_w =37.98 kDa, PDI = 1.56; M_w = 1.31 kDa, PDI = 1.02; M_w = 0.83 kDa, PDI 1.01, Appendix C) and contains trace amounts of copper as evidenced by XRF, as well as silicon hydride (peak at 2050 cm^{-1})[185] and silicon hydroxide (peaks at 3600-3800 cm^{-1})[186] moieties as evidenced by FTIR (Appendix C). The trace amounts of copper are believed to be a residual impurity resulting from the process used in the production of the silicone oil [187]. Since the silicone oil contains reactive functional groups (hydride and hydroxide), the presence of the copper leads to a thermally activated one-part condensation silicone cure to form an elastomer (a property also seen in control experiments using only bulk samples of the silicone oil).

The silica shell is crucial to provide mechanical stability to the structure during the thermal annealling process. Without the silica shell, the structure collapsed and results in a polymerized silicone without shape retention. FTIR of the samples, performed during the first and second temperature ramp, showed no major chemical changes occur as compared to the chemical annealed sample (Appendix C). The printed structures in this case, however, were mechanically robust and

able to recover from significant degrees of deformation (see below). Taken together, the data suggest that the two-stage temperature ramp of the thermal annealing cycle leads to the evolution of residual water from the structure and coalescing of the dispersed phase, the silicone oil, to form a continuous silicone matrix encapsulated in silica. How the low wt% of SDS and PEO that remain are dispersed in the final silicone structure is not fully understood based on the data currently available. We simply note that their presence seems to have little impact on the mechanical properties of the final structures, a point discussed in greater detail in the section that follows.

After the final thermal annealing step, the resulting material was an elastomer that was stable when exposed to both organic and aqueous solvents, a property not native to the emulsion. Thermogravimetric analysis of the elastomer showed increased thermal stability with minimal mass loss at temperatures less than 380 ^{o}C (Figure 5.5c). This is comparable to reports in the literature, which show the onset of thermal breakdown of PDMS to be around 350 °C [184]. Polymerization of the dispersed silicone oil through thermal annealing is further confirmed by SEM/EDX (Figure 5.5d) showing a smooth continuous surface composed of silicon and carbon.

The ability to introduce enhanced mechanical stability to the structure in response to an external force is critical for the structure to robustly perform in a multitude of applications such as might be required for a soft actuator. The modification of the mechanical performance of the structure through post-printing transformation also highlights the fundamental principles and novelty of 3D printing to transform a 3D printed structure. The Young's modulus of the thermal annealed sample was measured and fit using the Oliver and Pharr model (Figure 5.6a). The Young's modulus of the material is 1.1 $\pm$ 0.4 MPa, which is comparable to the elastic modulus of PDMS (0.57 MPa – 3.7 MPa)[188] and a factor of up to 500 times greater than the linear viscoelastic modulus of the printed emulsion (2-3 kPa). With the increase in the modulus, printed

and processed tubes interconnected with suspended filaments were able to support a glass coverslip with a 10g weight without any visible deformation (Figure 5.6b and SI Video 4). Further, the material exhibits reversible extreme buckling and elastic recovery (recovers ε_{true} ~ -1.6) compared to the printed emulsion which plastically flows at a yield strain γ_y ~ 0.3 (Appendix C). The ability for the sample to undergo extreme buckling and compressive strain from a 50g weight with a full recovery is shown in Figure 5.6c. The drastic modification and enhancement to the mechanical properties of the material is due to the thermal polymerization of the dispersed silicone phase of the sample.

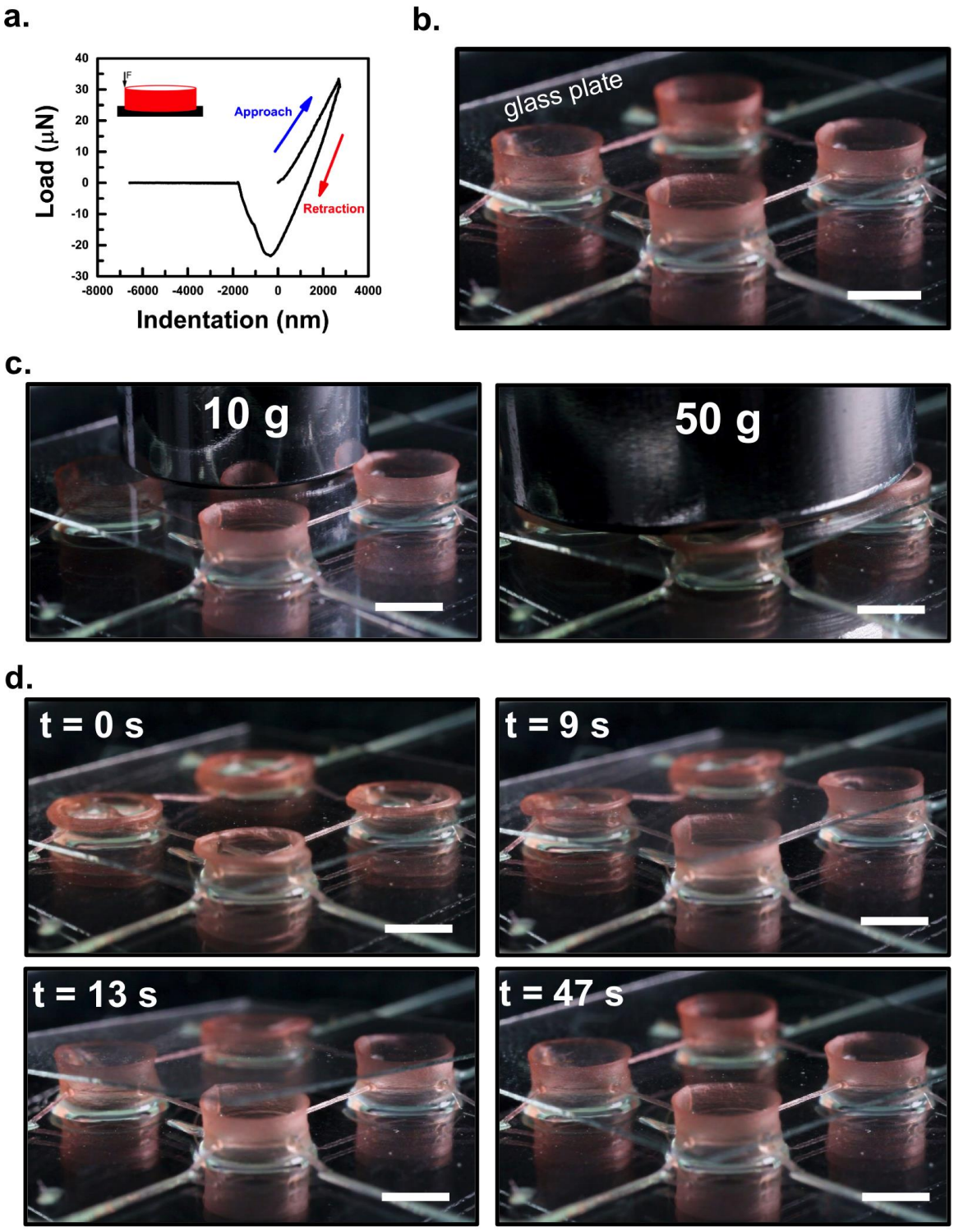

Figure 5.6. a. Force curve of thermally annealed particle-free emulsion obtained using a nanoindenter on the edge of a thermally annealed tube, macro image of tubes interconnected with suspended filaments of thermally annealed 8M PEO emulsion with Rhodamine 6G, scale bar 5 mm b. with glass cover slip, c. with glass cover slip supporting a 10 g weight and buckling under a 50 g weight, d. time sequence of recovery after buckling.

5.3 Conclusions and Outlook

Particle-free emulsions with poly (ethylene oxide) were developed as an alternative ink for the production of elastomeric structures. Due to the ease of deformation of the silicone oil in the dispersed phase the material was able to be extruded through a 1 μm diameter tip to create intricate patterns. The shear flow properties were not significantly affected by the presence or molecular weight of the poly (ethylene oxide). Increasing the molecular weight of poly (ethylene oxide) drastically changes the extensibility of the material. Emulsions with extensional failure strain of 500% or greater allow for gap spanning and increased rate of printing to both reduce die swell and control filament diameter size. Post-printing transformation through a two-step annealing process, chemical and thermal, allows for fabrication of 3D printed elastomers. The elastomer was able to buckle and recover from extreme compression strain (compress to approximately 20% original height of structure) with no observable damage to the structure.

The primary innovation of this work is the introduction of particle-free emulsions as a novel and exemplary class of yield-stress fluids for direct-write 3D printing at previously unachievably small filament diameters and with excellent shape retention. Though the properties of the new material system are sufficient for printing 3D structures, as demonstrated in Section 5.2.3, post-printing transformations are necessary to improve the material properties to be more broadly useful as engineering materials. Possible future directions of this work include both optimizing properties for printability and developing additional strategies to transform and improve the properties after printing. Other direct-write emulsion materials achieve superior properties through the incorporation of nanoparticles [173,189], however this compromises the ability for the material to be printed through small diameter nozzles. Preliminary work has been done to incorporate a

photocrosslinkable material, poly(2-hydroxyethyl) methacrylate, in the continuous aqueous phase of the presented emulsion, demonstrating an alternative method for post-printing toughening.

5.4 Materials and Methods

Materials:

Sodium dodecyl sulfate (SDS), silicone oil with a viscosity of 1000 cSt (at 25 °C), poly (ethylene oxide) (average M_v 400,000, 600,000, ~900,000, ~1,000,000, ~4,000,000, ~8,000,000 powder), Congo Red, Rhodamine 6G, methylene blue (1.5 g/ 100 mL), silicone tetrachloride (99%), hexanes (ACS Reagent grade), 200 proof ethyl alcohol, and isopropyl alcohol (ACS Reagent grade) were purchased from Sigma-Aldrich and used without modification.

Methods:

Particle-Free Stock Emulsion:

Silicone oil was homogenized with a mixture of SDS in deionized water to produce the stock oil-in-water emulsions. The overall weight-percentages for the stock emulsions were 90 wt% oil, 3.34 wt% SDS, 6.66 wt% water. All components were added to a beaker and homogenized at 5000 rpm for 5 minutes using an IKA T-18 homogenizer with an S18N-19G dispersing element attachment.

Particle-Free Emulsion with Poly (ethylene oxide) Inks:

Poly (ethylene oxide) solutions of each M_v were prepared by dispersing the appropriate powder in a small amount of ethyl alcohol (co-solvent) at 30 °C and 200 rpm using a magnetic stirrer; deionized water was then quickly added to result in 1 wt% PEO solutions. Using measurements of intrinsic viscosity for PEO solutions reported by Kawaguchi et al. in dL/g [190], the overlap concentration (c*) was estimated as the inverse of the intrinsic viscosity assuming a density for PEO of 1.21 g/ml. The range of concentration normalized by overlap concentration for the PEO

solutions was from 0.04 to 20. Each ink was produced by hand-mixing the stock emulsion and a PEO solution in a 9-to-1 weight ratio. A 0 wt% PEO (deionized water only) ink was produced as a control material. For imaging, PEO solutions were prepared with Congo red (0.6 wt%), Rhodamine 6G (0.09 wt%), or methylene blue (0.1 wt%). All inks were centrifuged at 3000 rpm for 5 minutes using a Thermo Scientific CL2 centrifuge before use or characterization.

Rheological characterization:

Shear Rheology:

Rheological characterization of steady flow and linear viscoelastic properties was performed on rotational rheometers (combined motor/transducer instruments, TA Instruments DHR-3 or AR-G2) using a parallel-plate geometry with a diameter of 20 millimeters and Peltier temperature control. Adhesive-backed 600 grit silicon carbide sandpaper was used to prevent slip. Materials were tested at multiple gaps to verify the absence of slip [22]. During characterization, the gap was continuously varied to maintain a normal force of 0 ± 0.1N and avoid edge fracture. For steady flow behavior, a range of shear rates were applied from low-to-high and the apparent steady stress was recorded. This data was fit to the Herschel-Bulkley model to obtain a yield stress value of approximately 200Pa. For linear viscoelasticity, an increasing oscillatory strain amplitude was applied at a frequency of 10 rad/s until failure of the material. Little frequency dependence was observed for any of the materials across the range of 0.1 to 30 rad/s. All experiments were performed at 25 °C and replicated thrice to obtain error bars.

Extensional Rheology:

Characterization for force-extension behavior and extensional strain-to-break were performed using a filament-stretching mode on a TA Instruments ARES-G2 rheometer (separated rotational motor/transducer, combined axial motor/transducer). For the filament-stretching experiments, a

parallel-plate geometry with a radius of R_0 = 4 millimeters and advanced Peltier system bottom plate were used. The samples were loaded at a gap of H_0 = 4 millimeters, resulting in an aspect ratio of $\Gamma_0 = H_0 / R_0 = 1$. A constant true strain rate, $\dot{\varepsilon}$ = 0.2 s^{-1}, was applied and engineering stress was recorded. Videos were taken during all extensional tests, and images were correlated with the measured load and displacement to determine the extensional strain-to-break. All experiments were performed at 25 °C and replicated thrice to obtain error bars.

3D Printing:

A custom-built 3D printer consisting of a pneumatic extruder (Ultimus V and HPx High-Pressure Dispensing Tool, Nordson EFD) mounted to a X, Y, Z motion controller (AGS-1000, Aerotech Inc., Pittsburgh, PA) was used. All inks were loaded into syringes with either stainless steel, straight tip (tip diameter range of 330-100 μm, Nordson EFD) or glass capillary, tapered tip (1 μm, World Precision Instruments, LLC) and the syringes were loaded into the pneumatic extruder. Structures were printed on either glass slides or cover slips.

Pressure Drop:

For each stainless steel, straight tip diameter, pressure was applied to the system for 10 s using the pneumatic extruder from the 3D printer described previously. If no extrusion of material was observed, the pressure was increased by 0.1 psi. The pressure (P_{flow}) was increased until sufficient pressure was applied for extrusion of a filament of the material with the diameter of the tip at a linear flow rate of 1 mm/s. The measured pressure (P_{flow}) was measured as the pressure drop at the syringe piston and assumed to be the same pressure at the entrance to the nozzle (P_{tip}).

Nozzle Movement Rate:

A stainless steel, straight tip (100 μm diameter) was used to determine the maximum nozzle movement rate for extrusion of a uniform filament. For all nozzle movement rates, the pressure

applied to the syringe was the pressure determined during the *Pressure Drop* (see prior experimental methods) for extruding the ink from a 100 μm diameter tip at a linear flow rate of 1 mm/s. The nozzle movement rate was increased in 1 mm/s increments to a maximum of 20 mm/s to determine the maximum nozzle movement rate.

Gap Spanning:

For each stainless steel, straight tip diameter, pressure (5x pressure determined for a linear flow rate of 1 mm/s) was applied to the system and the material was extruded across a template with different gap sizes ranging from 0.25-10 mm at a nozzle movement rate of 10 mm/s. The material was determined to span a gap if there was no sagging or change in the filament diameter (filament thinning) over the gap distance upon qualitative optical inspection.

Elastomer Synthesis:

3D printed emulsion structures were placed in a desiccator connected with a three-way valve to a three-necked 100 mL round bottom flask. The desiccator was sealed and the entire system was evacuated using a laboratory vacuum pump. The valve to the round bottom flask was closed and silicon tetrachloride (5-15 mL, dependent on the number and size of structure) was added via syringe. The valve was opened and heated via a heat gun for 1 min to allow the silicon tetrachloride vapor to diffuse into the desiccator. The samples reacted with silicon tetrachloride vapor overnight. The samples were then removed from the desiccator and thermally annealed in a box furnace (73^{o}C for 30 min, 143^{o}C for 1 h, and 292^{o}C for 1 h). The samples were allowed to cool to room temperature and then washed sequentially with hexanes, isopropanol, and water.

Elastomer characterization:

X-Ray Fluorescence (XRF):

A Shimadzu EDX-700 System (100μA, 50 kV, beam size diameter of 1 mm) with a rhodium source and purged with helium was used for XRF measurments. An elemental survey was performed to determine trace metals in the samples.

Gel Permeation Chromatography (GPC)

A Waters1515 Isocratic HPLC pump equipped with a Waters (2998) Photodiode Array Detector, a Waters (2414) Refractive Index Detector, a Waters (2707) 96-well autosampler in THF at 30 °C, and a series of 4 Waters HR Styragel columns (7.8 x 300mm, HR1, HR3, HR4, and HR5) was used for GPC measurements. Monodisperse polystyrene standards were used to calibrate the instrument.

Fourier Transform Infrared Spectroscopy (FTIR):

A FTS-6000 FTIR spectrometer (Bio-Rad, Cambridge, MA) with DTGS detector, KBr beam splitter, and ceramic source was used for all IR measurements. Spectra were collected using a spectral resolution of 4 cm^{-1} with a modulation of 5 kHz and a 1.2 kHz low pass filter. Single beam spectra were co-added (64 scans) and referenced to ZnSe. For polarized measurements, a KRS-5 Au wire grid polarizer was used. Single-beam spectra were transformed using Varian Resolutions Pro software.

Thermogravimetric Analysis (TGA):

A TGA (TA Instruments) was used for all measurements. All samples were analyzed in a nitrogen environment. Two different heating cycles were performed: 1) linear temperature ramp (10 ^{o}C/min) from room temperature to 700^{o}C and 2) ramp (5 ^{o}C/min) to 73^{o}C, hold for 30 min,

ramp (5 ^{o}C/min) to 143^{o}C, hold for 1 h, ramp (10 ^{o}C/min) to 292^{o}C, hold for 1 h. Data was analyzed using TA Instrumental Analysis software.

Scanning Electron Microscopy (SEM) with Energy Dispersive X-Ray Spectroscopy (EDX):

An Emitech K575 sputter coater was used to apply a non-conductive 2.5 nm layer of a 60:40 Au/Pd alloy (applied current of 20 mA for 10 seconds, deposition rate of 2.5 Å/s) coating to the samples prior to imaging. Coated samples were immobilized onto a metallic sample exchanger using carbon tape and loaded into a Hitachi S4700 Scanning Electron Microscope. The samples were imaged using an extracting voltage of 10 kV and a beam current of 10 μA. EDX was carried out using an Oxford instrument on imaged sections of the sample via 15 keV X-ray irradiation and data was accumulated for 300 seconds to give the resulting spectra using Iridium software.

Modulus Characterization:

A Piuma Nanoindenter was used for all measurements. Indentations were performed with a probe (tip radius of 9.0 μm, stiffness of E_{eff} = 44 N/m, Poisson's ratio approximately of ν=0.5, calibration factor of 1.3) over 10 μm relative displacement and overall indentation time of 6 s. Piuma Dataviewer Version 1.0 by Optics was used to analyze the data and the retraction portion of the indentation curve was fit to the Oliver and Pharr model (lower load limit was set to 65% of the maximum load (P_{max}) and upper load limit set to 85% of the maximum load (P_{max})).

Imaging:

Microstructural observations were made using an Olympus IX71 inverted fluorescence microscope with a GS3-U3-23S6M-C Point Grey CCD camera and a mercury vapor lamp light source. Micrographs were recorded with a 10x UPlanSApO or 63x Zeiss LD Plan NEO air immersion objective lenses at various locations across samples. Macro images were taken with a

Canon EOS 5D Mark II DSLR camera with an MP-E 65mm lens and a UVP Black-Ray B-100AP UV Lamp.

Data Analysis and Fitting:

Figure 5.1a was generated from digitizing literature data [166–177] of steady shear flow or large-amplitude oscillatory shear using WebPlotDigitizer on Chrome. Using OriginPro 2016, digitized steady shear data of stress versus strain-rate was fit to the Herschel-Bulkley model in applicable regions to obtain the shear yield stress. If necessary, a parallel-plate correction was performed prior to fitting [47]. All fits had an adjusted R^2 value of at least 0.90. For large-amplitude oscillatory shear data, the stress at the crossover of G' and G'' was taken as the yield stress. The minimum tip diameter was taken as reported. Microstructure type was taken as reported or categorized based on the authors' best judgement of the dominant microstructural yield-stress mechanism of the reported material. Note that many of these materials are complex multi-component systems and the listed category is for the presumed "dominant" yield-stress mechanism.

Chapter 6: Gelation under stress of hydrogels

6.1 Introduction

In this chapter, I investigate the effect of dynamic flow during gelation of aqueous methylcellulose (MC), a material that forms a brittle gel at elevated temperatures under quiescent conditions, and thus would ordinarily not be considered a yield-stress fluid. Gelation is typically studied with "quiescent" conditions and neglects the paradigm that dynamic conditions, even a small applied stress, can dramatically change properties such as gelation temperature and the resulting structure and mechanical properties of a material. I control the applied stress during temperature-ramp gelation to systematically explore processing-to-property relations. Flow makes gelation more difficult, evidenced by an increased apparent gelation temperature, and lowers its mechanical properties, evidenced by a decreased hot gel elastic modulus and decreased apparent failure stress. In extreme cases, formation of a fully percolated polymer network is inhibited and a soft granular yield-stress fluid is formed, rather than a brittle gel. This work hypothesizes that sufficiently high stresses during gelation trigger a transition between two metastable fibril structures that have been previously investigated in literature. Our findings of a stress-dependent gel temperature raise questions for other rheological tests that measure gel temperature at finite stress, such as small amplitude oscillatory shear (SAOS). Our systematic approach here should serve as a paradigm for verifying any rheology-based gelation measurements, namely, to measure gelation as a function of applied stress, and report the limit where stress goes to zero. This work was done in collaboration with Dow Chemical Company who supplied material, characterized the molecular weight of the relevant polymer, and helped develop the project direction.

The industrial, consumer, and scholarly importance of methylcellulose (MC) is immense. The hydrophobic modification of cellulose—the most abundant material in nature—yields MC which has been utilized to considerable effect in pharmaceuticals research [191–193], food products [194–196], building materials [197,198], packaging films [199,200], solar cells [201], fuel cells [202,203], nano-particle synthesis [204,205], and research on cell culturing [206–208]. The most immediately intriguing aspect of aqueous MC is its uncommon ability to form a turbid, thermoreversible gel at elevated temperatures as shown in Figure 1a. Partially substituting methyl moieties onto the anhydroglucose (AGU) repeat unit of cellulose in the C2, C3, and C6 positions results in MC that is water-soluble at low temperatures and gels at high temperatures. There has been much progress made in studying the structure and rheological properties of the solution and gel states [209–218], as well as the dependence of gelation on degree of substitution [219], concentration [209,220], and heating rate [212].

Almost the entire rich body of work that exists on gelling aqueous MC focuses on gels that form in a completely- or quasi-undisturbed state. Under these quiescent conditions, MC has been observed to form a fibrillar gel network [210,211]. This network results from a conformational change of MC polymers in solution from coils to rings and self-assembly into fibrils [221] [222]. The material shown in Figure 6.1a was gelled in this quiescent manner, and the ultimate mode of failure is fracture at some critical shear stress, rather than yielding and flowing.

However, for many of the applications mentioned above and others, the properties of quiescently-gelled MC may be totally unrepresentative of how the material will actually behave under finite stress conditions, as will be shown here. Under appropriate processing conditions (e.g. strong shear while heating), completely different properties result. Shown in Figure 1b, heating under a strong controlled *shear rate* breaks down the gel network and results in a soft granular

yield-stress fluid that flows. The effect of controlled shear rate conditions during temperature-ramp gelation of aqueous MC was investigated by Knarr and Bayer [223] who found that forcing a constant deformation rate will destroy any gel network that forms on heating, and causes gelation to occur at higher temperatures. They did not measure the resulting rheological properties after gelation, and since they applied a deformation rate rather than stress, they could not observe a fully-formed gel under loaded conditions.

The importance of investigating the effect of dynamic conditions on structure formation has been identified for many other material systems with network microstructures, including colloidal suspensions [224]. However, most studies use either controlled deformation rate conditions [103,225–230], or very low stress conditions [231].

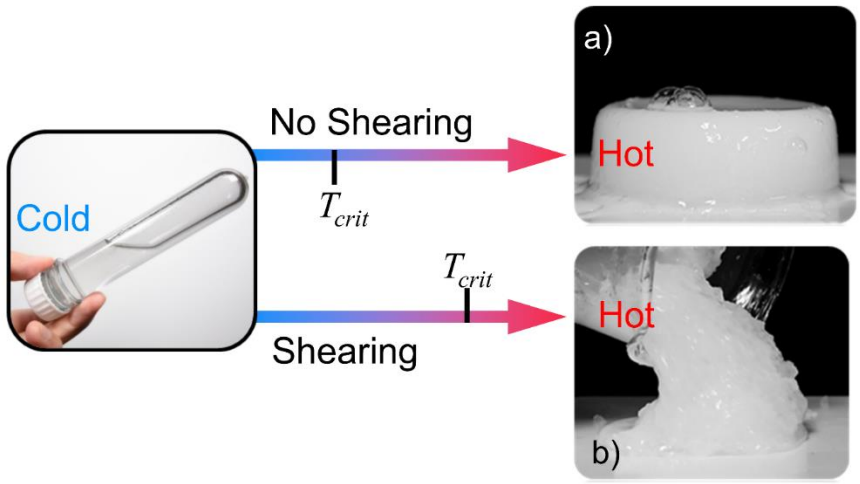

Figure 6.1. Images of gels resulting from heating aqueous MC solutions. (a) Gel formed while undisturbed during heating. (b) Gel formed while exposed to shear from a rotating mixer.

In this work, I systematically apply constant unidirectional shear stresses while heating to allow probing of properties in both the liquid and gel states for a range of concentrations of aqueous MC. These properties are compared to those obtained from quiescent gelation using a common heating rate of 1 °C/min. This work will refer to gelation under constant unidirectional non-zero

shear stress as “dynamic gelation”. In contrast to controlled deformation conditions that have been found to always break down a network, applying a moderate stress allows the formation of a fully-percolated gel network strong enough to bear the applied load but that has properties different from the quiescently-gelled material. One expects that vanishingly small stresses would have little-to-no effect on structure formation, and therefore material properties, but that sufficiently high stresses could lead to preferential orientation of the gel structure and rupture at the most tenuous connections of the network.

Applied unidirectional stress, rather than rate, is common in applications, such as a coating applied to a vertical surface subject to gravitational loading. For these limited values of applied stress, I observe significant variation in the resulting gel temperatures and a huge dynamic range of gel properties. The effect of controlled-stress conditions is highly relevant to gelation during processes such as film formation, surface coating through impact, particle settling, and pressure-driven flow. For these processes and other applications, the processing-to-property space that is generated here reveals the possibility of catastrophic inaccuracy when not taking processing/application conditions into account with this widely used polymer, and provides a protocol for investigating these conditions with other materials that may structure under flow.

6.2 Materials and Methods

Methylcellulose used in this study was provided by The Dow Chemical Company under the trade name METHOCEL™ A15. The MC material was characterized by size-exclusion chromatography to obtain the absolute molecular weight distribution and differential solution viscosity by the method of Li [232]. The molecular weight distribution was monomodal with number- and weight- average molecular weights of 22 and 47 kg/mol, respectively. The

differential solution viscosity data (28 °C, 0.02−0.2 wt % MC) relative to that for solvent were converted into intrinsic viscosity [η], and this intrinsic viscosity (167 ml/g) was used to compute the critical overlap concentration ($c^* \approx \eta^{-1} = 0.0059$ g/mL). The degree of methyl ether substitution (*DS* = 1.9 mol –OCH3/mole AGU) was measured by an approach reported elsewhere [233].

Prior to use, MC was dried under vacuum at 60 °C for a minimum of 12 h. A density of 1.39 g/mL was used for MC, and the volume fraction was calculated assuming volume additivity as used in other MC studies [212,216]. Solutions were prepared by adding MC powder to half of the required volume of deionized water at 70 °C with constant stirring for 10 min without additional heating, creating an opaque dispersion. The remaining water (~21 °C) was then added gradually over 1 min, and the solution was allowed to continue stirring for an additional 10 min. The solution was then stirred in an ice bath for 10 min and stored at 4 °C for a minimum of 12 h to fully hydrate the polymer before use. The resulting solutions were transparent at low concentrations to translucent at higher concentrations. MC solutions were prepared over the range of 1 to 8 wt% which nominally is the range of 1.75c* to 13c*.

Outside the scope of this work is direct characterization of the microstructure. A fibrillar gel network structure has been reported for MC polymers of molecular weight 150 kg/mol and higher [221], but there is currently a lack of evidence regarding the precise microstructure of the material used in this study (M_w approximately 50 kg/mol, details given above). The material used in this study becomes optically turbid (Figure 1), similar to higher molecular weight materials [212], indicating the presence of relatively large scale heterogeneities in the microstructure. To the authors' knowledge, microstructure characterization under shear flow has never been attempted for this material, and is complicated due to the relatively high temperatures involved. This could

be possible with experimental setups that combine rheometry and structure characterization (scattering [234,235] or confocal [236,237]), but this is outside the scope of the work here.

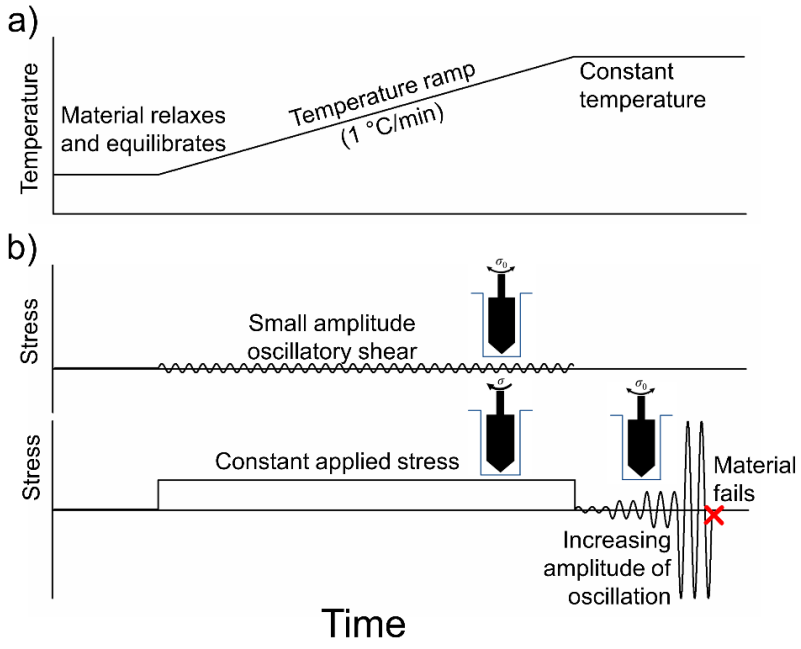

Figure 6.2. Schematics of a) applied thermal history and b) stress applied simultaneously. In all tests, the material is allowed to relax and equilibrate at zero applied stress and 20 °C before the temperature ramp begins. For determining the linear viscoelastic gel temperature, small amplitude oscillatory shear (SAOS) flow is applied. For dynamic gelation, a constant unidirectional stress is applied. At 80 °C, an increasing oscillatory stress amplitude is applied until failure, providing the hot gel moduli and apparent failure stress.

Prior to rheological testing, solutions were degassed to prevent/minimize bubble formation when warming. Figure 6.2 schematically shows the applied thermal history and stress scheduling. Unless otherwise noted, characterization was performed on a TA Instruments DHR-3 or AR-G2 rotational rheometer (combined motor/transducer instruments) using a DIN concentric cylinder cup (30.4mm diameter) and sandblasted bob (28mm diameter, 42mm immersed length) geometry with Peltier temperature control. To inhibit dehydration, a thin layer of mineral oil with a density of 0.838 g/mL obtained from Sigma-Aldrich was floated over the surface of the MC solution. For all experiments, the sample equilibrated at 20 °C and 0 Pa applied stress for 10 minutes before

warming to the final temperature at a rate of 1 °C/min. All experiments were repeated thrice to obtain error bars; error bars smaller than data points are not shown.

To obtain the quiescent gelation temperature, small-amplitude oscillatory shear measurements were performed at a frequency of 0.1 rad/s and stress amplitude of 0.1Pa which is within the linear regime for all the tested quiescently gelled concentrations. This provided the viscoelastic storage and loss moduli, G' and G'', respectively, as a function of temperature. All gel temperatures labeled "0 Pa" are from small-amplitude oscillatory shear (SAOS) tests (small stress centered about 0 Pa).

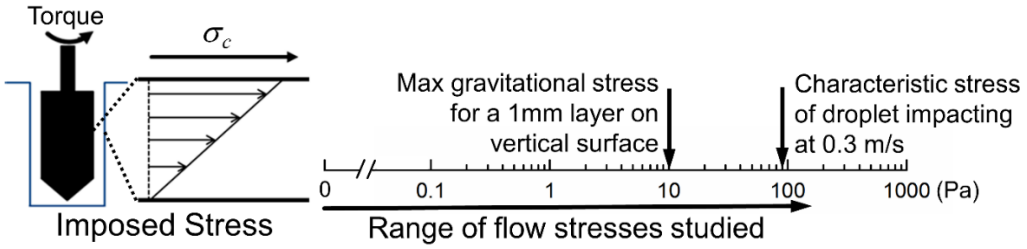

Figure 6.3. Range of stress magnitudes applied during gelation in this work using a combined motor/transducer (controlled torque) rheometer with a concentric cylinder geometry. Characteristic stress magnitudes of relevant applications are indicated (calculation given in Appendix D).

For dynamic gelation, constant unidirectional stress, σ_c, was applied and the resulting instantaneous shear rate $\dot{\gamma}(t)$, provided the apparent viscosity, $\eta = \sigma/\dot{\gamma}(t)$, as a function of temperature. The range of stresses investigated here is shown in Figure 6.3, along with benchmark values of stress for context (see Appendix D for calculation details). At 80 °C an increasing oscillatory stress amplitude was applied at a frequency of 3 rad/s until the apparent failure stress, σ_Y*, was observed. The SAOS data was found to be insensitive to the oscillation frequency for all materials at 80 °C within our experimental window (0.1 to 100 rad/s). For all tests at 80 °C, the ratio of G'' to G' (i.e. $\tan(\delta) = G''/G'$) in the linear plateau region was less than 0.1 and G'' is omitted

from plots for clarity. A special case of the constant-stress gelation is $\sigma_c = 0$, to which this work will refer to as "true quiescent" gelation. All hot gel properties (elastic modulus *G'* and failure stress σ_Y*) labeled "0 Pa" are from true quiescent tests. For some high concentrations in the concentric cylinder geometry, the apparent failure stress exceeded what could be applied by the maximum instrument torque. For these materials, the hot gel properties were obtained by performing the dynamic gelation tests using a 40mm sandblasted parallel plate on the previously-specified rheometers with a Peltier flat plate and an applied mineral oil barrier. Due to maximum rheometer rotation speeds, each concentration had a different maximum stress that could be applied.

6.3 Results

6.3.1 Gel Point and Liquid Properties

The gelation of MC of higher molecular weights than the variety studied here has been shown to satisfy the Winter and Chambon criteria [238,239] and show a frequency-independent gel temperature only for concentrations above an entanglement threshold ($c_e \approx 10c^*$) [212]. For determining the quiescent gel temperature as our baseline for comparison, this work pragmatically chooses to use the temperature $T(G' = G'')$, at which the viscoelastic storage modulus, G', crosses over the loss modulus, *G''* [240] at an angular oscillation frequency of 0.1 rad/s. Though this is not a true, frequency-independent gel point, it is a practical alternative given that one is limited to lower frequencies by instrument inertia [46], which is a significant issue at low MC concentrations. Additionally, I am only seeking a point-of-reference for comparison to the dynamic gel temperature. At a frequency of 0.1 rad/s (chosen to minimize inertia effects), the crossover gel

temperature, $T(G'=G'')$, decreases as the MC concentration rises, and this dependence is consistent with literature [209,212,220]; quiescent gel temperature measurements are provided in Appendix D.

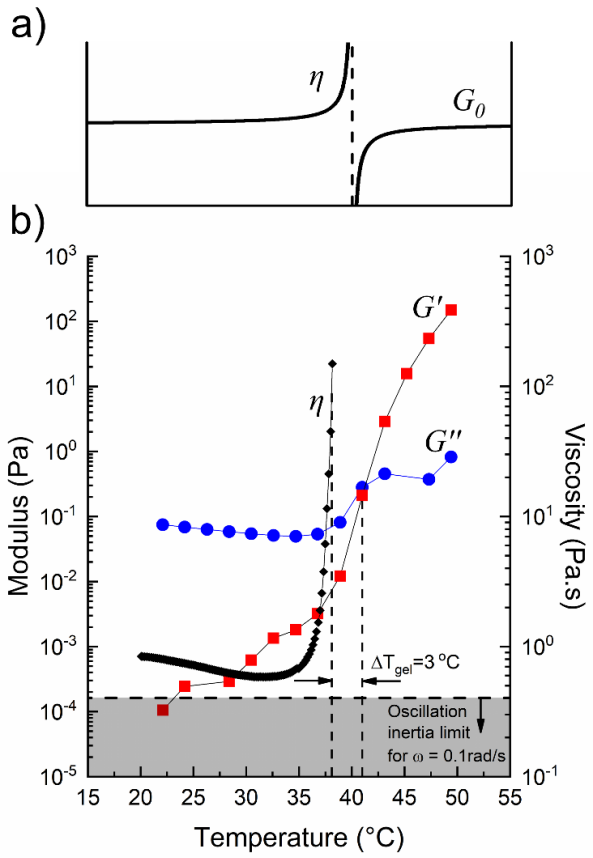

Figure 6.4. Gel point from viscosity divergence. a) Schematic of the gel point T_{gel} as either the temperature at which the instantaneous apparent viscosity η diverges or as the onset temperature of a non-zero shear elastic modulus G_0. b) Viscoelastic moduli and viscosity growth of aqueous MC (8 wt.%) while warming from 20 to 80 °C at 1 °C/min. G' and G'' are measured with SAOS (oscillation frequency = 0.1 rad/s, stress amplitude = 0.1 Pa) and T_{gel} is estimated as $T(G'=G'')$. η is measured by applying a constant shear stress (0.1 Pa) and T_{gel} is estimated as the temperature associated with the maximum slope, $T(d\eta/dT_{max})$. The difference in the measured gel temperatures is the expected precision of the dynamic gel temperature.

For dynamic gelation tests, a constant unidirectional stress is applied. With no oscillatory deformation, I do not have access to the viscoelastic moduli. Thus, this work uses the fundamental definition of the gel temperature as the temperature at which the viscosity, η, diverges to infinity

[47], as depicted schematically in Figure 6.4a. When using this definition, the ability to measure very small rates of deformation is a factor, and thus practically this work determines the gel temperature using the first maximum of $\frac{d\eta}{dT}$ when the instantaneous apparent viscosity becomes immeasurable (solidification). A similar protocol was used to determine the gel temperature of a triblock copolymer system, but only for stresses small enough to not significantly affect the properties of the material [241]. Figure 4b overlays the modulus and viscosity growth for the same MC concentration with the same magnitude of applied stress. Using the two different definitions of gel temperature ($G'(\omega) = G''(\omega)$ and $\left.\frac{d\eta}{dT}\right|_{max}$), I obtain the expected precision of our dynamic gel temperature as approximately 3 °C.

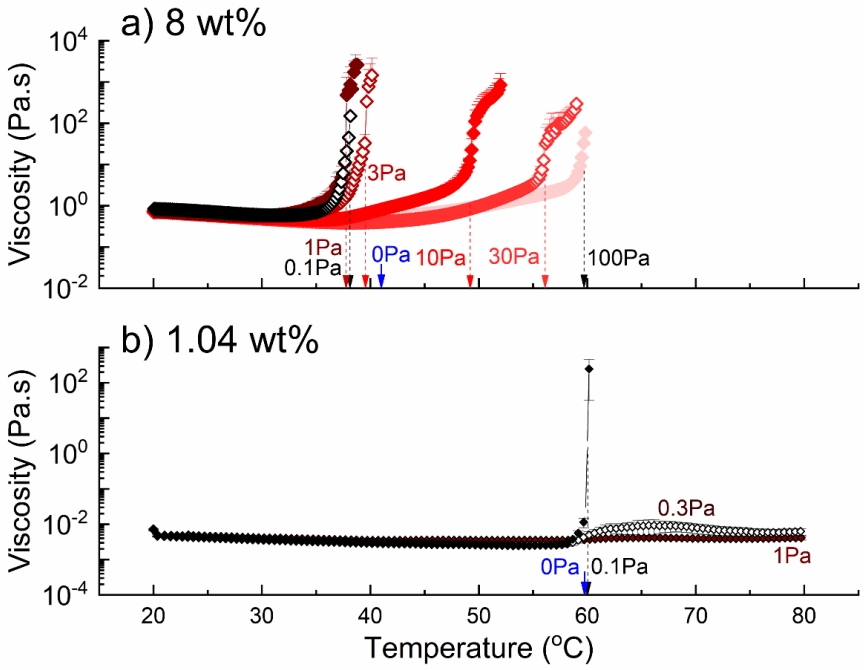

Figure 6.5. Growth of the steady shear viscosity for aqueous MC a) 8 wt% and b) 1.04 wt% while warming from 20 to 80 °C at 1 °C/min and being subjected to selected shear stresses. The gelation temperatures $T_{gel}(d\eta/dT_{max})$ are marked with down-pointing arrows labeled with the applied shear stress. Increasing stresses alternate between open and filled symbols. For reference, also marked are the gelation temperatures $T_{gel}(G' = G'')$ measured with SAOS (blue arrows).

Figure 5.5 shows the growth of the steady shear viscosity during dynamic gelation for the highest and lowest MC concentrations characterized. In Figure 6.5a, for 8 wt% MC, it is shown that $\left.\frac{d\eta}{dT}\right|_{max}$ occurs at higher temperatures as stress rises, meaning that the gel temperature *increases as the applied stress rises* (i.e. it is more difficult to gel the material). Compared to the quiescent gel temperature (blue arrow labeled "0 Pa"), applying a stress of 100 Pa delays gelation by approximately 20 °C when warming at 1 °C/min. Figure 6.5b shows that for lower concentrations at sufficiently high stresses, the viscosity never diverges, indicating that the imposed stress is not allowing a fully-percolated gel network to form. Materials that do not show a diverging viscosity can be considered to not gel while a sufficiently high stress is being applied; however, once the stress is removed, it is apparent from viscoelastic measurements that a soft viscoelastic solid forms (i.e. $G' > G''$).

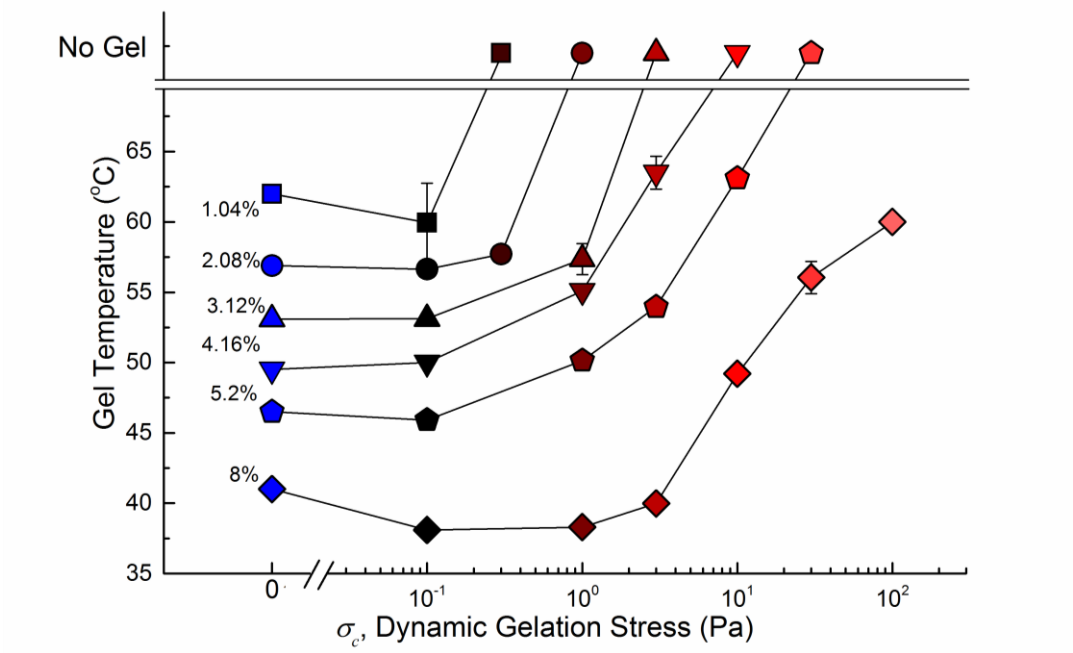

Figure 6.6. Apparent gel temperature for different concentrations of aqueous MC as a function of the applied dynamic stress. The aqueous MC material is solid-like at temperatures exceeding each curve.

The gel temperature results for all studied concentrations and applied stresses are summarized by the phase space in Figure 6.6. The figure summarizes the extensive sets of studies reported in Appendix D. For all concentrations, the gel temperature increases as the applied stress rises until a critical shear stress is reached when gelation is inhibited.

For this MC material, this work attributes the inhibition of gelation to either the destruction or prevention of fibril network connections due to flow stress, which is counteracted by the propensity to form fibrils and a percolated network at elevated temperature. When gelation is completely inhibited ('No Gel' location in Figure 6), it is likely that network formation is still occurring, but on length scales that do not span the full sample size until after the dynamic gelation stress is removed (and flow ceases). Evidence for this is visual (e.g. Figure 1b with the soft granular yield-stress material) and with measured rheology: when the stress is removed, a soft solid forms with an apparent failure stress below that applied when the gel formed as discussed in the next section.

We note that the phase space of Figure 6 is only representative of the particular MC material and heating rate used here; however, I anticipate that the trend of increased gel temperature or inhibited gelation under dynamic flow conditions is general to other thermally-gelling materials and heating rates. Clearly, if one's application relies on gelation occurring at a particular temperature, an unaccounted-for delay or inhibition of this process could have unfavorable implications. Yet, this phenomenon could also allow for more design freedom in the available material properties; if one does not want a material to gel in a hot environment, applying a flow stress will inhibit gelation.

6.3.2 Hot Gel Properties

After forming hydrogels with the same applied thermal and constant shear stress history, the hot gel was subjected to oscillatory shear flow at successively higher stress amplitudes until apparent failure was observed. The viscoelastic storage modulus, G'_1 [242], of the hot hydrogel was fit to a constant value in the plateau region to obtain G'_{LVE}. Apparent failure manifested as extreme non-linearity. Since I lack direct visual observation within the rheometer geometry, it is unclear if the failure is cohesive (due to sample yield) or adhesive (due to boundary slip). Thus, I emphasize the *apparent* nature of this failure stress, σ_Y^*, and that it may not be a true material property but is still representative of mechanical failure of the material.

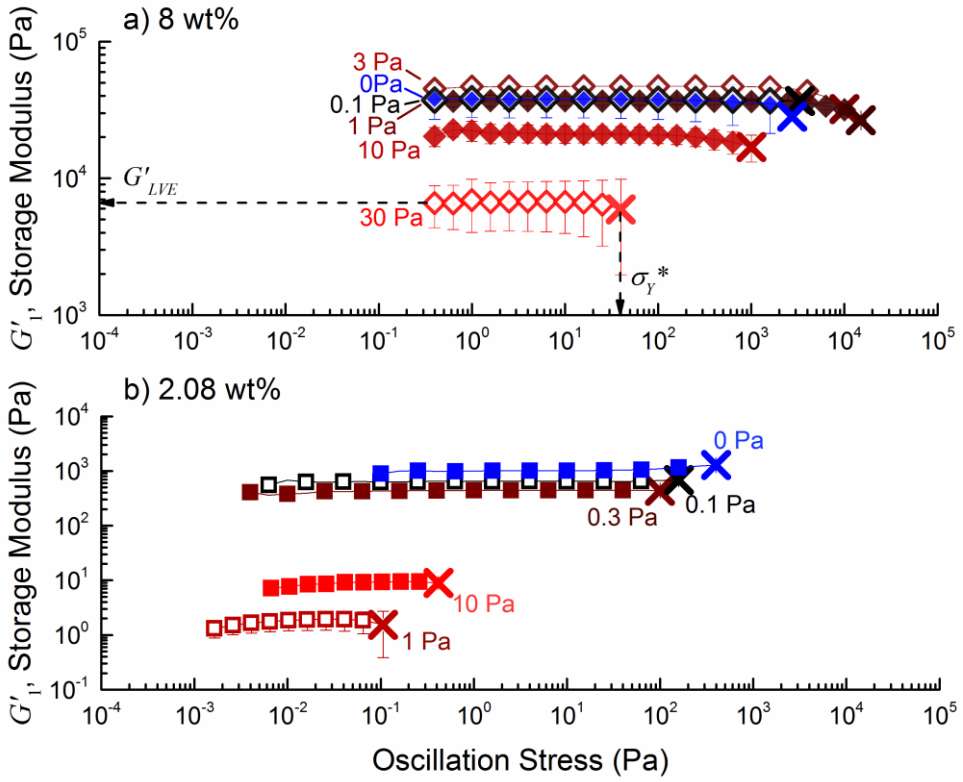

Figure 6.7. Hot hydrogel modulus (3 rad/s, 80 °C) from oscillatory shear flow for a set of aqueous MC materials a) 8 wt% and b) 2.08 wt% warmed from 20 to 80 °C at 1 °C/min while being subjected to a constant shear stress (0, 0.1, 1, 3, 10, or 30 Pa). Each stress amplitude sweep is truncated at the apparent failure stress (shown by × symbols). G'_{LVE} is obtained from a fit to the plateau at low oscillation stress. In the plateau region, $0.02 < \tan(\delta) < 0.1$. Symbols alternate between filled and open symbols with increasing dynamic flow stress. In regions of overlapping data sets, data point density is decreased for readability.

Figure 6.7 shows the viscoelastic storage modulus for MC a) 8 wt% and b) 2.08 wt% gelled under increasing stresses. As noted previously, for all materials, in the linear plateau region, $\tan(\delta)$ is less than 0.1 and G'' is omitted from plots for clarity. The shown error bars are from repeat experiments; each data set is truncated at the lowest observed apparent failure stress (× symbols). It must also be noted that the blue "0 Pa" data set is from the so-called "true quiescent" gelation test (no rheological probing during temperature ramp) and not from the SAOS temperature ramp. The non-linear rheology has been well-documented for MC materials of higher molecular weight than considered here[216]. The MC material in this study does not display stress-stiffening

behavior in large-amplitude oscillatory shear (LAOS). For 8 wt%, across two-and-a-half decades of applied flow stress, σ_c, the resulting hot gel storage modulus decreases by an order of magnitude (the gel is much less stiff), and the apparent failure stress decreases by over an order of magnitude (the gel breaks much more easily). This general trend is observed across all tested concentrations, but as shown for 2.08wt% (σ_c = 10 Pa), this trend becomes non-monotonic for lower concentrations at sufficiently high applied stress. With increasing flow stress, the resulting hot gel modulus stops decreasing and begins to increase, but does not come close to recovering the quiescent hot gel modulus.

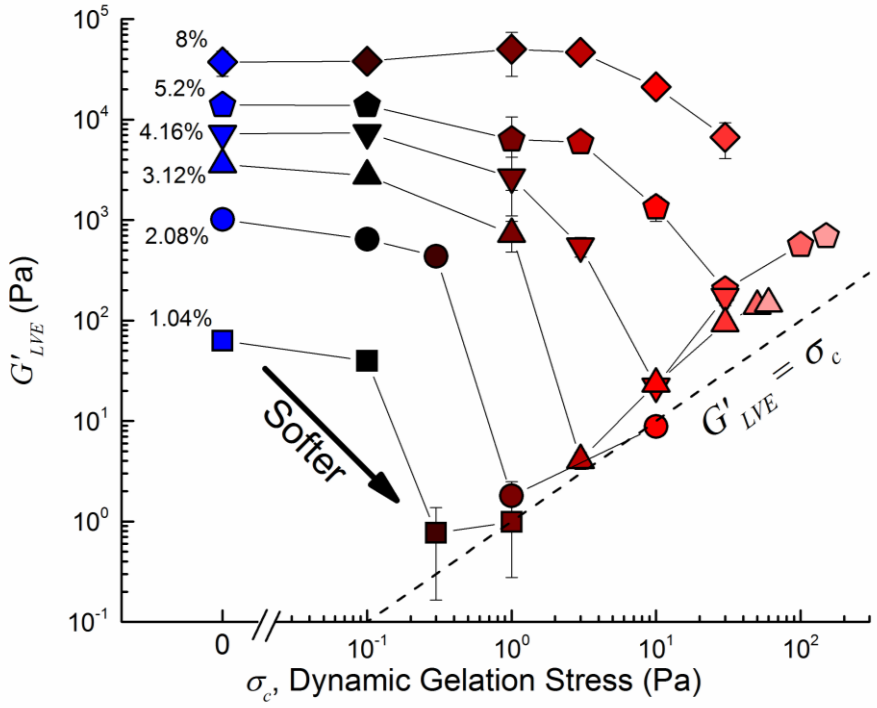

Figure 6.8. Linear viscoelastic storage modulus for various MC concentrations at 80 °C as a function of the dynamic gelation stress (the stress applied during gelation). The dashed line represents $G'_{LVE} = \sigma_c$, indicating direct proportionality.

Figure 8 summarizes the storage modulus measurements for all tested concentrations and applied stress conditions. The detailed viscoelastic data that Figure 6.8 summarizes is available Appendix D. Dramatically softer gels are formed under increasingly dynamic conditions. At low gelation stresses, G'_{LVE} is within error of the true quiescent modulus. At higher gelation stresses, G'_{LVE} is always below the true quiescent modulus, but is not monotonically decreasing. Interestingly, all measured MC concentrations less than 8 wt% show an unexpected non-monotonic trend where the sharp decrease in G'_{LVE} is followed by a gradual increase as the dynamic gelation stress increases. Furthermore, I observe that this gradual increase follows approximately along the line of $G'_{LVE} = \sigma_c$ which indicates that after a concentration-dependent critical stress is imposed, the hot gel modulus becomes insensitive to MC concentration and directly proportional to the dynamic gelation stress.

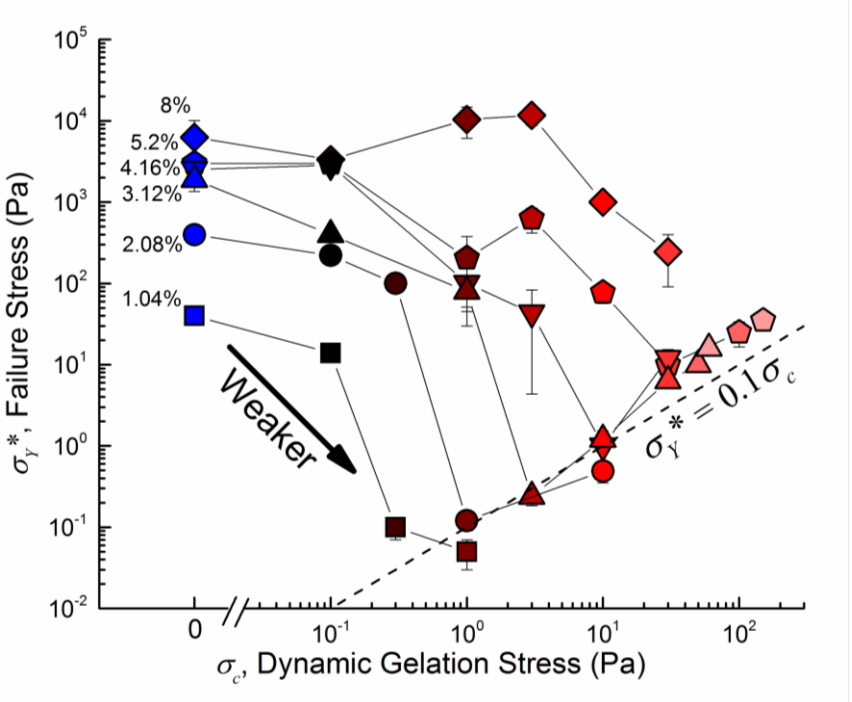

Figure 6.9. Apparent failure stress, σ_Y*, for various MC concentrations at 80 °C as a function of the dynamic gelation stress (the applied stress during gelation). The dashed line represents, $\sigma_Y^* = 0.1\ \sigma_c$ indicating direct proportionality.

Figure 6.9 summarizes the failure stress measurements for all studied concentrations and applied shear stresses and shows that dynamic conditions can also lead to dramatically weaker gels. Detailed viscoelastic data that Figure 6.9 summarizes is available Appendix D. Though the trends for σ_Y* are not as clear as for G'_{LVE} (likely due to it not being a true material property as discussed above), the same overall decrease followed by a concentration-insensitive increase is observed for concentrations below 8%. Above the concentration-dependent critical stress, materials appear to follow close to the line of $\sigma_Y^* = 0.1\,\sigma_c$. It is somewhat intuitive that if a significantly disruptive stress is applied during hydrogel formation, the resulting microstructure cannot support a load greater than this stress (e.g. here, it fails at 10% of the dynamic load applied during the temperature ramp). However, the non-monotonic and concentration-insensitive nature of this trend is unintuitive; increasing the disruptive stress beyond a certain level actually strengthens and stiffens the material (though not as stiff as hydrogels formed under quiescent conditions).

The implications for this huge range of resulting mechanical properties are apparent. In the example of a gelling film on a vertical surface, for MC, a 1mm thick layer results in a stress at the surface of approximately 10 Pa (see Appendix D). For a concentration such as 2.08%, this means that rather than being able to support a load of 600 Pa (true quiescent failure stress), the film would fail at a loading of less than 1 Pa.

The dramatic changes in mechanical properties suggest significant microstructural differences between materials gelled quiescently versus those gelled with dynamic applied stress conditions. Direct characterization of the microstructure is outside the scope of this work. However, here this work conjectures on the possible microstructural explanations of the behavior of the material

below and above some concentration-dependent critical dynamic gelation stress. Below the critical stress, the modulus and failure stress of the material is unaffected or decreases. Above the critical stress, the modulus and failure stress both increase.

Below the critical stress, as partially discussed in the delay/inhibition of the gel temperature, I hypothesize that while the dynamic gelation stress is applied, dense fibril network formations are only allowed to form on length scales smaller than the full sample size, as shown in Figure 1b. After this stress is removed, a sample-spanning network could still form by bridging these smaller domains, resulting in an overall sparser connectivity when compared to the quiescent gelation case and a softer and weaker material as observed. It is significant that these fibril-based networks are always softer than the quiescently-gelled material. This rules out the hypothesis that, in this low gelation stress regime, thicker fibrils may be formed due to associations under flow, as this would increase the stiffness of the hot gel. The rheological behavior in the hot state is consistent with a gel network rather than a microgel suspension such as Carbopol [43], or a wet granular material. The catastrophically nonlinear nature of the mechanical failure of the hot gel suggests fracture or surface debonding of a network, rather than reversible yield and flow as would be expected if the material remained in the granular state similar to that shown in Figure 61b.

An overall sparser connectivity would explain why disrupting the microstructure formation in this way leads to softer and weaker gels, but does not explain the non-monotonic nature of these properties seen in lower concentrations. Above the critical gelation stress, the modulus and failure stress increase. This behavior suggests that at the concentration-dependent critical stress, the overall character of the microstructure undergoes a dramatic shift. Ginzburg et al. [222] found through simulations that MC polymers may self-assemble into fibrillar networks in two possible configurations depending on concentration: tubes of polymer rings, and bundles of aligned

polymers. Only the former configuration is consistent with cryogenic transmission electron microscopy and small angle neutron scattering observations of a quiescently gelled fibrillar network of MC (higher molecular weights than studied here), such as a uniform fibril diameter of 15±2nm [210,211,221]. Thus, Ginzburg et al. [222] hypothesize the existence of some unaccounted for kinetic or thermodynamic factor that is unfavorable to the formation of the latter, aligned and bundled configuration. Given our results that suggest a dramatic shift in the configuration of the microstructure at a concentration-dependent critical stress (non-monotonic stiffness and failure stress), I hypothesize that above the critical applied stress during gelation, MC polymers tend to stretch and align, favoring the formation of a bundled fibrillar network with no polymeric rings. If this is the case, as the dynamic gelation stress is increased, polymer molecules would be more strongly aligned, and the aggregated bundles would be thicker, stiffer, and stronger as a result. This also suggests that dynamically-gelled MC materials would likely have lower uniformity of fibril diameters than has been found for quiescently gelled materials. Methods are still needed to enable experimental visualization of this phenomenon and to validate this hypothesis.

6.4 Conclusions and Outlook

We applied constant shear stresses during the gelation of aqueous methylcellulose to obtain rheological properties in both the liquid and hot gel states across a wide range of MC concentrations and dynamic stresses. Applying stress was found to make gelation more difficult (i.e. gel temperature increased) or inhibit gelation entirely until removal of the applied load. Significantly softer and weaker gels were formed under dynamic conditions, with lower

concentrations showing non-monotonic dependence of properties on σ_c. Outside the scope of this work is the effect of an oscillatory stress (as in SAOS) on gel temperature and properties. However, given the sensitivity of some concentrations to a relatively small unidirectional stress (e.g. for 2.08%, G'_{LVE} decreasing by over two orders of magnitude at σ_c = 1 Pa), this raises questions for any gelation test performed at finite stress magnitude, including SAOS. This work recommends the protocol presented here, of reporting true-quiescent properties that are approached in the limit of zero applied stress to verify any SAOS measurement. This protocol of applied stress is not limited to materials that exhibit a "gel temperature" and can also be applied to any materials where flow may affect structure formation including the restructuring of thixotropic materials, or the deposition of frontally polymerizing materials [161]. Additionally, here I only characterize hot gel properties in the same direction as the applied stress (i.e. the rotational direction). I conjecture that for a networked microstructure, there should be some alignment in the plane of the unidirectional applied stress, which triggers a transition in the configuration of the MC fibrils to a more aligned structure, leading to an increasing stiffness and strength. This also suggests that properties such as stiffness, failure stress, diffusivity, etc., may be anisotropic [243]. Characterization of such anisotropic properties would serve as interesting future studies, including rheological, structural, and transport properties through MC networks.

Chapter 7: Conclusions and outlook

The objectives of this thesis were to establish the design relationships between performance, rheological properties, material structure/formulation, and processing for key yield-stress fluids, and to provide methodologies that can be applied to a wide variety of other rheologically-complex materials. The results presented here have already been implemented in research outside the scope of this thesis and provide frameworks for the rheological design of yield-stress fluids. Model materials presented here enable systematic exploration of the role of extensibility with yield-stress fluids. Finally, the protocol of dynamic gelation, which includes reporting true-quiescent properties that are approached in the limit of zero applied stress, should potentially be applied to any material that transitions to a more structured state to verify other rheological measurements (e.g. small-amplitude oscillatory shear).

In Chapter 2, this work established a paradigm for the design of rheologically-complex materials focused on the rheology-to-structure inverse problem for model yield-stress fluids. I believe that anyone wishing to utilize yield-stress fluids in application would benefit from the methods presented here, and from making use of our early-stage database. Obvious further extensions of this work are to include additional features and secondary properties of yield-stress fluids beyond steady shear flow behavior. Thixotropic effects, pre-yield viscosity, pre-yield elasticity, yield strain, inhomogeneous yielding, and viscoelasticity are all neglected in our work and have significant potential impacts in the application of these materials. Despite this, the fact that it is easy to see where to go next and where this work can be extended is a positive thing that indicates its potential influence. The development of similar design ontologies should be carried out for other key phenomena of rheology including thixotropy and viscoelasticity. Hopefully

someday, this framework will lead to the development of design tools for rheologically complex materials on the level of Professor Michael Ashby's famous work on materials selection [28,126,244].

Chapter 3 developed a paradigm that yield-stress fluids may be highly extensible materials, a perspective that until now has been significantly underdeveloped in favor of more "paste-like" yield-stress fluids [245]. This work demonstrated that archetypal yield-stress fluids are inappropriate models for studying applications where extensibility may be important and formulated and characterized a candidate highly-extensible model yield-stress fluid. As our characterization method was limited to a single extension rate, a more thorough investigation of the effect of extension rate on the extensibility of yield-stress fluids should be conducted, as well as a systematic study of what performance target range our model material can achieve by varying the formulation and processing. The results of such a study might show that our candidate model material only quantitatively matches the extensibility of materials like gum at a very limited range of extension rates. However, the fact that our simply formulated material captures the important extensional behavior at even a single extension rate makes it a more suitable model material than *any* of the other common model yield-stress fluids. Potential refinement of the design of this material to achieve particular performance targets remains as future work. As demonstrated, the characterization protocol introduced in this chapter can be applied to a wide variety of yield-stress fluids and was utilized for the subsequent studies of 3D printing and performance magic applications.

Performance magic is a passion that I was fortunate to develop significantly in graduate school. In Chapter 4, I applied the methodologies presented in Chapter 3 to characterize a rheologically interesting performance magic material, Mystic Smoke. The results there serve as a useful

pedagogical tool and explain the “magical” behavior. This project was a successful blending of my personal hobby, a project in a class on polymer rheology taught by Professor Simon Rogers, and my research interests. The playful application has inspired contributions to scientific outreach and new uses of research materials. Future studies of this material should include a more thorough investigation of other rheological properties that may impact the performance (e.g. extensional viscosity), leading to a complete set of property targets to achieve this interesting behavior that has potential applications in additive manufacturing.

Chapter 5 made use of the design framework presented in Chapter 2, and the characterization protocol presented in Chapter 3, to present a novel material for direct-write 3D printing ink. This work introduced concentrated particle-free emulsions as materials that can address the significant challenge of direct-write 3D printing at nozzle diameters less than 10 microns. By varying the amount of polymer additive, key relations between printing performance and ink rheology were established, and an extensibility property target for higher-speed printing was determined. This is hardly the only property target that can be developed for direct-write 3D printing, and further studies should investigate scaling laws and strategies for achieving minimum yield stresses, viscoelastic moduli, and maximum thixotropic timescales. The contribution of particle-free emulsions as an additional material for printing is only impactful if further advances can be made in post-printing transformations to improve mechanical properties. One such post-printing transformation of the material into an elastomer was presented in Chapter 5. Preliminary work has been performed with Dr. Sean Lehman in the Nuzzo research group to develop a photo-curable emulsion that makes use of poly(2-hydroxyethylmethacrylate) with a lithium phosphinate photoinitiator. Emulsions are already widely used for their encapsulation properties; the innovation

of concentrated emulsions as direct-write 3D printing materials has the potential to inspire a huge number of post-processing methods.

Setting aside direct-write 3D printing, the emulsion system introduced in Chapter 5 is remarkable in how the steady shear flow rheology and linear viscoelasticity is essentially unaffected by the molecular weight of the PEO additive, while the extensibility can be controlled to be drastically different. Shown in Figure 7.1 is the extensibility property space developed in Chapter 3 with the PEO emulsion included. With this material system, we cover nearly the entire observed range of extensional strain-to-break with a very small distribution of shear yield stress values. In this way, this material truly is a model system for investigating the effects of extensional rheology for yield-stress fluid applications and should be applied to many other flow scenarios of interest including droplet impact [94,97]. Exhaustive shear and extensional rheological characterization should be performed on this model system to determine the ways that shear rheology may begin to differ, and the range of different extensional properties that can be achieved.

Chapter 6 focused on the effect of processing on a thermally gelling material, aqueous methylcellulose, which when sheared under appropriate conditions forms a granular yield-stress fluid. This work shows the potentially catastrophic impact that neglecting processing conditions can have, and thus this work recommends that for any application where structuring may occur under flow, our protocol of reporting true-quiescent properties and the effect of finite stress be performed. This methodology is being applied as part of a collaboration with Jia En Aw, and Mostafa Yourdkhani; and Professors Nancy Sottos, Scott White, Jeff Moore, and Philippe Geubelle in the Autonomic Material Systems group at the University of Illinois. Preliminary work outside the scope of this thesis is investigating the effect of applied stress on the bulk polymerization of a dicyclopentadiene system used in 3D printing [161] and suggests an

enhancement of the polymerization process above a critical stress. Additional work has also been performed with this system to develop rheological design criteria for this innovative method of 3D printing.

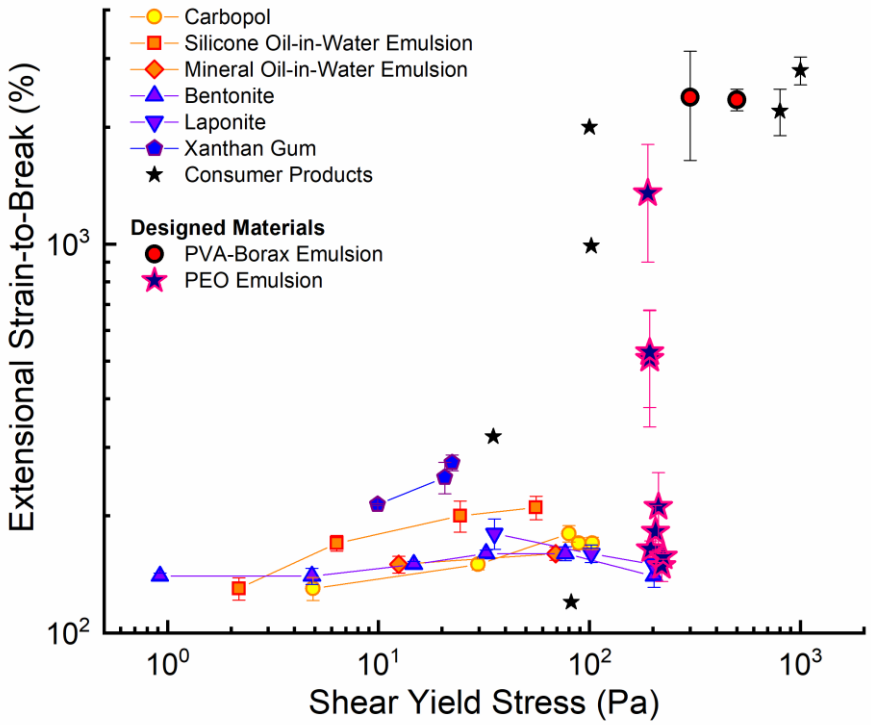

Figure 7.1 Ashby-style co-plot of all materials studied here including designed model systems (PVA-borax emulsion in Chapter 3, direct-writable PEO emulsion in Chapter 5). Error bars shown are the standard deviation from repeated experiments.

To conclude, this thesis is an important collection of design frameworks, methodologies, and case-studies devoted to developing the full design toolbox for yield-stress fluids. In the future, to effectively design complex materials will mean completely integrating performance-to-rheology target setting, rheology-to-structure ideation and formulation, and structure-to-processing optimization. This will enable rheology and soft matter communities to better design and engineer materials to achieve novel functionality that incorporates the rheologically complex.

References

[1] R.H. Ewoldt, Extremely Soft: Design with Rheologically Complex Fluids, Soft Robot. 1 (2013) 12–20. http://online.liebertpub.com/doi/abs/10.1089/soro.2013.1508 (accessed September 25, 2013).

[2] M. Denny, The role of gastropod pedal mucus in locomotion, Nature. 285 (1980) 160–161. doi:10.1038/285160a0.

[3] K. Autumn, Mechanisms of Adhesion in Geckos, Integr. Comp. Biol. 42 (2002) 1081–1090. doi:10.1093/icb/42.6.1081.

[4] R.E. Shadwick, Mechanical design in arteries, J. Exp. Biol. 202 (1999) 3305–13.

[5] C. Laschi, M. Cianchetti, B. Mazzolai, L. Margheri, M. Follador, P. Dario, Soft Robot Arm Inspired by the Octopus, Adv. Robot. 26 (2012) 709–727. doi:10.1163/156855312X626343.

[6] E. Cheung, M. Sitti, Adhesion of Biologically Inspired Polymer Microfibers on Soft Surfaces, Langmuir. 25 (2009) 6613–6616. doi:10.1021/la900997p.

[7] Q. Barral, G. Ovarlez, X. Chateau, J. Boujlel, B. Rabideau, P. Coussot, Adhesion of yield stress fluids, Soft Matter. (2010) 1343–1351. doi:10.1039/b922162j.

[8] P. COUSSOT, Saffman–Taylor instability in yield-stress fluids, J. Fluid Mech. 380 (1999) S002211209800370X. doi:10.1017/S002211209800370X.

[9] D. Bonn, M.M. Denn, L. Berthier, T. Divoux, S. Manneville, Yield stress materials in soft condensed matter, Rev. Mod. Phys. 89 (2017) 35005. doi:10.1103/RevModPhys.89.035005.

[10] H.A. Barnes, The yield stress — a review or “ panta rhei ”— everything flows ?, J. Non-

Newtonian Fluid Mech. 81 (1999) 133–178. doi:10.1016/S0377-0257(98)00094-9.

[11] P.C.F. Møller, J. Mewis, D. Bonn, Yield stress and thixotropy: on the difficulty of measuring yield stresses in practice, Soft Matter. 2 (2006) 274. doi:10.1039/b517840a.

[12] C.J.E. Santos, A.Z. Nelson, E. Mendoza, R.H. Ewoldt, W.M. Kriven, Design and fabrication of ceramic beads by the vibration method, J. Eur. Ceram. Soc. 35 (2015) 3587–3594. doi:10.1016/j.jeurceramsoc.2015.05.018.

[13] A. Sun, S. Gunasekaran, Yield Stress in Foods: Measurements and Applications, Int. J. Food Prop. 12 (2009) 70–101. doi:10.1080/10942910802308502.

[14] B.G. Compton, J.A. Lewis, 3D-printing of lightweight cellular composites, Adv. Mater. (2014) 5930–5935. doi:10.1002/adma.201401804.

[15] T. Bhattacharjee, S.M. Zehnder, K.G. Rowe, S. Jain, R.M. Nixon, W.G. Sawyer, T.E. Angelini, Writing in the granular gel medium, Sci. Adv. 1 (2015) e1500655–e1500655. doi:10.1126/sciadv.1500655.

[16] W. Wen, X. Huang, P. Sheng, Electrorheological fluids: structures and mechanisms, Soft Matter. 4 (2008) 200–210. doi:10.1039/B710948M.

[17] J. de Vicente, D.J. Klingenberg, R. Hidalgo-Alvarez, Magnetorheological fluids: a review, Soft Matter. 7 (2011) 3701. doi:10.1039/c0sm01221a.

[18] K.C. Smith, Y.-M. Chiang, W. Craig Carter, Maximizing Energetic Efficiency in Flow Batteries Utilizing Non-Newtonian Fluids, J. Electrochem. Soc. 161 (2014) A486–A496. doi:10.1149/2.011404jes.

[19] E.A. Appel, M.W. Tibbitt, M.J. Webber, B.A. Mattix, O. Veiseh, R. Langer, Self-assembled hydrogels utilizing polymer–nanoparticle interactions, Nat. Commun. 6 (2015) 6295. doi:10.1038/ncomms7295.

[20] P. Møller, A. Fall, V. Chikkadi, D. Derks, D. Bonn, An attempt to categorize yield stress fluid behaviour., Philos. Trans. A. Math. Phys. Eng. Sci. 367 (2009) 5139–5155. doi:10.1098/rsta.2009.0194.

[21] N.J. Balmforth, I. a. Frigaard, G. Ovarlez, Yielding to Stress: Recent Developments in Viscoplastic Fluid Mechanics, Annu. Rev. Fluid Mech. 46 (2014) 121–146. doi:10.1146/annurev-fluid-010313-141424.

[22] Q.D. Nguyen, D. V Boger, Measuring the Flow Properties of Yield Stress Fluids, Annu. Rev. Fluid Mech. 24 (1992) 47–88.

[23] G.A. Hazelrigg, A Framework for Decision-Based Engineering Design, J. Mech. Des. 120 (1998) 653. doi:10.1115/1.2829328.

[24] K. Ulrich, S.D. Eppinger, Product design and development, 5th ed., McGraw-Hill, New York, 2012. http://www.worldcat.org/title/product-design-and-development/oclc/791505360?referer=br&ht=edition (accessed September 26, 2012).

[25] J. Hirtz, R. Stone, D. McAdams, S. Szykman, K. Wood, A functional basis for engineering design: Reconciling and evolving previous efforts, Res. Eng. Des. 13 (2002) 65–82. doi:10.1007/s00163-001-0008-3.

[26] A. Winter, V. Govindarajan, Engineering Reverse Innovations, Harv. Bus. Rev. 93 (2015) 80–89.

[27] E. de Bono, Lateral Thinking, Penguin Books, New York, NY, 1977.

[28] M.F. Ashby, Material selection in mechanical design., Fourth Edi, Butterworth-Heinemann, Boston, MA, 2011.

[29] D.D. Braun, M.R. Rosen, The Rheology Modifiers Handbook Practical Use & Application, William Andrew Publication, Norwich, N.Y., 2000.

[30] M. Ash, I. Ash, Handbook of Rheology Modifiers, Synapse Information Resources Inc., 2006.

[31] U. Brockel, W. Meier, G. Wagner, Product Design and Engineering, Wiley-VCH Verlag GmbH & Co. KGaA, Weinheim, Germany, 2013. doi:10.1002/9783527654741.

[32] H.H. Winter, M. Mours, The cyber infrastructure initiative for rheology, Rheol. Acta. 45 (2006) 331–338. doi:10.1007/s00397-005-0041-7.

[33] G.B. Olson, Designing a New Material World, Science (80-.). 288 (2000) 993–998. doi:10.1126/science.288.5468.993.

[34] H.M. Jaeger, Celebrating Soft Matter's 10th Anniversary: Toward jamming by design, Soft Matter. 11 (2015) 12–27. doi:10.1039/C4SM01923G.

[35] M.Z. Miskin, H.M. Jaeger, Evolving design rules for the inverse granular packing problem., Soft Matter. 10 (2014) 3708–3715. doi:10.1039/c4sm00539b.

[36] P.M. Reis, H.M. Jaeger, M. van Hecke, Designer Matter: A perspective, Extrem. Mech. Lett. 5 (2015) 25–29. doi:10.1016/j.eml.2015.09.004.

[37] S.C. Glotzer, Assembly engineering: Materials design for the 21st century (2013 P.V. Danckwerts lecture), Chem. Eng. Sci. 121 (2015) 3–9. doi:10.1016/j.ces.2014.09.045.

[38] A. Jain, J.A. Bollinger, T.M. Truskett, Inverse methods for material design, AIChE J. 60 (2014) 2732–2740. doi:10.1002/aic.14491.

[39] A. Zakutayev, X. Zhang, A. Nagaraja, L. Yu, S. Lany, T.O. Mason, D.S. Ginley, Z. A., Theoretical Prediction and Experimental Realization of New Stable Inorganic Materials Using the Inverse Design Approach, J. Am. Chem. Soc. 135 (2013) 10048–10054. doi:10.1021/ja311599g.

[40] G.D. Moggridge, E.L. Cussler, Chemical Product Design, 2nd Editio, Cambridge

University Press, Cambridge, 2012.

[41] R.H. Ewoldt, C. Clasen, a. E. Hosoi, G.H. McKinley, Rheological fingerprinting of gastropod pedal mucus and synthetic complex fluids for biomimicking adhesive locomotion, Soft Matter. 3 (2007) 634. doi:10.1039/b615546d.

[42] T.R. Gruber, Toward principles for the design of ontologies used for knowledge sharing, Int. J. Hum. Comput. Stud. 43 (1995) 907–928. doi:10.1006/ijhc.1995.1081.

[43] J.M. Piau, Carbopol gels: Elastoviscoplastic and slippery glasses made of individual swollen sponges Meso- and macroscopic properties, constitutive equations and scaling laws, J. Nonnewton. Fluid Mech. 144 (2007) 1–29. doi:10.1016/j.jnnfm.2007.02.011.

[44] Y.M. Joshi, Model for cage formation in colloidal suspension of laponite, J. Chem. Phys. 127 (2007). doi:10.1063/1.2779026.

[45] W.E. Rochefort, S. Middleman, Rheology of Xanthan Gum: Salt, Temperature, and Strain Effects in Oscillatory and Steady Shear Experiments, J. Rheol. (N. Y. N. Y). 31 (1987) 337. doi:10.1122/1.549953.

[46] R.H. Ewoldt, M.T. Johnston, L.M. Caretta, Experimental challenges of shear rheology with case studies in biological complex fluids, in: S.E. Spagnolie (Ed.), Complex Fluids Biol. Syst., Springer, 2015: pp. 207–241. doi:10.1007/978-1-4939-2065-5_6.

[47] C.W. Macosko, Rheology Principles, Measurements, and Applications, Wiley, New York, 1994.

[48] P. Coussot, Q.D. Nguyen, H.T. Huynh, D. Bonn, Viscosity bifurcation in thixotropic, yielding fluids, J. Rheol. (N. Y. N. Y). 46 (2002) 573–589. doi:10.1122/1.1459447.

[49] H. Emady, M. Caggioni, P. Spicer, Colloidal microstructure effects on particle sedimentation in yield stress fluids, J. Rheol. 57 (2013) 1761–1772. doi:10.1122/1.4824471.

[50] G. Pahl, W. Beitz, Engineering Design - A Systematic Approach, Springer London, London, 1996. doi:10.1007/978-1-4471-3581-4.

[51] M. Graham, A. Slocum, R.M. Sanchez, Teaching High School Students and College Freshmen Product Development by Deterministic Design With PREP, J. Mech. Des. 129 (2007) 677. doi:10.1115/1.2722334.

[52] F. Da Cruz, F. Chevoir, D. Bonn, P. Coussot, Viscosity bifurcation in granular materials, foams, and emulsions, Phys. Rev. E - Stat. Nonlinear, Soft Matter Phys. 66 (2002) 1–7. doi:10.1103/PhysRevE.66.051305.

[53] F. Sciortino, Disordered materials: One liquid, two glasses., Nat. Mater. 1 (2002) 145–146. doi:10.1038/nmat752.

[54] F. Sciortino, P. Tartaglia, Glassy colloidal systems, Adv. Phys. 54 (2005) 471–524. doi:10.1080/00018730500414570.

[55] A. Burmistrova, R. von Klitzing, Control of number density and swelling/shrinking behavior of P(NIPAM–AAc) particles at solid surfaces, J. Mater. Chem. 20 (2010) 3502. doi:10.1039/b923969c.

[56] C. Clasen, B.P. Gearing, G.H. McKinley, The flexure-based microgap rheometer (FMR), J. Rheol. (N. Y. N. Y). 50 (2006) 883. doi:10.1122/1.2357190.

[57] M. Le Merrer, R. Lespiat, R. Höhler, S. Cohen-Addad, Linear and non-linear wall friction of wet foams, Soft Matter. 11 (2015) 368–381. doi:10.1039/C4SM01557F.

[58] D.A. WEITZ, J.S. HUANG, SELF–SIMILAR STRUCTURES AND THE KINETICS OF AGGREGATION OF GOLD COLLOIDS, in: Kinet. Aggreg. Gelation, Elsevier, 1984: pp. 19–28. doi:10.1016/B978-0-444-86912-8.50010-9.

[59] Y.D. Liu, H.J. Choi, Electrorheological fluids: smart soft matter and characteristics, Soft

Matter. 8 (2012) 11961. doi:10.1039/c2sm26179k.

[60] W. Mickel, S. Münster, L.M. Jawerth, D. a Vader, D. a Weitz, A.P. Sheppard, K. Mecke, B. Fabry, G.E. Schröder-Turk, Robust pore size analysis of filamentous networks from three-dimensional confocal microscopy., Biophys. J. 95 (2008) 6072–6080. doi:10.1529/biophysj.108.135939.

[61] H. Senff, W. Richtering, Temperature sensitive microgel suspensions: Colloidal phase behavior and rheology of soft spheres, J. Chem. Phys. 111 (1999) 1705–1711. doi:10.1063/1.479430.

[62] H. Princen, A. Kiss, Rheology of foams and highly concentrated emulsions: IV. An experimental study of the shear viscosity and yield stress of concentrated emulsions, J. Colloid Interface Sci. 128 (1989) 176–187. doi:10.1016/0021-9797(89)90396-2.

[63] Y. Otsubo, R.K. Prud'homme, Rheology of oil-in-water emulsions, Rheol. Acta. 33 (1994) 29–37. doi:10.1007/BF00453461.

[64] R. Pal, Effect of droplet size on the rheology of emulsions, AIChE J. 42 (1996) 3181–3190. doi:10.1002/aic.690421119.

[65] T.G. Mason, New fundamental concepts in emulsion rheology, Curr. Opin. Colloid Interface Sci. 4 (1999) 231–238. doi:10.1016/S1359-0294(99)00035-7.

[66] J.R. Seth, L. Mohan, C. Locatelli-Champagne, M. Cloitre, R.T. Bonnecaze, A micromechanical model to predict the flow of soft particle glasses, Nat. Mater. 10 (2011) 838–843. doi:10.1038/nmat3119.

[67] M. Dinkgreve, J. Paredes, M. a. J. Michels, D. Bonn, Universal rescaling of flow curves for yield-stress fluids close to jamming, Phys. Rev. E. 92 (2015) 12305. doi:10.1103/PhysRevE.92.012305.

[68] S. Cohen-Addad, R. Höhler, O. Pitois, Flow in Foams and Flowing Foams, Annu. Rev. Fluid Mech. 45 (2013) 241–267. doi:10.1146/annurev-fluid-011212-140634.

[69] J. Buitenhuis, S. Förster, Block copolymer micelles: Viscoelasticity and interaction potential of soft spheres, J. Chem. Phys. 107 (1997) 262–272. doi:10.1063/1.474346.

[70] F. Renou, J. Stellbrink, G. Petekidis, Yielding processes in a colloidal glass of soft star-like micelles under large amplitude oscillatory shear (LAOS), J. Rheol. (N. Y. N. Y). 54 (2010) 1219. doi:10.1122/1.3483610.

[71] R.C. Kramb, C.F. Zukoski, Nonlinear rheology and yielding in dense suspensions of hard anisotropic colloids, J. Rheol. (N. Y. N. Y). 55 (2011) 1069–1084. doi:10.1122/1.3613978.

[72] R.C. Kramb, C.F. Zukoski, Exploration of the volume fraction above which suspensions of spherical and weakly anisotropic colloid particles cannot flow, J. Rheol. (N. Y. N. Y). 55 (2011) 1085. doi:10.1122/1.3613983.

[73] T. Jiang, C. Zukoski, Dynamic localization and shear-induced hopping of particles: A way to understand the rheology of dense colloidal dispersions, J. Rheol. (N. Y. N. Y). 58 (2014) 1277–1299. doi:10.1122/1.4866038.

[74] H.M. Jaeger, S.R. Nagel, R.P. Behringer, Granular solids, liquids, and gases, Rev. Mod. Phys. 68 (1996) 1259–1273. doi:10.1103/RevModPhys.68.1259.

[75] E. Brown, H.M. Jaeger, Dynamic jamming point for shear thickening suspensions, Phys. Rev. Lett. 103 (2009) 1–4. doi:10.1103/PhysRevLett.103.086001.

[76] I.M. Krieger, The Second Electroviscous Effect in Polymer Latices, J. Rheol. (N. Y. N. Y). 20 (1976) 29. doi:10.1122/1.549428.

[77] N.P. Chafe, J.R. de Bruyn, Drag and relaxation in a bentonite clay suspension, J. Nonnewton. Fluid Mech. 131 (2005) 44–52. doi:10.1016/j.jnnfm.2005.08.010.

[78] N.J. Alderman, G.H. Meeten, J.D. Sherwood, Vane rheometry of bentonite gels, J. Nonnewton. Fluid Mech. 39 (1991) 291–310. doi:10.1016/0377-0257(91)80019-G.

[79] P. Coussot, Q.D. Nguyen, H.T. Huynh, D. Bonn, Avalanche Behavior in Yield Stress Fluids, Phys. Rev. Lett. 88 (2002) 175501. doi:10.1103/PhysRevLett.88.175501.

[80] S. Jabbari-Farouji, H. Tanaka, G.H. Wegdam, D. Bonn, Multiple nonergodic disordered states in Laponite suspensions: A phase diagram, Phys. Rev. E - Stat. Nonlinear, Soft Matter Phys. 78 (2008) 1–10. doi:10.1103/PhysRevE.78.061405.

[81] B. Ruzicka, E. Zaccarelli, A fresh look at the Laponite phase diagram, Soft Matter. 7 (2011) 1268. doi:10.1039/c0sm00590h.

[82] S. Jatav, Y.M. Joshi, Rheological signatures of gelation and effect of shear melting on aging colloidal suspension, J. Rheol. (N. Y. N. Y). 58 (2014) 1535–1554. doi:10.1122/1.4887344.

[83] D.J. Klingenberg, C.F. Zukoski, Studies on the steady-shear behavior of electrorheological suspensions, Langmuir. 6 (1990) 15–24. doi:10.1021/la00091a003.

[84] P.J. Rankin, A.T. Horvath, D.J. Klingenberg, Magnetorheology in viscoplastic media, Rheol. Acta. 38 (1999) 471–477. doi:10.1007/s003970050198.

[85] J.M. GINDER, L.C. DAVIS, L.D. ELIE, RHEOLOGY OF MAGNETORHEOLOGICAL FLUIDS: MODELS AND MEASUREMENTS, Int. J. Mod. Phys. B. 10 (1996) 3293–3303. doi:10.1142/S0217979296001744.

[86] D.G. Wallace, J. Rosenblatt, Collagen gel systems for sustained delivery and tissue engineering, Adv. Drug Deliv. Rev. 55 (2003) 1631–1649. doi:10.1016/j.addr.2003.08.004.

[87] M.J. Solomon, P.T. Spicer, Microstructural regimes of colloidal rod suspensions, gels, and glasses, Soft Matter. 6 (2010) 1391–1400. doi:10.1039/B918281K.

[88] C.P.J. Bennington, R.J. Kerekes, J.R. Grace, The yield stress of fibre suspensions, Can. J.

Chem. Eng. 68 (1990) 748–757. doi:10.1002/cjce.5450680503.

[89] G.M.H. Wilkins, P.T. Spicer, M.J. Solomon, Colloidal system to explore structural and dynamical transitions in rod networks, gels, and glasses, Langmuir. 25 (2009) 8951–8959. doi:10.1021/la9004196.

[90] V. Trappe, V. Prasad, L. Cipelletti, P.N. Segre, D.A. Weitz, Jamming phase diagram for attractive particles., Nature. 411 (2001) 772–5. doi:10.1038/35081021.

[91] M. Fuchs, M.E. Cates, Schematic models for dynamic yielding of sheared colloidal glasses, Faraday Discuss. 123 (2003) 267–286. doi:10.1039/b205629a.

[92] R. Buscall, Effect of long-range repulsive forces on the viscosity of concentrated latices: comparison of experimental data with an effective hard-sphere model, J. Chem. Soc. Faraday Trans. 87 (1991) 1365. doi:10.1039/ft9918701365.

[93] W.B. Russel, D.A. Saville, W.R. Schowalter, Rheology, in: Colloid. Dispersions, Cambridge University Press, Cambridge, 1989: pp. 456–506. doi:10.1017/CBO9780511608810.017.

[94] B.C. Blackwell, M.E. Deetjen, J.E. Gaudio, R.H. Ewoldt, Sticking and splashing in yield-stress fluid drop impacts on coated surfaces, Phys. Fluids. 27 (2015) 43101. doi:10.1063/1.4916620.

[95] A.S. Negi, C.O. Osuji, Time-resolved viscoelastic properties during structural arrest and aging of a colloidal glass, Phys. Rev. E - Stat. Nonlinear, Soft Matter Phys. 82 (2010) 1–4. doi:10.1103/PhysRevE.82.031404.

[96] G. Ovarlez, L. Tocquer, F. Bertrand, P. Coussot, Rheopexy and tunable yield stress of carbon black suspensions, Soft Matter. 9 (2013) 5540. doi:10.1039/c3sm27650c.

[97] B.C. Blackwell, M.E. Deetjen, J.E. Gaudio, R.H. Ewoldt, QUANTITATIVE MEASURES

OF YIELD-STRESS FLUID DROP IMPACTS ON COATED SURFACES, At. Sprays. 27 (2017) 337–343. doi:10.1615/AtomizSpr.2017017381.

[98] P. Coussot, F. Gaulard, Gravity flow instability of viscoplastic materials: The ketchup drip, Phys. Rev. E. 72 (2005) 31409. doi:10.1103/PhysRevE.72.031409.

[99] G. German, V. Bertola, The free-fall of viscoplastic drops, J. Nonnewton. Fluid Mech. 165 (2010) 825–828. doi:10.1016/j.jnnfm.2010.03.012.

[100] N.M. Wereley, L. Pang, Nondimensional analysis of semi-active electrorheological and magnetorheological dampers using approximate parallel plate models, Smart Mater. Struct. 7 (1999) 732–743. doi:10.1088/0964-1726/7/5/015.

[101] R.E. Corman, L. Rao, N. Ashwin Bharadwaj, J.T. Allison, R.H. Ewoldt, Setting Material Function Design Targets for Linear Viscoelastic Materials and Structures, J. Mech. Des. 138 (2016) 51402. doi:10.1115/1.4032698.

[102] V. Grenard, T. Divoux, N. Taberlet, S. Manneville, Timescales in creep and yielding of attractive gels, Soft Matter. 10 (2014) 1555. doi:10.1039/c3sm52548a.

[103] N.C. Acevedo, A.G. Marangoni, Functionalization of Non-interesterified Mixtures of Fully Hydrogenated Fats Using Shear Processing, Food Bioprocess Technol. 7 (2014) 575–587. doi:10.1007/s11947-013-1110-z.

[104] K.N. Nordstrom, E. Verneuil, P.E. Arratia, A. Basu, Z. Zhang, A.G. Yodh, J.P. Gollub, D.J. Durian, Microfluidic rheology of soft colloids above and below jamming, Phys. Rev. Lett. 105 (2010) 1–4. doi:10.1103/PhysRevLett.105.175701.

[105] M. Cloitre, R. Borrega, F. Monti, L. Leibler, Glassy Dynamics and Flow Properties of Soft Colloidal Pastes, Phys. Rev. Lett. 90 (2003) 68303. doi:10.1103/PhysRevLett.90.068303.

[106] E. Walz, K. Jahnke, M. Holinger, E. Gast, B. Elliot-Litchfield, M. Ludeke, Building Your

Creativity: Tools For Having Ideas and Bringing Them to Be, Stipes Publishing Co., 2016.

[107] C. Chung, B. Degner, D.J. McClements, Rheology and microstructure of bimodal particulate dispersions: Model for foods containing fat droplets and starch granules, Food Res. Int. 48 (2012) 641–649. doi:10.1016/j.foodres.2012.06.011.

[108] M. Zrinyi, Intelligent polymer gels controlled by magnetic fields, Colloid Polym. Sci. 278 (2000) 98–103. doi:10.1007/s003960050017.

[109] H. McGee, On Food and Cooking: The Science and Lore of The Kitchen, Scribner, New York, NY, 2004.

[110] U.T. Gonzenbach, A.R. Studart, E. Tervoort, L.J. Gauckler, Ultrastable particle-stabilized foams, Angew. Chemie - Int. Ed. 45 (2006) 3526–3530. doi:10.1002/anie.200503676.

[111] C. Krämer, M. Schauerte, T.L. Kowald, R.H.F. Trettin, Three-phase-foams for foam concrete application, Mater. Charact. 102 (2015) 173–179. doi:10.1016/j.matchar.2015.03.004.

[112] M. Helgeson, S. Moran, H. An, P. Doyle, Mesoporous organohydrogels from thermogelling photocrosslinkable nanoemulsions, Nat. Mater. 11 (2012) 344–352. doi:10.1038/nmta3248.

[113] E. Dickinson, Emulsion gels: The structuring of soft solids with protein-stabilized oil droplets, Food Hydrocoll. 28 (2012) 224–241. doi:10.1016/j.foodhyd.2011.12.017.

[114] S. Rose, A. Prevoteau, P. Elzière, D. Hourdet, A. Marcellan, L. Leibler, Nanoparticle solutions as adhesives for gels and biological tissues., Nature. 505 (2014) 382–5. doi:10.1038/nature12806.

[115] D. Derks, A. Lindner, C. Creton, D. Bonn, Cohesive failure of thin layers of soft model adhesives under tension, J. Appl. Phys. 93 (2003) 1557–1566. doi:10.1063/1.1533095.

[116] R.H. Ewoldt, P. Tourkine, G.H. McKinley, A.E. Hosoi, Controllable adhesion using field-

activated fluids, Phys. Fluids. 23 (2011) 73104. doi:10.1063/1.3608277.

[117] C.A. Dahlquist, An Investigation into the Nature of Tack, Adhes. Age. 2 (1959) 25.

[118] L. Martinetti, A.M. Mannion, W.E. Voje, R. Xie, R.H. Ewoldt, L.D. Morgret, F.S. Bates, C.W. Macosko, A critical gel fluid with high extensibility: The rheology of chewing gum, J. Rheol. (N. Y. N. Y). 58 (2014) 821–838. doi:10.1122/1.4874322.

[119] A.L. Rutz, K.E. Hyland, A.E. Jakus, W.R. Burghardt, R.N. Shah, A multimaterial bioink method for 3D printing tunable, cell-compatible hydrogels, Adv. Mater. 27 (2015) 1607–1614. doi:10.1002/adma.201405076.

[120] N.P. Suh, Axiomatic Design: Advances and Applications, Oxford University Press, New York, NY, 2001.

[121] J.S. Linsey, I. Tseng, K. Fu, J. Cagan, K.L. Wood, C. Schunn, A Study of Design Fixation, Its Mitigation and Perception in Engineering Design Faculty, J. Mech. Des. 132 (2010) 41003. doi:10.1115/1.4001110.

[122] D.K. Schneiderman, M.A. Hillmyer, Aliphatic Polyester Block Polymer Design, Macromolecules. 49 (2016) 2419–2428. doi:10.1021/acs.macromol.6b00211.

[123] U. Akalp, S.J. Bryant, F.J. Vernerey, Tuning tissue growth with scaffold degradation in enzyme-sensitive hydrogels: a mathematical model, Soft Matter. 12 (2016) 7505–7520. doi:10.1039/c6sm00583g.

[124] N.A. Lynd, F.T. Oyerokun, D.L. O'Donoghue, D.L. Handlin, G.H. Fredrickson, Design of soft and strong thermoplastic elastomers based on nonlinear block copolymer architectures using self-consistent-field theory, Macromolecules. 43 (2010) 3479–3486. doi:10.1021/ma902517v.

[125] R. Budynas, K. Nisbett, Shigley's Mechanical Engineering Design, 10th ed., McGraw-Hill

Education, 2014.

[126] M.F. Ashby, K. Johnson, Materials and Design: The Art and Science of Material Selection in Product Design, 2nd Editio, 2010.

[127] B.M. Kudrowitz, D. Wallace, Assessing the quality of ideas from prolific, early-stage product ideation, J. Eng. Des. 24 (2013) 120–139. doi:10.1080/09544828.2012.676633.

[128] H. Dubberly, How do you design? A Compendium of Models, Dubberly Design Office, 2008.

[129] N.J. Balmforth, N. Dubash, A.C. Slim, Extensional dynamics of viscoplastic filaments: II. Drips and bridges, J. Nonnewton. Fluid Mech. 165 (2010) 1147–1160. doi:10.1016/j.jnnfm.2010.06.004.

[130] J. Boujlel, P. Coussot, Measuring the surface tension of yield stress fluids, Soft Matter. 9 (2013) 5898. doi:10.1039/c3sm50551k.

[131] M. Aytouna, J. Paredes, N. Shahidzadeh-Bonn, S. Moulinet, C. Wagner, Y. Amarouchene, J. Eggers, D. Bonn, Drop formation in non-newtonian fluids, Phys. Rev. Lett. 110 (2013) 1–5. doi:10.1103/PhysRevLett.110.034501.

[132] K. Niedzwiedz, H. Buggisch, N. Willenbacher, Extensional rheology of concentrated emulsions as probed by capillary breakup elongational rheometry (CaBER), Rheol. Acta. 49 (2010) 1103–1116. doi:10.1007/s00397-010-0477-2.

[133] L. Martinie, H. Buggisch, N. Willenbacher, Apparent elongational yield stress of soft matter, J. Rheol. (N. Y. N. Y). 57 (2013) 627. doi:10.1122/1.4789785.

[134] G.H. McKinley, T. Sridhar, Filament-Stretching Rheometry of Complex Fluids, Annu. Rev. Fluid Mech. 34 (2002) 375–415. doi:DOI 10.1146/annurev.fluid.34.083001.125207.

[135] M.L. Sentmanat, Miniature universal testing platform: From extensional melt rheology to

solid-state deformation behavior, Rheol. Acta. 43 (2004) 657–669. doi:10.1007/s00397-004-0405-4.

[136] D.M. Hoyle, S.M. Fielding, Criteria for extensional necking instability in complex fluids and soft solids. Part II imposed tensile stress and force protocols, arXiv. (2016) 1–30. doi:10.1122/1.4965037.

[137] M. Yao, G.H. McKinley, Numerical simulation of extensional deformations of viscoelastic liquid bridges in filament stretching devices, J. Nonnewton. Fluid Mech. 74 (1998) 47–88. doi:10.1016/S0377-0257(97)00052-9.

[138] A.Y. Malkin, C.J.S. Petrie, Some conditions for rupture of polymer liquids in extension, J. Rheol. (N. Y. N. Y). 41 (1997) 1–25. doi:10.1122/1.550881.

[139] P.P. Bhat, S. Appathurai, M.T. Harris, M. Pasquali, G.H. McKinley, O.A. Basaran, Formation of beads-on-a-string structures during break-up of viscoelastic filaments, Nat. Phys. 6 (2010) 625–631. doi:10.1038/nphys1682.

[140] F.J. Galindo-Rosales, J.P. Segovia-Gutiérrez, F.T. Pinho, M.A. Alves, J. de Vicente, Extensional rheometry of magnetic dispersions, J. Rheol. (N. Y. N. Y). 59 (2015) 193–209. doi:10.1122/1.4902356.

[141] M. Sentmanat, High rate extensional flow behavior of confectionery products - objectifying “mouthfeel,” in: Soc. Rheol. Annu. Meet., 2007. http://www.rheology.org/SoR07a/ViewPaper.aspx?ID=154.

[142] G.H. McKinley, A. Tripathi, How to extract the Newtonian viscosity from capillary breakup measurements in a filament rheometer, J. Rheol. (N. Y. N. Y). 44 (2000) 653. doi:10.1122/1.551105.

[143] D. Rees, Basic Engineering Plasticity: An Introducting With Engineering and

Manufacturing Applications, Butterworth-Heinemann, 2012.

[144] M. Considère, Memoire sur l'emploi du fer et de l'acier dans les constructions, Ann. Des Ponts Chausées. 9 (1885) 574.

[145] P.I. Vincent, The necking and cold-drawing of rigid plastics, Polymer (Guildf). 1 (1960) 7–19. doi:10.1016/0032-3861(60)90003-3.

[146] J.W. Hutchinson, H. Obrecht, Tensile Instabilities in Strain-Rate Dependent Materials, Fracture. 1 (1977).

[147] G.H. McKinley, O. Hassager, The Considère condition and rapid stretching of linear and branched polymer melts, J. Rheol. (N. Y. N. Y). 43 (1999) 1195–1212. doi:10.1122/1.551034.

[148] R.C. Hibbeler, Mechanics of Materials, Pearson Prentice hall, 2014.

[149] G.F. Biehn, M.L. Ernsberger, Polyvinyl Alcohol as an Emulsifying Agent, Ind. Eng. Chem. 40 (1948) 1449–1453. doi:10.1021/ie50464a024.

[150] A. Sanz, I. Martinez, Minimum volume for a liquid bridge between equal disks, J. Colloid Interface Sci. 93 (1983) 235–240. doi:10.1016/0021-9797(83)90401-0.

[151] K.L. Maki, Y. Renardy, The dynamics of a viscoelastic fluid which displays thixotropic yield stress behavior, J. Nonnewton. Fluid Mech. 181–182 (2012) 30–50. doi:10.1016/j.jnnfm.2012.06.007.

[152] Y. Renardy, H. V Grant, Erratum: "Stretch and hold: The dynamics of a filament governed by a viscoelastic constitutive model with thixotropic yield stress behavior" [Phys. Fluids 28(5) 053104 (2016)], Phys. Fluids. 28 (2016) 89902. doi:10.1063/1.4960578.

[153] D. Gómez-Díaz, J.M. Navaza, L.C. Quintáns-Riveiro, Effect of Temperature on the Viscosity of Honey, Int. J. Food Prop. 12 (2009) 396–404.

doi:10.1080/10942910701813925.

[154] R.R. Myers, J.C. Miller, A.. Zettlemoyer, The splitting of thin liquid films. Kinematics, J. Colloid Sci. 14 (1959) 287–299. doi:10.1016/0095-8522(59)90053-4.

[155] C. Gay, L. Leibler, On Stickiness, Phys. Today. 82 (1999) 48–52.

[156] T. Svitova, O. Theodoly, S. Christiano, R.M. Hill, C.J. Radke, Wetting Behavior of Silicone Oils on Solid Substrates Immersed in Aqueous Electrolyte Solutions, Langmuir. 18 (2002) 6821–6829. doi:10.1021/la020006x.

[157] F.J. Galindo-Rosales, M.A. Alves, M.S.N. Oliveira, Microdevices for extensional rheometry of low viscosity elastic liquids: a review, Microfluid. Nanofluidics. 14 (2013) 1–19. doi:10.1007/s10404-012-1028-1.

[158] S.L. Anna, G.H. McKinley, Elasto-capillary thinning and breakup of model elastic liquids, J. Rheol. (N. Y. N. Y). 45 (2001) 115–138. doi:10.1122/1.1332389.

[159] T. ul Islam, P.S. Gandhi, Viscous Fingering in Multiport Hele Shaw Cell for Controlled Shaping of Fluids, Sci. Rep. 7 (2017) 16602. doi:10.1038/s41598-017-16830-3.

[160] G. Laput, X. “Anthony” Chen, C. Harrison, 3D Printed Hair, in: Proc. 28th Annu. ACM Symp. User Interface Softw. Technol. - UIST ’15, ACM Press, New York, New York, USA, 2015: pp. 593–597. doi:10.1145/2807442.2807484.

[161] I.D. Robertson, M. Yourdkhani, P.J. Centellas, J.E. Aw, D.G. Ivanoff, E. Goli, E.M. Lloyd, L.M. Dean, N.R. Sottos, P.H. Geubelle, J.S. Moore, S.R. White, Rapid energy-efficient manufacturing of polymers and composites via frontal polymerization, Nature. Accepted (2018).

[162] A. Sydney Gladman, E.A. Matsumoto, R.G. Nuzzo, L. Mahadevan, J.A. Lewis, Biomimetic 4D printing, Nat. Mater. 15 (2016) 413–418. doi:10.1038/nmat4544.

[163] M. Wehner, R.L. Truby, D.J. Fitzgerald, B. Mosadegh, G.M. Whitesides, J.A. Lewis, R.J. Wood, An integrated design and fabrication strategy for entirely soft, autonomous robots, Nature. 536 (2016) 451–455. doi:10.1038/nature19100.

[164] S.J. Song, J. Choi, Y.D. Park, S. Hong, J.J. Lee, C.B. Ahn, H. Choi, K. Sun, Sodium Alginate Hydrogel-Based Bioprinting Using a Novel Multinozzle Bioprinting System, Artif. Organs. 35 (2011) 1132–1136. doi:10.1111/j.1525-1594.2011.01377.x.

[165] A.D. Valentine, T.A. Busbee, J.W. Boley, J.R. Raney, A. Chortos, A. Kotikian, J.D. Berrigan, M.F. Durstock, J.A. Lewis, Hybrid 3D Printing of Soft Electronics, Adv. Mater. 29 (2017) 1–8. doi:10.1002/adma.201703817.

[166] E. Feilden, E.G.T. Blanca, F. Giuliani, E. Saiz, L. Vandeperre, Robocasting of structural ceramic parts with hydrogel inks, J. Eur. Ceram. Soc. 36 (2016) 2525–2533. doi:10.1016/j.jeurceramsoc.2016.03.001.

[167] J. Zhong, G.X. Zhou, P.G. He, Z.H. Yang, D.C. Jia, 3D printing strong and conductive geo-polymer nanocomposite structures modified by graphene oxide, Carbon N. Y. 117 (2017) 421–426. doi:10.1016/j.carbon.2017.02.102.

[168] Y. Shao, D. Chaussy, P. Grosseau, D. Beneventi, Use of Microfibrillated Cellulose/Lignosulfonate Blends as Carbon Precursors: Impact of Hydrogel Rheology on 3D Printing, Ind. Eng. Chem. Res. 54 (2015) 10575–10582. doi:10.1021/acs.iecr.5b02763.

[169] Y. Zhang, J.R.G. Evans, Morphologies developed by the drying of droplets containing dispersed and aggregated layered double hydroxide platelets, J. Colloid Interface Sci. 395 (2013) 11–17. doi:10.1016/j.jcis.2012.09.089.

[170] K. Sun, T.S. Wei, B.Y. Ahn, J.Y. Seo, S.J. Dillon, J.A. Lewis, 3D printing of interdigitated Li-ion microbattery architectures, Adv. Mater. 25 (2013) 4539–4543.

doi:10.1002/adma.201301036.

[171] K. Cai, J. Sun, Q. Li, R. Wang, B. Li, J. Zhou, Direct-writing construction of layered meshes from nanoparticles-vaseline composite inks: Rheological properties and structures, Appl. Phys. A Mater. Sci. Process. 102 (2011) 501–507. doi:10.1007/s00339-010-5955-y.

[172] J.T. Muth, D.M. Vogt, R.L. Truby, Y. Mengüç, D.B. Kolesky, R.J. Wood, J.A. Lewis, Embedded 3D printing of strain sensors within highly stretchable elastomers, Adv. Mater. 26 (2014) 6307–6312. doi:10.1002/adma.201400334.

[173] C. Minas, D. Carnelli, E. Tervoort, A.R. Studart, 3D Printing of Emulsions and Foams into Hierarchical Porous Ceramics, Adv. Mater. 28 (2016) 9993–9999. doi:10.1002/adma.201603390.

[174] J.T. Muth, P.G. Dixon, L. Woish, L.J. Gibson, J.A. Lewis, Architected cellular ceramics with tailored stiffness via direct foam writing, Proc. Natl. Acad. Sci. 114 (2017) 1832–1837. doi:10.1073/pnas.1616769114.

[175] G. Siqueira, D. Kokkinis, R. Libanori, M.K. Hausmann, A.S. Gladman, A. Neels, P. Tingaut, T. Zimmermann, J.A. Lewis, A.R. Studart, Cellulose Nanocrystal Inks for 3D Printing of Textured Cellular Architectures, Adv. Funct. Mater. 27 (2017). doi:10.1002/adfm.201604619.

[176] J.O. Hardin, T.J. Ober, A.D. Valentine, J.A. Lewis, Microfluidic printheads for multimaterial 3D printing of viscoelastic inks, Adv. Mater. 27 (2015) 3279–3284. doi:10.1002/adma.201500222.

[177] J.N. Hanson Shepherd, S.T. Parker, R.F. Shepherd, M.U. Gillette, J.A. Lewis, R.G. Nuzzo, 3D microperiodic hydrogel scaffolds for robust neuronal cultures, Adv. Funct. Mater. 21 (2011) 47–54. doi:10.1002/adfm.201001746.

[178] V. Vogel, M. Sheetz, Local force and geometry sensing regulate cell functions, Nat. Rev. Mol. Cell Biol. 7 (2006) 265–275. doi:10.1038/nrm1890.

[179] A.M. Pekkanen, R.J. Mondschein, C.B. Williams, T.E. Long, 3D Printing Polymers with Supramolecular Functionality for Biological Applications, Biomacromolecules. 18 (2017) 2669–2687. doi:10.1021/acs.biomac.7b00671.

[180] A. Badea, J.M. McCracken, E.G. Tillmaand, M.E. Kandel, A.W. Oraham, M.B. Mevis, S.S. Rubakhin, G. Popescu, J. V. Sweedler, R.G. Nuzzo, 3D-Printed pHEMA Materials for Topographical and Biochemical Modulation of Dorsal Root Ganglion Cell Response, ACS Appl. Mater. Interfaces. 9 (2017) 30318–30328. doi:10.1021/acsami.7b06742.

[181] Y. Gai, J.W. Khor, S.K.Y. Tang, Confinement and viscosity ratio effect on droplet break-up in a concentrated emulsion flowing through a narrow constriction, Lab Chip. 16 (2016) 3058–3064. doi:10.1039/C6LC00478D.

[182] M.N. Jones, The interaction of sodium dodecyl sulfate with polyethylene oxide, J. Colloid Interface Sci. 23 (1967) 36–42. doi:10.1016/0021-9797(67)90082-3.

[183] E.J. Park, J.K. Sim, M.-G. Jeong, H.O. Seo, Y.D. Kim, Transparent and superhydrophobic films prepared with polydimethylsiloxane-coated silica nanoparticles, RSC Adv. 3 (2013) 12571. doi:10.1039/c3ra42402b.

[184] N.S. Tomer, F. Delor-Jestin, L. Frezet, J. Lacoste, Oxidation, Chain Scission and Cross-Linking Studies of Polysiloxanes upon Ageings, Open J. Org. Polym. Mater. 2 (2012) 13–22. doi:10.4236/ojopm.2012.22003.

[185] D. Xu, L. Sun, H. Li, L. Zhang, G. Guo, X. Zhao, L. Gui, Hydrolysis and silanization of the hydrosilicon surface of freshly prepared porous silicon by an amine catalytic reaction, New J. Chem. 27 (2003) 300–306. doi:10.1039/b204359a.

[186] B.C. Smith, Infrared Spectral Interpretation: A Systematic Approach, CRC Press, Boca Raton, FL, 1998.

[187] L. Rösch, P. John, R. Reitmeier, Silicon Compounds, Organic, in: Ullmann's Encycl. Ind. Chem., Wiley-VCH Verlag GmbH & Co. KGaA, Weinheim, Germany, 2000. doi:10.1002/14356007.a24_021.

[188] Z. Wang, A.A. Volinsky, N.D. Gallant, Crosslinking effect on polydimethylsiloxane elastic modulus measured by custom-built compression instrument, J. Appl. Polym. Sci. 131 (2014). doi:10.1002/app.41050.

[189] M.R. Sommer, L. Alison, C. Minas, E. Tervoort, P.A. Rühs, A.R. Studart, 3D printing of concentrated emulsions into multiphase biocompatible soft materials, Soft Matter. 13 (2017) 1794–1803. doi:10.1039/C6SM02682F.

[190] S. Kawaguchi, G. Imai, J. Suzuki, A. Miyahara, T. Kitano, K. Ito, Aqueous solution properties of oligo- and poly(ethylene oxide) by static light scattering and intrinsic viscosity, Polymer (Guildf). 38 (1997) 2885–2891. doi:10.1016/S0032-3861(96)00859-2.

[191] V. Ramesh Babu, M. Sairam, K.M. Hosamani, T.M. Aminabhavi, Preparation of sodium alginate-methylcellulose blend microspheres for controlled release of nifedipine, Carbohydr. Polym. 69 (2007) 241–250. doi:10.1016/j.carbpol.2006.09.027.

[192] E. Touitou, M. Donbrow, Influence of additives on (hydroxyethyl) methylcellulose properties: relation between gelation temperature change, compressed matrix integrity and drug release profile, Int. J. Pharm. 11 (1982) 131–148. doi:10.1016/0378-5173(82)90049-7.

[193] K. Mitchell, J.L. Ford, D.J. Armstrong, P.N.C. Elliott, C. Rostron, J.E. Hogan, The influence of concentration on the release of drugs from gels and matrices containing

Methocel, Int. J. Pharm. 100 (1993) 155–163. doi:10.1016/0378-5173(93)90086-U.

[194] D.A. Bell, Methylcellulose as a structure enhancer in bread baking, Cereal Foods World. 35 (1990) 1001–1006.

[195] T. Sanz, A. Salvador, G. Vélez, J. Muñoz, S.M. Fiszman, Influence of ingredients on the thermo-rheological behaviour of batters containing methylcellulose, Food Hydrocoll. 19 (2005) 869–877. doi:10.1016/j.foodhyd.2004.11.003.

[196] J. Bousquières, C. Michon, C. Bonazzi, Functional properties of cellulose derivatives to tailor a model sponge cake using rheology and cellular structure analysis, Food Hydrocoll. 70 (2017) 304–312. doi:10.1016/j.foodhyd.2017.04.010.

[197] M.R. Du, H.W. Jing, W.H. Duan, G.S. Han, S.J. Chen, Methylcellulose stabilized multi-walled carbon nanotubes dispersion for sustainable cement composites, Constr. Build. Mater. 146 (2017) 76–85. doi:10.1016/j.conbuildmat.2017.04.029.

[198] F.K. Akthar, J.R.G. Evans, High porosity (> 90%) cementitious foams, Cem. Concr. Res. 40 (2010) 352–358. doi:10.1016/j.cemconres.2009.10.012.

[199] A. Pinotti, M.A. García, M.N. Martino, N.E. Zaritzky, Study on microstructure and physical properties of composite films based on chitosan and methylcellulose, Food Hydrocoll. 21 (2007) 66–72. doi:10.1016/j.foodhyd.2006.02.001.

[200] M.-C. CHEN, G.H.-C. YEH, B.-H. CHIANG, Antimicrobial and Physicochemical Properties of Methylcellulose and Chitosan Films Containing a Preservative, J. Food Process. Preserv. 20 (1996) 379–390. doi:10.1111/j.1745-4549.1996.tb00754.x.

[201] M.A. Mingsukang, M.H. Buraidah, M.A. Careem, I. Albinsson, B.E. Mellander, A.K. Arof, Investigation of counter electrode materials for gel polymer electrolyte based quantum dot sensitized solar cells, Electrochim. Acta. 241 (2017) 487–496.

doi:10.1016/j.electacta.2017.04.151.

[202] B.C. Church, T.H. Sanders, R.F. Speyer, J.K. Cochran, Thermal expansion matching and oxidation resistance of Fe-Ni-Cr interconnect alloys, Mater. Sci. Eng. A. 452–453 (2007) 334–340. doi:10.1016/j.msea.2006.10.149.

[203] J. Pusz, A. Smirnova, A. Mohammadi, N.M. Sammes, Fracture strength of micro-tubular solid oxide fuel cell anode in redox cycling experiments, J. Power Sources. 163 (2007) 900–906. doi:10.1016/j.jpowsour.2006.09.074.

[204] D.K. Bhui, A. Misra, Synthesis of worm like silver nanoparticles in methyl cellulose polymeric matrix and its catalytic activity, Carbohydr. Polym. 89 (2012) 830–835. doi:10.1016/j.carbpol.2012.04.017.

[205] D.K. Bhui, S. Pyne, P. Sarkar, H. Bar, G.P. Sahoo, A. Misra, Temperature controlled synthesis of silver nanostructures of variable morphologies in aqueous methyl cellulose matrix, J. Mol. Liq. 158 (2011) 170–174. doi:10.1016/j.molliq.2010.11.014.

[206] M. Ogawa, R.T. Parmley, B.L. Harvely, S.S. Spicer, Human Marrow Erythropoiesis in Culture. I. Characterization of Methylcellulose Colony Assay, Blood. 48 (1976) 407–417.

[207] S. Goldblum, Y.-K. Bae, W.F. Hink, J. Chalmers, Protective Effect of Methylcellulose and Other Polymers on Insect Cells Subjected to Laminar Shear Stress, Biotechnol. Prog. 6 (1990) 383–390. doi:10.1021/bp00005a011.

[208] L. Yang, M.H. Soonpaa, E.D. Adler, T.K. Roepke, S.J. Kattman, M. Kennedy, E. Henckaerts, K. Bonham, G.W. Abbott, R.M. Linden, L.J. Field, G.M. Keller, Human cardiovascular progenitor cells develop from a KDR+ embryonic-stem-cell-derived population, Nature. 453 (2008) 524–528. doi:10.1038/nature06894.

[209] N. Sarkar, Thermal gelation properties of methyl and hydroxypropyl methylcellulose, J.

Appl. Polym. Sci. 24 (1979) 1073–1087. doi:10.1002/app.1979.070240420.

[210] J.R. Lott, J.W. McAllister, S.A. Arvidson, F.S. Bates, T.P. Lodge, Fibrillar structure of methylcellulose hydrogels, Biomacromolecules. 14 (2013) 2484–2488. doi:10.1021/bm400694r.

[211] J.R. Lott, J.W. McAllister, M. Wasbrough, R.L. Sammler, F.S. Bates, T.P. Lodge, Fibrillar Structure in Aqueous Methylcellulose Solutions and Gels, Macromolecules. 46 (2013) 9760–9771. doi:10.1021/ma4021642.

[212] S. a. Arvidson, J.R. Lott, J.W. McAllister, J. Zhang, F.S. Bates, T.P. Lodge, R.L. Sammler, Y. Li, M. Brackhagen, Interplay of phase separation and thermoreversible gelation in aqueous methylcellulose solutions, Macromolecules. 46 (2013) 300–309. doi:10.1021/ma3019359.

[213] J.P.A. Fairclough, H. Yu, O. Kelly, A.J. Ryan, R.L. Sammler, M. Radler, Interplay between gelation and phase separation in aqueous solutions of methylcellulose and hydroxypropylmethylcellulose, Langmuir. 28 (2012) 10551–10557. doi:10.1021/la300971r.

[214] A. Haque, E.R. Morris, Thermogelation of methylcellulose. Part I: molecular structures and processes, Carbohydr. Polym. 22 (1993) 161–173. doi:10.1016/0144-8617(93)90137-S.

[215] C. Clasen, W.M. Kulicke, Determination of viscoelastic and rheo-optical material functions of water-soluble cellulose derivatives, Prog. Polym. Sci. 26 (2001) 1839–1919. doi:10.1016/S0079-6700(01)00024-7.

[216] J.W. McAllister, J.R. Lott, P.W. Schmidt, R.L. Sammler, F.S. Bates, T.P. Lodge, Linear and Nonlinear Rheological Behavior of Fibrillar Methylcellulose Hydrogels, ACS Macro Lett. 4 (2015) 538–542. doi:10.1021/acsmacrolett.5b00150.

[217] T. Chatterjee, A.I. Nakatani, R. Adden, M. Brackhagen, D. Redwine, H. Shen, Y. Li, T. Wilson, R.L. Sammler, Structure and properties of aqueous methylcellulose gels by small-angle neutron scattering, Biomacromolecules. 13 (2012) 3355–3369. doi:10.1021/bm301123a.

[218] T. Kato, M. Yokoyama, A. Takahashi, Melting temperatures of thermally reversible gels IV. Methyl cellulose-water gels, Colloid Polym. Sci. 256 (1978) 15–21. doi:10.1007/BF01746686.

[219] R. Bayer, M. Knarr, Thermal precipitation or gelling behaviour of dissolved methylcellulose (MC) derivatives-Behaviour in water and influence on the extrusion of ceramic pastes. Part 1: Fundamentals of MC-derivatives, J. Eur. Ceram. Soc. 32 (2012) 1007–1018. doi:10.1016/j.jeurceramsoc.2011.11.025.

[220] K. Kobayashi, C. Huang, T.P. Lodge, Thermoreversible Gelation of Aqueous Methylcellulose Solutions, Macromolecules. 32 (1999) 7070–7077. doi:10.1021/ma990242n.

[221] J.W. McAllister, P.W. Schmidt, K.D. Dorfman, T.P. Lodge, F.S. Bates, Thermodynamics of Aqueous Methylcellulose Solutions, Macromolecules. 48 (2015) 7205–7215. doi:10.1021/acs.macromol.5b01544.

[222] V. V. Ginzburg, R.L. Sammler, W. Huang, R.G. Larson, Anisotropic self-assembly and gelation in aqueous methylcellulose-theory and modeling, J. Polym. Sci. Part B Polym. Phys. 54 (2016) 1624–1636. doi:10.1002/polb.24065.

[223] M. Knarr, R. Bayer, The shear dependence of the methylcellulose gelation phenomena in aqueous solution and in ceramic paste, Carbohydr. Polym. 111 (2014) 80–88. doi:10.1016/j.carbpol.2014.04.078.

[224] J. Vermant, M.J. Solomon, Flow-induced structure in colloidal suspensions, J. Phys. Condens. Matter. 17 (2005) 187–216. doi:10.1088/0953-8984/17/4/R02.

[225] F.R. Lupi, D. Gabriele, B. de Cindio, Effect of Shear Rate on Crystallisation Phenomena in Olive Oil-Based Organogels, Food Bioprocess Technol. 5 (2012) 2880–2888. doi:10.1007/s11947-011-0619-2.

[226] S. Da Pieve, S. Calligaris, E. Co, M.C. Nicoli, A.G. Marangoni, Shear Nanostructuring of Monoglyceride Organogels, Food Biophys. 5 (2010) 211–217. doi:10.1007/s11483-010-9162-3.

[227] F.M. Alvarez-Mitre, J.A. Morales-Rueda, E. Dibildox-Alvarado, M.A. Charó-Alonso, J.F. Toro-Vazquez, Shearing as a variable to engineer the rheology of candelilla wax organogels, Food Res. Int. 49 (2012) 580–587. doi:10.1016/j.foodres.2012.08.025.

[228] M. Chopin-Doroteo, J.A. Morales-Rueda, E. Dibildox-Alvarado, M.A. Charó-Alonso, A. de la Peña-Gil, J.F. Toro-Vazquez, The Effect of Shearing in the Thermo-mechanical Properties of Candelilla Wax and Candelilla Wax-Tripalmitin Organogels, Food Biophys. 6 (2011) 359–376. doi:10.1007/s11483-011-9212-5.

[229] W. Carvalho, M. Djabourov, Physical gelation under shear for gelatin gels, Rheol. Acta. 36 (1997) 591–609. doi:10.1007/BF00367355.

[230] R. Campos, A.G. Marangoni, Crystallization dynamics of shear worked cocoa butter, Cryst. Growth Des. 14 (2014) 1199–1210. doi:10.1021/cg4017273.

[231] N. Badiei, A.M. Sowedan, D.J. Curtis, M.R. Brown, M.J. Lawrence, A.I. Campbell, A. Sabra, P.A. Evans, J.W. Weisel, I.N. Chernysh, C. Nagaswami, P.R. Williams, K. Hawkins, Effects of unidirectional flow shear stresses on the formation, fractal microstructure and rigidity of incipient whole blood clots and fibrin gels, Clin. Hemorheol. Microcirc. 60

(2015) 451–464. doi:10.3233/CH-151924.

[232] Y. Li, H. Shen, J.W. Lyons, R.L. Sammler, M. Brackhagen, D.M. Meunier, Size-exclusion chromatography of ultrahigh molecular weight methylcellulose ethers and hydroxypropyl methylcellulose ethers for reliable molecular weight distribution characterization, Carbohydr. Polym. 138 (2016) 290–300. doi:10.1016/j.carbpol.2015.11.003.

[233] U.S.P. and N. Formulary, Methylcellulose, in: United States Pharmacop. Natl. Formul., United Book Press, Inc, Baltimore, MD, 2012: pp. 3868–3869.

[234] G.G. Fuller, Optical Rheometry of Complex Fluids, Oxford University Press, New York, 1995.

[235] A.P.R. Eberle, L. Porcar, Flow-SANS and Rheo-SANS applied to soft matter, Curr. Opin. Colloid Interface Sci. 17 (2012) 33–43. doi:10.1016/j.cocis.2011.12.001.

[236] S.K. Dutta, A. Mbi, R.C. Arevalo, D.L. Blair, Development of a confocal rheometer for soft and biological materials, Rev. Sci. Instrum. 84 (2013). doi:10.1063/1.4810015.

[237] G. Colombo, J. Vermant, High speed confocal imaging of sheared colloidal gels, in: Soc. Rheol. Annu. Meet., 2017. https://www.rheology.org/sor17a/ViewPaper?ID=143.

[238] H.H. Winter, F. Chambon, Analysis of Linear Viscoelasticity of a Crosslinking Polymer at the Gel Point, J. Rheol. (N. Y. N. Y). 30 (1986) 367–382. doi:10.1122/1.549853.

[239] F. Chambon, H.H. Winter, Linear Viscoelasticity at the Gel Point of a Crosslinking PDMS with Imbalanced Stoichiometry, J. Rheol. (N. Y. N. Y). 31 (1987) 683–697. doi:10.1122/1.549955.

[240] J. Desbrières, M. Hirrien, S.B. Ross-Murphy, Thermogelation of methylcellulose: Rheological considerations, Polymer (Guildf). 41 (2000) 2451–2461. doi:10.1016/S0032-3861(99)00413-9.

[241] B. Stoeber, Z. Yang, D. Liepmann, S.J. Muller, Flow control in microdevices using thermally responsive triblock copolymers, J. Microelectromechanical Syst. 14 (2005) 207–213. doi:10.1109/JMEMS.2004.839330.

[242] R.H. Ewoldt, Defining nonlinear rheological material functions for oscillatory shear, J. Rheol. (N. Y. N. Y). 57 (2013) 177–195. doi:10.1122/1.4764498.

[243] G. Colombo, S. Kim, T. Schweizer, B. Schroyen, C. Clasen, J. Mewis, J. Vermant, Superposition rheology and anisotropy in rheological properties of sheared colloidal gels, J. Rheol. (N. Y. N. Y). 61 (2017) 1035–1048. doi:10.1122/1.4998176.

[244] M.F. Ashby, Materials and Sustainable Development, Butterworth-Heinemann, Oxford, 2014.

[245] X. Zhang, O. Fadoul, E. Lorenceau, P. Coussot, Yielding and Flow of Soft-Jammed Systems in Elongation, Phys. Rev. Lett. 120 (2018) 48001. doi:10.1103/PhysRevLett.120.048001.

Appendix A:
Supplementary Information for Chapter 2

A.1 Detailed Rheological Data

Figures A.1 through A.6 depict the repeated experiments for each material formulation with uncorrected values of stress (see Section 2.3 for formulation and correction specifics). For each formulation, a representative data set was corrected and validated for lack of slip with an experiment performed at a smaller gap (500 μm). Comparisons of corrected data at the two tested gaps are shown in Figures A.7 through A.12. In the case of the emulsions, at a smaller gap, the measured stress can be significantly higher; this can be attributed to a confinement effect, where the suspended droplets are more tightly packed at the smaller gap. In no cases is the measured stress at the small gap smaller than at the larger gap (outside of the experimental error from repeat experiments). Therefore, we have no evidence of slip occurring for any of the formulations shown.

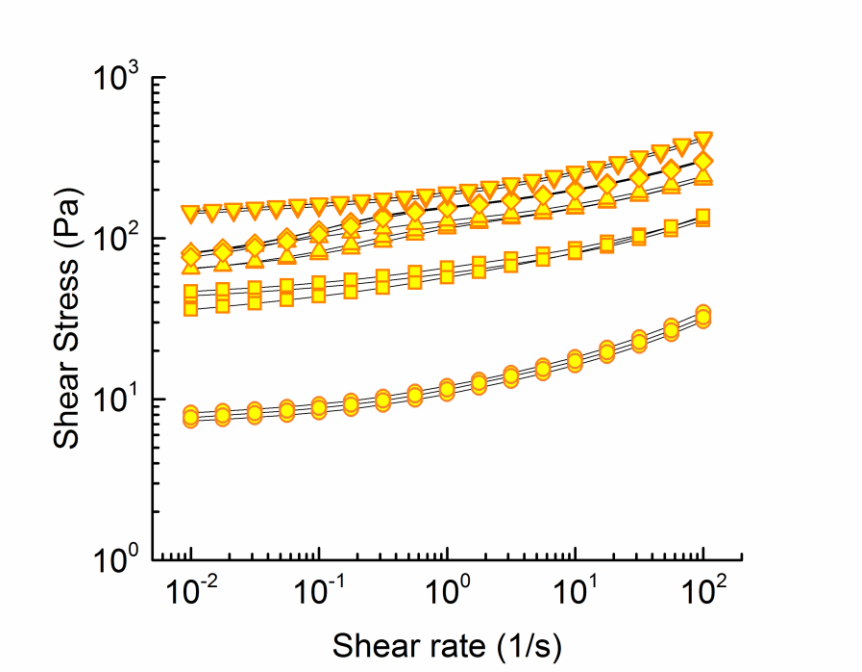

Figure A.1. Uncorrected, repeat, steady state, simple shear flow experiments from high to low rate for Carbopol of 0.1, 0.15, 0.2, 0.25, 0.5 %wt. Each symbol type corresponds to a particular concentration. A higher concentration increases the yield stress.

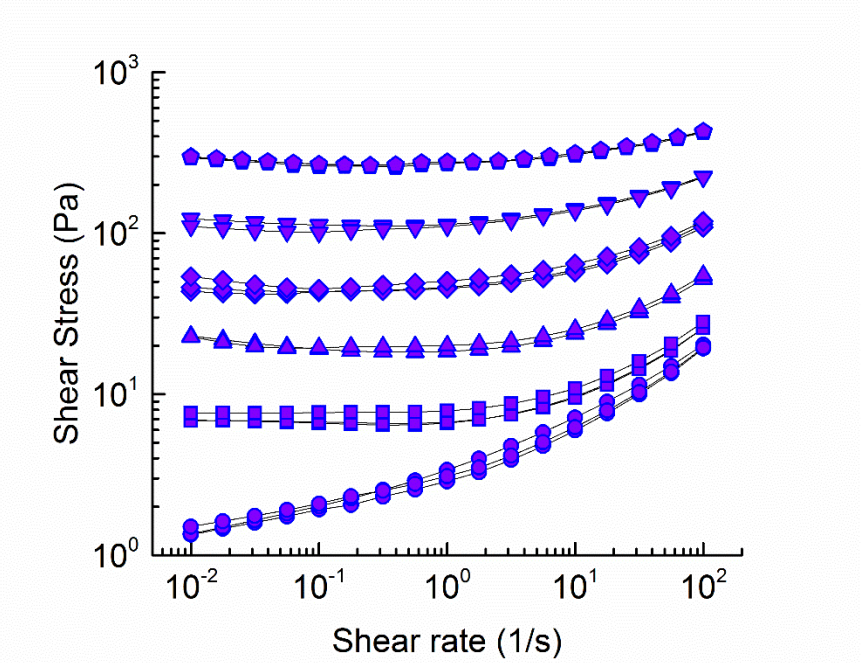

Figure A.2. Uncorrected, repeat, steady state, simple shear flow experiments from high to low rate for Bentonite of 7, 8, 9, 10, 11, 12 %wt. Each symbol type corresponds to a particular concentration. A higher concentration increases the yield stress.

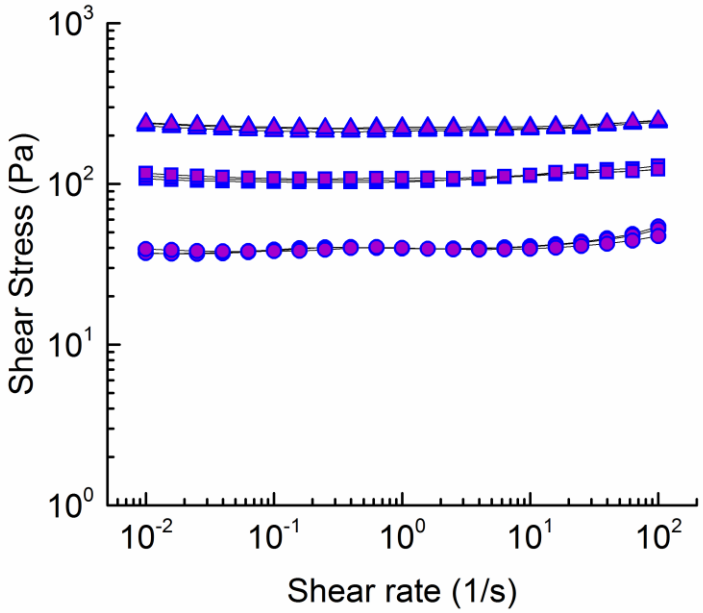

Figure A.3. Uncorrected, repeat, steady state, simple shear flow experiments from high to low rate for Laponite of 3, 4, 5 %wt. Each symbol type corresponds to a particular concentration. A higher concentration increases the yield stress.

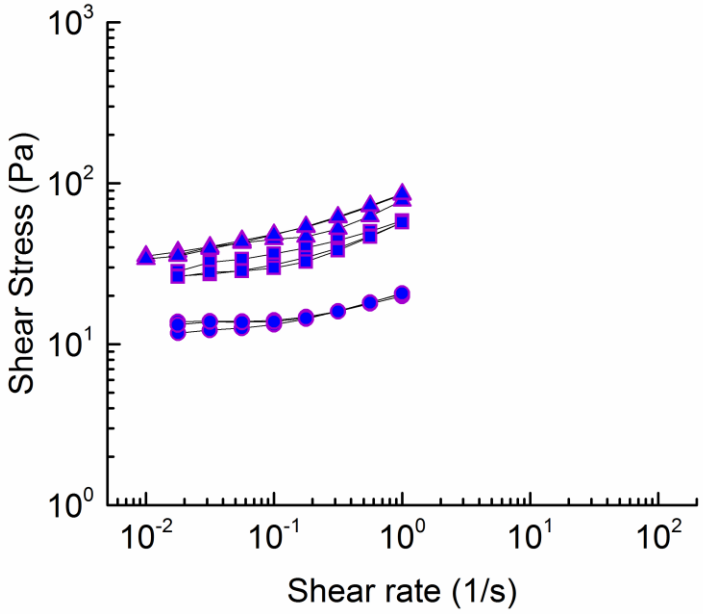

Figure A.4. Uncorrected, repeat, steady state, simple shear flow experiments from low to high rate for Xanthan Gum of 2, 4, 5 %wt. Each symbol type corresponds to a particular concentration. A higher concentration increases the yield stress.

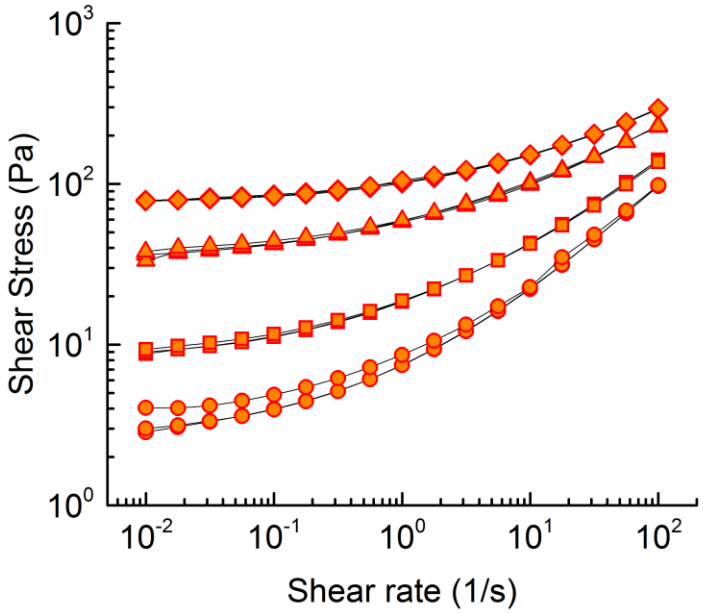

Figure A.5. Uncorrected, repeat, steady state,simple shear flow experiments from high to low rate for silicone oil-in-water emulsions of 65, 70, 75, 80 %wt oil. Each symbol type corresponds to a particular concentration. A higher concentration increases the yield stress.

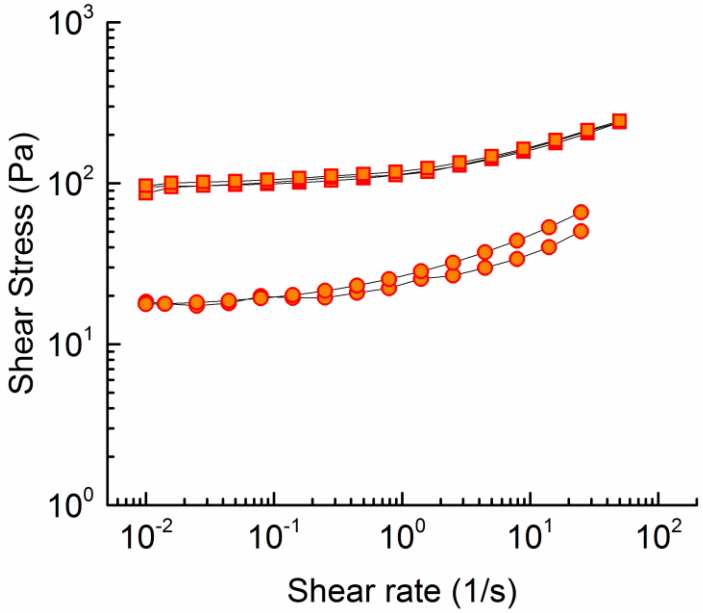

Figure A.6. Uncorrected, repeat, steady state, simple shear flow experiments from high to low rate for mineral oil-in-water emulsions of 65, 75 %wt oil. Each symbol type corresponds to a particular concentration. A higher concentration increases the yield stress.

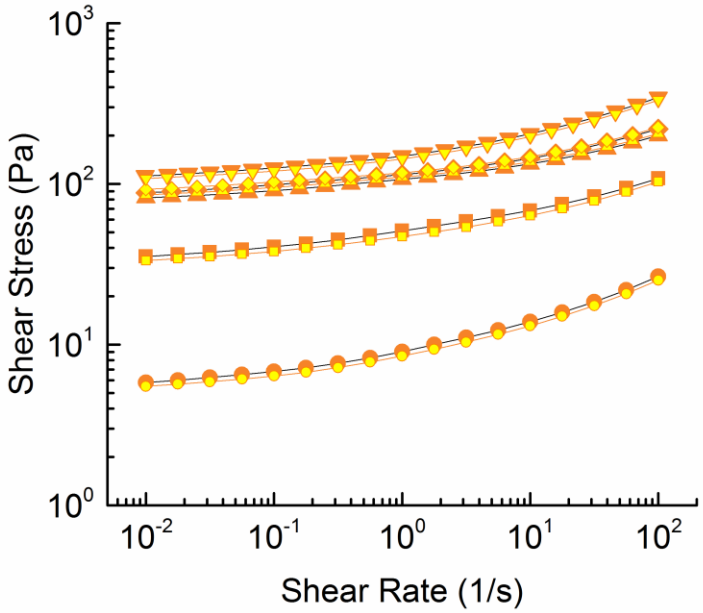

Figure A.7. Corrected, steady state, simple shear flow experiments from high to low rate for Carbopol of 0.1, 0.15, 0.2, 0.25, 0.5 %wt at different gap heights. The small yellow symbols are for a gap of 1000μm, the large orange symbols are for a gap of 500μm. Each symbol type corresponds to a particular concentration. A higher concentration increases the yield stress.

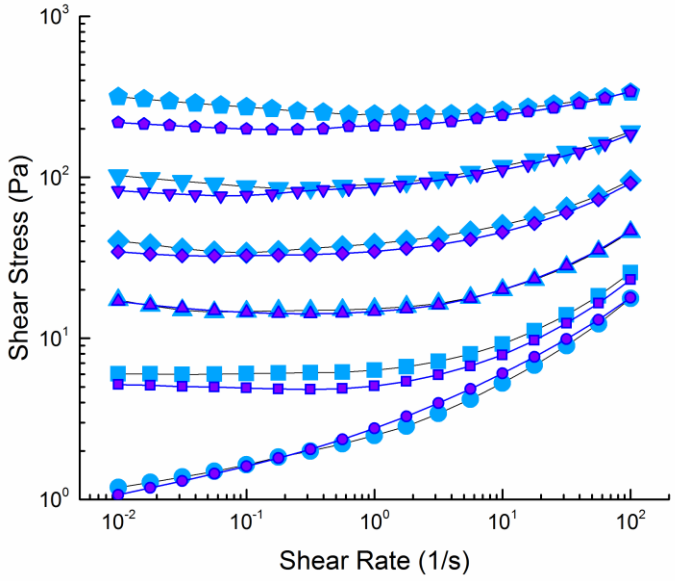

Figure A.8. Corrected, steady state, simple shear flow experiments from high to low rate for Bentonite of 7, 8, 9, 10, 11, 12 %wt at different gap heights. The small purple symbols are for a gap of 1000μm, the large blue symbols are for a gap of 500μm. Each symbol type corresponds to a particular concentration. A higher concentration increases the yield stress.

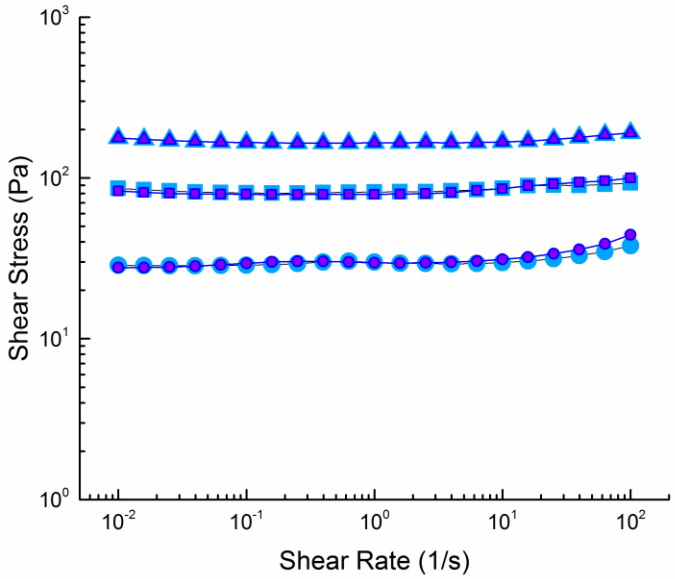

Figure A.9. Corrected, steady state, simple shear flow experiments from high to low rate for Laponite of 3, 4, 5 %wt at different gap heights. The small purple symbols are for a gap of 1000μm, the large blue symbols are for a gap of 500μm. Each symbol type corresponds to a particular concentration. A higher concentration increases the yield stress.

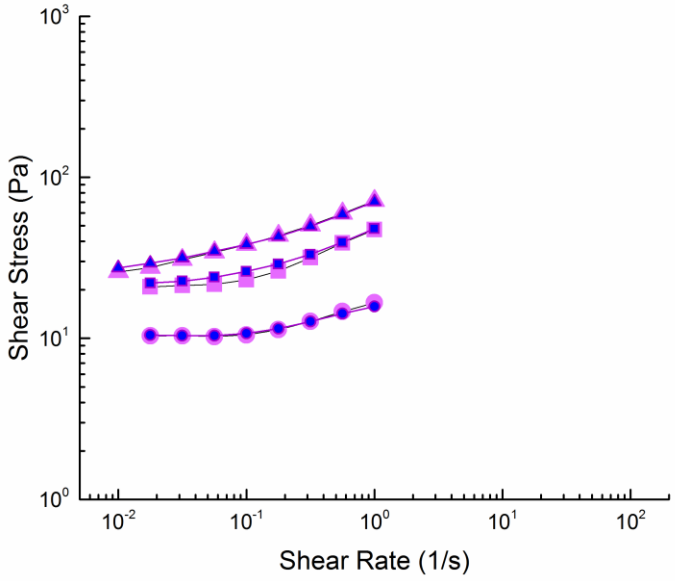

Figure A.10. Corrected, steady state, simple shear flow experiments from low to high rate for Xanthan Gum at 2, 4, 5 %wt at different gap heights. The small blue symbols are for a gap of 1000μm, the large magenta symbols are for a gap of 500μm. Each symbol type corresponds to a particular concentration. A higher concentration increases the yield stress.

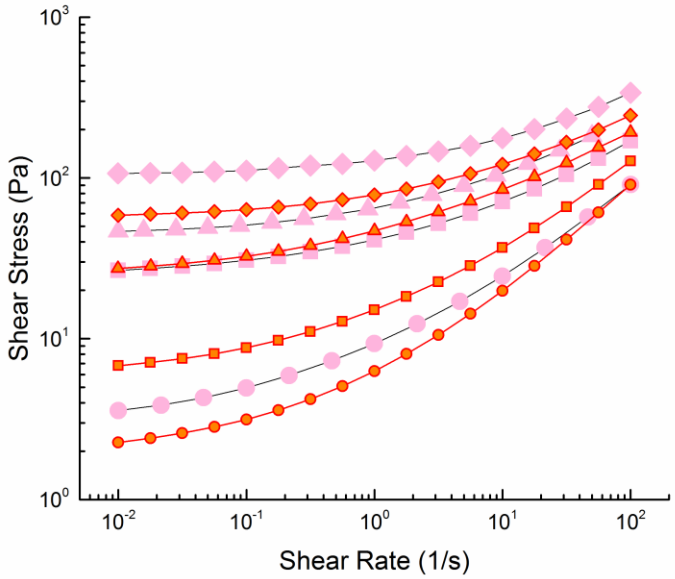

Figure A.11. Corrected, steady state, simple shear flow experiments from high to low rate for silicone oil-in-water emulsions of 65, 70, 75, 80 %wt at different gap heights. The small orange symbols are for a gap of 1000μm, the large pink symbols are for a gap of 500μm. Each symbol type corresponds to a particular concentration. A higher concentration increases the yield stress. Higher stresses at the smaller gap indicate a confinement effect.

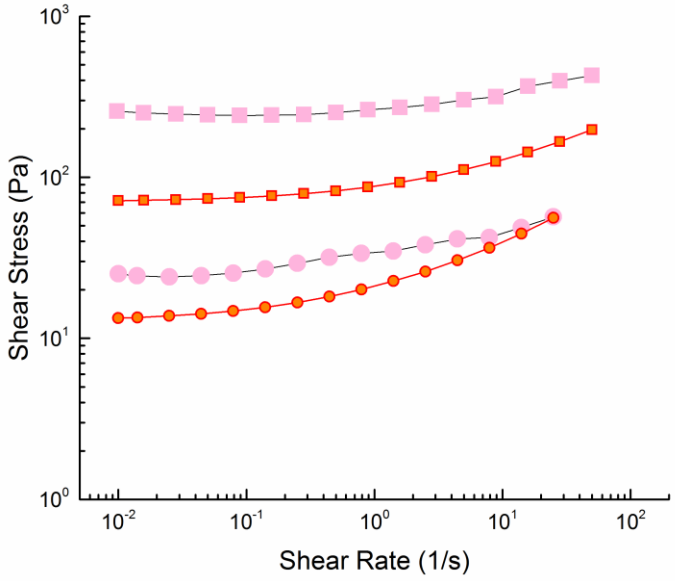

Figure A.12. Corrected, steady state, simple shear flow experiments from high to low rate for mineral oil-in-water emulsions of 65, 75 %wt at different gap heights. The small orange symbols are for a gap of 1000μm, the large pink symbols are for a gap of 500μm. Each symbol type corresponds to a particular concentration. A higher concentration increases the yield stress. Higher stresses at the smaller gap indicate a confinement effect.

A.2 Comparison of High-dimensional Data

The reader may question how necessary low-dimensional descriptions are when selecting between different candidate materials. It is fairly uncomplicated to compare the full flow curves of a few materials and discern qualitative differences in yield stress and even high-rate viscosity. Co-plotted in Figure A.13 are the full flow curves of the over twenty materials characterized in this work. Even for this limited database, it is not feasible to efficiently select or rank particular materials based on some performance target. Presented only with Figure A.13, ranking materials based on critical shear-rate (as in Section 2.5.1) would be an outrageously cumbersome task.

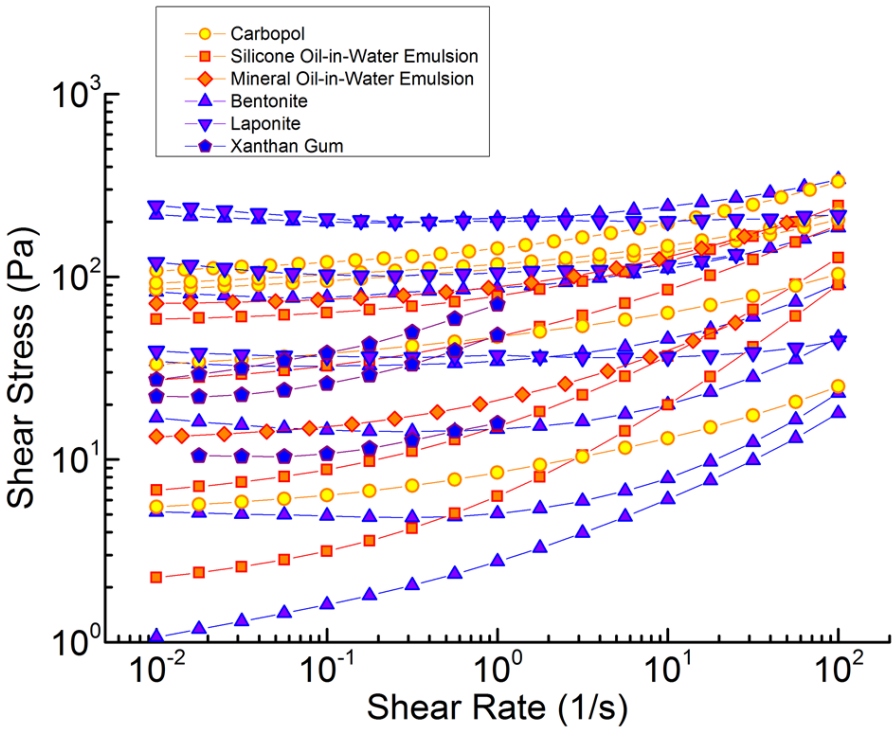

Figure A.13. Comparing the high-dimensional flow data of a significant number of materials is an ineffective method of rationally selecting materials. For this reason, low dimensional descriptions are necessary for design.

Appendix B:
Supplementary Information for Chapter 3

B.1 Considère Criteria for a Generalized Newtonian Fluid

This appendix provides a demonstration of the instability in extension of all Generalized Newtonian Fluid models (including Bingham and Herschel-Bulkley) according to the Considère criterion. This process has been used to predict the failure strain for constitutive equations that describe the behavior of polymer melts [147]. The Considère criterion states that homogeneous uniaxial elongation occurs provided the strain is less than the strain at which the maximum of the force occurs. In other words, a material is stable in uniaxial extension in the Z-direction for

$$\frac{dF_z}{d\varepsilon} > 0 \tag{B.1}$$

where F_z is the tensile force and ε is the applied true strain. For constant strain rate $\dot{\varepsilon}_0$,

$$\frac{dF_z}{d\varepsilon} = \frac{dF_z}{dt}\frac{1}{\dot{\varepsilon}_0} \tag{B.2}$$

and for total stress tensor $\underline{\underline{\sigma}}(t)$, cross-sectional area $A(t)$, free surface in r-direction, and uniaxial extensional viscosity $\eta_u(t)$,

$$F_z(t) = [(\sigma_{zz}(t) - \sigma_{rr}(t)]A(t) = \dot{\varepsilon}_0 \eta_u(t) A(t) \,. \tag{B.3}$$

Therefore,

$$\frac{dF_z}{d\varepsilon} = \eta_u(t)\frac{dA}{dt} + A(t)\frac{d\eta_u}{dt} \quad . \tag{B.4}$$

For an incompressible generalized Newtonian fluid model (i.e. $\underline{\underline{\sigma}} = \eta(\dot{\gamma})\underline{\underline{\dot{\gamma}}}$), where $\underline{\underline{\dot{\gamma}}} = \underline{\nabla v} + (\underline{\nabla v})^{\mathrm{T}}$, and $\dot{\gamma} = \sqrt{\frac{1}{2}\underline{\underline{\dot{\gamma}}} : \underline{\underline{\dot{\gamma}}}} = \sqrt{3}\dot{\varepsilon}_0 = \text{constant}$,

$$\frac{dA}{dt} < 0 \tag{B.5}$$

$$\frac{d\eta_u}{dt} = 0 . \tag{B.6}$$

Therefore,

$$\frac{dF}{d\varepsilon} < 0 \tag{B.7}$$

at all times. Therefore, for any assumed $\eta(\dot{\gamma})$, including the re-formatted Herschel-Bulkley model where $\eta(\dot{\gamma}) = \frac{\sigma_Y}{\dot{\gamma}} + \frac{\sigma_Y}{\dot{\gamma}_{critical}}\dot{\gamma}^{n-1}$, stable uniaxial elongation is never guaranteed.

B.2 Detailed Extensional Rheology Data

Figures B.1 through B.6 depict the repeated transient extensional experiments for each material formulation. The bold data points are the averages of the repeat experiments (faded data points). For each experiment, the rupture strain was determined based on concurrent video. The average rupture strain is indicated by the vertical dotted line; the shaded region is the standard deviation from the repeat experiments. A constant true strain rate of 0.2 s^{-1} was used for all experiments.

Figures B.7 through B.9 depict the rheological characterization of the application-relevant materials in both shear and extension except for Mystic Smoke, the characterization of which is given in Chapter 4.

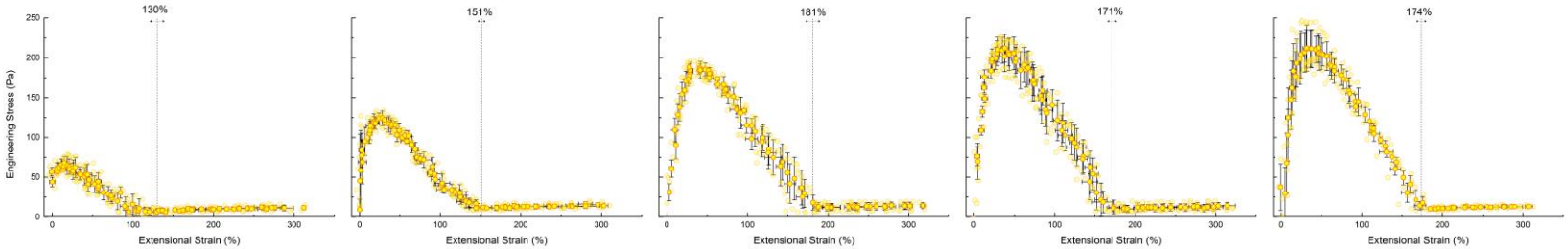

Figure B.1. Extensional engineering stress curves for Carbopol of 0.1, 0.15, 0.2, 0.25, 0.5 %wt additive from left to right tested using the ARES-G2 filament stretching experimental setup. The bold data points are the average of repeated experiments (faded data points) which provide the error bars. The vertical dashed lines depicts the average strain-to-break which was found by correlating the extensional stress curves with video images. The horizontal arrows below the strain-to-break labels depict the standard deviation in the strain-to-break from repeated experiments. A constant true strain-rate of 0.2 was used for all extensional tests.

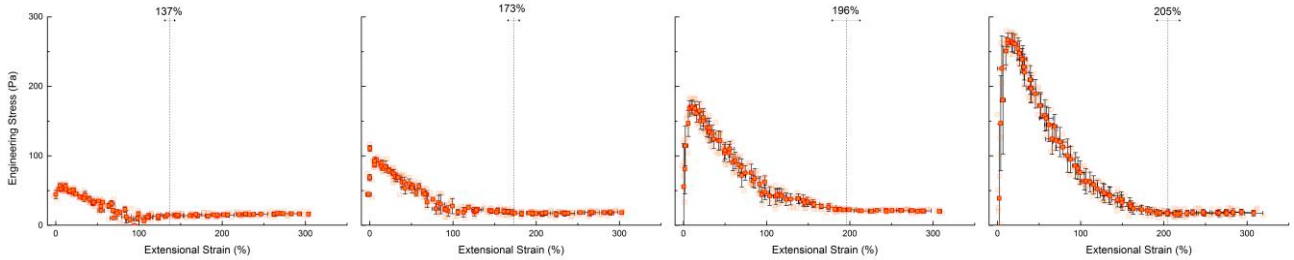

Figure B.2. Extensional engineering stress curves for silicone oil-in-water emulsions of 65, 70, 75, 80 %wt oil from left to right tested using the ARES-G2 filament stretching experimental setup. The bold data points are the average of repeated experiments (faded data points) which provide the error bars. The vertical dashed lines depicts the average strain-to-break which was found by correlating the extensional stress curves with video images. The horizontal arrows below the strain-to-break labels depict the standard deviation in the strain-to-break from repeated experiments. A constant true strain-rate of 0.2 was used for all extensional tests.

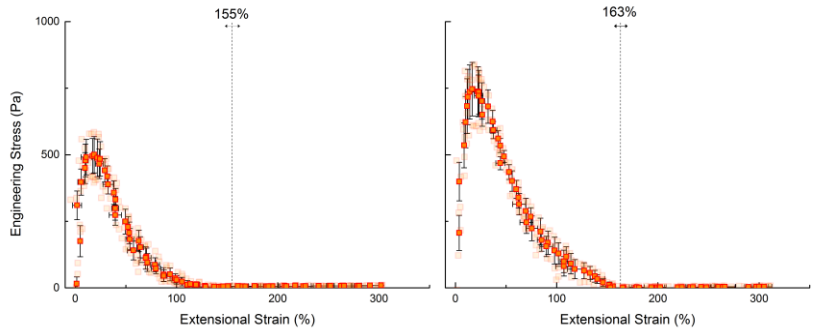

Figure B.3. Extensional engineering stress curves for mineral oil-in-water emulsions of 65, 75%wt oil from left to right tested using the ARES-G2 filament stretching experimental setup. The bold data points are the average of repeated experiments (faded data points) which provide the error bars. The vertical dashed lines depicts the average strain-to-break which was found by correlating the extensional stress curves with video images. The horizontal arrows below the strain-to-break labels depict the standard deviation in the strain-to-break from repeated experiments. A constant true strain-rate of 0.2 was used for all extensional tests.

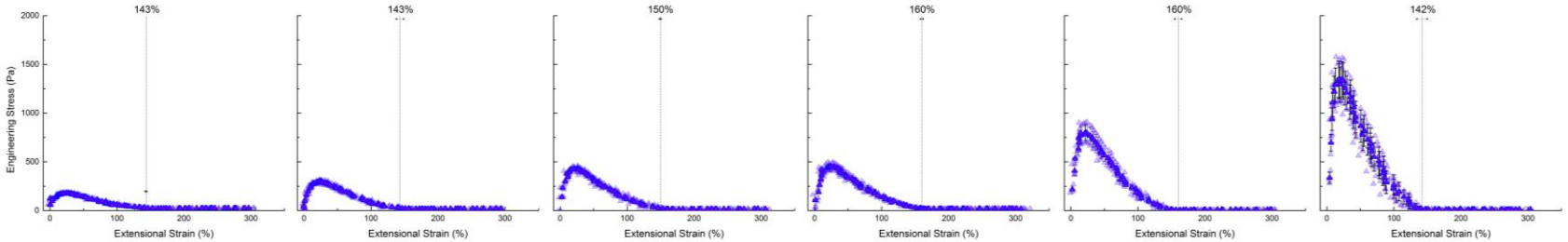

Figure B.4. Extensional engineering stress curves for Bentonite 7, 8, 9, 10, 11, 12 %wt of additive from left to right tested using the ARES-G2 filament stretching experimental setup. The bold data points are the average of repeated experiments (faded data points) which provide the error bars. The vertical dashed lines depicts the average strain-to-break which was found by correlating the extensional stress curves with video images. The horizontal arrows below the strain-to-break labels depict the standard deviation in the strain-to-break from repeated experiments. A constant true strain-rate of 0.2 was used for all extensional tests.

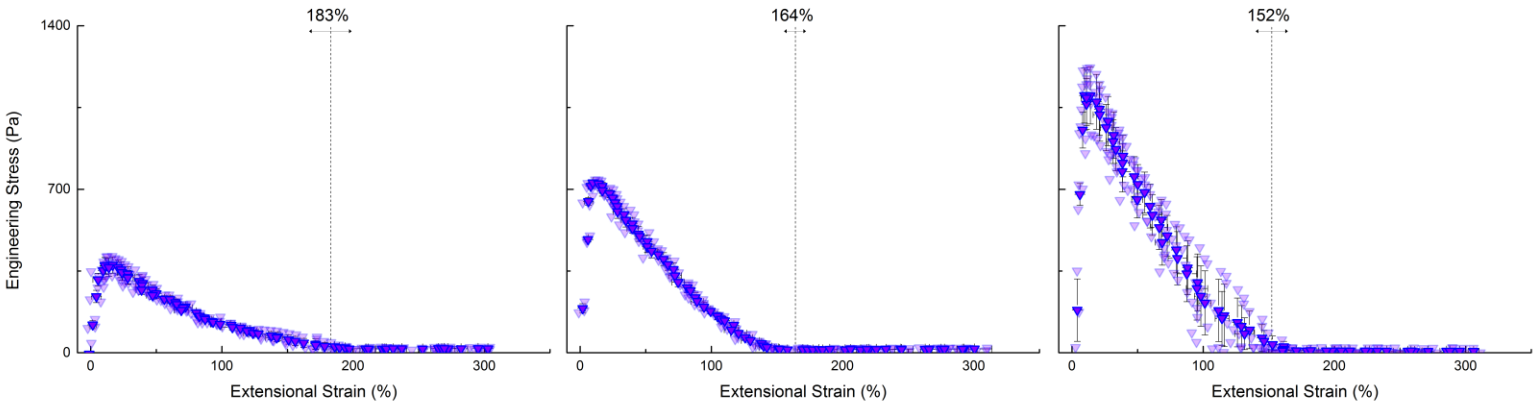

Figure B.5. Extensional engineering stress curves for Laponite 3, 4, 5 %wt of additive from left to right tested using the ARES-G2 filament stretching experimental setup. The bold data points are the average of repeated experiments (faded data points) which provide the error bars. The vertical dashed lines depicts the average strain-to-break which was found by correlating the extensional stress curves with video images. The horizontal arrows below the strain-to-break labels depict the standard deviation in the strain-to-break from repeated experiments. A constant true strain-rate of 0.2 was used for all extensional tests.

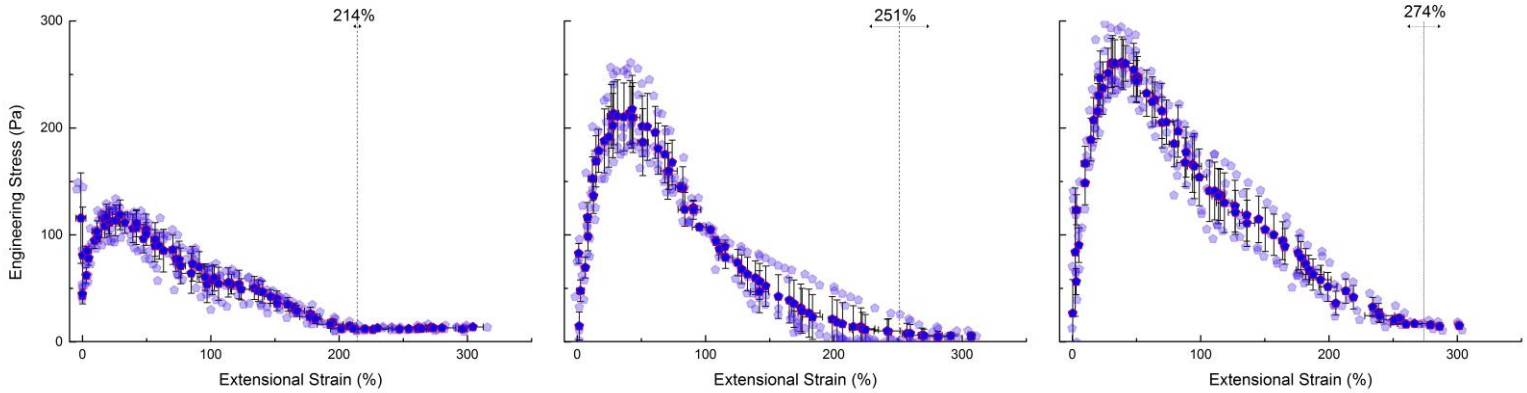

Figure B.6 Extensional engineering stress curves for Xanthan Gum of 2, 4, 5 %wt of additive from left to right tested using the ARES-G2 filament stretching experimental setup. The bold data points are the average of repeated experiments (faded data points) which provide the error bars. The vertical dashed lines depicts the average strain-to-break which was found by correlating the extensional stress curves with video images. The horizontal arrows below the strain-to-break labels depict the standard deviation in the strain-to-break from repeated experiments. A constant true strain-rate of 0.2 was used for all extensional tests.

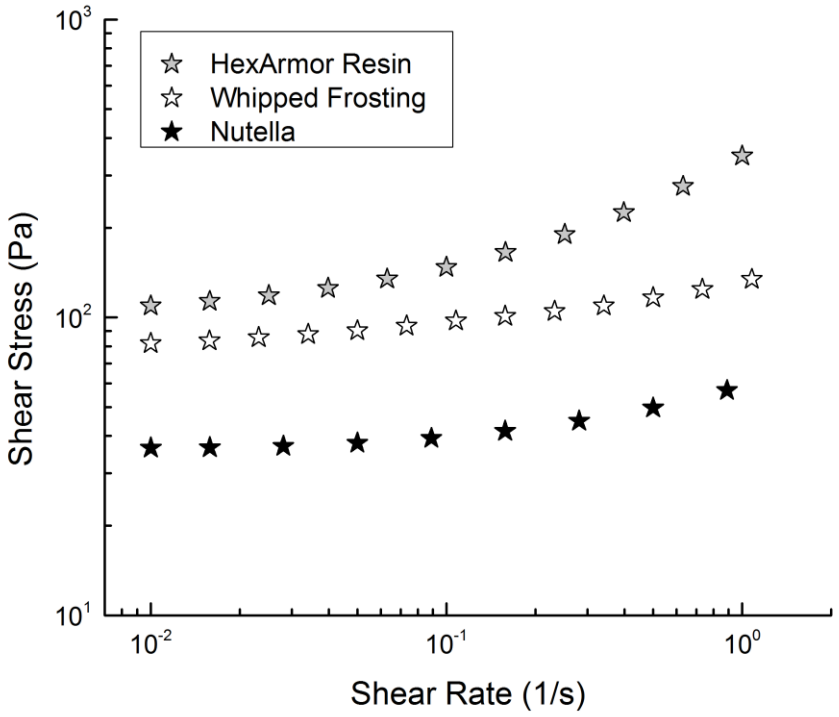

Figure B.7. Steady simple shear flow from high to low rate for three consumer products which show extensibility. All tests were from high to low shear rate, and so the low-rate plateaus indicate the dynamic yield stress.

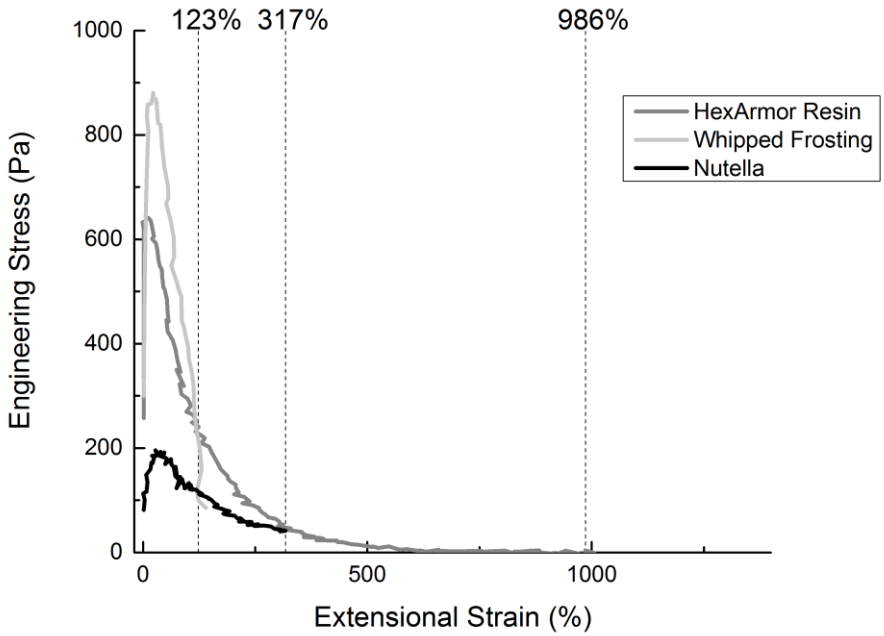

Figure B.8. Extensional engineering stress curves for three consumer products tested using the ARES-G2 filament stretching experimental setup. The vertical dashed lines depicts the average strain-to-break which was found by correlating the extensional stress curves with video images. A constant true strain-rate of 0.2 was used for all extensional tests.

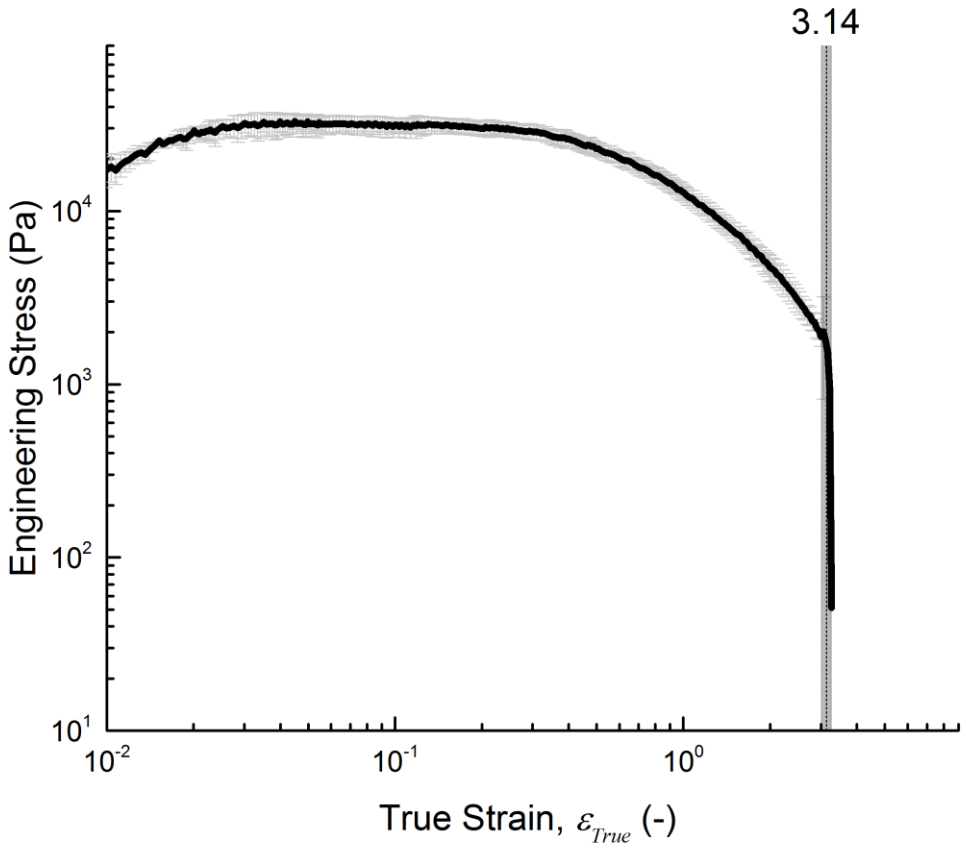

Figure B.9. Extensional engineering stress curves for three repeat experiments on Laffy Taffy at 37 °C using the SER3 counter-rotating-drum stretching experiment. The black curve shows the average of the three gray curves. For comparison with other materials, the true strain was related to engineering strain with Equation (2). The vertical dashed line depicts the average strain-to-break which was found by correlating the extensional stress curves with video images. A constant true strain-rate of 0.2 was used for all extensional tests.

B.3 Characterization of 50 wt% oil model formulation

Figure B.10 shows the characterization from steady shear flow of the proposed model material (creep characterization given in Section 3.4.2), including a 50wt% oil formulation. No apparent yield-stress behavior is observed for the 50wt% formulation.

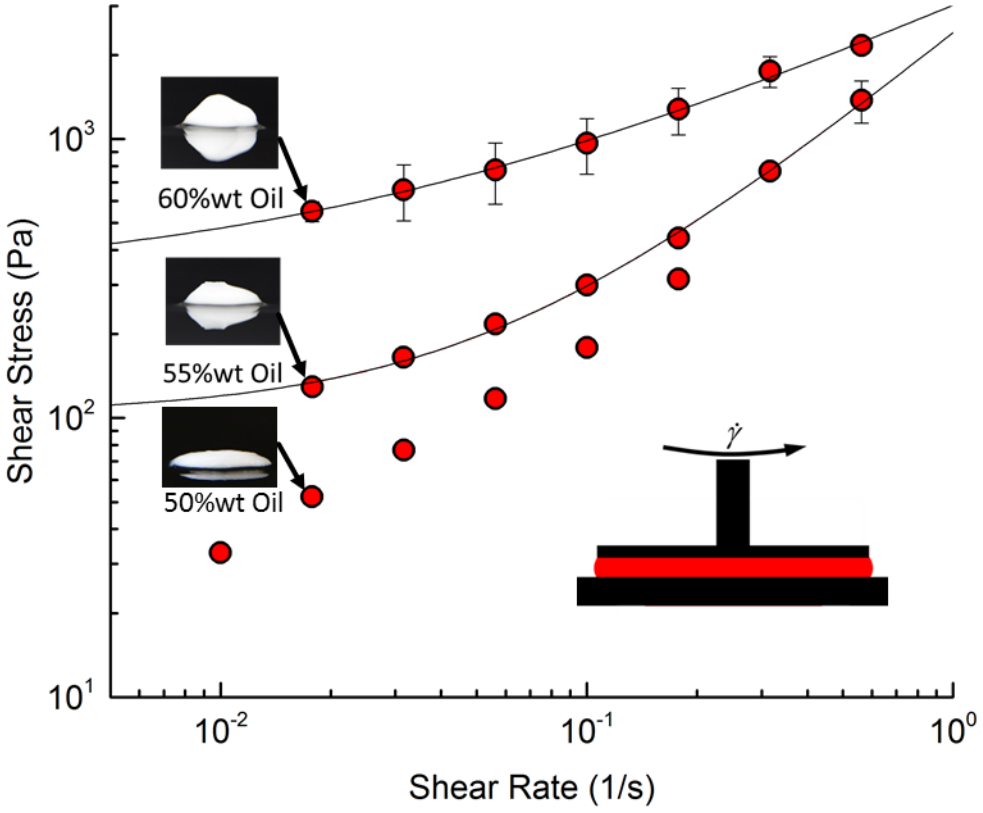

Figure B.10. Steady simple shear flow from low to high shear rate at a gap of 1000 μm for three formulations of the proposed model material made with 50, 55, and 60wt% Silicone Oil. Increasing the oil droplet concentration results in increased flow stress. Lines indicate the fit to a Herschel-Bulkley model. Error bars are the result of repeated experiments. The 50wt% oil concentration did not show a yield stress and was not repeatedly tested. The width of each photo is 20mm.

Appendix C:
Supplementary Information for Chapter 5

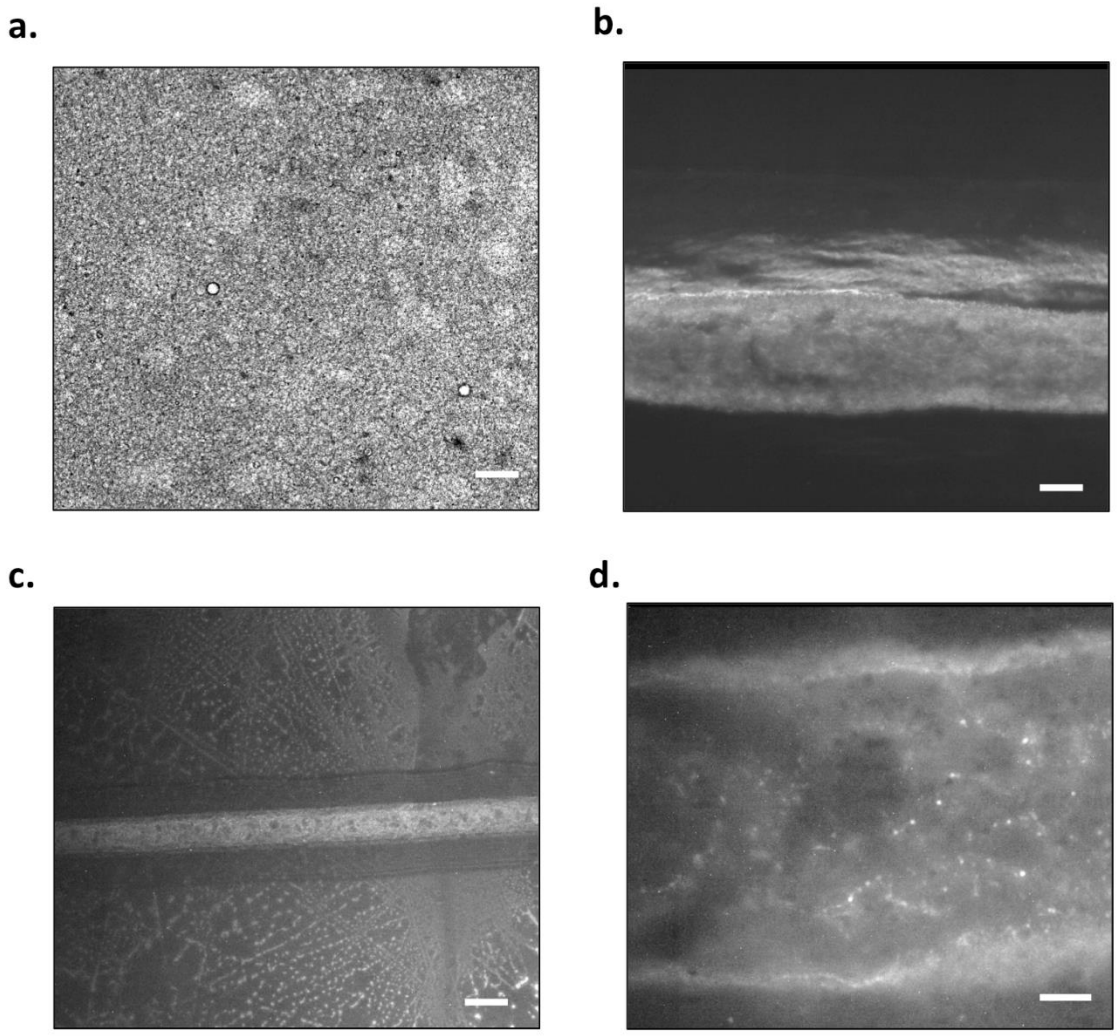

Figure C.1. a. Transmitted brightfield microscopy of bulk No PEO emulsion with Congo Red, scale bar 50 μm, fluorescence microscopy of line pattern of No PEO emulsion with Congo Red printed at 1 mm/s, b. 100 μm diameter tip, scale bar 50 μm, c. 1 μm diameter tip, scale bar 50 μm, d. 1 μm diameter tip, scale bar 10 μm.

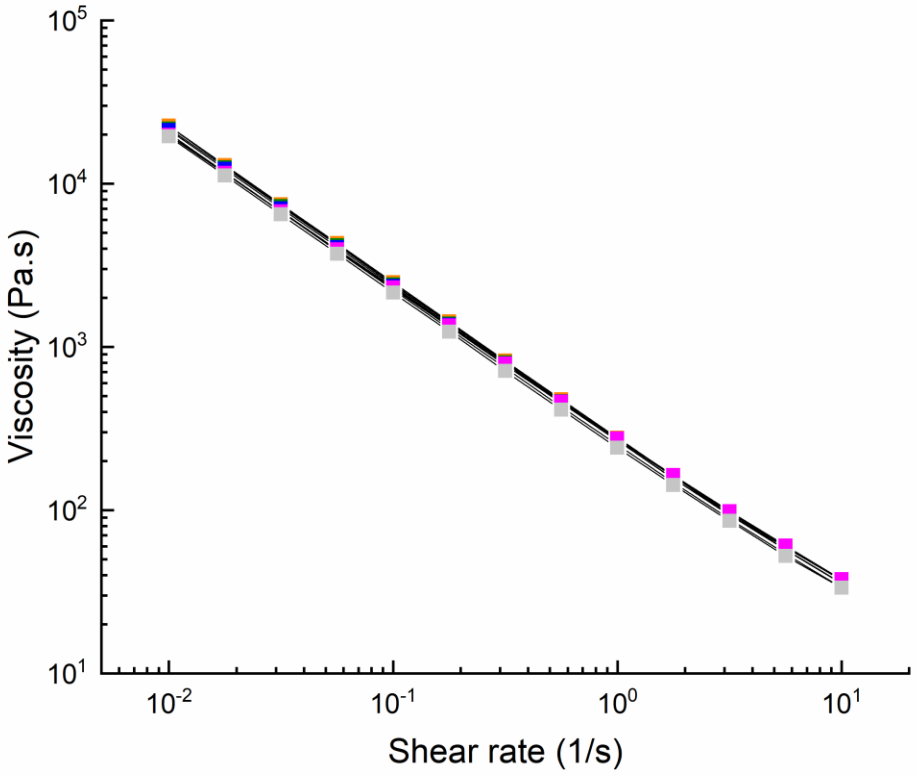

Figure C.2. Viscosity as a function of shear rate for No PEO (black), 400 K PEO (red), 600 K PEO (orange), 900 K PEO (green), 1 M PEO (blue), 4 M PEO (purple), 5 M PEO (pink), 8 M PEO (gray), error bars are smaller than data points. Viscosity is calculated from data points in Figure 2b.

a.

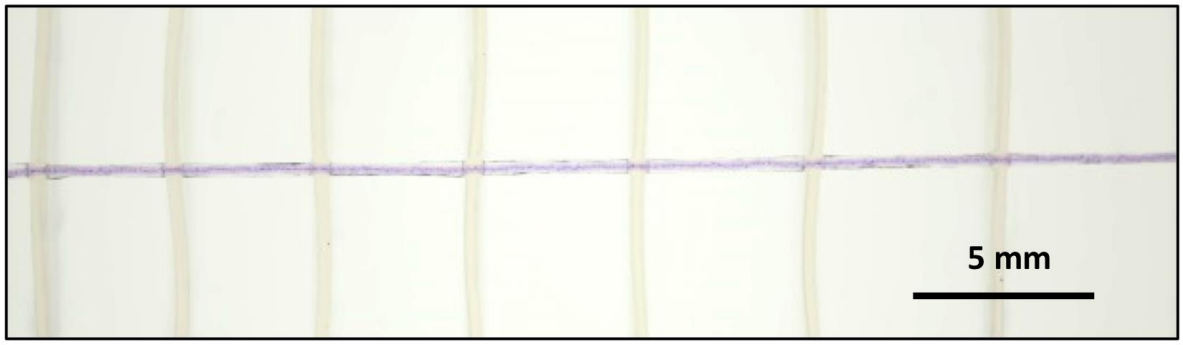

b.

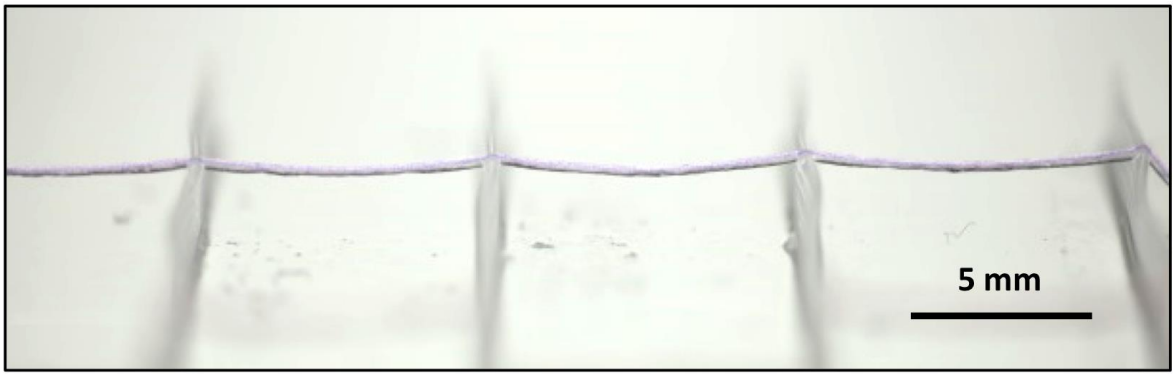

Figure C.3. Template for gap spanning experiment with successful gap spanning of 8M PEO emulsion with methylene blue filament printed with a 100 μm tip, a. top view, b. side view.

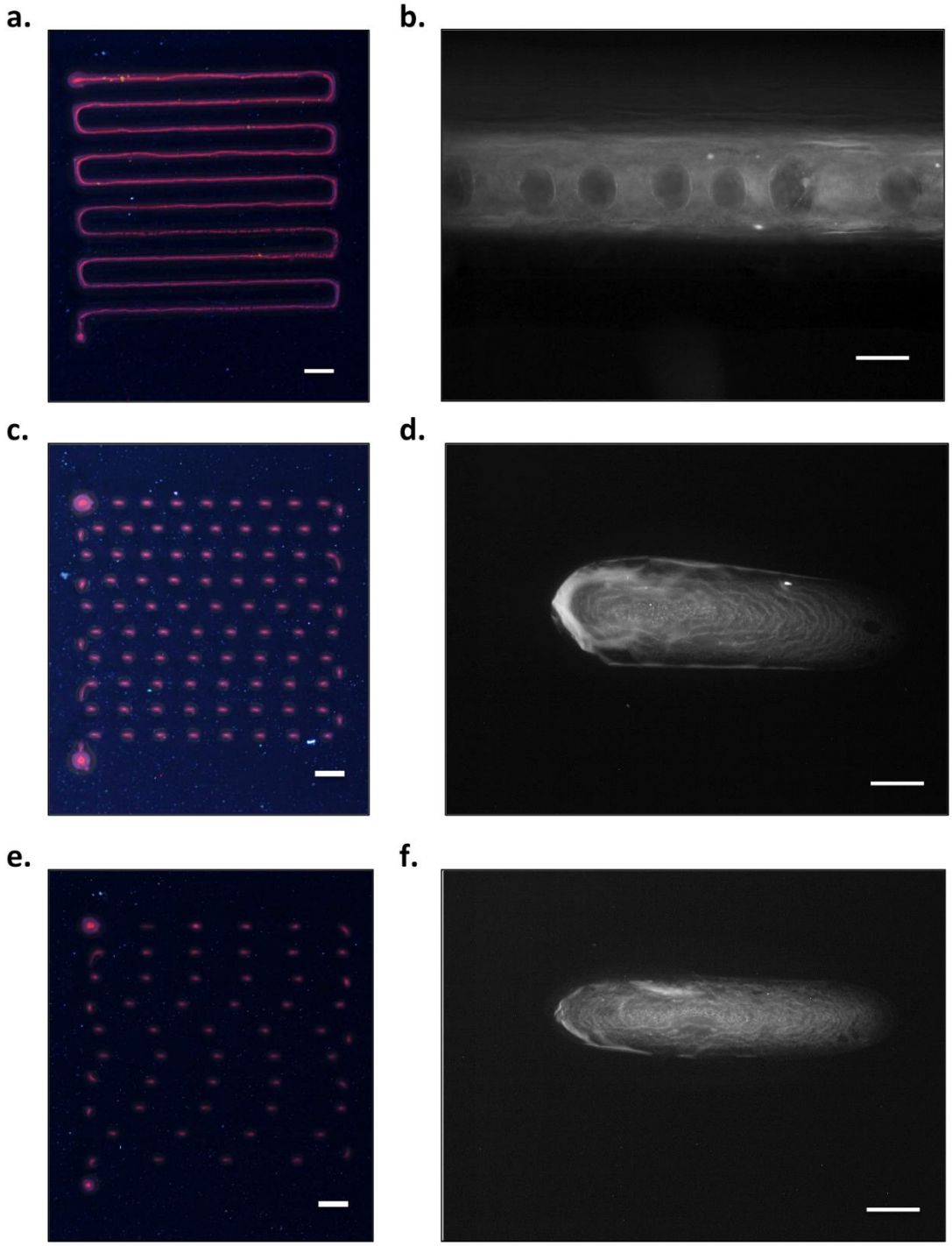

Figure C.4. Macro fluorescence image of line pattern of No PEO emulsion with Rhodamine 6G printed with 100 μm diameter tip printed at a. 1 mm/s, scale bar 1 mm, c. 10 mm/s, scale bar 1 mm, e. 20 mm/s, scale bar 1 mm. Fluorescence microscopy of line pattern of No PEO emulsion with Congo Red printed with 100 μm diameter tip printed at b. 1 mm/s, scale bar 100 μm, d. 10 mm/s, scale bar 100 μm, e. 20 mm/s, scale bar 100 μm.

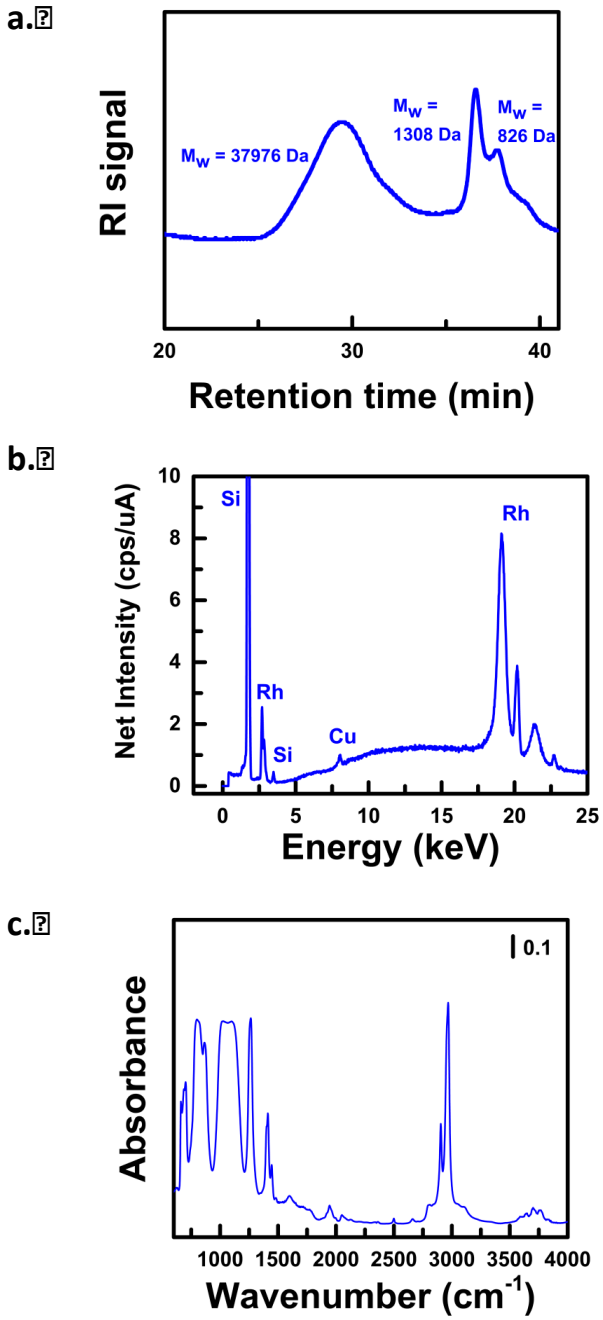

Figure C.5. a. GPC of unmodified silicone oil, b. survey of elements of unmodified silicone oil using XRF with a rhodium source, c. FTIR of unmodified silicone oil.

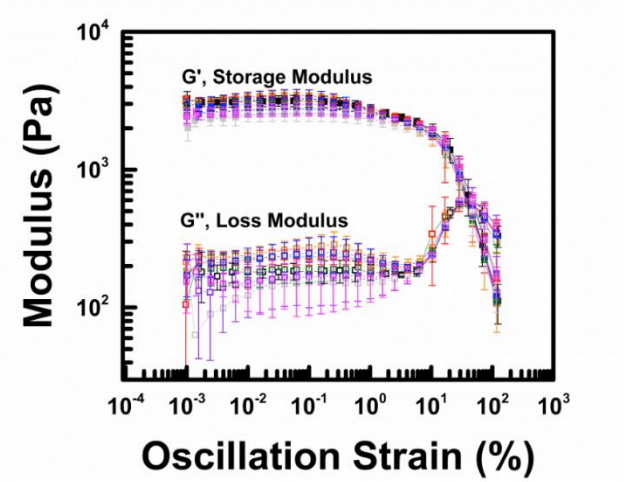

Figure C.6. Storage modulus (*G'*) and loss modulus (*G''*) as a function of oscillation strain for No PEO (black), 400 K PEO (red), 600 K PEO (orange), 900 K PEO (green), 1 M PEO (blue), 4 M PEO (purple), 5 M PEO (pink), 8 M PEO (gray), error bars are from repeat measurements.

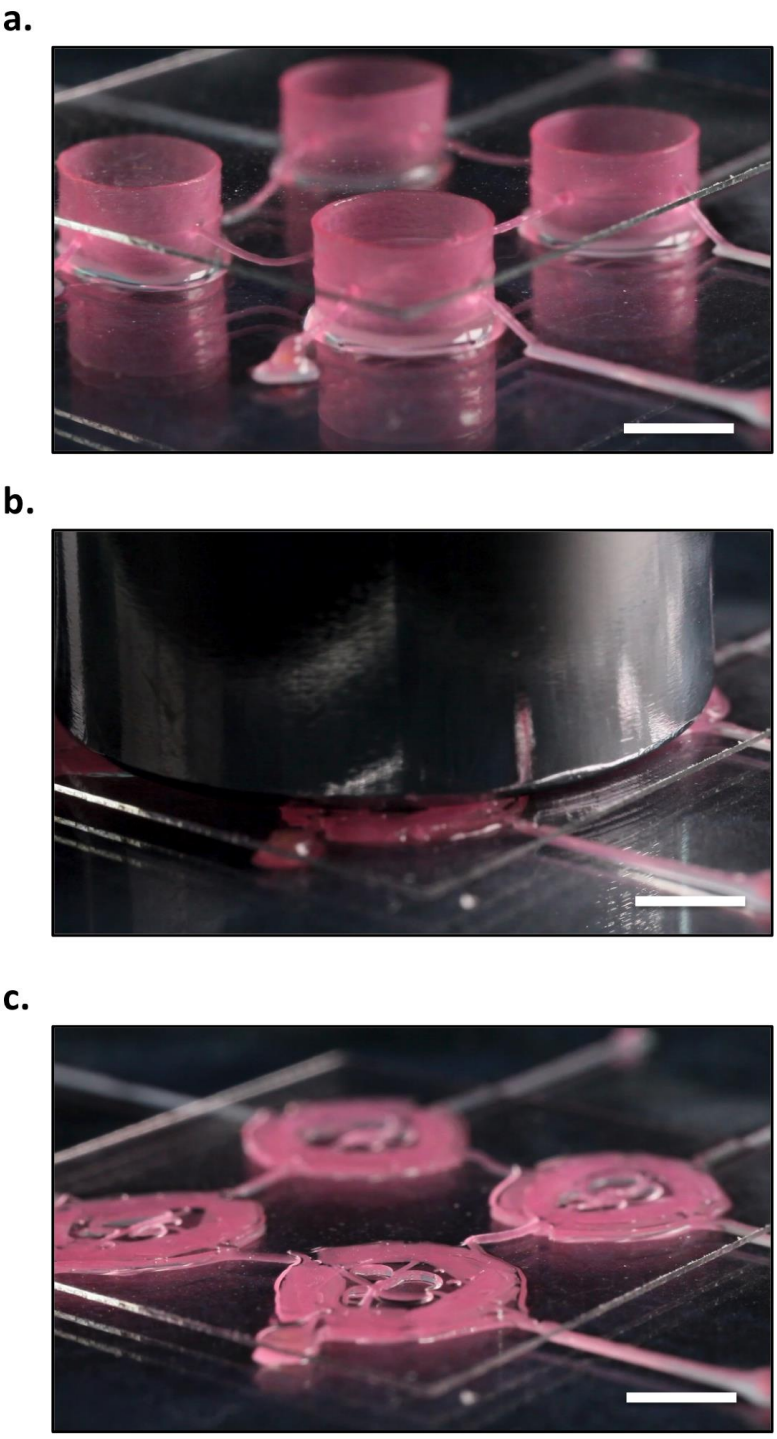

Figure C.7. Macro images of tubes interconnected with suspended filaments of chemically annealed 8M PEO emulsion with Rhodamine 6G, scale bar 5 mm a. with glass cover slip, b. with glass cover slip and 50 g weight, c. after 50 g weight removed.

Appendix D:
Supplementary Information for Chapter 6

D.1 Application Stress Magnitudes

This section demonstrates the calculations of representative stress magnitudes relevant for several application scenarios. In all of these scenarios, we will assume a density of water for the material (ρ = 1000 kg.m^{-3}). Naturally, methylcellulose solutions have a density slightly greater than water, but this is insignificant for the estimates here.

D.1.1 Gravitational stress on a vertical surface.

Given a uniform layer shown in Figure D.1A, with free-body diagram shown in Figure D.1B, the maximum stress, σ, distributed over the contact area, *bc*, is balanced by the weight of the layer, *W*.

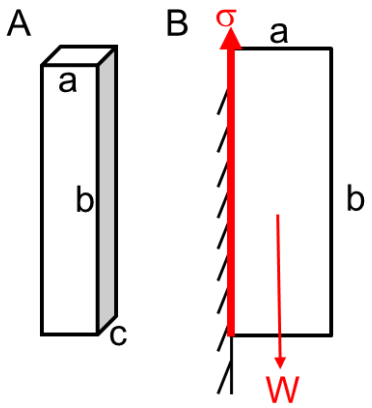

Figure D.1. A) Uniform layer with B) free-body diagram. Maximum shear stress occurs at the wall contact

Assuming uniform density, for a given maximum stress, $\sigma_{\max}$, balancing the forces and solving for the maximum thickness results in

$$a_{\max} = \frac{\sigma_{\max}}{\rho g} \ , \tag{D.1}$$

where g is the gravitational constant. More specifically, we can approximate the maximum gravitational stress of a layer of thickness, a, with density of water on a vertical surface with Earth gravitational constant as

$$\sigma_{\max} \approx \left(10^4 \frac{\mathrm{N}}{\mathrm{m}^3} \right) a \ . \tag{D.2}$$

For example, a 1mm thick coating experiences a maximum stress $\sigma_{\max} \approx 10$ Pa, as indicated in Figure 2 in the main paper.

D.1.2 Characteristic stress of droplet impact.

Given a spherical drop of diameter D, impacting a surface at a velocity v, we can develop a scaling law that relates a characteristic impact stress to the velocity of the droplet. Using the work-energy theorem, where the change in kinetic energy is equal to the work done on the droplet, we can represent the work done as,

$$\sigma\left(\text{Area}\right)\left(\text{Distance}\right) \sim \sigma\left(D^2\right)\left(D\right), \tag{D.3}$$

which we set equal to the change in kinetic energy for the droplet to come to rest,

$$\frac{1}{2} m v^2 = \frac{1}{2} \rho V v^2 \tag{D.4}$$

where V is the volume of the droplet which is proportional to D^3, and ρ is the density which we will approximate as that of water. Solving for the characteristic stress provides an estimate of stress that is consistent with the dynamic pressure to stagnate fluid flow,

$$\begin{aligned} \sigma &\sim \rho v^2 \\ &\approx \left(10^3 \frac{\text{kg}}{\text{m}^3}\right) v^2 \end{aligned} \tag{D.5}$$

Droplet velocities during spray coating can vary over a wide range. Perhaps on the slower end, consider a velocity of 0.3 m/s, which relates to characteristics stresses at impact of almost 100 Pa, as indicated in Figure 2 of the main text.

D.1.3 Characteristic stress of particle settling.

A gelled sample could inhibit particle sedimentation (or rising of air bubbles), but only if gelation can still occur under the associated dynamic stress conditions. Given a particle of diameter D, with a density difference comparable to the density of the surrounding medium ($\Delta\rho = \rho$, e.g. for an air bubble, or a particle at twice the density of the liquid), the characteristic stress scales as,

$$\sigma \sim \frac{\text{Net Weight/Buoyant Force}}{\text{Area}} \sim \frac{\rho g D^3}{D^2} \ . \tag{D.6}$$

Thus, for density differences on the order of water, and surface gravitational strength, the characteristic stress is estimated by

$$\sigma \approx \left(10^4 \frac{\text{N}}{\text{m}^3}\right) D \, . \tag{D.7}$$

For example, 1 mm diameter particles are associated with stresses on the order of 10 Pa, easily enough to disrupt gel formation for the formulations considered in this work.

D.2 Full Rheological Data

D.2.1 Quiescent Gel Point

Figures D.2 through D.6 show the small amplitude oscillatory shear (SAOS) measurements performed using the protocol detailed in the Experimental Section for all tested concentrations not shown in the main work. The "0 Pa" gel temperature for each concentration was determined from the crossover of *G'* and *G"*, except for 2.08%, the gel temperature of which was determined from the maximum slope of the moduli. Sub-dominant modulus data past the gel point was often difficult to resolve, particularly at higher concentrations; regions with non-physical moduli (i.e. negative values) are omitted for clarity. All error bars are from three repeat measurements; error bars not shown are smaller than the data points.

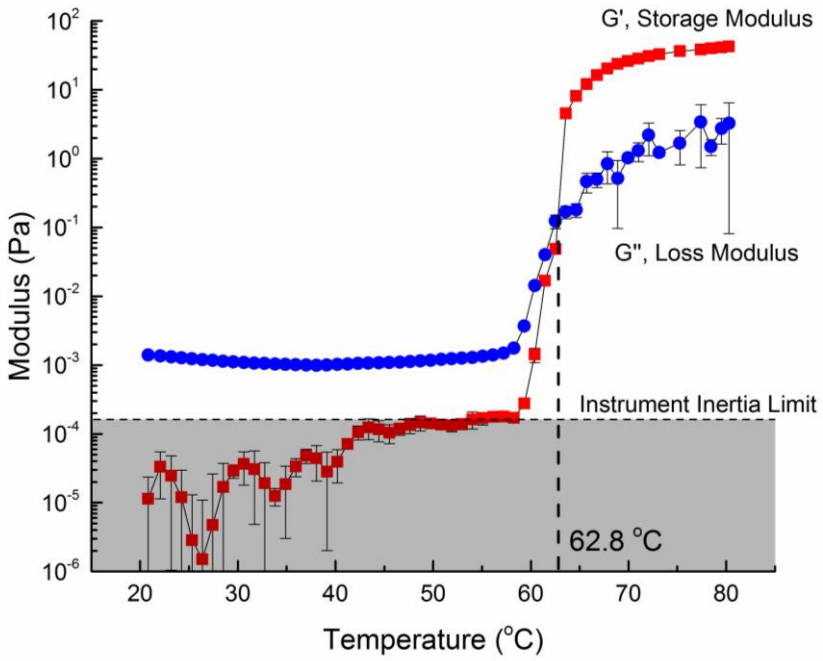

Figure D.2. *G'* and *G"* from SAOS measurements for MC 1.04% (oscillation frequency = 0.1 rad/s, stress amplitude = 0.1 Pa) while warming from 20 to 80°C at 1°C/min.

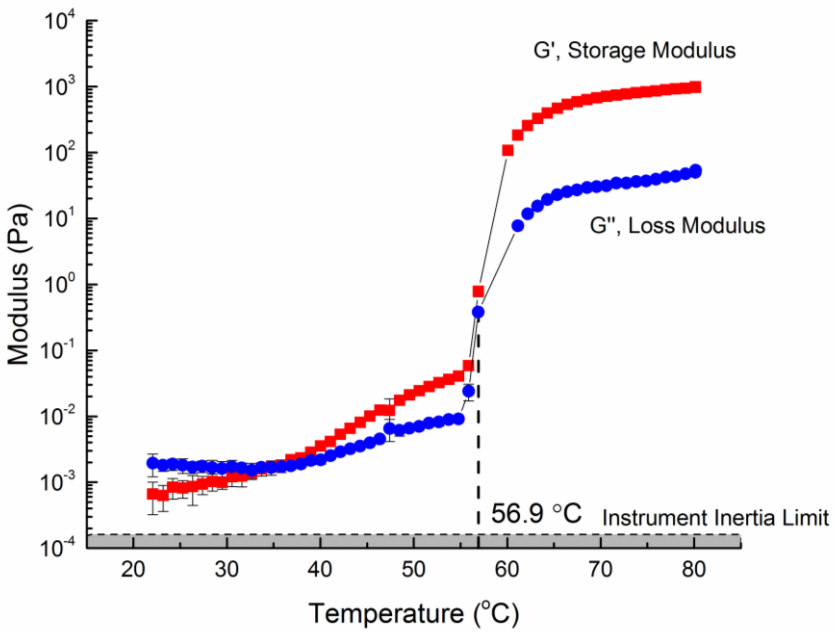

Figure D.3. *G'* and *G''* from SAOS measurements for MC 2.08% (oscillation frequency = 0.1 rad/s, stress amplitude = 0.1 Pa) while warming from 20 to 80°C at 1°C/min. Gel temperature was determined from the maximum slope of the moduli.

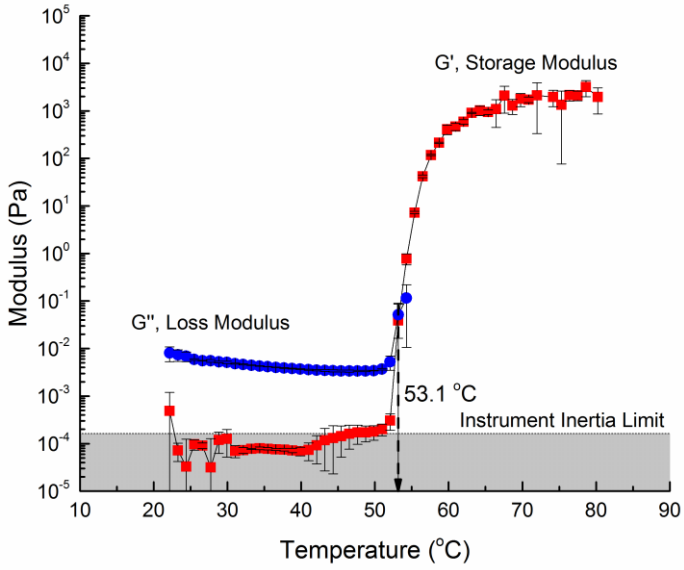

Figure D.4. *G'* and *G''* from SAOS measurements for MC 3.12% (oscillation frequency = 0.1 rad/s, stress amplitude = 0.1 Pa) while warming from 20 to 80°C at 1°C/min.

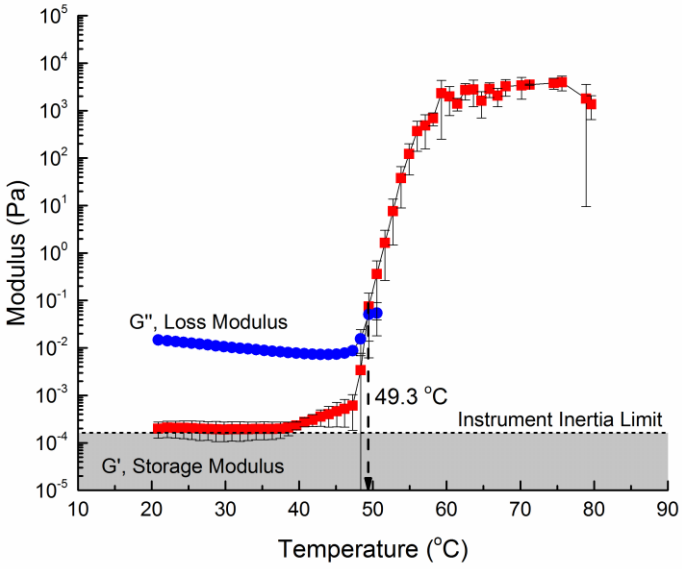

Figure D.5. *G′* and *G″* from SAOS measurements for MC 4.16% (oscillation frequency = 0.1 rad/s, stress amplitude = 0.1 Pa) while warming from 20 to 80°C at 1°C/min.

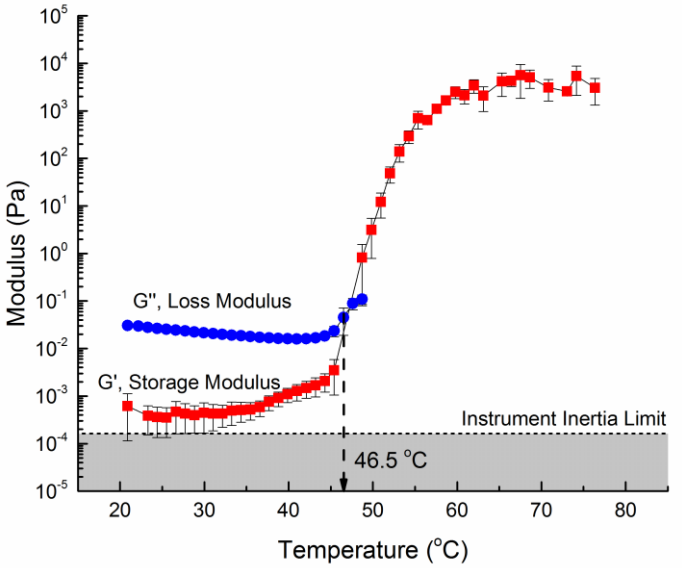

Figure D.6. *G′* and *G″* from SAOS measurements for MC 5.2% (oscillation frequency = 0.1 rad/s, stress amplitude = 0.1 Pa) while warming from 20 to 80°C at 1°C/min.

D.2.2 Dynamic Gel Point

Figures D.7 through D.10 show the dynamic gelation measurements performed using the protocol detailed in the Experimental Section for all tested concentrations not shown in the main work. The "0 Pa" gel temperature denotes the quiescent gel temperature. All error bars are from three repeat measurements; error bars not shown are smaller than the data points.

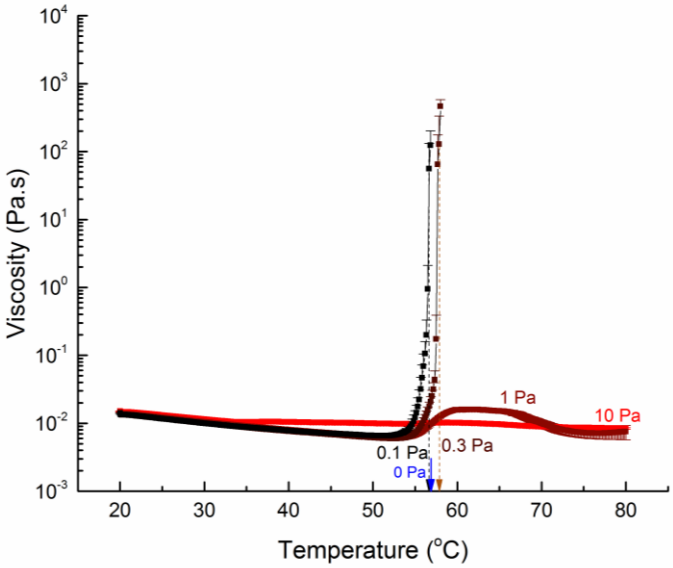

Figure D.7. Growth of the steady shear viscosity for MC 2.08% while warming from 20 to 80 °C at 1 °C/min while being subjected to selected shear stresses. The gelation temperatures $T_{gel}(d\eta/dT_{max})$ are marked with down-pointing arrows labeled with the applied shear stress.

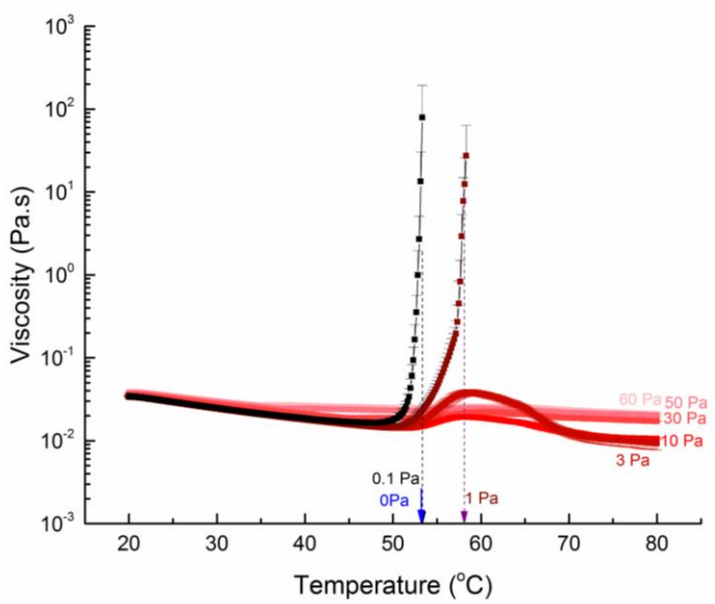

Figure D.8. Growth of the steady shear viscosity for MC 3.12% while warming from 20 to 80 °C at 1 °C/min while being subjected to selected shear stresses. The gelation temperatures $T_{gel}(d\eta/dT_{max})$ are marked with down-pointing arrows labeled with the applied shear stress.

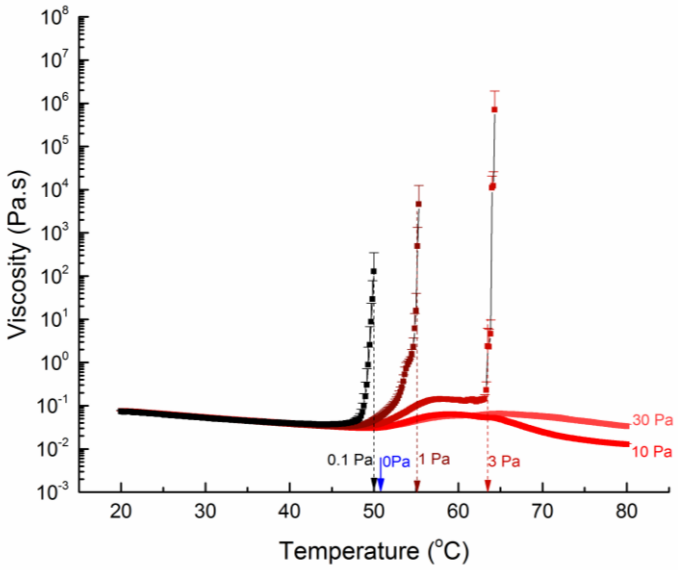

Figure D.9. Growth of the steady shear viscosity for MC 4.16% while warming from 20 to 80 °C at 1 °C/min while being subjected to selected shear stresses. The gelation temperatures $T_{gel}(d\eta/dT_{max})$ are marked with down-pointing arrows labeled with the applied shear stress.

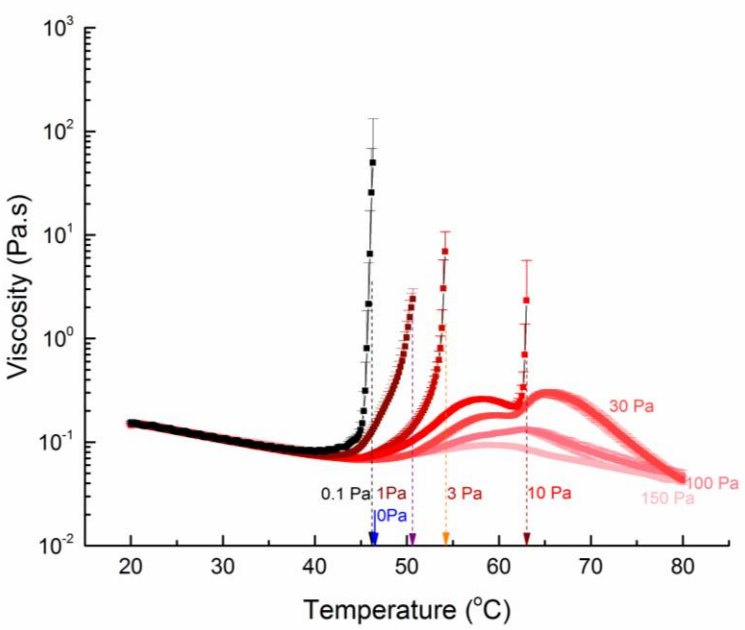

Figure D.10. Growth of the steady shear viscosity for MC 5.2% while warming from 20 to 80 °C at 1 °C/min while being subjected to selected shear stresses. The gelation temperatures $T_{gel}(d\eta/dT_{max})$ are marked with down-pointing arrows labeled with the applied shear stress.

D.2.3 Hot Gel Properties

Figures D.11 through D.14 show the hot gel storage modulus (G') obtained using the protocol detailed in the Experimental Section for all tested concentrations not shown in the main work. G" is omitted for clarity. In the linear viscoelastic region, G"/ G' is always less than 0.1. The "0 Pa" moduli are from the "true quiescent" tests. All error bars are from three repeat measurements; error bars not shown are smaller than the data points. Data sets are truncated at first observed apparent failure.

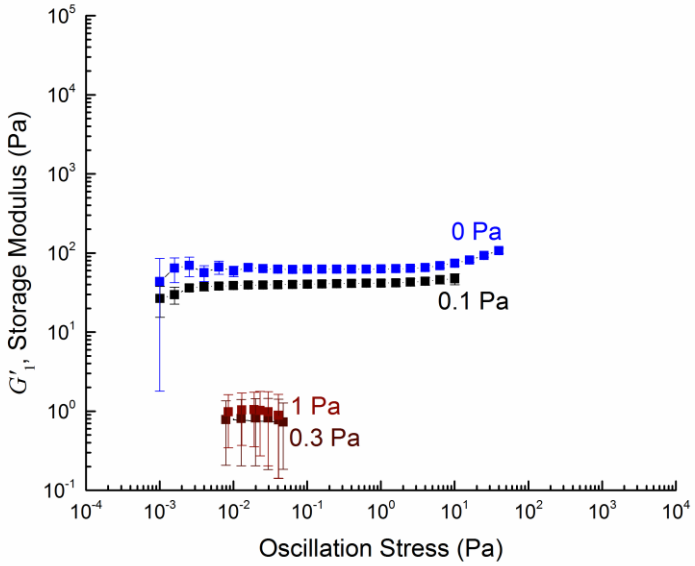

Figure D.11. LAOS measurements (3 rad/s, 80 °C) for MC 1.04% warmed from 20 to 80 °C at 1 °C/min while being subjected to a constant shear stress. Each stress amplitude sweep is truncated at the apparent failure stress. G'_{LVE} is obtained from a fit to the plateau at low oscillation stress.

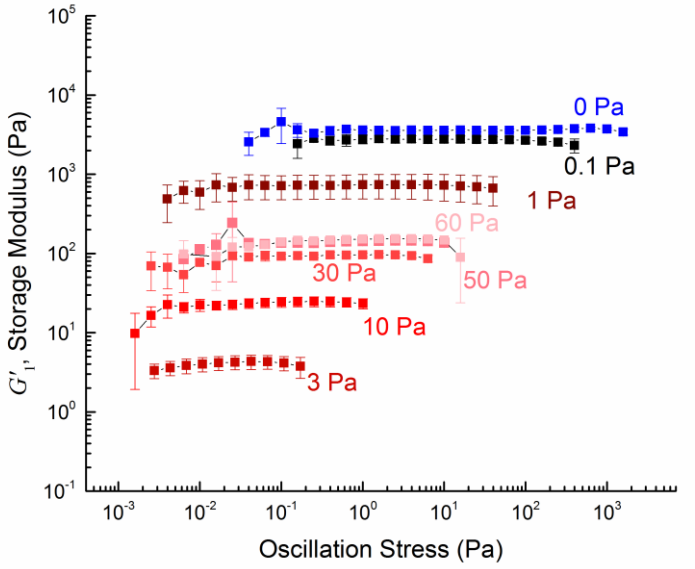

Figure D.12. LAOS measurements (3 rad/s, 80 °C) for MC 3.12% warmed from 20 to 80 °C at 1 °C/min while being subjected to a constant shear stress. Each stress amplitude sweep is truncated at the apparent failure stress. G'_{LVE} is obtained from a fit to the plateau at low oscillation stress.

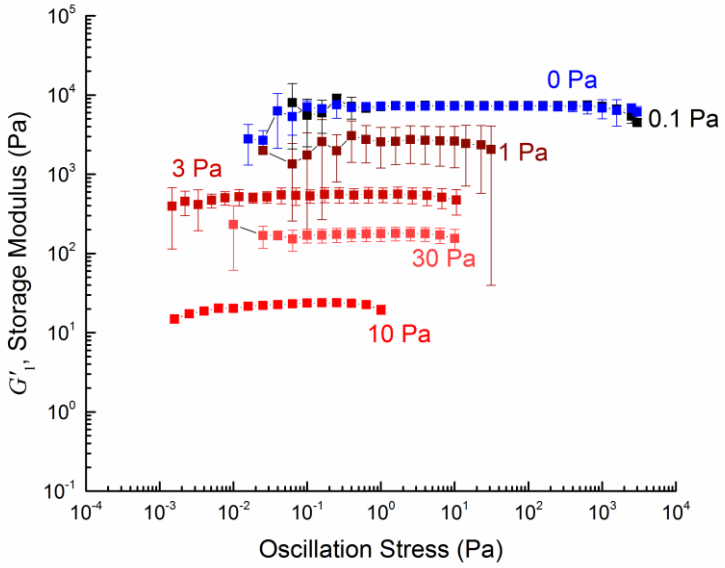

Figure D.13. LAOS measurements (3 rad/s, 80 °C) for MC 4.16% warmed from 20 to 80 °C at 1 °C/min while being subjected to a constant shear stress. Each stress amplitude sweep is truncated at the apparent failure stress. G'_{LVE} is obtained from a fit to the plateau at low oscillation stress.

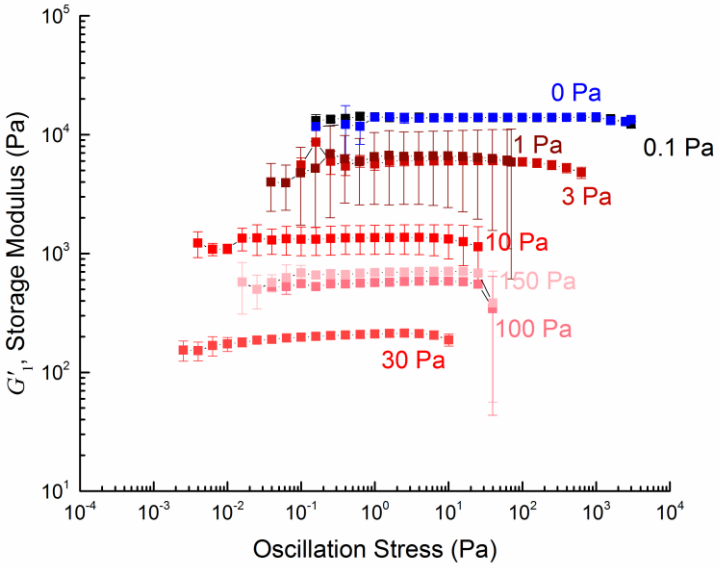

Figure D.14. LAOS measurements (3 rad/s, 80 °C) for MC 5.2% warmed from 20 to 80 °C at 1 °C/min while being subjected to a constant shear stress. Each stress amplitude sweep is truncated at the apparent failure stress. G'_{LVE} is obtained from a fit to the plateau at low oscillation stress.